London’s Global University

UCL

Mechanisms of Therapeutic Protein Aggregation During Peristaltic Pumping

by

Thomas Benjamin Fanthom

A thesis submitted for the degree of

Doctor of Engineering

in

The Department of Biochemical Engineering

UCL

September 2023

Declaration

I, Thomas Benjamin Fanthom, confirm that the work presented in my thesis is my own. Where information has been delivered from other sources, I confirm that this has been indicated in the thesis.

Thomas Benjamin Fanthom, 22 September 2023

Abstract

This research delves into the stability of recombinant botulinum neurotoxin during bioprocessing, focusing on the challenges posed by turbulent hydrodynamic flow, shear forces, and peristaltic pumping mechanisms. Developing ultra scale down devices to understand the factors governing protein aggregation and monomer loss is essential for the efficient production of therapeutic proteins.

In the first study, a comprehensive analysis of flow regimes inside a spinning disc device using computational fluid dynamics gave deeper insights into the flow regimes during operation. Monomer loss and particle formation data gathered from size-exclusion chromatography and backgrounded membrane imaging highlights that turbulent hydrodynamic flow is a significant contributor to -ve BoNT/E protein aggregation.

In the second study, a comparative analysis was conducted between a spinning disc device and a closed-loop peristaltic pump device, revealing distinct driving forces governing protein-protein and protein-interface interactions. The spinning disc device's unsuitability as a mimic for peristaltic pumping highlighted the need to explore peristaltic pumping mechanisms further.

The third study focused on developing novel methodologies to isolate and assess the impact of various peristaltic pump parameters on monomer loss and protein aggregation. Pump speed, occlusion, and tubing type underscored the crucial role of interfaces in protein adsorption, disruption, aggregation, and particle generation, emphasising their importance in process development and

pump setup. Strain on peristaltic pumping via tubing expansion and relaxation caused minor monomer losses, with tubing material influencing the extent of these losses. Solid-solid interface contact was identified as a significant contributor to monomer loss as a function of contact area.

In conclusion, this research highlights the solid-solid contact mechanism as the primary driver of protein aggregation during peristaltic pumping. The disruption and the reconstitution of these films create a challenging cycle in peristaltic pump applications. Understanding the underlying mechanisms behind monomer loss and protein aggregation is crucial for the bioprocessing industry to optimise production processes and ensure the stability of therapeutic proteins.

Impact Statement

Bioprocessing extends beyond the production of advanced therapeutic biologics, encompassing emerging fields like synthetic food production, notably dairy (whey) proteins. This thesis, while primarily focused on biopharmaceutical contexts, strives to offer valuable scientific insights and ultra-scale-down methodologies that can benefit researchers in both industry and academia engaged in the development of biologics manufacturing processes.

Our initial efforts centred on a comprehensive fluidic characterisation of the spinning disc ultra-scale-down device. This investigation aimed to delve into the hydrodynamic flow and shear forces it generates. Turbulence and shear forces during bioprocessing are linked to protein instabilities, jeopardising the effectiveness of therapeutics and the formation of product related impurities, for example aggregates, that pose risks to patient health. A deeper understanding of scale-down systems equips researchers to assess the stability of biological products and enhances process development by reducing the resources, time, and costs typically associated with such endeavours.

Spinning disc technology finds applications not only as ultra-scale-down tools within the in pharmaceutical industry but also as process intensification solutions, such as spinning disc reactors, in the chemical industry industrial. The knowledge we've made publicly available here can readily be transferred to researchers in industry and academia working on similar devices, promoting synergy across sectors.

Peristaltic pumping plays a pivotal role in the biologics industry, yet the mechanisms behind protein aggregation have remained elusive. The final chapter of this thesis delves into the impact of peristaltic pump parameters on protein aggregation, unravelling the primary mechanisms driving this phenomenon through innovative methodologies. Additionally, we shed light on the often-overlooked role of occlusion, a parameter critical to peristaltic pump efficiency, but conspicuously absent from the available literature.

The culmination of this work has been disseminated through four conferences, including three poster presentations (two at national and one at an international conference) and two oral presentations (one at a national conference with a poster and one at an international conference) and a peer-reviewed publication. The open-access nature of the peer-reviewed publication ensures accessibility not only to fellow researchers but also to the broader public, fostering collaboration and knowledge dissemination.

In summary, the expertise, knowledge, and insights generated in this thesis have far-reaching implications, transcending the boundaries of biopharmaceuticals and spanning into emerging fields like synthetic food production and the chemical industry. By enhancing our understanding of scale-down systems and unravelling the mysteries of peristaltic pumping mechanisms, this research equips both industry and academia with the tools needed to advance biologics manufacturing processes, reduce costs, and improve product quality, ultimately benefiting patient health and food production efficiency.

Publications

A significant portion of the work that follows has been submitted or published in a peer reviewed journal and presented in poster and oral form. Details of these can be found below.

Peer reviewed publications:

Fanthom, T. B., Wilson, C., Gruber, D., & Bracewell, D. G. (2023). Solid-Solid Interfacial Contact of Tubing Walls Drives Therapeutic Protein Aggregation During Peristaltic Pumping. *Journal of Pharmaceutical Sciences*. https://doi.org/10.1016/j.xphs.2023.08.012

Conference presentations:

Fanthom, T. B., Wilson, C., Gruber, D., & Bracewell, D. G. (2021, November 24). Identification of root cause mechanisms of therapeutic protein loss in peristaltic pumping operations. *18th Annual BioProcessUK Conference*. (Poster presentation)

Fanthom, T. B., Wilson, C., Gruber, D., & Bracewell, D. G. (2022, August 9). Solid-solid interface contact drives therapeutic protein degradation during peristaltic pumping. *Protein Stability Conference*. (Poster presentation).

Fanthom, T. B., Wilson, C., Gruber, D., & Bracewell, D. G. (2022, November 16). Solid-solid interface contact drives therapeutic protein degradation during peristaltic pumping. *19th Annual BioProcessUK Conference*. (Oral and poster presentation).

Fanthom, T. B., Wilson, C., Gruber, D., & Bracewell, D. G. (2023, August 15). Solid-solid Interfacial Tubing Contact During Peristaltic Pumping is a Primary Mechanism of Therapeutic Protein Aggregation. *Division of Biochemical Technology of the American Chemical Society (ACS BIOT))*. (Oral presentation).

Acknowledgements

Thank you to my supervisors Prof. Daniel Bracewell and David Gruber for their unwavering support and mentorship throughout this project. Their scientific curiosity, industry knowledge and personal approach has been constantly motivating. Thank you also to Christopher Wilson and Edward Busby whose guidance and expertise was invaluable. Creating all the various “Heath Robinson” devices over the years has been testing, but rewarding and fun.

The project would not have been possible without support from the Engineering and Physical Sciences Research Council (EPSRC) and Ipsen Biopharm Ltd. It was tremendous working with the very talented people at Ipsen who were always at hand to help.

My colleagues and friends have been integral to my EngD experience, and it would not have been the same without them. Roman Labbe, Jack Firth and Georg von Massow – thanks for being there in the lab, at lunches, at the pub and being a part of Team OMV. Our entrepreneurship journey, with Prof. Kenth Gustafsson and Tiffany Hood, has been exciting since the beginning and will continue to be just so.

The Department of Biochemical Engineering has been the most supportive, collaborative, friendly and inspirational community to be a part of. Thanks to the Head of Department Prof. Gary Lye, all the Academic and Teaching staff, Professional Services staff, and research fellows and assistants who are all instrumental in nurturing this.

Thank you to my parents, Tracey and Neil, who have from always allowed me the freedom to experience the world through my own eyes.

Finally, Greta, thank you for all the joy that you give me.

Table of Contents

Table of Figures

List of Tables

List of Abbreviations

Abs	Absorbance
AEX	Anion exchange chromatography
BD	Binding domain
BMI	Backgrounded membrane imaging
BoNT	Botulinum neurotoxin
CAD	Computer aided design
CFD	Computational fluid dynamics
CPP	Critical process parameter
CQA	Critical quality attribute
CV	Column volume
DAD	Diode-array detector
DLS	Dynamic light scattering
ECD	Equivalent circular diameter
EMA	European Medicines Agency
HC	Heavy chain
HCl	Hydrochloric acid
HIC	Hydrophobic interaction chromatography
HPLC	High-performance Liquid Chromatography

ICH	International Council for Harmonisation of Technical Requirements for Pharmaceuticals for Human Use
IEX	Ion exchange chromatography
IgG	Immunoglobulin G
IIDC	Isothermal interfacial compression-dilation
LC	Light chain
MWCO	Molecular weight cut-off
NaCl	Sodium chloride
NaOH	Sodium hydroxide
NTA	Nanoparticle tracking analysis
PES	Polyethersulfone
PFA	Perfluoroalkoxy
PFlex	Puri-Flex
Ph. Eur.	European Pharmacopeia
pI	Isoelectric point
PMed	PharMed BPT
PVDF	Polyvinylidene fluoride
SD	Standard deviation
SEC	Size-exclusion chromatography
SEM	Scanning electron microscopy

SIMI	Side-illuminated membrane imaging
Si-Pt	Platinum-cured silicone
Si-Pt Bio	BioPharm platinum-cured silicone
SLS	Static light scattering
SS	Stainless steel
SST	Shear stress transport
TD	Translocation domain
TFF	Tangential flow filtration
Tygon	Tygon E-Lab
UF/DF	Ultrafiltration/diafiltration
UPLC	Ultra-performance liquid chromatography
USD	Ultra scale-down
USP-NF	United States Pharmacopeia-National Formulary
UV-Vis	Ultraviolet visible wavelength

List of Notations

C_0	Concentration at time *0*
C_t	Concentration at time *t*
d_i	Disc diameter (mm)
d_{id}	Tubing inner diameter (mm)
d_o	Chamber diameter (mm)
$d_{particle}$	Particle diameter (µm)
h	Gap between peristaltic roller and occlusion bed (mm)
h_i	Disc height (mm)
h_o	Chamber height (mm)
h_r	Hours
k	Protein decay coefficient (hr^{-1})
l	Length of tubing after strain
l_0	Length of tubing
M	Concentration ($mol.L^{-1}$)
min	Minutes
P95	95th percentile
px	Pixel
R^2	Coefficient of determination
Re	Reynolds number

r_g	Radial gap (mm)
RPM	Rotations per minute
s	Seconds
s^{-1}	Shear strain rates
t	Time (mins, hr)
t_{wall}	Tubing wall thickness (mm)
T_{agg}	Temperature of aggregation (^oC)
T_m	Apparent melting temperature (^oC)
T_{onset}	Temperature of onset aggregation (^oC)
U_1	Tip speed ($m.s^{-1}$)
Y+	Dimensionless wall distance for a wall-bounded flow
Y_+ max	Maximum dimensionless wall distance for a wall-bounded flow
y_g	Axial gap (mm)
ε	Turbulent energy dissipation rate ($m^2.s^{-3}$)
ε_{max}	Maximum turbulent energy dissipation rate ($m^2.s^{-3}$)
η	Kolmogorov length scale (μm)
μ	Dynamic viscosity ($kg.m^{-1}.s^{-1}$, Pa.s)
v	Kinematic viscosity ($m^2.s^{-1}$)
ρ	Fluid density ($kg.m^{-1}$)
ω	Rotational speed ($rad.s_{-1}$)

1 Introduction

1.1 Botulinum Neurotoxin (BoNT)

1.1.1 Introduction and mechanism of action

Botulinum neurotoxins (BoNTs) represent the most potent compounds known and have found remarkable success as therapeutic proteins. They belong to a family of proteins produced by the bacterium Clostridium botulinum, causing the rare yet severe illness known as 'Botulism.' If left untreated, Botulism can be lethal due to the development of flaccid paralysis. This neuroparalytic condition is primarily attributed to botulinum neurotoxins (BoNTs)

BoNTs are highly neuro-specific and extremely toxic, with a lethal dose as low as 1 $ng.kg^{-1}$ (Montal, 2010). Despite their inherent toxicity, they have demonstrated significant therapeutic potential in treating various neurological diseases. Serotype-A is the most commercially relevant BoNT, serving as the primary active pharmaceutical ingredient in three of the largest BoNT-based drugs on the market: abobotulinumtoxinA, incobotulinumtoxinA, and onabotulinumtoxinA. These drugs are approved for clinical use across 20 different medical indications. For example, abobotulinumtoxinA can be used clinically to treat cervical dystonia, upper-limb spasticity and lower-limb spasticity (Simpson *et al.*, 2016).

Currently, several natural serotypes of BoNTs (A-G, identified as BoNT-A, BoNT-E, etc.) are known to exist, each varying in their targeting of nerve synapse proteins, potency, onset time, and duration of action. The focus of this thesis is on BoNT/E, a 150kDa toxin composed of two key chains linked by a single bisulfide bond: the heavy chain (HC) at 100kDa and the light chain (LC) at 50kDa (Montal, 2010; Rossetto and Montecucco, 2018). The HC consists of two functional domains—the binding domain (BD) and the translocation domain (TD)—while the LC itself serves as an endopeptidase. For illustration, the structures of BoNT/A and BoNT/E are shown in Figure 1-1.

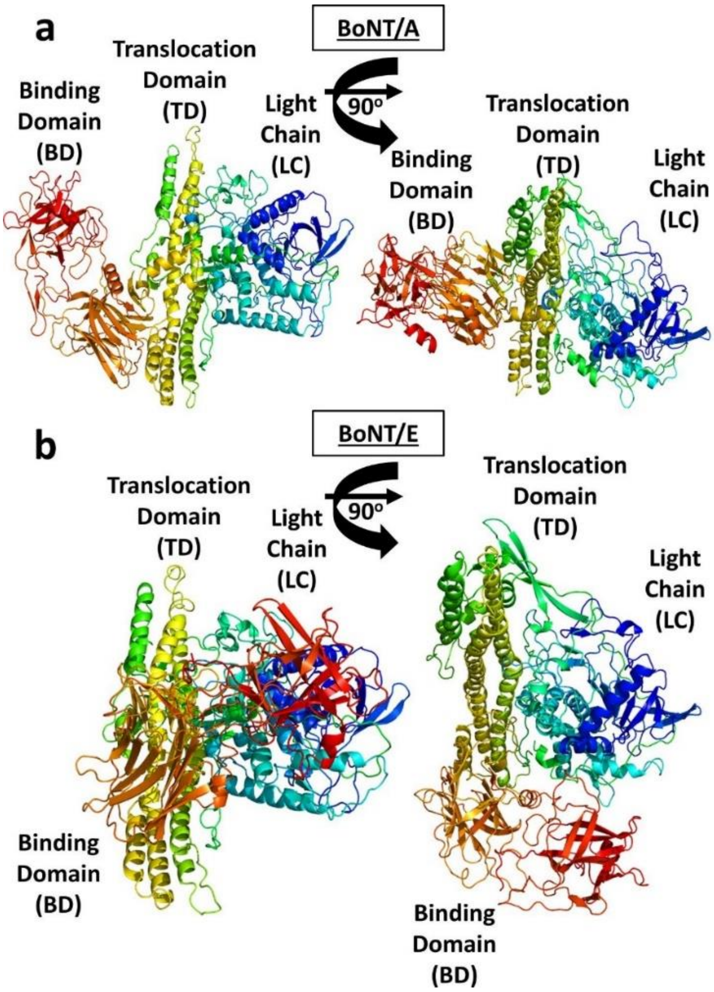

Figure 1-1 Botulinum neurotoxin (BoNT) structure. (a) BoNT/A and (b) BoNT/E and their domains Right side images show a 90º 'top-down' view of the structure (Lalaurie et al (2022)).

1.1.2 Mechanism of Action

Infection naturally occurs following the ingestion of meat contaminated with Clostridium botulinum, leading to the colonisation of the gastrointestinal tract. Within this environment, Botulinum neurotoxins (BoNTs) are produced in association with a progenitor complex, providing protection against low pH and proteolytic cleavage (Gu *et al.*, 2012). This protective complex allows BoNTs to traverse the gut lining intact and enter the bloodstream.

BoNTs exhibit a high binding affinity for nerve terminals, facilitated by their binding domain (BD). This binding is finely tuned by a dipole within the structure, promoting interactions with membrane receptors known as polysialogangliosides (PSG) through dipole orientation (Fogolari *et al.*, 2009). The interaction between the BD and its receptor initiates internalisation into the neuron.

Once internalised, BoNTs are encapsulated within endocytic vesicles during endocytosis. During vesicle maturation, the internal pH decreases from 7.4 to 4.0-5.0 that initiate conformational changes observed in various BoNT serotypes and domains (such as BoNT/E, BoNT/A-HC, and BoNT/A-LC) that expose hydrophobic regions or residues (Cai *et al.*, 2006; Chellappan *et al.*, 2015; Lalaurie *et al.*, 2022). These changes are thought to promote interactions with endosomal membranes.

Subsequently, the translocation domain (TD) forms a transmembrane channel through the endosomal membrane, allowing an unfolded LC chain to be translocated into the cytoplasm. Once inside the cytoplasm, the LC chain undergoes refolding and bisulfide bond reduction (Fischer and Montal, 2007).

Depending on the BoNT serotype, the LC then cleaves the specific proteins involved in the soluble N-ethylmaleimide-sensitive factor attachment protein (SNAP) receptor (SNAP-Receptor; SNARE) complex, such as vesicle-associated membrane proteins (VAMP), SNAP, and Syntaxin. This cleavage disrupts the process of neurotransmission, ultimately preventing the release of neurotransmitters causing muscle paralysis (Montal, 2010; Rossetto, Pirazzini and Montecucco, 2014).

1.1.3 Manufacturing

In nature, Botulinum neurotoxins (BoNTs) are produced by the bacterium Clostridium botulinum. However, in modern bioprocessing, Escherichia coli (E. coli) is typically engineered to express the toxin and various domains (Chen *et al.*, 2010; Gao *et al.*, 2010). Traditional purification methods for BoNT toxins involved precipitation and centrifugation steps. However, contemporary industrial bioprocessing utilises filtration and chromatography processes, as described by Gessler (2005) (Gessler, 2005).

Following the fermentation process, microfiltration is employed initially to clarify cells from the culture supernatant, followed by ultrafiltration. The retentate is then subjected to a series of chromatography steps for purification and polishing. Initially, hydrophobic interaction chromatography (HIC) is utilised to remove ribonucleic acid (RNA). Subsequently, the eluate undergoes desalting and buffer exchange before anion-exchange chromatography (AEX) is employed. Finally, a further desalting and buffer exchange step is conducted, culminating in cation exchange chromatography (CEX) (Gessler, 2005). This purification process is followed by appropriate fill and finish steps, during which BoNTs are formulated with excipients to stabilise the product during lyophilisation and reconstitution, as well as for liquid formulation.

Modern processing techniques have not only enhanced the safety of BoNT manufacturing for operators, mitigating the inherent risks associated with handling the deadly toxin, but they have also improved product accessibility through scalability and adherence to safety protocols. However, a significant challenge in BoNT manufacturing is its sensitivity to aggregation (Johnson, 2018). This propensity is likely a result of the protein's susceptibility to conformational changes during pH shifts, leading to the exposure of hydrophobic regions and subsequent aggregation.

1.2 Protein Aggregation

Protein aggregation remains a persistent challenge in the biomanufacturing of therapeutic proteins. This problem can arise from a combination of conformational (relating to the protein structure itself) and colloidal (relating to the interactions with other proteins) instabilities, which are regulated by intrinsic protein properties (relating to the surface charge, folding energy etc.) (Wu *et al.*, 2010) or extrinsic solution properties (relating to the pH, ionic strength, excipients, concentration etc.) (Garidel, Blume and Wagner, 2015).

Aggregation can lead to reduced manufacturing process yields, reduced therapeutic effectiveness and impact product quality which poses safety risks for patients (Jiskoot *et al.*, 2012; Rosenberg, Verthelyi and Cherney, 2012). For instance, submicron and subvisible aggregates of adalimumab (a monoclonal antibody used against some arthritis conditions) have been shown to induce cytokine release and T cell proliferation *in vitro* (Moussa *et al.*, 2016; Heljo *et al.*, 2023a). Indicating that they could cause immune inflammatory response if administered into patients.

Aggregation occurs when higher-order secondary and tertiary protein structures unfold, revealing hidden hydrophobic regions (Roberts, 2014). This can often correspond to the loss of α-helices and β-sheets motifs within proteins as they lose their structural integrity (Chi *et al.*, 2005; Bee, Chiu, *et al.*, 2009; Tyagi *et al.*, 2009). Notably, β-sheet motifs play a role in the association of unfolded proteins during aggregation and formation of highly-ordered amyloid aggregates (Riek, 2017). However, the exposure of these hydrophobic regions to the surrounding solvent increases the free energy of the system, which is considered the driving force behind aggregation (Berrill, Biddlecombe and Bracewell, 2011).

1.2.1 Aggregation Reversibility and Linkage

Aggregation processes can involve both reversible and irreversible mechanisms. When proteins undergo localised or partial unfolding, they may temporarily expose hydrophobic regions, leading to the formation of reversible monomer clusters or self-associations (Banks *et al.*, 2012). This reversible aggregation can occur under conditions that are thermodynamically favourable for the transition of the protein from its native state to partially unfolded but reversible states. An example of such a process has been proposed as an adaptive autoregulatory response in endogenous proteins that helps cells adapt to thermal stress (Wallace *et al.*, 2015). These reversible oligomers form due to reversible intermolecular forces, such as van der Waal forces electrostatic attractions and hydrophobic interactions, which drive the formation of complexes like dimers and trimers (Fernández and Minton, 2009; Amin *et al.*, 2014). Consequently, these aggregates can be dissolved, and their formation can often be mitigated by manipulating extrinsic properties, such as dilution or changes in pH and ionic strength, which modulate intermolecular electrostatic attractions (Minton, 2007). The effects of pH, ionic strength and surfactants on this process will be discussed later.

No model has been able to satisfy all protein aggregation processes, however the Lumry-Eyring nucleated polymerisation model and condensation adaption is one such generalised model (Andrews and Roberts, 2007; Li and Roberts, 2009). In this model, the initiation of aggregation typically involves reversible unfolding and oligomerisation until a nucleation point is reached. At this point, irreversible chain polymerisation through monomer addition ensues. Aggregates are often held together by strong non-covalent contacts and are challenging to reverse or entirely irreversible, even after dilution or changes in pH. Their formation depends on the distortion or unfolding of proteins to expose regions that form strong contact points, primarily driven by highly hydrophobic interactions between monomers that can overcome electrostatic repulsions. It is these aggregates that do not readily disassociate in vivo that pose the greatest risk of eliciting immunogenic reactions compared to monomers (Moussa *et al.*, 2016; Heljo *et al.*, 2023a).

1.2.2 Aggregate Growth and Sizes

Aggregation is the process of monomers coming together to form progressively larger multi-monomer structures. Three mechanisms have been proposed to govern their growth: 1) nucleation, 2) chain polymerisation (CP), and 3) aggregate-associative polymerisation (AP) (Li and Roberts, 2009). Nucleation marks the initiation of irreversible aggregation, followed by the polymerisation of monomers and the formation of aggregate structures. CP involves growth through the addition of monomers, while AP entails the condensation of aggregates (Nicoud *et al.*, 2014).

As a result of monomer polymerisation, aggregates can transition from nanometre-scale oligomers to macro-scale structures, forming visible particles that can reach millimetre lengths. However, from an immunogenicity perspective, submicron and subvisible particles pose a greater concern due to their potential immunogenic risk in patients (Moussa *et al.*, 2016; Heljo *et al.*, 2023a). Therefore, particles should not be treated as equals, and a more critical examination should be based on differences in size and morphology, including the shape of particles, which can be branched, globular, or elongated.

The morphologies of particle can be captured by particle analysis techniques such as micro-flow imaging (MFI) and backgrounded membrane imaging (BMI) which operate within the 2 µm to 300 µm (MFI) and 2 µm to 5mm (BMI) (Schleinzer *et al.*, 2023). Until recently, extracting meaningful data from the hundreds to thousands of images generated during sample analysis has been limited to basic observations and image analysis techniques, missing the potential for deeper insights into particle characteristics. However, machine learning and multivariate data analysis tools can now process these images to extract features from particles and characterise their morphologies, enabling a better understanding of the underlying factors contributing to particle formation

(Witeof *et al.*, 2021; Greenblott *et al.*, 2022; Thite *et al.*, 2022). These advanced analytical techniques can facilitate rapid root-cause analysis in bioprocess development and help mitigate protein aggregation issues.

1.3 Aggregation Mechanisms

Biologics, including cells, proteins, and viral vectors, are vulnerable to a variety of stresses throughout the bioprocessing journey, which can jeopardise the quality and efficacy of the final product. These stresses can encompass hydrodynamic shear forces, biologic interactions in the bulk fluid, mechanical and chemical factors, as well as the phenomenon of adsorption onto interfaces, occurring between solid and liquid phases or at air-liquid boundaries.

The adsorption of proteins onto interfaces during bioprocessing can significantly exacerbate aggregation. These interfaces represent the planes situated at the junctures of different phases, including air-liquid (Bee *et al.*, 2012; Koepf *et al.*, 2017, 2018; Žuntar *et al.*, 2022), liquid-liquid (immiscible like oil), solid-liquid (Biddlecombe *et al.*, 2007, 2009; Tavakoli-Keshe *et al.*, 2014) and even the triple-phase boundaries of air-liquid-solid (Frachon *et al.*, 2016). Figure 1-2, Figure 1-3 and Figure 1-4 illustrate various protein aggregation mechanisms involved during protein-interface interactions.

The diverse materials that biologics encounter during processing, such as stainless-steel pipes, vessels, polyvinylidene fluoride filters, and chromatography resins with agarose beads, coupled with fluctuations in physiochemical conditions (pH, ionic strength, excipients), as well as the hydrodynamic forces at play (mixing, pumping, centrifugation), collectively exert influence over the rate at which aggregation may occur. These factors, in combination, present formidable challenges in the preservation of biologic product quality and efficacy during the bioprocessing journey.

1.3.1 Hydrodynamic Flow and Shear in the Presence of Interfaces

Shear stresses, which represent the velocity gradient through parallel layers of fluid, have been extensively studied for their role in protein aggregation, with two primary theories regarding their influence. On one hand, shear forces have been thought to distort protein structures, exposing hydrophobic regions that can drive aggregation. On the other hand, shear generates turbulence, enhancing mass transfer and interactions between proteins and interfaces, but could disrupt proteins adsorbed to surface as illustrated in Figure 1-2. To understand these forces and assist in process development for industrial bioprocessing, scale-down/ultra scale-down (USD) models are often created.

USD models aim to evaluate the stability of biological materials under simulated shear forces that occur during bioprocessing. Two common geometries for these models are capillary flow and rotating disc flow. Capillary flow exposes materials to shear at the entry and exit points of the capillary, typically maintaining laminar flow inside. In contrast, rotating disc flow involves a disc that generates turbulent flow within a closed chamber, with the highest shear at the disc's tip (Rayat *et al.*, 2016).

Table 1-1 presents shear rate values observed in various bioprocess unit operations. To put these values in context, the human arterial system experiences peak shear rates of around 1,600s^{-1} (Stroev, Hoskins and Easson, 2007). Some literature examples investigating flow-induced protein aggregation under reported shear rates can be found in the work of Grigolato and Arosio (2020) (Grigolato and Arosio, 2020).

Interestingly, at extreme shear rates of up to $10^8 s^{-1}$, human serum albumin did not aggregate when pumped through a micro-orifice (Duerkop *et al.*, 2018). Additionally, IgG1 antibody exposure to shear rates of 250,000s^{-1} did not lead to aggregation, but detectable aggregates formed when processing with a rotating rheometer at 20,000s^{-1} in the presence of air-liquid interfaces (Bee, Stevenson, *et al.*, 2009).

Table 1-1 Shear rates observed in typical bioprocessing unit operations.

Unit Operation	**Shear Rates**	**Reference**
Bioreactor (4L)	275s^{-1}	(García-Salas *et al.*, 2021)
Tangential flow filtration (TFF)	500-6,000s^{-1}	(Fernandez-Cerezo *et al.*, 2019; Perry *et al.*, 2023)
Pumps		
- Piston pump	325s^{-1}	(Dreckmann *et al.*, 2020)
- Peristaltic pump	4,000s^{-1}	(Dreckmann *et al.*, 2020)
- Rotary lobe pump	300,000s^{-1}	(Kamaraju, Wetzel and Kelly, 2010)
Needle (20-gauge)	20,000s^{-1}	(Bee, Stevenson, *et al.*, 2009)

Extensional flow is another stress imposed on to biologics during fluidic flow which describes a velocity gradient in the direction of flow. A protein molecule in this type of flow would experience an extensional force and potentially elongation of the molecule cause by the faster flow in front and slower flow behind (Dobson *et al.*, 2017; Willis *et al.*, 2018). In the work of Willis *et al*, a device was used to carefully expose three different IgG1 molecules to extensional flow by passing these through a narrow capillary using two syringes connected at each end (Willis *et al.*, 2018). The number of passes and the velocity of passes were reported to increase the amount of insoluble protein aggregate content in pellets formed by centrifuging samples.

Air-liquid interfaces have been shown to cause more damage to biologics compared to solid-liquid interfaces without air. For example, hermetically sealed pilot-scale centrifuges induced greater damage than non-hermetically sealed ones, resulting in poorer clarification performance (Hutchinson *et al.*, 2006). The inclusion of an air-liquid interface in a sealed chamber with a rotating disc used to generate high shear (25,000s^{-1}) in the presence of solid-liquid interfaces significantly increased monomer loss (Biddlecombe, 2009).

Biddlecombe et al. also demonstrated the effect of a rotating disc generating shear up to 34,000s^{-1} in the presence of solid-liquid interfaces on the monomer loss and aggregation of monoclonal antibodies (Biddlecombe *et al.*, 2007). In this highly turbulent environment, a non-linear relationship between shear and the monomer reduction rate was observed.

However, it's important to note that the relationship between shear rates, protein monomer loss, and aggregation is complex and can be influenced by factors beyond shear rates. For example, the physical design of equipment may trap and recirculate biologics, increasing their exposure time to stressors (Dreckmann *et al.*, 2020).

The complex interplay between shear and hydrodynamic flow is explored in the work of Grigolato and Arosio, who found that monoclonal antibody loss in microfluidic channels pumped by microliter syringes depended on the number of passages through the device but not on flow rates corresponding to shear rates up to 260,000s^{-1} (Grigolato and Arosio, 2020). They suggest that hydrodynamic flow and shear stress should be considered together, as they can disrupt protein layers adsorbed onto solid-liquid interfaces, allowing for additional adsorption.

Overall, there are mixed results regarding the effect of shear rates on protein monomer loss and aggregation. This may be due to variations in device design and a lack of reporting on laminar/turbulent flow regimes. Capillary-based devices (such as the microliter syringes) can produce extremely high shear rates in the absence of turbulence, while rotating disc devices typically generate shear rates in line with those seen in most industrial bioprocessing unit operations, which often involve turbulent flow. However, an agreement can be made that a mechanistic synergy exists between interfaces and hydrodynamic flow.

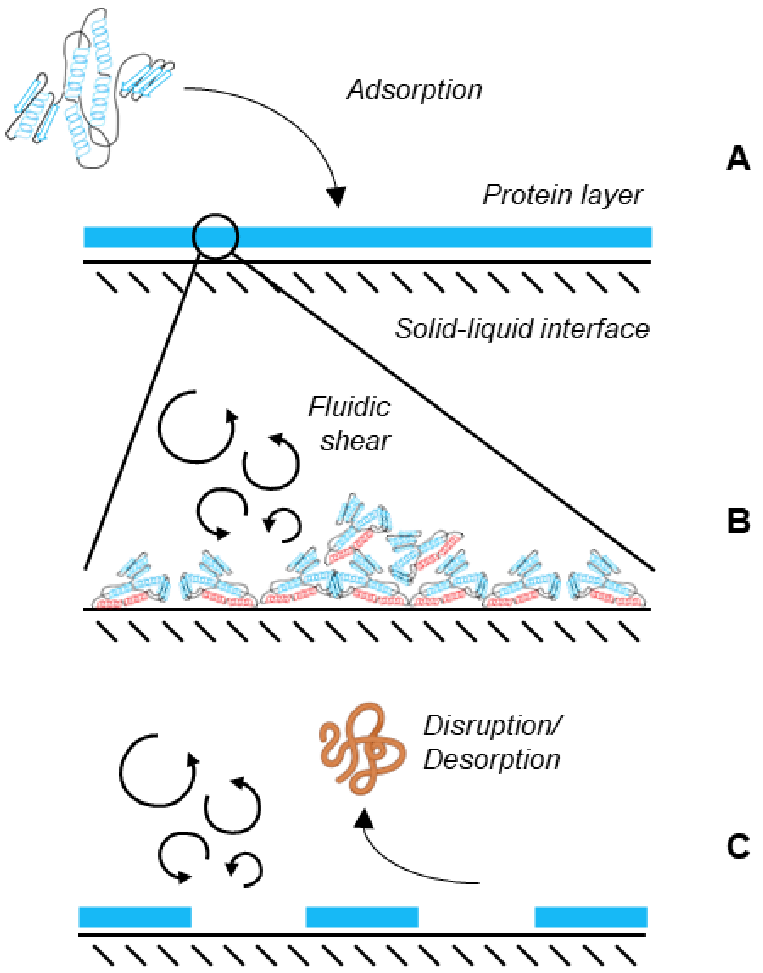

Figure 1-2 Illustration of protein interactions with solid-liquid interfaces. (A) Proteins adsorb to solid-liquid interfaces forming a protein layer where (B) it can be disturbed by fluidic shear forces and lead to (C) the desorption of protein aggregates.

1.3.2 Factors Affecting Interface Adsorption

1.3.2.1 Intrinsic Properties of Solid-liquid Interfaces

The adsorption of proteins to interfaces is influenced by various forces, including electrostatic and hydrophobic interactions, and the intrinsic properties of the solid material can affect the strength of these forces. In bioprocessing, it is crucial to characterise these interfaces, considering both the protein's susceptibility to aggregation and the interplay with hydrodynamic flow and interface interactions.

Studies have shown that the material composition of the solid interface plays a significant role in protein adsorption and aggregation (Gomme *et al.*, 2006; Tyagi *et al.*, 2009; Bee *et al.*, 2010; Nayak *et al.*, 2011; Kalonia *et al.*, 2018; Grigolato and Arosio, 2020). For instance, in a microfluidic channel shear study by Grigolato et al., switching from glass microliter syringes to polypropylene ones of identical size resulted in an increase of remaining monomer from 30% to 95% during flow (Grigolato and Arosio, 2020). Furthermore, introducing silicon oxide (SiO_2) nanoparticles into the polypropylene syringe drastically reduced remaining monomer from 95% to 0%, underscoring the significance of solid-liquid interfaces in protein aggregation.

Peristaltic pumping, commonly used in bioprocessing, offers a range of tubing materials for engineers to choose from during process development. Research by Her at al. (2020) highlighted the significant impact of different tubing types on submicron and subvisible particle formation during the peristaltic pumping of monoclonal antibodies (Her *et al.*, 2020). They found that the choice of tubing material could lead to as much as a three-fold increase in particle formation when using constant pump parameters.

Surface modifications to solid interfaces can potentially offer solutions to modulate the rates of protein adsorption and aggregation during bioprocessing. For example, Biddlecombe (2009) applied hydrophobic and hydrophilic siloxane coatings to a rotating disc used to generate shear in the presence of solid-liquid interfaces (Biddlecombe, 2009). These modifications led to a three-fold increase in monomer reduction rates for the hydrophobic coating and a two-fold increase for the hydrophilic one during shear up to 24,000 s^{-1}, highlighting the complex role of surface free energy and protein adsorption.

In addition, Wu and Randolph manipulated the surface charge of stainless-steel surfaces in a piston pump and observed that protein particle formation was 12-fold greater at a net surface charge of -70 mV compared to +70 mV, indicating the significant role of electrostatic forces between stainless steel surfaces and proteins (Wu and Randolph, 2020).

Further modifications to stainless steel surfaces can involve reducing surface roughness. Biddlecombe *et al*. (2009) demonstrated that changing the average surface roughness of stainless-steel rotating discs from 145 nm to 25 nm reduced the monomer reduction rate three-fold during shear up to 24,000 s^{-1} (Biddlecombe *et al.*, 2009).

Stainless steel is a preferred material in industrial bioprocessing equipment due to its high corrosion resistance and ease of cleaning. The data suggests that in such equipment, the surface roughness of stainless steel should be polished as smoothly as practical, and controlling the net surface charge can help prevent protein adsorption and aggregation. These modifications can also contribute to reducing fouling and improving cleaning-in-place performance during bioprocessing (Avila-Sierra, Zhang and Fryer, 2019; Ávila-Sierra, Zhang and Fryer, 2021).

1.3.2.2 Mechanical Disruption to Interfaces

Disturbances to protein layers formed at solid-liquid interfaces and air-liquid interfaces can lead to their desorption, allowing for the adsorption of additional protein monomers, and these forces can work together to perpetuate protein aggregation in systems. For example, Sediq *et al*. (2016) observed that the abrasion of a magnetic stirrer at the solid-liquid interface of a beaker resulted in the loss and aggregation of monoclonal antibodies (Sediq *et al.*, 2016). They showed that halving the contact area of the stirrer led to a reduction in monomer loss from 94% to 99% and decreased microparticle formation from 1.7×10^6 particles.ml^{-1} to 0.1×10^6 particles.ml^{-1}.

Jing *et al*. (2022) noted that grinding freeze-dried monoclonal antibody formulations induced greater subvisible particle formation upon reconstitution, along with indications of changes in the protein's secondary structure (Jing *et al.*, 2022). The aggregates and fragments observed were covalent in nature, potentially stemming from the formation of free radicals during grinding, which were detected by the oxidation of Methionine (Met) to form Methionine S-oxide (Met(O)).

As previously discussed, Grigolato and Arosio (2019) found that the loss of monoclonal antibodies during flow through microfluidic channels depended on the number of passages through the device (Grigolato and Arosio, 2020). They suggested that both hydrodynamic flow and shear stress should be considered together, as hydrodynamic flow and mechanical scraping could disrupt protein layers adsorbed onto solid-liquid interfaces, allowing for additional adsorption.

Figure 1-3 illustrates protein aggregation during the of scraping of solid-solid interfaces.

Considering the synergistic relationship between the rate of protein adsorption (r_{ads}) and the rate of disruption by mechanical scraping (r_{dis}) of protein layers, the rate of aggregation in this study was limited by the rate of mechanical scraping caused by the linear actuation of the syringe ($r_{ads} >> r_{dis}$). It has been observed that the establishment of protein layers onto solid-liquid interfaces takes less than one second (Deiringer *et al.*, 2022). Therefore, faster actuation of the syringe may reduce the time available for adsorption at the solid-liquid interfaces and subsequent disruption caused by the syringe, making rads the limiting factor.

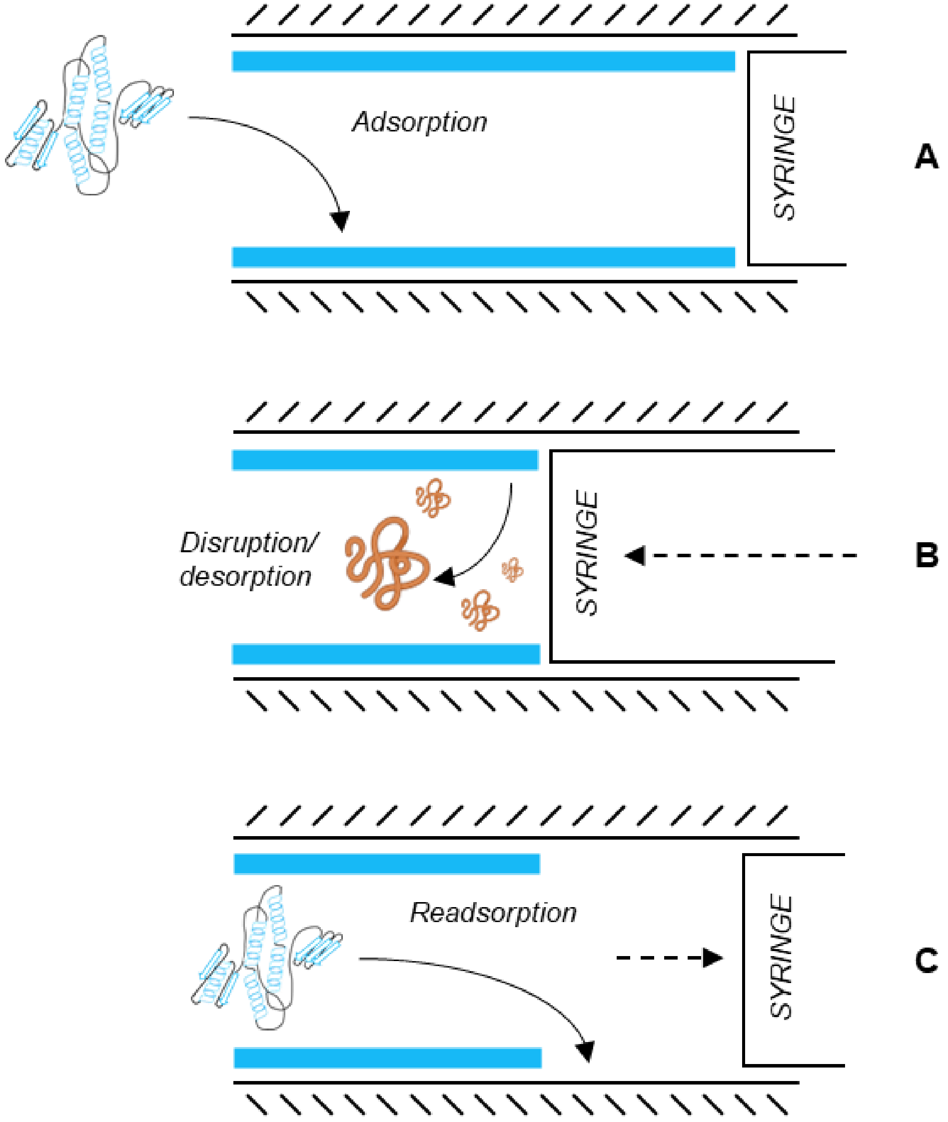

Figure 1-3 Illustration of mechanical disruption of protein layers on solid-liquid interfaces. (A) Proteins adsorb to solid-liquid interfaces forming a protein layer where (B) the solid-interfaces of a syringe (for example) can scrape or grind along the interface and lead to mechanical disrupsion of protein layers and (C) cause desorption of protein aggregates.

Air-liquid interfaces are more flexible and malleable compared to the rigid surfaces of solid-liquid interfaces. Consequently, studies have shown that rotating or dropping drug product vials containing protein solutions to mimic packing and transport processes can lead to the formation of protein aggregates (Bee *et al.*, 2012; Randolph *et al.*, 2015). During this process, the expansion of the air-liquid interface allows for protein adsorption to the newly accessible surface area. However, protein particle formation occurs exclusively when the interface is reversed during the compression of the interfaces (Bee *et al.*, 2012). Protein layers on expanded air-liquid interfaces are believed to condense and clump together when the interface surface area is reduced, leading to the desorption of protein particles. This mechanism is referred to as isothermal interfacial compression-dilation (IICD) of air-liquid interfaces and has been extensively studied in the literature (Bee *et al.*, 2012; Lin *et al.*, 2016; Koepf *et al.*, 2017). Figure 1-4 illustrates the protein aggregation during air-liquid interface IICDs.

Randolph *et al*. (2015) observed that dropping vials containing human growth hormone resulted in mechanical shock upon impact, causing the formation of subvisible protein particles (Randolph *et al.*, 2015). The extent of particle formation increased depending on the height from which the vials were dropped. However, there were no significant differences in monomer loss. Interestingly, the study also observed the presence of gelatinous globules of proteins adhered to the glass vial walls after dropping. Some of these recovered globules showed signs of oxidative damage to the protein's structure, likely induced by free radicals formed during cavitation upon impact. However, the inconsistent findings did not provide conclusive evidence regarding this phenomenon. Nevertheless, it was noted that the mass of adherent protein recovered from the vial walls increased with the height of the drop (Randolph *et al.*, 2015).

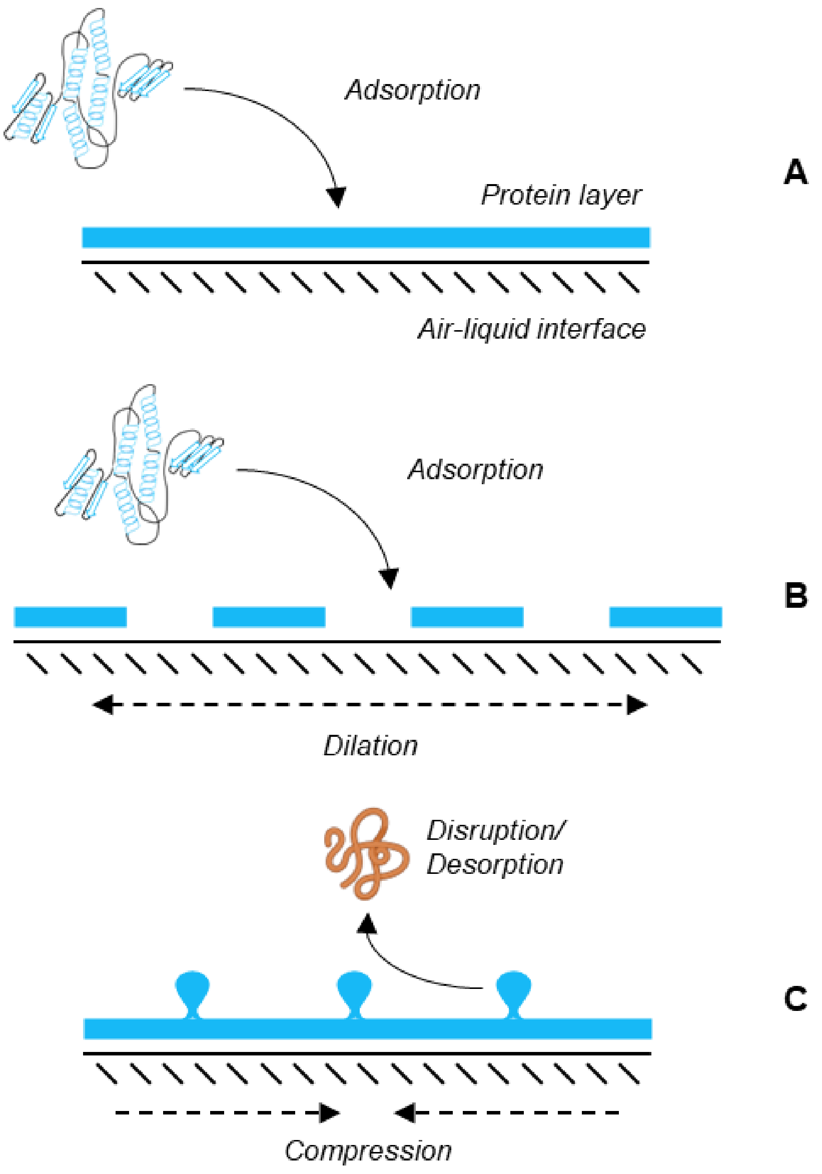

Figure 1-4 Illustration of isothermal interfacial compression-dilation (IICD) cycles of air-liquid interfaces. (A) Proteins adsorb to air-liquid interfaces forming a protein layer where (B) dilation of the interface allows further adsorption followed by (C) a compression of the interface that condenses and disrupts protein layers and desorbing protein aggregates.

In a different study, it was found that radical formation induced by cavitation resulting from mechanical methods like pumping and flow through a micro-orifice did not significantly alter protein structural integrity. However, aggregation was observed and attributed to the growth of bubbles associated with cavitation (Duerkop *et al.*, 2018). While radicals produced in substantial quantities can potentially lead to protein aggregation, the levels typically observed during bioprocessing are not expected to induce protein aggregation. Nevertheless, it should be noted that air-liquid interfaces pose a greater concern in this regard (Duerkop *et al.*, 2018).

The mechanism of IICDs could potentially be relevant to solid interfaces that are known to be less rigid than the stainless-steel materials typically studied during solid-liquid interface aggregation. Therefore, it is important to explore the behaviour of more malleable materials, such as thermoplastic elastomers and silicone, in the context of protein aggregation. A significant scenario where these compressive forces come into play with elastomer materials is during peristaltic pumping where the rotating rollers occlude tubing repeatedly to positively displace liquid. Understanding how different interface materials respond to mechanical stresses is essential for effectively managing protein aggregation during bioprocessing.

1.4 Physiochemical Conditions and Excipients

The process of protein aggregation is profoundly influenced by electrostatic forces, fostering interactions among proteins themselves and with the surfaces they may adhere to. This phenomenon carries importance in the field of formulation optimisation, a discipline that has been regarded as an 'art' (Wang and Ohtake, 2019).

Formulation optimisation primarily aims to bolster the stability of pharmaceutical proteins during transportation and extend their shelf-life by changing extrinsic properties (relating to the pH, ionic strength, excipients, concentration etc.). However, in the dynamic and ever-changing landscape of bioprocessing, proteins inevitably encounter a milieu of shifting physiochemical conditions, particularly during processes like ion exchange chromatography (IEX), hydrophobic interaction chromatography (HIC), and tangential flow filtration (TFF). Understanding how these physiochemical conditions drive protein aggregation is pivotal for developing strategies to prevent it.

1.4.1 pH

Proteins exhibit amphiprotic properties as they can interact with both acids and bases at their carboxylic and amine functional groups by donating and accepting protons. Consequently, pH can influence the charge of these functional groups, thereby affecting the overall net charge of the protein. This, in turn, has an impact on the electrostatic forces involved in protein-protein and protein-interface interactions (McUmber, Randolph and Schwartz, 2015; Deiringer et al., 2022). Therefore, pH plays a crucial role in influencing the extent of aggregation by modulating the electrostatic forces of attraction between proteins and interfaces. Figure 1-5 illustrates how pH modulates electrostatic forces.

Under extreme pH conditions in highly acidic or alkaline solutions, proteins may undergo cleavage, deamidation, and oxidation, leading to alterations in their structural conformation and stability (Kristinsson and Hultin, 2004; Zhao *et al.*, 2020; Li *et al.*, 2022). When the pH approaches the isoelectric point (pI) of proteins—where they have a net-neutral charge in solution—the forces acting between proteins become neutral. It is frequently observed in aggregation studies that maximum protein loss or aggregation occurs for several proteins at or near their pI (Bremer *et al.*, 2004; Majhi *et al.*, 2006; Biddlecombe *et al.*, 2009; Woldeyes *et al.*, 2019; Wood *et al.*, 2020).

In the context of BoNTs, Bai *et al*. observed that pH affects the monomer half-life (hr) during incubation at 42°C of the heavy chain (HC) of a recombinant serotype-C (rBoNT/C) (Bai *et al.*, 2011). At both 0mM NaCl and 150mM NaCl, reducing the pH from pH 8 to pH 4 significantly reduced the half-life. It was noted that the BoNT tertiary structure undergoes slight conformational changes under low pH conditions, corresponding to an increase in the rate of aggregation.

1.4.2 Ionic Strength

Ionic strength plays a significant role in modulating protein aggregation by influencing the electrostatic forces involved (Biddlecombe *et al.*, 2009; Chakroun *et al.*, 2016). The presence of salts in solution can lead to changes in protein structural conformations and affect protein-protein interactions (PPIs) (Wang *et al.*, 2013; Calero-Rubio *et al.*, 2018). Typically, salt ions interact with proteins through a phenomenon known as charge shielding, where layers of ions accumulate near a charged surface. Figure 1-5 illustrates how ionic strength modulated electrostatic forces.

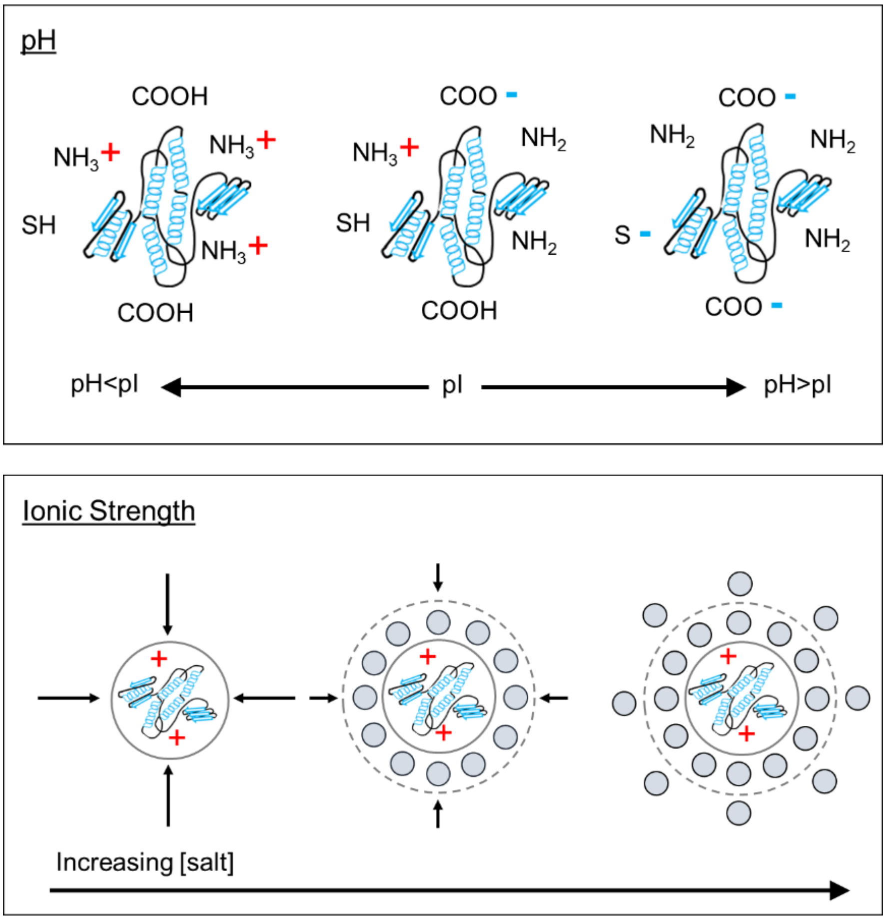

Figure 1-5 Illustration of pH and ionic strength effect on protein stability. (Top) Solution pH can affect the overall net-charge of proteins. (Bottom) Salt ions in solution act to shield electric potential (black arrows).

To illustrate, when electrostatic forces favour protein-interface interactions, increasing ionic strength can shield these forces, reducing their impact. Biddlecombe *et al*. demonstrated this effect during shear-induced aggregation of a monoclonal antibody. Above the isoelectric point (pI) of the antibody, an increase in ionic strength decreased monomer loss by shielding the favourable electrostatic forces that drive protein adsorption. However, below the pI, the opposite effect was observed (Biddlecombe *et al.*, 2009).

In the context of BoNTs, Bai *et al*. observed a significant decrease in the monomer half-life (hr) of the heavy chain (HC) of recombinant serotype-C (rBoNT/C) when incubated at 42°C and pH 4 upon the addition of 150mM NaCl. However, this effect was not significant at pH 8 (Bai *et al.*, 2011). Increasing the ionic strength at acid pH thus can stabilise rBoNT/C-HC.

1.4.3 Excipients

Excipients are essential for maintaining the native conformation of biologic molecules and shielding them from destabilising forces such as protein intercalation with interfaces. To counteract this, surfactants can be introduced in low amounts to compete with the protein at interfaces, preventing it from unfolding and aggregating. The most common surfactants used in 80% of all approved biological drug products are polysorbate 80 (PS80) and polysorbate (PS20) and are present in concentrations ranging from 0.001-1% (w/v) (Martos *et al.*, 2017). Whilst there are different commercial grades available, for example Multicompendial and Chinese pharmacopeia, there is no difference in their functionality in aggregation mitigation (Grabarek *et al.*, 2019).

Surfactants play a vital role in reducing aggregation through two key mechanisms. Firstly, they compete with proteins at interfaces, where their adsorption is thermodynamically favourable, preventing protein unfolding and aggregation at the surface. Secondly, in solution, surfactants can form complexes with exposed hydrophobic regions of unfolded proteins, essentially acting as refolding chaperones (Bam, 1998; Khan, Mahler and Kishore, 2015).

For example, Biddlecombe *et al*. demonstrated that varying the concentrations of PS20 and PS80 reduced IgG4 monomer loss. Both surfactants were found to compete for interfacial adsorption against IgG4, leading to decreased monomer loss rates when concentrations were increased (Biddlecombe *et al.*, 2009). Numerous studies have regularly shown support that surfactants can effectively prevent monomer loss and protein particle formation induced by protein-interface interactions during (Biddlecombe *et al.*, 2009; Daniel J. Callahan, Stanley and Li, 2014; Sediq *et al.*, 2016; Her *et al.*, 2020; Wu and Randolph, 2020)

However, Rafferty *et al*. (2017) noted that the addition of surfactants can pose challenges in controlling tangential flow filtration (TFF) diafiltration operations. These challenges arise from the inconsistent filtration of surfactant sizes, which can exist in monomer, micelle, or larger non-spherical micelle forms, as well as interactions between proteins and surfactants that can hinder separation via TFF(Rafferty *et al.*, 2017)

1.4.4 Temperature

The influence of temperature on particles in solution and protein structure is a well-established phenomenon; however, the interplay between these two factors plays a complex role in driving aggregation. Temperature changes in solutions affect the system's internal energy, impacting diffusion rates and particle collisions, following the Arrhenius relationship. It's worth noting that the Arrhenius behaviour for proteins remains valid within a narrow temperature window (Oliva, Fariña and Llabrés, 2016). Beyond this range, it diverges due to temperature-induced effects on proteins, such as compromised conformational stability and an increase in the number of unfolded states (Wang and Roberts, 2013).

Under high shear conditions, temperature variations within the typical apparent melting temperature (T_m) of IgG1 did not induce any changes in monomer formation (Biddlecombe *et al.*, 2009). It's plausible that exceeding the protein's melting temperature could lead to thermal-induced aggregation.

In the context of BoNTs, Bai *et al*. observed changes in the apparent melting temperature (T_m) of the heavy chain (HC) of recombinant serotype-C (rBoNT/C). Under pH 8 and 150mM NaCl conditions, the HC had a T_m of 57.1°C. However, reducing the pH to pH 4 and pH 3.5 at 150mM NaCl decreased the T_m to 49.9°C and 44.8°C, respectively (Bai *et al.*, 2011). This suggested that rBoNT/C-HC is more susceptible to temperature-induced instabilities at low pH conditions. For reference, monoclonal antibodies have been observed to have T_m values ranging from 55-70°C (Goldberg *et al.*, 2011; Tavakoli-Keshe *et al.*, 2014).

1.5 Aggregation in Pumping

An often-overlooked aspect of bioprocessing is the role of pumping equipment used to facilitate transport and handling of biologics within bioreactors, piping and downstream processing equipment. There are many pumping systems available to process engineers that present advantages for certain operations and scales, such as bulk-transport of cell culture from a 10,000L bioreactor using radial pumps or high-precision dosing millilitre-volumes of liquid formulations into drug product vials using piston pumps. While pumps are essential for ensuring efficient and consistent bioproduction, they also present a potential challenge: the risk of biologic damage and protein aggregation.

From the perspective of protein aggregation, pumps are complex hydrodynamic environments often with mechanical moving parts in contact with the processed fluid that present stresses to biologics that often cause damage. Mechanical shear, turbulence, pressure, and material-differences are all stressors that can compromise the stability of proteins, leading to their unfolding and aggregation. This section will discuss the factors contributing to this phenomenon.

1.5.1 Shear and Aggregation During Pumping

In bioprocessing, shear rates and protein aggregation during pumping can significantly vary based on the type and design of the pump system employed. Rotary lobe pumps, with their higher rotational speeds, often generate relatively higher shear rates, potentially leading to increased protein aggregation. Conversely, peristaltic pumps, employing gentle squeezing action, tend to offer lower shear rates, minimising the risk of protein denaturation and aggregation. This illustrates the differences in shear rates observed within piston, rotary and peristaltic pumps during operation observed in available literature Table 1-1.

To compare different pump systems, Nayak *et al*. conducted continuous recirculation of bulk drug product using five different pump systems: rolling diaphragm, peristaltic, time-pressure and two piston pumps, one with a stainless-steel chamber and another with a ceramic chamber. The resulting protein particle formation during pumping were used to rank the performance of pumps: piston (ceramic), piston (stainless-steel), rolling diaphragm, time-pressure and peristaltic pump (most to least particles) (Nayak *et al.*, 2011).

Furthermore, the choice of pump materials plays a pivotal role in modulating aggregation through solid-liquid pump interfaces. This is shown in the work of Nayak *et al*. where the ceramic head of the piston pump produced three-fold more protein particles compared to the stainless-steel counterpart (Nayak *et al.*, 2011). Careful consideration of pump design and operation is essential to mitigate shear-induced protein aggregation and maintain the integrity of bioprocessed materials.

1.5.2 Peristaltic Pumping

Peristaltic pumping is a common choice for transporting sensitive biologics, primarily owing to its ability to maintain lower shear rates (as presented in Table 1-1) and to reduce protein aggregation compared to alternative pumping solutions (Nayak *et al.*, 2011).

The operation of a peristaltic pump is based on the principle of peristalsis. It employs a flexible tube within a pump head and a rotor equipped with rollers, generating a sequence of pockets within the tube. As the rotor rotates, these pockets are successively occluded, creating positive pressure that propels fluid through the tube. Simultaneously, negative pressure forms behind the moving roller, and the tube relaxes to its original shape behind the occlusion point, generating a suction effect that draws more fluid from the source.

The distinctive features of this system are rooted in its mode of operation. These include the absence of cleaning requirements due to the use of single-use tubing, straightforward operation, rapid priming during setup, and the indirect handling of biologics within tubing, safeguarding against mechanical shear effects and reducing the risk of contamination and damage. However, it is worth noting that despite these advantages, protein aggregation can still occur, and the underlying mechanisms remain unknown.

1.5.2.1 Peristaltic Tubing

Differences in material properties, including surface roughness, surface coatings, and composition, at solid-liquid interfaces have been recognised as influential factors in protein aggregation. Various types of tubing are available for use in peristaltic pumping, each possessing different characteristics suitable for different applications. For instance, some are designed for pumping viscous fluids, while others are tailored for handling corrosive materials requiring high chemical resistance or pharmaceutical products necessitating high sterility and minimal leeching.

Her *et al*. conducted research that underscored the significant impact of tubing material choice on protein aggregation during the peristaltic pumping of monoclonal antibody (mAb) solutions. Their findings revealed that different tubing materials could result in up to a three-fold increase in the formation of submicron and subvisible particles (Her and Carpenter, 2019). In addition, protein particle formation during pumping of mAb solution showed different dependence on parameters pump seed and acceleration. For instance, acceleration showed no impact on the formation of submicron particles, however increasing pump velocity led to the higher nanoparticle levels (Her *et al.*, 2020). However, an extensive study testing the performance of different tubing has not been conducted.

1.5.2.2 Tubing Spallation

Spallation, a phenomenon in peristaltic pumping, refers to the shedding of foreign particles from tubing into the pumped solution. This issue has been recognised for a long time in the context of haemodialysis medical devices, with early literature highlighting occlusion as a contributing factor (Bommer *et al.*, 1985; Barron *et al.*, 1986; Briceño and Runge, 1992). These studies summarise that reducing occlusion led to a decrease in particle spallation into the blood flow. A more in-depth discussion of occlusion will follow.

Barron *et al*. advanced this work by demonstrating that the rate of particle spallation and the size distribution of particles depended on the tubing material type and the specific peristaltic pump used (Barron *et al.*, 1986). Scanning electron microscopy (SEM) and 3D laser scanning microscopy imagery of tubing morphology revealed that spallation originated from the pumped section of the tubing, and an increase in material roughness correlated with higher levels of spallation (Saller *et al.*, 2015). Tubing wear after pumping was evident through the presence of cracks, grooves, ridges, and adherent particles (Barron *et al.*, 1986; Saller *et al.*, 2015). Interestingly, silicone tubing was found to shed more particles compared to alternatives like PVC, PTFE, and certain composites (Barron *et al.*, 1986; Bahal and Romansky, 2002). However, similar tubing types display different spallation rates based on the manufacture it was sourced from (Saller *et al.*, 2015). Importantly, silicone particles from tubing did not result in changes in turbidity or the presence of subvisible and visible protein particles (Saller *et al.*, 2018).

1.5.2.3 Occlusion of Tubing

Occlusion parameters are severely under reported in literature and manufacture guidelines in peristaltic pump operations, despite them being one of the most important parameters required to setup peristaltic pumps. Occlusion influences the compressive and dilating forces of the moving rollers acting on tubing, creating pockets that facilitate fluid movement. Improper occlusion settings can result in clearances between tubing walls, leading to internal backflow of pumped fluid and causing slippage, ultimately reducing pumping efficiency.

During occlusion, two significant events transpire: tubing stretching and contact of inner tubing walls. The stretching of tubing may induce expansion and relaxation cycles at the solid-liquid interfaces, potentially serving as a mechanism for protein aggregation, akin to the isothermal compression-dilatational (IICD) cycles observed at air-liquid interfaces (Bee *et al.*, 2012; Lin *et al.*, 2016; Koepf *et al.*, 2017).

Additionally, occlusion brings the solid interfaces of inner tubing walls into contact, forming pockets of fluid that facilitate fluid movement. This solid-solid interface contact may trigger protein aggregation through mechanisms like those of scraping, friction, and grinding, as discussed earlier (Sediq *et al.*, 2016; Jing *et al.*, 2022). Figure 1-6 attempts to illustrate how the combination of expansion-relaxation of solid-liquid interfaces and solid-solid interface contact, along with the contact of opposing tubing walls, can impact proteins absorbed to surfaces.

Gomme *et al*. stressed the significance of correct setup and maintenance in pump operations, particularly in the context of rotary lobe pumps. Incorrect setup or poor maintenance of these pumps can lead to reduced efficiency and induce aggregation. In rotary lobe pumps, aggregation tends to increase when there is excessive clearance between the lobe and the pump enclosure, resulting in back-slippage of fluid, diminished pumping efficiency, prolonged fluid residence time, and potential exposure to shear stress (Gomme *et al.*, 2006). Failing to comprehend how peristaltic pumping parameters influence protein aggregation could result in unnecessary product losses and diminished product quality due to the introduction of impurities into drug products.

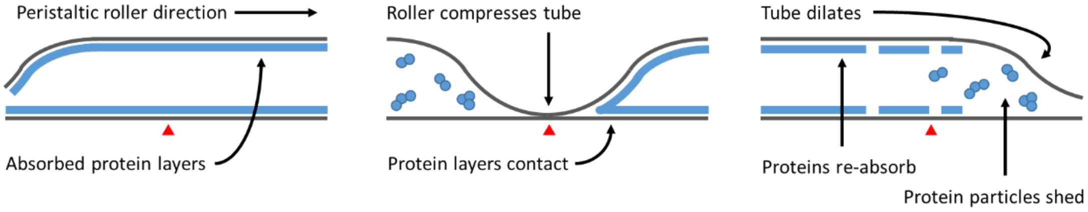

Figure 1-6 Illustration of occlusion on peristaltic tubing and protein aggregation. Compression of tubing may disturb solid-liquid interfaces via expansion-relaxation or solid-solid interface contact mechanically disrupting protein layers. Red arrow indicates a static point along the tubing.

1.6 Aggregate Analytical Techniques

Due to the immunogenic risk aggregates pose to patients, regulations are currently in-place urging the control and monitoring of these during a bioprocess. United State Pharmacopeia (USP) Chapters <787> and <788>, and European Pharmacopeia (Ph. Eur.) Chapter 2.9.19, all require reports of the number of particles in injectable solutions that are greater than 10µm and greater than 25µm (Pharmacopeia, 2006, 2018; Schleinzer *et al.*, 2023). These are two separate thresholds (>10µm and >25µm) that independently report the number of particles above these sizes. This chapter explores some of the common technique employed and those used in this thesis.

1.6.1 Size-exclusion Chromatography

Size-exclusion chromatography (SEC) is a standard and widely-used analytical separation technique to quantify monomers and the formation of aggregates, such as oligomers. Separation is based on the exclusion of analyte particles from pores within particles that make up resin inside chromatography columns. The column's porous particles (stationary phase) offer greater accessible volume for smaller molecules, allowing them to pass through. In contrast, larger molecules are excluded and elute earlier.

Ultra-High-Performance Liquid Chromatography (UPLC) represents a higher throughput chromatography technique that achieves superior resolution by utilising particles smaller than 2µm, compared to the >2µm particles used in High-Performance Liquid Chromatography (HPLC). However, the use of finer particles increases system backpressure, typically exceeding 400bar for 150mm columns and surpassing 700bar for 300mm columns, necessitating high-performance pump equipment.

Drawbacks associated with SEC analysis encompass several factors. Firstly, there is the potential for sample dilution during analysis, which can pose the risk of dissociation of non-covalent aggregates (Mahler and Jiskoot, 2012), as well as reversible self-associated aggregates (Al-Ghobashy *et al.*, 2017). Furthermore, the need to develop optimal running buffer formulations is essential to limit protein-column interactions. Running buffers may inadvertently promote the refolding and disassociation of aggregates, which is a concern.

1.6.2 Backgrounded Membrane Imaging

Background membrane imaging (BMI) is a recently introduced technique that analyses dry particles dispersed on a flat membrane using microscopy imaging. It offers automated high-throughput particle analysis, capable of detecting particles with effective circular diameters ranging from 2µm to 4mm. Sample application, requiring as little as 25µL, is done on a 96-well plate membrane filter. Prior to sample application, images of the membrane are captured to establish the 'background,' which is then subtracted from post-sample images to eliminate pre-existing artifacts.

BMI employs brightfield illumination above the membrane to count and size particles. Additionally, side-illuminated membrane imaging (SIMI) captures light scattered by particles on the membrane, aiding in the identification of rigid foreign particles such as glass and polystyrene, distinguishing them from protein particles.

The advantages of BMI include enhanced visualisation and detection of translucent protein particles, as well as the ability to differentiate foreign particles from proteinaceous ones. However, it's worth noting that particle sizes may be slightly overestimated due to their settling on their larger sides on the membrane surface (Schleinzer *et al.*, 2023).

1.6.3 Light Scattering

Light scattering for particle analysis measures light scattering direction and intensity to ascertain particle characteristics such as size, shape, and concentration (system-dependent). Static light scattering (SLS) yields absolute particle size/molecular weight values, while dynamic light scattering (DLS) can determine particle polydispersity and hydrodynamic diameter through Brownian motion tracking.

Both techniques may exhibit a bias toward larger particles in polydisperse solutions due to the relationship between light intensity and hydrodynamic diameter, potentially introducing errors (Stetefeld, McKenna and Patel, 2016). Analysis is rapid, non-destructive, and suitable for sample volumes as low as 12µL. However, concentrated samples may necessitate dilution, potentially impacting aggregate stability (Al-Ghobashy *et al.*, 2017).

SLS, often combined with temperature ramping, detects aggregation onset, enabling determination of protein apparent melting temperature (T_m) and aggregation temperature (T_{agg}). This aids in assessing protein conformational and colloidal stability during formulation development. Aggregation temperature can be determined at sensitive wavelengths (266 nm and 473 nm) for detecting small and large protein particle formation.

1.6.4 Nanoparticle Tracking Analysis

Nanoparticle tracking analysis (NTA) is a powerful technique that can effectively monitor the Brownian behaviour of individual particles within the size range of 0.1µm to 1µm and analysis is most dependable when working within a concentration range of 10^7-10^8particles.mL^{-1} (Tian *et al.*, 2016). NTA offers several advantages over Dynamic Light Scattering (DLS), especially for polydisperse particles in solution. These advantages include the ability to track individual particles, gain size-distributed particle concentrations, achieve better peak resolution, and experience less interference from the presence of larger particles (Vasudev, Mathew and Afonina, 2015). However, there is still the possibility of bias towards larger particles.

One of the notable benefits of NTA is its rapid analysis time, non-destructive nature, and the use of small sample volumes, typically around 0.5 mL for equilibration and analysis. Nevertheless, it's important to acknowledge that NTA has often been considered semi-quantitative due to various factors, including instrument settings, operator judgment, and potential interference in the analysis process (Vasudev, Mathew and Afonina, 2015).

2 Project Objectives

Botulinum neurotoxins, despite their inherent toxicity, have demonstrated significant therapeutic potential in treating various neurological diseases. However, a significant challenge in BoNT manufacturing is its susceptibility to aggregation. Despite, there is very little literature that explores the stability of botulinum neurotoxin during hydrodynamic flow conditions and high shear in the presence of changing physiochemical conditions that are characteristic of environments in typical industrial bioprocesses.

Peristaltic pumping is known for being a low shear pump solution for handling sensitive biologics and is ubiquitous throughout bioprocesses. However, little is known about the stresses involved in protein aggregation during the peristaltic pumping of therapeutic proteins in tangential flow filtration (TFF), specifically the dynamic changes in physiochemical conditions caused by imposed shear stress.

A literature review has revealed various aggregation models prevalent in bioprocessing. It is unlikely that these models operate independently, and they respond differently to alterations in solution conditions, such as pH and ionic strength. These changes influence protein-protein and protein-interface interactions. In a unit operation like TFF, where pH and ionic strength dynamically fluctuate, electrostatic forces continually change, impacting the rate of aggregation and monomer loss.

To accurately quantify the impact of each aggregation model, techniques must be employed, and new ones developed to effectively isolate these models from one another for measurement. Consequently, this thesis aims to investigate the aggregation mechanisms within peristaltic pumping.

2.1 Objective 1: Explore the Impact of Solid-Liquid Interfaces, Hydrodynamic Flow and Shear on the Stability of Botulinum Neurotoxin Serotype-E

Solid-liquid interfaces are inescapable during the bioprocessing of therapeutic proteins, yet the dynamics between these and hydrodynamic flow, shear and turbulence on the monomer loss and protein particle formation of botulinum neurotoxin serotype-E have not been investigated.

This objective aims to use a spinning disc scale down device, where hydrodynamic flow and shear is generated in a controlled environment, to gain a baseline understanding of the stability of endopeptidase negative (i.e., non-toxic) botulinum neurotoxin serotype-E (-ve BoNT/E). This can be evaluated alongside updated computational fluid dynamic (CFD) models to predict the turbulent conditions inside the device during operation to improve our knowledge of the hydrodynamic workings of the device. Monomer and particle formation will be quantified, in unison, using size-exclusion chromatography and backgrounded membrane imaging to understand the kinetics of protein aggregation during shear and reveal the particle morphologies that form as result.

Chapter 3 shows the latest CFD simulations that predict flow regimes inside the spinning disc device at different rotational speed and the resulting protein decay coefficients and particle formation during experimental processing of -ve BoNT/E during operation.

2.2 Objective 2: Assess the Impact of Physiochemical Conditions on the Stability of Botulinum Neurotoxin Serotype-E during Bioprocessing in a Comparative Study of a Spinning Disc vs. a Peristatic Pump

During bioprocessing, it's necessary to manipulate physiochemical conditions to separate the product from impurities. However, botulinum neurotoxins can undergo slight conformational changes in response to these conditions, such as changes in pH, as part of their natural mechanism of action. This response may inadvertently introduce instabilities and complications in the bioprocessing by exposing hydrophobic regions that drive protein aggregation.

Biologics' stability is often assessed using ultra-scale down (USD) models, like the spinning disc device. However, most USD methodologies reported have primarily examined product stability under static conditions, which doesn't fully capture the dynamic nature of bioprocesses.

This objective aims to use the spinning disc device to explore how different physiochemical conditions (both static and dynamic) impact the stability of -ve BoNT/E. Additionally, since peristaltic pumping mechanisms remain largely unknown, we will develop a novel ultra-scale down device and compare it to the spinning disc device in terms of protein aggregation kinetics and particle morphologies to assess its suitability as a process mimic.

Chapter 4 presents the changes in stability of -ve BoNT/E in the spinning disc device and a novel peristaltic pump USD device under different physiochemical conditions. The aggregation kinetics and particle morphologies are explored, and stability is cross examined with available thermal stability and molecular dynamics data. Dynamic physiochemical changes are explored when processing of the toxin in the spinning disc device.

2.3 Objective 3: Investigate the Impact of Peristaltic Pump Parameters on Protein Aggregation by Developing Novel Scale-Down Devices

Peristaltic pumping is ubiquitous throughout bioprocesses, however little is known about how peristaltic pump parameters, such as tubing type, pump speed and occlusion, which are essential for correct pump operation, impact protein aggregation. This objective aims to develop novel ultra scale down devices and conclude which are the primary mechanisms driving of protein aggregation during peristaltic pumping.

Chapter 5 expands the used of the scale-down peristaltic pump device in Chapter 3 and explores how peristaltic pump parameters effect protein aggregation of two model proteins: -ve BoNT/E and tocilizumab during pump operation. Creation of additional novel ultra scale down devices attempt to isolate expansion-relaxation of solid-liquid interfaces of peristaltic tubing and solid-solid interface contact of inner tubing walls to study their impact determined to be the root cause of protein aggregation.

3 Navigating Turbulent Waters: Shear-Induced Aggregation of Botulinum Neurotoxin Therapeutics

3.1 Chapter Summary

Botulinum neurotoxins (BoNTs) are a successful group of therapeutic proteins that can be used to treatment neuromuscular indications. However, their sensitivity to forming protein aggregates is troublesome during bioprocessing. Many mechanisms can cause protein aggregation to occur - one type extant throughout bioprocessing is shear-/flow-induced aggregation via adsorption to solid-liquid interfaces. To observe this mechanism, a spinning disc device was used to create and control an environment of high fluidic turbulence to investigate the stability of different proteins. In this chapter, the hydrodynamic environment of the device was thoroughly characterised using computational fluid dynamics (CFD) to understand how the flow regime changes at different rotational speed (RPM) of the spinning disc. When processing endopeptidase negative botulinum neurotoxin serotype-E (-ve BoNT/E) inside the device, samples were taken at regular 15-minute intervals and analysed using size-exclusion chromatography (SEC) to quantify monomer and backgrounded membrane imaging (BMI) to quantify the formation of protein particles.

Based on CFD predictions, Reynolds number (Re) linearly increased at a rate of 2.7 Re.RPM^{-1} and the device was fully turbulent above 3700RPM. Shear rates increased second order like, reaching up to 220,000s^{-1} at 12000RPM. When processing -ve BoNT/E in the device, 50% of monomer was remaining after two hours at 12000RPM and 100% of monomer remained after a two-

hour incubation control. Protein decay coefficients, based on the rate constants of an exponential decay function fitted to monomer loss data, correlated linearly with shear rates and exponentially with Reynolds number (Re). In laminar flow regimes (Re < 10,000), there was a lag-phase in the change of protein decay coefficients whilst turbulent regimes (Re > 10000) accelerated the increase in coefficients. When quantifying particles, concentrations increased linearly over time and, after processing -ve BoNT/E at 12,000 RPM, 800,000 particles.mL^{-1} was measured equivalent to a total particle area of 4.1x10^{7} μm^{2}·ml^{-1}. Larger particles formed.at higher turbulent flow.

Based on particle formation, two rates were calculated: the rate of particle formation (particles.mL^{-1}.min^{-1}) and the rate of particle area growth (μm^{2}·ml^{-1}.min^{-1}). Like protein decay coefficients, both rates increased exponentially against Re number. However, against shear strains rates, the rate of particle formation increased linearly, and the rate of particle area growth increased exponentially. At 12,000 RPM or 32,000 Re attained rates were 6.8x10^{3} particles.mL^{-1}.min^{-1} and 3.6x10^{5} μm^{2}·ml^{-1}.min^{-1}. Again, laminar flow was a lag phase for particle growth and turbulence led to the rapid increase in particle concentration and particle area. In turbulent regimes, Kolmogorov length scale eddies as small as 2.1 μm were predicted to form at 12,000 RPM thus being within the size range of the protein particles formed and potentially interacting with each other. However, their effect on particle size was inconclusive.

Based on other literature, shear strain rates were not expected to directly cause monomer loss and protein aggregation. Hydrodynamic flow and turbulence have often been overlooked. In this chapter, under laminar flow conditions, a lag-phase in monomer loss and aggregation was clear. This could be due to a combination of 1) reduced protein-protein interactions in the bulk solution and 2) reduced mass transfer of proteins to the solid-liquid interface. In turbulent flow, which is driven by eddy motion, points 1) and 2) are increased causing monomer loss and aggregation. The spinning disc device coupled with BMI yielded a strong method to investigate the effect of turbulence on aggregation, however improvements to the CFD model mesh and a suitable particle analyser would have allowed for a better understanding of the role of Kolmogorov eddies on particle size.

3.2 Introduction

Botulinum neurotoxins (BoNT) are the most potent compounds known but are a successful group of therapeutic proteins. They are a family of proteins produced by the bacterium *Clostridium botulinum* and cause the disease ‘Botulism’, a flaccid paralysis illness which is rare but severe in humans that can be lethal if not treated in time. Whilst the family of proteins are divided up into seven currently known serotypes assigned A through to G. The protein structure, 150kDa in size, composes of two key chains: the heavy chain (100kDa, HC) and the light chain (50kDa, LC), which are joined together by one bisulfide bond. The HC includes two-functional domains: a binding domain (BD) and a translocation domain (TD), whilst the LC itself is an endopeptidase.

Infection is naturally caused after ingestion of contaminated meat and colonisation of the gastro-intestinal tract. Here, BoNTs are produced with a progenitor complex to protect it against low pH and proteolytic cleavage (Gu *et al.*, 2012) where it can traverse the gut lining intact and into the bloodstream.

BoNTs have a high binding affinity to nerve terminals, but due to their poor diffusivity they rely upon the host's circulatory system to spread throughout their body. Once the BoNT reaches a nerve terminal, the BD domain binds to luminal vesicle protein domains found on the neuron surface which initiates internalisation into the neuron inside. BoNTs encapsulated inside endocytic vesicles during endocytosis remain in-wait until the vesicle matures into a late endosome during which the internal pH lowers to ~5. Responding to this, the TD domain forms a transmembrane channel through the vesicle membrane through which a now unfolded-LC chain is translocated into the cytoplasm followed by refolding and bisulfide bond reduction (Fischer and Montal, 2007). Then the LC cleaves SNARE proteins (VAMP, SNAP and Syntaxin) involved in neurotransmission (Montal, 2010), preventing neurotransmitter release.

Despite the natural danger of these toxins, their mechanism of action, low diffusivity and potency has enabled successful commercialisation of BoNT therapeutics since 1989 (Whitcup, 2021) to treat patients with neurological disorders. Since 1989, the manufacturing bioprocesses of these BoNT therapies has moved from natural production of BoNT with its progenitor complex (900kDa) in *Clostridium botulinum* to recombinant expression of the active 150kDa BoNT in *Escherichia coli*. Due to the potency of BoNTs requiring typical drug product formulations as low as 0.44ng per vial, the commercial scale to sustain a global supply was reported to be within 100Ls (Frevert, 2010).

Purification of BoNTs was modernised from precipitation, centrifugation and crystallisation steps to standardised and scalable bioprocess unit operations such as tangential flow filtration (TFF) and chromatography. Whilst these advancements have improved drug product purity, efficacy and safety in modern day manufacturing, the inherent sensitivity of BoNTs to forming protein aggregates (Toth, Smith and Ahmed, 2009; Bai *et al.*, 2011) during bioprocessing risks the formation of product impurities and reduced yields.

Protein aggregation can be caused by several different mechanisms during bioprocessing and they remain an ongoing challenge to overcome. Aggregation can be caused by the unfolding of protein monomers which exposes reactive sites for non-specific protein-protein interactions and formation of higher-order structures (Simpson, Good and Leach, 2020). This process can be the outcome of different protein interactions with the environment (adsorption to interfaces such as solid-liquid or air-liquid) (Biddlecombe *et al.*, 2009; McUmber, Randolph and Schwartz, 2015; Kalonia *et al.*, 2018; Deiringer *et al.*, 2022; Žuntar *et al.*, 2022), chemical-processes (such as oxidation of stabilising disulphide bonds) or mechanical processes (such as solid-solid interface contact, expansion-relaxation of interfaces) (Bee *et al.*, 2012; Sediq *et al.*, 2016; Deiringer and Friess, 2022a; Fanthom *et al.*, 2023).

Investigation of these mechanisms often requires unique and purpose build devices or methodologies to study protein aggregation. In one such example, a specifically designed device has been developed at UCL Biochemical Engineering to carefully produce controllable turbulent flow conditions by a rapidly spinning disc and study solid-liquid interfacial aggregation. It has shown that materials, roughness, excipients, temperature and shear strain rates can affect rates of protein monomer loss and protein aggregation (Biddlecombe *et al.*, 2007, 2009; Tavakoli-Keshe *et al.*, 2014).

Shear forces describe the velocity difference in adjacent bodies moving parallel to each other. It is extant throughout bioprocess unit operations: centrifugation (Zhang *et al.*, 2007), tangential flow filtration (TFF) (Arunkumar *et al.*, 2016; Wang *et al.*, 2017) and filling (Nayak *et al.*, 2011; Dreckmann *et al.*, 2020) and has been hotly debated on its role in protein aggregation. Currently, a consensus has been reached that unless the protein in question has a functional means to respond to shear forces, the underlying energy in shear is normally not enough to overcome the intramolecular forces within protein structures and cause their unfolding and exposure of reactive sites (Jaspe and Hagen, 2006; Bee, Stevenson, *et al.*, 2009; Bekard *et al.*, 2011; Lippok *et al.*, 2016; Sparkes and Holland, 2017; Grigolato and Arosio, 2020).

Whilst this is an ongoing debate, turbulence has been poorly reported alongside scale-down devices used to investigate monomer loss and protein aggregation. This is despite our deep understanding for its role in driving mass transfer processes and protein aggregation driven by mechanisms involving adsorption processes at interfaces or interactions in bulk fluid that requires mass transfer to fundamentally drive this.

This chapter aims to continue previous works that have investigated shear forces on protein monomer loss and aggregation using a custom shear generation device (Biddlecombe *et al.*, 2007, 2009; Tavakoli-Keshe *et al.*, 2014) but observe the effects on the loss of endopeptidase negative, i.e., non-toxic, botulinum neurotoxin serotype-E (-ve BoNT/E). Moreover, knowing that hydrodynamics and turbulence are key for the mass transfer of proteins from the bulk solution to the interface, this chapter will better characterise the hydrodynamics inside the device using computational fluid dynamics. Findings will be linked to any clear monomer loss or protein aggregate formation using new backgrounded membrane imaging (BMI) techniques to greater understand the role of hydrodynamic flow on protein particle size and concentration.

3.3 Materials and Methods

3.3.1 Spinning Disc Device

The spinning disc device is used to generate and control a high-shear environment to simulate the effects of shear and surface adsorption to solid-liquid interfaces on proteins during bioprocessing. A picture of this device can be seen in Figure 3-1 The sample chamber of the spinning disc device (30mm x 17mm) holds a stainless-steel disc (26mm x 8mm) used to generate high-shear when spinning. A cooling jacket surrounds the sample chamber to maintain temperature during applying high-shear rates while eliminating the air-liquid interface (Biddlecombe *et al.*, 2007, 2009; Tavakoli-Keshe *et al.*, 2014). The spinning disc was prepared by sanding down with 420 grit paper, rinsing with MilliQ and passivation of the surface with 50mM citric acid followed by a further rinse step. A similar procedure at this grit size gave a disc surface roughness average of approximately 90nm.

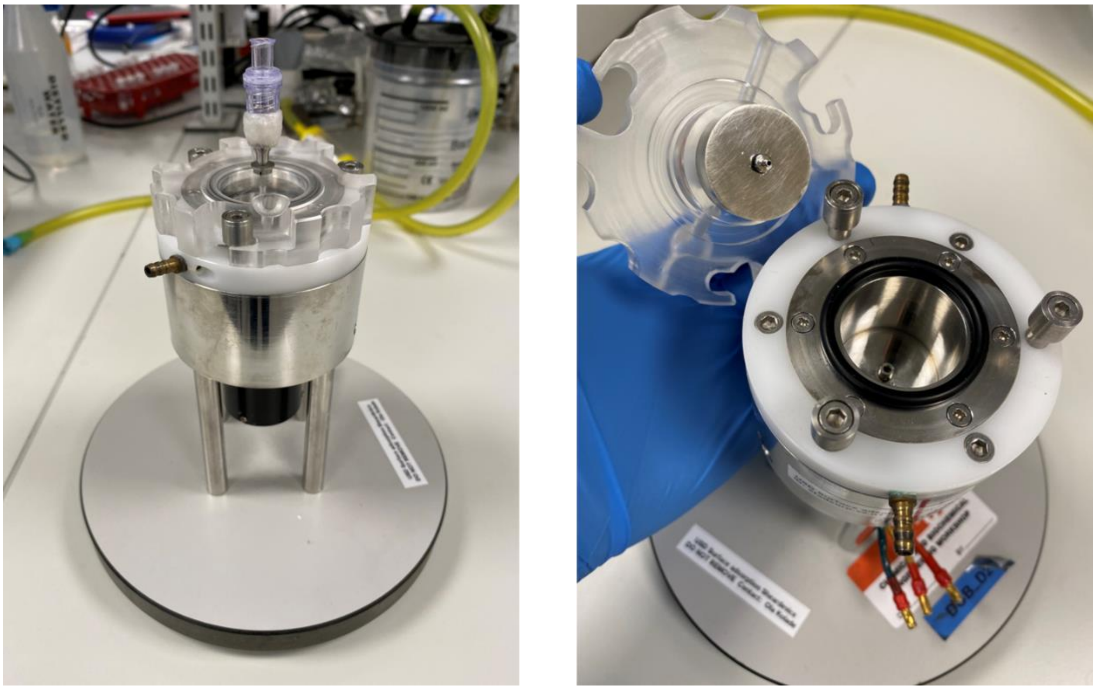

Figure 3-1 Picture of the spinning disc device (left) and a look at the disc and sample chamber (right).

3.3.2 Shear Predictions Using Computational Fluid Dynamics

A computer aided design (CAD) model representing a rotor (spinning disc) enclosed inside a stator (sample chamber walls) of dimensions given in Table 3-1 was built to resolve fluidic flow regimes within the spinning disc device was performed using computational fluid dynamics (CFD) simulations (Ansys, Inc., CFX version 17.0, Canonsburg, PA). Simulations were run on an Intel® CORE i7-8650 CPU with four processors of 1.9 GHz with 16Gb RAM. A one-quarter section of the disc was modelled as a 3D-cross section because of rotational symmetry and available computational power. The rotating disc was set as an individual wall boundary with no slip.

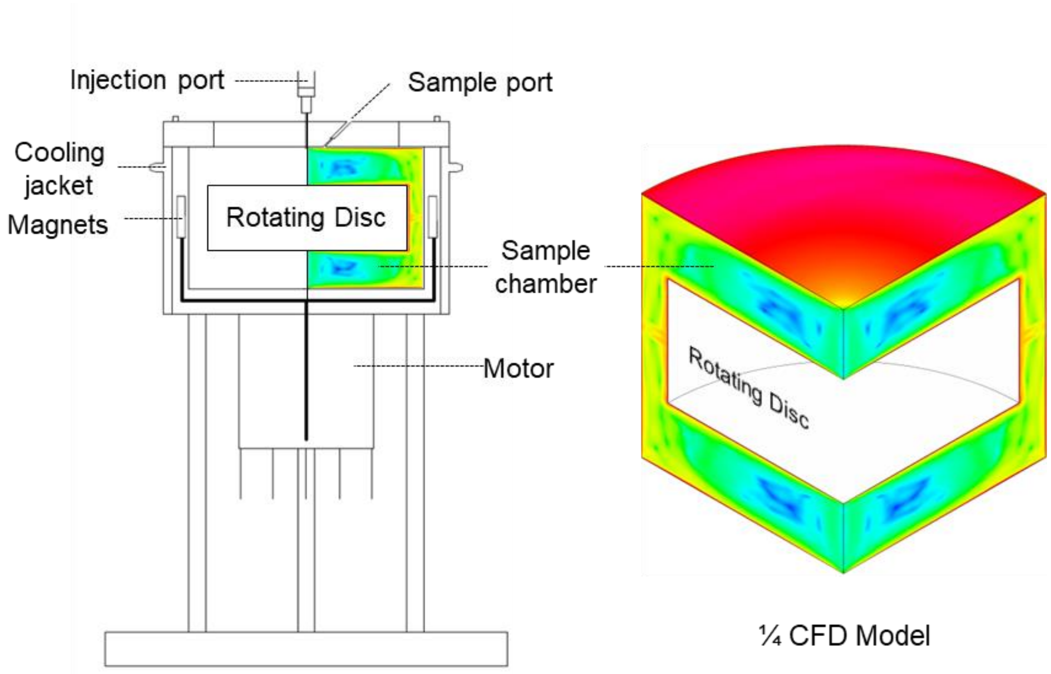

Figure 3-2 Illustration of the spinning disc disc and CFD modelled sections.

The fluid model selected was shear stress transport (SST) (Menter, 1993), i.e., a combination of k-ε, which solves high-Reynolds flow in the turbulent layer, and k-ω, which solves low-Reynolds flow in the viscous sublayer. To capture viscous sublayer flow at walls, an inflated mesh was used with the first cell height iterated at each rotational speed (RPM) of the spinning disc. This process was conducted to achieve a maximum Y^+ (dimensionless wall distance for a wall-bounded flow) of 2.0 within 10% tolerance on all walls of the spinning disc device model. For reference, the viscous sublayer has a Y^+ below 5.

Disc RPMs simulated were 3000, 6000, 7500, 9000 and 12000RPM. All simulations were meshed with approximately 6.0 million elements, varying slightly due to different iterated inflation meshes at each RPM, and solved until reaching the defined number of iterations of 200 and converging within a residual error of $1x10^{-4}s^{-1}$ and conservation error of 0.01. 6 million mesh elements were decided as suitable for the final CFD models for all tested disc RPM speeds after a mesh independent study and observing the change in Y+ and shear rate values (Appendix Figure 9-3, Figure 9-4 and Figure 9-5). Mesh element sizes and convergence conditions supplied accurate results at an acceptable process time for each simulation.

Table 3-1 Spinning disc device dimensions.

	Notation/equation	**Dimension (mm)**
Chamber diameter	d_o	30.0
Disc diameter	d_i	26.0
Chamber height	h_o	17.0
Disc height	h_i	8.0
Radial gap	$r_g = \frac{d_o - d_i}{2}$	2.0
Axial gap	$y_g = \frac{h_o - h_i}{2}$	4.5

3.3.3 Materials

Stock solution of an endopeptidase negative (i.e., non-toxic) botulinum neurotoxin serotype-E, herein referred to as -ve BoNT/E, was provided by Ipsen Biopharm (Wrexham, UK). This stock solution is intermediate material and partially purified hence host-cell proteins are present in the mix, but -ve BoNT/E makes up more than 80% of the total protein content. The stock solution was buffer exchanged using Slide-A-Lyzer® G2 2,500 MWCO PES 70mL dialysis cassettes bought from Thermo Scientific (Rockford, IL, USA). Dialysis was conducted following manufacturer’s instructions to exchange the protein stock solution buffer with a formulation buffer forming of 0.1M sodium phosphate 0.1M sodium chloride (pH 7.5) using a total dialysate buffer volume that is 200-times the sample volume used. This formulation was used throughout all experiments in this chapter. All buffer components were acquired from Sigma-Aldrich Co. (St. Louis, MO, USA) and water obtained from a Milli-Q® Advantage A10 water system (Merck KGaA, Darmstadt, Germany).

The protein concentration was adjusted to 0.2mg.ml^{-1} using the formulation buffer and final concentration confirmed by a Little Lunatic UV-Vis Spectrophotometer (Unchained, Pleasanton, CA). After formulation, the solution was filtered through a 0.22µm PVDF filter and kept at 4^{o}C prior to use. Before their use in any studies, protein solutions were filtered once again using the same filter to remove any particles that may have formed during storage. Protein solutions were not left in the fridge for any longer than one week before their use. All formulations within this chapter were conducted at 0.2mg.ml^{-1} 0.1M sodium phosphate 0.1M sodium chloride (pH 7.5).

3.3.4 Spinning Disc Device Operation

The shear device was filled with protein solution through a one-way injection valve on the top of the device via the injection port, being sure to remove all air. The temperature was kept at 20^{o}C using a thermostat chilled water bath (LAUDA-Brinkmann, Delran, NJ, United States) set to a pre-determined temperature calibrated against the rotational speed (RPM) of the spinning disc and pumped through the cooling jacket. -ve BoNT/E was processed for two-hours at the following disc speeds: 0RPM, 6000RPM, 7500RPM, 9000RPM and 12000RPM. 7500RPM was conducted in triplicate (n=3) and the experimental standard deviation (SD=1) applied to other disc speeds.

Samples of 100µL were taken from the device at 15-minute intervals by displacing the chamber sample with buffer formulation. In between samples, the device was cleaned by operating at 9000RPM for 15 mins each with 40mM phosphoric acid, then MilliQ®, then 40mM sodium hydroxide and a final MilliQ® step.

3.3.5 Reynolds Number and Kolmogorov Eddy Length Determination

Rotational Reynolds number (Re) of the spinning disc was calculated using Equation 3-3 (Reinke, Schmidt and Beckmann, 2018). This is a function of the radial gap, r_g (Equation 3-1), and tip speed, U_1 (Equation 3-2). The diameter of the spinning disc chamber is d_o and diameter of the spinning disc is d_i. Fluid density ρ and dynamic viscosity μ were assumed to be that of water at 20°C and standard pressure. Kolmogorov length scale η eddies were calculated using Equation 3-4 where the kinematic viscosity v was assumed to be that of water at 20°C and standard pressure. Turbulent energy dissipation rate ε was taken as the maximum value predicted in computational fluid dynamic (CFD) simulations at each disc speed.

$$r_g = \frac{d_o - d_i}{2}$$

Equation 3-1

$$U_1 = \omega_1 * R_1$$

Equation 3-2

$$Re = \frac{r_g * U_1 * \rho}{\mu}$$

Equation 3-3

$$\eta \equiv \frac{\upsilon^{3\frac{1}{4}}}{\varepsilon}$$

Equation 3-4

3.3.6 Size-Exclusion Chromatography

Analysis and quantification of samples was conducted using an Agilent Technologies 1260 Infinity LC System (Santa Clara, CA) with degasser, binary pump, injector, temperature controller and diode-array detector (DAD). A Waters Corporation (Herts, UK) Acquity UPLC Protein BEH SEC 4.6x150mm 1.7µm size-exclusion column and Acquity UPLC Protein BEH SEC Guard Column was equipped to the system. Analysis was conducted at 0.2ml.min^{-1} and 25^{o}C with a 0.22µm filtered mobile phase formulated at 0.1M L-Arginine 50mM sodium phosphate 0.1M sodium chloride (pH 7.0). MilliQ® water was used in buffers and sourced from a Merck KGaA (Darmstadt, Germany) Advantage A10 water system.

The column was first equilibrated with 5CVs of mobile phase before 10µL samples were injected. Sample preparation was conducted by centrifugation at 18,000g for 10mins at 4^{o}C. Proteins were quantified using a wavelength absorbance at 280nm with reference at 550nm. Where samples were recovered from studies using buffer displacement, the fractions of monomer quantities calculated using Equation 3-5, where the protein concentration at time t is C_t and the protein concentration at time 0 is C_0 based on integrated peaks and adjusted using a dilution factor. Protein decay coefficient, k, was calculated at each disc rotational speed based on the exponential decay function (Equation 3-6, rearranged to Equation 3-7). The column was calibrated by injecting a sample of the BEH200 SEC Protein Standard Mix (Waters, Herts, UK) to correlate column elution time with species molecular weight (Appendix Figure 9-1 and Figure 9-2).

$$Fraction\ of\ monomer\ remaining = \frac{C_t}{C_0} * 1.01 \qquad \text{Equation 3-5}$$

$$C_{(t)} = C_0 e^{-k*t} \qquad \text{Equation 3-6}$$

$$\ln\left(\frac{C_{(t)}}{C_0}\right) = -k * t \qquad \text{Equation 3-7}$$

3.3.7 Backgrounding Membrane Imaging

Backgrounded membrane imaging (BMI) was performed using the Horizon system (Halo Labs, Burlingame, CA). All processed samples were diluted 1:16 to be within the 7% membrane coverage analysis threshold. Samples were diluted in their respective buffer and 25μL was applied to the wells of a 0.4μm filter plate for vacuum filtration inside a laminar flow hood. Image analysis was conducted using Horizon Vue image analysis software using the recommended software algorithm. Particle sizes are reported as the pixel area where one pixel is equivalent to 1μm^2.

3.3.8 Particle Data Analysis and Selection

Particle data obtained from BMI analysis was structured into a tidy-format table with dimensions of 9 columns and ~19,000 rows where each row represents an individual particle detected. Key variables included are disc speed (RPM), timepoint (min), intensity, SIMI intensity, equivalent circular diameter (ECD, µm), aggregate surface area by pixel coverage (px, 1px = 1µm^2), aggregate surface area by ECD (µm^2), perimeter (µm^2), circularity, convexity and aspect ratio. Data selection was conducted by filtering and excluding particles with SIMI intensity less than 0 and greater then 20, and aggregate surface area less than 18µm^2. These values were determined carefully by analysis of foreign particles produced during a negative control study processing buffer and eliminating particles in the lower limits of detection in the Horizon BMI system.

3.3.9 Statistics

Linear and non-linear regression analysis on data was performed using OriginPro Version 2023b 64-bit SR1 data analysis software (OriginLab Corporation, Northampton, MA). performing ordinary least squares (OLS) method. T-tests were calculated using the two-sample model and significance level at $p < 0.05$. Shapiro-Wilk test at a significance level of $p < 0.05$ was used to assess the normality of particle data. Kolmogorov-Smirnov test was used to test the fit of particle data to Weibull, Gamma and Exponential distribution function at a significance level of $p < 0.05$. ANOVA analysis was used to determine linear regression slopes of particle concentration and total particle area change that were significantly different from zero at the $p < 005$ level.

3.4 Results and Discussion

3.4.1 Model Set-up, Iterating Y+ and Mesh Size on Computational Fluid Dynamic Simulations

Computational fluid dynamic (CFD) simulations were conducted on a one-quarter model of the spinning disc device following the symmetry about rotational axis (Figure 3-3). In CFD simulations, Y+ is a non-dimensional and normalised distance perpendicular from the local wall. It can be used to set the first cell height in a mesh and helps to determine whether the mesh cell is within the viscous sub-layer (where viscous forces and laminar flow dominate) or turbulent regime. It therefore aids generating inflated mesh structures close to walls to resolve the viscous sub-layer.

An inflation mesh was therefore used on all device walls (disc and chamber, Figure 3-3) with the first cell height iterated at each disc rotational speed to achieve a maximum Y+ ($Y+_{max}$) value of 2.0 within a tolerance of 10%. These interfaces were set up with no-slip boundary conditions, whilst the internal interfaces were set with periodic boundaries given the rotational symmetry of the chamber. The values of first cell heights to achieve $Y+_{max} < 2.0$ on these walls are shown in Figure 3-4 and Y+ distribution across walls are shown by contours in Figure 3-5 and Figure 3-6.

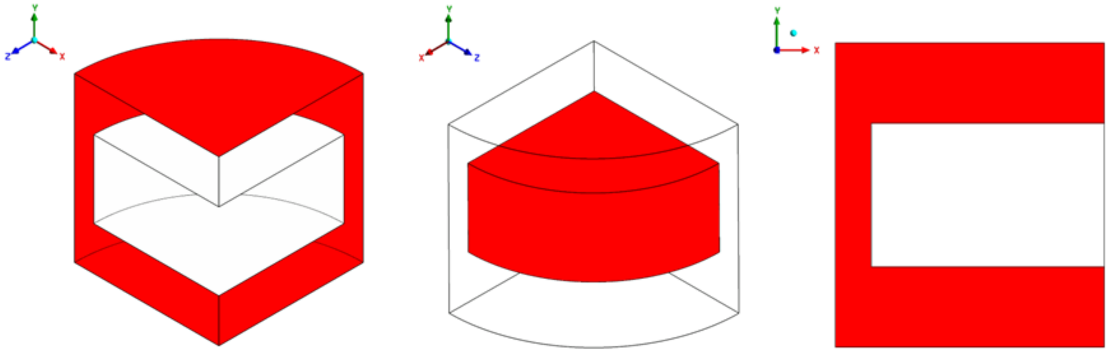

Figure 3-3 Interfaces of the spinning disc device CFD model treated with no slip-boundaries (red): (a) chamber walls, (b) disc walls and (c) fluidic domain.

6 million mesh elements were decided as suitable for the final CFD models for all tested disc RPM speeds after a mesh independent study and observing the change in Y+ and shear rate values (Appendix Figure 9-3, Figure 9-4 and Figure 9-5). This was done by conducting CFD simulations of the spinning disc device at 12,000 RPM with different meshes containing 1.6x10^{6}, 2.6x10^{6}, 6.1x10^{6} and 1.9x10^{6} elements. The shear rate values were then compared from each meshed model to find the number of elements at which these shear values no longer change.

For meshed models with elements above 6.1x10^{6} the mean shear rate across the disc edge at the first cell height along no longer significantly change at 2.2x10^{5}, where the next mesh model at 19x10^{6} elements yielded the same mean shear rate of 2.2x10^{5} (Appendix Figure 9-4 and Figure 9-5). Y+ values in each mesh independent study remained under 2.0 and were similar along the disc edge (Appendix Figure 9-3). 6 million elements was therefore deemed a suitable mesh size to perform all RPM simulations under the convergence conditions to supply accurate results at an acceptable process time for each simulation.

When increasing disc RPM the first cell heights decrease, most notably between 3000 RPM and 6000 RPM, as the faster spinning of the disc is expected to increase turbulence and thereby reducing the viscous sub-layer thickness requiring a smaller first cell height to maintain Y+$_{max}$ < 2.0.

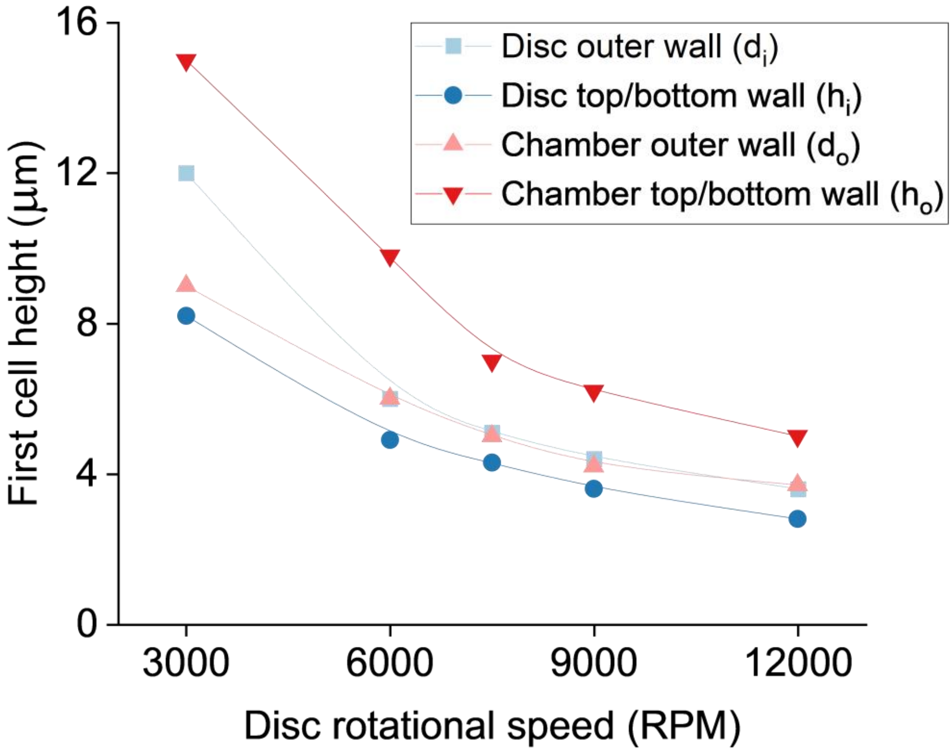

Figure 3-4 First cell heights of the CFD inflated mesh. Disc's outer wall (d_i), and top/bottom (h_i) walls, and the chamber's outer wall (d_o) and top/bottom walls (h_o) to achieve Y+$_{max}$ < 2.0.

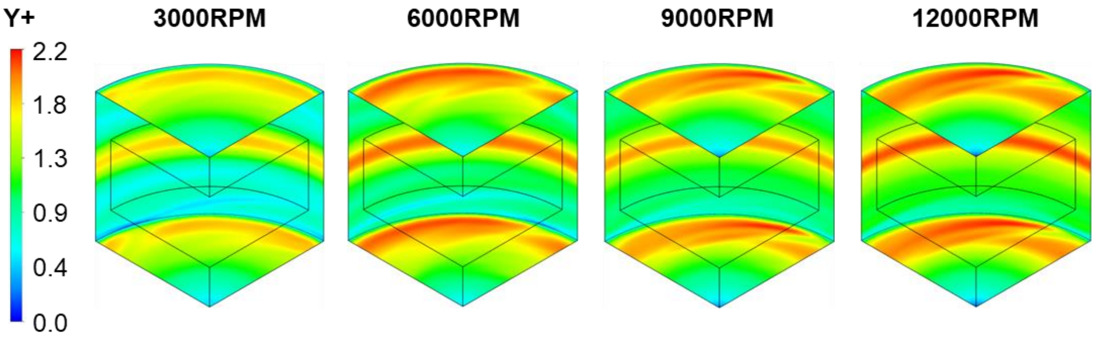

Figure 3-5 Y+ values across the spinning disc device chamber walls. CFD was simulated under 3000, 6000, 9000 and 12000RPM and data is representative of a steady state.

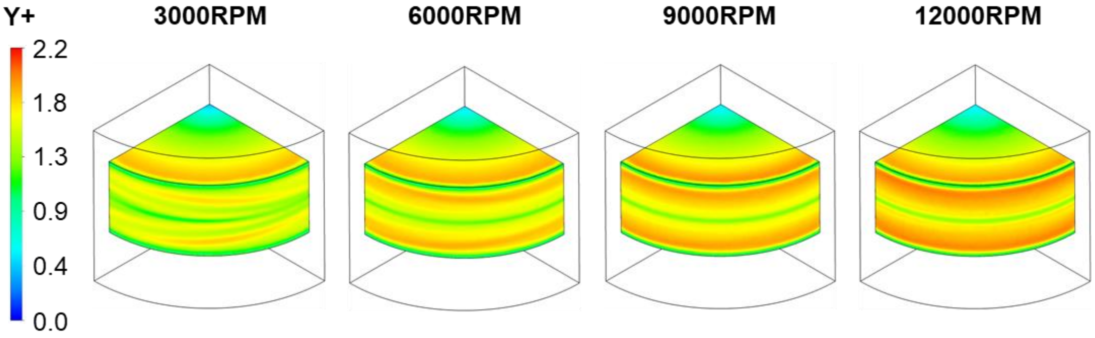

Figure 3-6 Y+ values across the spinning disc device disc walls. CFD was simulated under 3000, 6000, 9000 and 12000RPM and data is representative of a steady state. At 3000RPM, features of predicted wavy Taylor vortex instabilities in the radial gap are seen on the disc outer wall compared to uniform Y+ at higher speeds.

3.4.2 Development of Turbulent Flow Regime Within the Spinning Disc Device

To visualise patterns of fluid flow and velocity, smoothed contours of velocity were extracted from CFD simulations at different spinning disc rotational speeds and are shown in Figure 3-7. Superimposed arrows on the contours for 12000 RPM illustrate the direction fluid flow within the device chamber (inferred from directional velocity at 12000 RPM in Appendix Figure 9-6) and will be described below.

The spinning disc acts as a bladeless compressor pumping the fluid in contact with the disc radially outward via centrifugal forces. When this fluid reaches the tip of the disc, it is drawn into the radial gap between the disc and the outer chamber wall, where it joins with fluid coming from the opposite side of the disc. The combined fluid is ejected from the disc and thrown into the adjacent chamber walls where it bifurcates into two streams. These streams leave the radial gap and travel along the chamber ceiling and floor where fluid is drawn-in axially towards the centre of the chamber via centripetal forces. These flow patterns predicted by CFD in our shear device are expected and typical of single-phase rotor-stator reactors used in, for example, process intensification in the chemical and pharmaceutical industries (Visscher *et al.*, 2013; Hop *et al.*, 2023).

In similar single-phase (liquid-phase) rotor-stator systems, flow phenomena called Taylor-Couette flow, which describes the formation of vortices in radial gaps between rotating spinning discs and a stationary cylindrical wall, are known to form and have been widely researched (Taylor, 1923; Watanabe and Furukawa, 2010; Hara *et al.*, 2015; Mulligan *et al.*, 2018). Similar phenomena are noticed in the spinning disc device.

In the CFD simulations of the spinning disc device, as Reynolds number increases centrifugal forces destabilise the flow in the radial gap to produce wavy vortex flow – this phenomena were described by Hara *et al*. (2015) (Hara *et al.*, 2015). At 3000 RPM (Re 8200) specifically, non-uniform chevrons of wavy vortex flow within the radial gap can be seen on the Y^+ contours of the disc wall shown in Figure 3-6 and occurs at similar Re number previously reported by Hara *et al.* (2015). The presence of wavy vortex flow indicate that the spinning disc device was transitioning into turbulent flow as increasing disc rotational speed increases Reynolds number. At 6000 RPM (Re 16200), the artefacts of these wavy vortices diminished as the chamber appears to enter a fully turbulent regime.

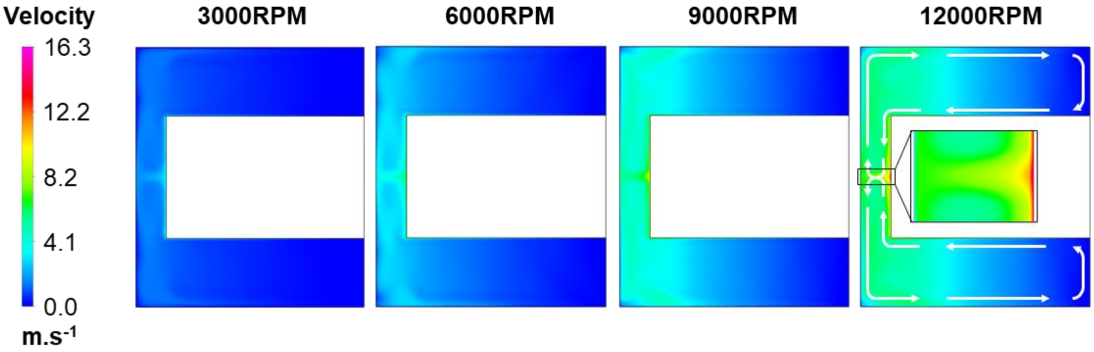

Figure 3-7 CFD analysis of fluid velocity magnitude in the spinning disc device. Superimposed white arrows in 12000RPM illustrate the movement of fluid pumped by the spinning disc informed by directional velocity. Insert for 12000RPM shows a zoomed-in view of flow within the radial gap. CFD was simulated under 3000, 6000, 9000 and 12000 RPM and data is representative of a steady state.

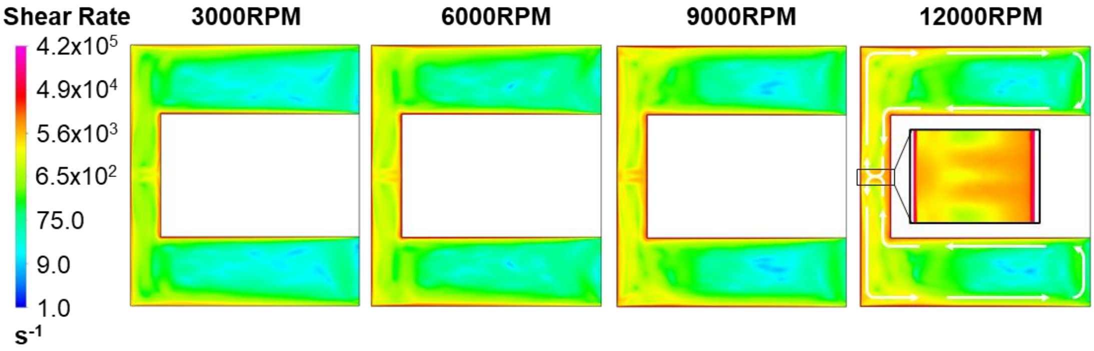

Figure 3-8 CFD analysis of shear rates in the spinning disc device. Superimposed white arrows illustrate the axial movement of fluid pumped by

the spinning disc. Insert for 12000RPM shows a zoomed-in view of shear strain rates within the radial gap. CFD was simulated under 3000, 6000, 9000 and 12000RPM and data is representative of a steady state.

This dissipation of wavy vortex flow occurs within 3000-6000 RPM (Re number 8200-16200) where Reynolds number, based on the tip speed, describes that the sample chamber transitions into fully turbulent flow. The increase in turbulent energy dissipation rate becomes apparent between 3000 and 6000 RPM further indicating the establishment of a turbulent flow regime (shown later in Figure 3-20).

3.4.3 Fluid Velocity, Reynolds Number and Shear Strain Rates

Due to non-slip conditions imposed in CFD simulations, the fluid in contact with the spinning disc has a velocity (m.s^{-1}) equal to the angular velocity (m.s^{-1}) along the radius of the disc at all simulated rotational speeds. The maximum fluid velocity (m.s^{-1}) within the device occurs at the 'tip' of the disc, within the radial gap, and is equal to the disc tip speed: 8.2 m.s^{-1} at 6000 RPM, 10.2 m.s^{-1} at 7500 RPM, 12.3 m.s^{-1} at 9000 RPM and 16.3 m.s^{-1} at 12000 RPM (Table 3-2). To characterise the turbulence within the device, Reynolds (Re) number, which is a dimensionless ratio of inertial forces and viscous forces, was used.

Three distinct flow regimes are described by Reynolds number: laminar flow (Re<2100), transitional flow (2100<Re<3500) and fully-established turbulent flow (Re>10000) (Paul, Atiemo-Obeng and Kresta, 2003). Using the fluid velocities and the dimensions of the shear device (Table 3-1 and Table 3-2), the rotational Re number was calculated using Equation 3-3 (Reinke, Schmidt and Beckmann, 2018). In the spinning disc device, Re number inside the radial gap increased linearly at a rate of by 2.72 RPM^{-1} (Figure 3-9-Right): 16200 at 6000 RPM, 20300 at 7500 RPM, 24300 at 9000 RPM and 32700 at 12,000 RPM. The shear device was predicted to enter a fully turbulent regime above 3700 RPM.

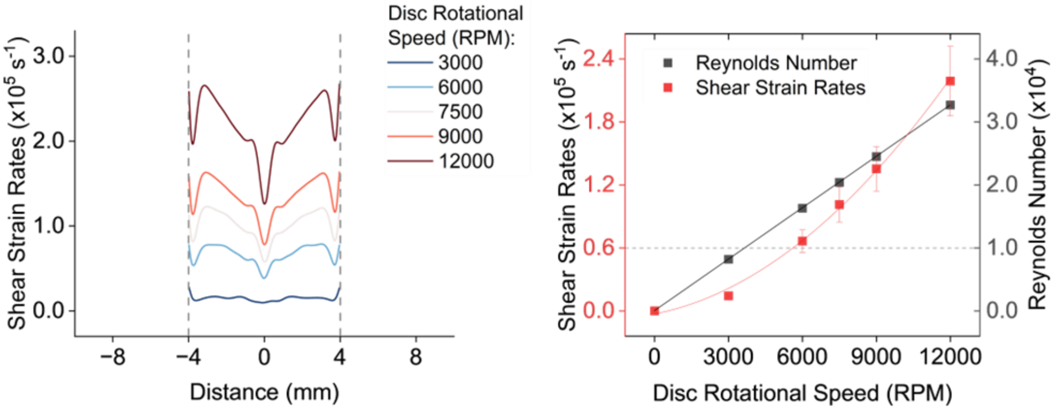

Figure 3-9 Spinning disc device shear rates and Reynolds number. (Left) Shear rates on the disc outer wall. Dashed vertical lines mark the boundaries of the top/bottom disc edge and distance is given from the centre of the disc. (Right) Mean shear rates with error bars showing standard deviation (SD=1) on the outer disc wall and Reynolds Number when increasing rotating disc speed (RPM). Reference line at Re 10,000 shows the threshold into a fully turbulent flow regime.

Figure 3-8 shows shear rate profiles retrieved and log-scale-coloured smoothed contours used to illustrate shear strain rates within the spinning disc device. In these, the highest shear strain rates were found close to the walls of the spinning disc and chamber due to the rapid dissipation of kinetic energy and momentum of fluid near the disc surface. Choosing 12000RPM as an example, within the bulk fluid at the centre of the radial gap shear strain rates reach 7000s^{-1}, however at the disc wall they can reach up to 220,000s^{-1}, 31-fold larger.

Based on Figure 3-7 and Figure 3-8, the radial gap is a region of strong hydrodynamic flow and is an area of interest in understanding the role of hydrodynamic flow and turbulence on protein loss and aggregate formation. Thus, shear strain rates were averaged across the surface of the disc edge in the radial gap and at a distance away from the disc wall equal to the first cell height used to reach $Y^{+}_{max} < 2.0$ - Figure 3-9-Left shows the change in shear strain rates along this profile.

The resulting mean shear strain rates taken from these profiles were: $0.67x10^5s^{-1}$ at 6000RPM $1.0x10^5s^{-1}$ at 7500RPM, $1.4x10^5s^{-1}$ at 9000RPM and $2.2x10^5s^{-1}$ at 12000RPM (Figure 3-9-Right). For comparison, the largest shear strain rates expected to occur during downstream processing is $20{,}000s^{-1}$ (Bee, Stevenson, *et al.*, 2009).

In the spinning disc device, shear strain rates increase with a second order-like relationship to disc rotational speed with an initial lag-phase followed by an acceleration in shear rates between disc rotational speeds of 0RPM and 6000RPM. This corresponded to the period when the disc device was transitioning into fully turbulent flow. Correlating shear strain rates within the established turbulent flow (above 3700RPM) gives a linear relationship with an increase of $25.5s^{-1}.RPM^{-1}$ and x-intercept at 3500RPM.

Table 3-2. Tip speed, Reynolds number, and shear strain rates in the spinning disc device at different disc speeds.

Disc rotational speed (RPM)	**Tip speed ($m.s^{-1}$)**	**Reynolds number (Re)**	**Shear rates (s^{-1})**
0	0.0	0	0
3,000	4.1	8,200	$0.14x10^5$

6,000	8.2	16,300	0.67x10^5
7,500	10.2	20,400	1.01x10^5
9,000	12.3	24,500	1.35x10^5
12,000	16.3	32,700	2.19x10^5

3.4.4 Flow-induced Monomer Loss of Endopeptidase Negative Botulinum Neurotoxin Serotype-E

Endopeptidase negative botulinum neurotoxin serotype-E (-ve BoNT/E) was processed in the shear device at different rotational speeds 0, 6000, 7500, 9000 and 12000RPM for two hours and at constant 20^{o}C. Processed samples (100μL) recovered from the device at regular fifteen-minute intervals became cloudier over time and increasing RPM worsened this. Visual observation of the samples turning cloudy indicated the formation of insoluble aggregates. Aliquots of samples were taken for centrifugation to pellet insoluble aggregates and recover the supernatant for monomer quantification using size exclusion chromatography (SEC).

A representative chromatograph for samples processed at 0RPM (control), 6000RPM and 12000RPM are shown in Figure 3-10. The peak at 7.4 minutes represents -ve BoNT/E monomer – confirmed by running a proteins standard. A control, two-hour incubation at 0RPM, was conducted to determine if protein adsorption on to solid-liquid interfaces inside the spinning disc device. However, there was no reported loss in monomer meaning that adsorption to the stainless-steel disc and chamber was minimal during two hours of incubation.

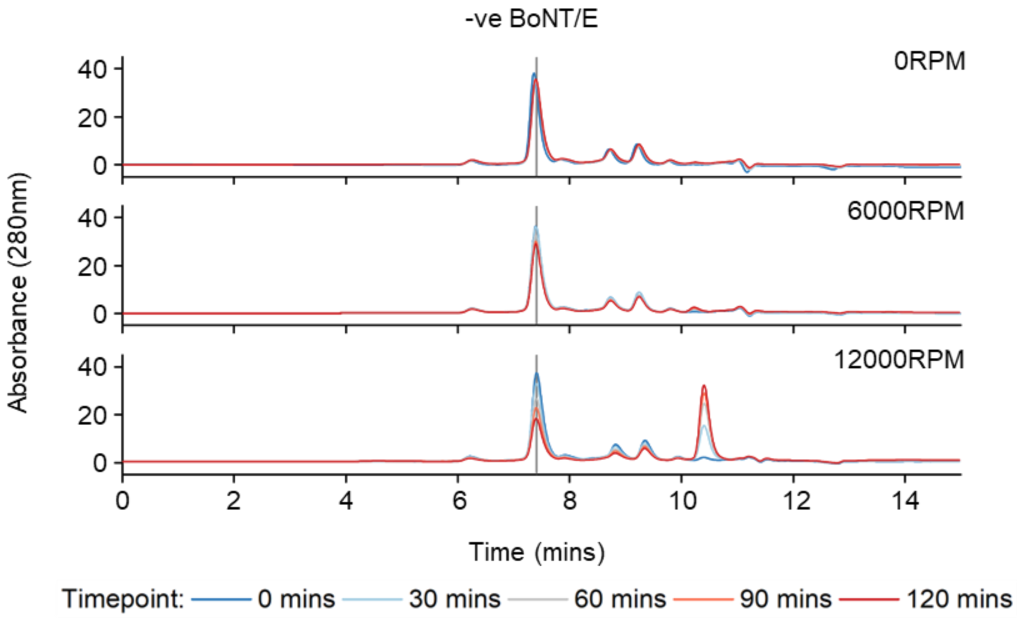

Figure 3-10 Size-exclusion chromatography analysis of -ve BoNT/E samples processed in the spinning disc device. Device speeds 0, 6000 and 12000RPM shown only and operated at 20ºC for two hours. -ve BoNT/E formulated at 0.2mg.ml^{-1} 0.1M sodium phosphate 0.1M sodium chloride (pH 7.5). Timepoints at 30-minute intervals are only shown.

Upon beginning shear by spinning the disc, -ve BoNT/E peaks in chromatographs were seen to decrease showing a loss of monomer. Samples were visually becoming cloudier over processing time, indicating the formation of insoluble protein aggregates/precipitates, however there was no appearance of dimers or higher-order oligomers in chromatographs. All peaks in chromatograms decrease during time spent processing under shear, apart from a peak eluting at 10.5mins which will be now discussed. At an elution time of 10.5mins a uniform peak is increasingly formed at higher RPM speeds. This alludes to the formation of a low-molecular weight species which compared to a protein standard show that this peak is equivalent to a protein of size 17-25kDa.

This occurrence has not been previously reported when using this device and may have resulted due to several possible reasons. Carryover of biologic contamination is possible but unlikely due to the acid and basic clean-in place method between each run. Its occurrence might be due to the model protein -ve BoNT/E used and a potential reduction in the sulfide bridge joining the heavy and light chains as described in the introduction. In stator-rotor systems, which describe devices such as the shear device, cavitation can occur (Reinke, Schmidt and Beckmann, 2018). This might be caused by cavitation within the spinning disc device.

Cavitation is the process where a decrease in the pressure of a liquid below the vapour pressure causes the formation of vapour bubbles. When these bubbles collapse, creating pressure shockwaves and extreme temperatures (Suslick, 1990) that can decompose water molecules and create oxygen and hydroxy radicals (Riesz and Kondo, 1992). These radicals harness the reducing power that can cause structural changes to proteins (Randolph *et al.*, 2015; Duerkop *et al.*, 2018; Valotta Rodrigues *et al.*, 2019). In stator-rotor systems, which describe devices such as the spinning disc device, cavitation has been observed to occur (Reinke, Schmidt and Beckmann, 2018). However, further work is needed to identify this species and confirm the presence of cavitation in this device.

The fraction of monomer remaining calculated using Equation 3-5, decreases exponentially during processing with this becoming more rapid when increasing the disc RPM (Figure 3-11). After processing -ve BoNT/E in the device at different RPM the fractions of monomer remaining were: 1.02 at 0 RPMM, 0.77 at 6000 RPM, 0.62 at 7500 RPM, 0.53 at 9000 RPM and 0.39 at

12000 RPM. To calculate the protein decay coefficient *k,* Equation 3-6 was used, which describes an exponential protein decay function, and rearranged into Equation 3-7. The logarithmic function of this equation was plotted against time, giving an adjusted R^2 >0.95, and the gradient *k* found*.* All samples processed followed the expected exponential decay function as previously reported when using this device (Biddlecombe *et al.*, 2007, 2009; Tavakoli-Keshe *et al.*, 2014).

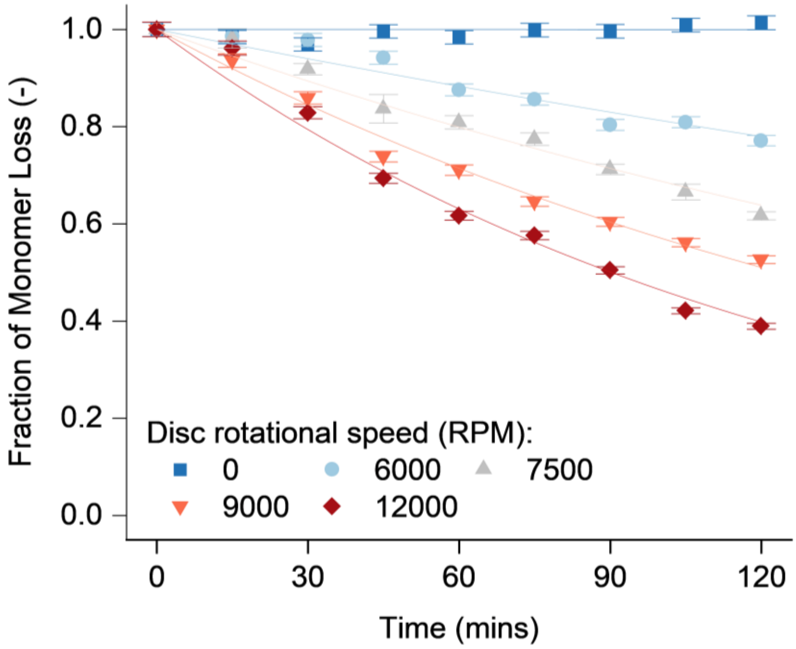

Figure 3-11 -ve BoNT/E loss during processing in the spinning disc device. Device operated at 20°C for two hours -ve BoNT/E formulated at 0.2mg.ml^{-1} 0.1M sodium phosphate 0.1M sodium chloride (pH 7.5). Error bars are representative of the standard deviation (SD=1) of triplcate samples (n=3) processed at 7500RPM.

Protein decay coefficients were plotted against shear and Reynold number to show the impact of these on -ve BoNT/E stability (Figure 3-12). Protein decay coefficients correlate on an exponential like relationship to Reynolds number with an adjusted R^2 ~0.99, whilst against shear rates (s^{-1}) correlate on a first order-like relationship with a R^2 ~0.99. The first-order correlation to shear is a different finding compared to previously reported second-order like relationships (Biddlecombe *et al.*, 2007, 2009; Tavakoli-Keshe *et al.*, 2014).

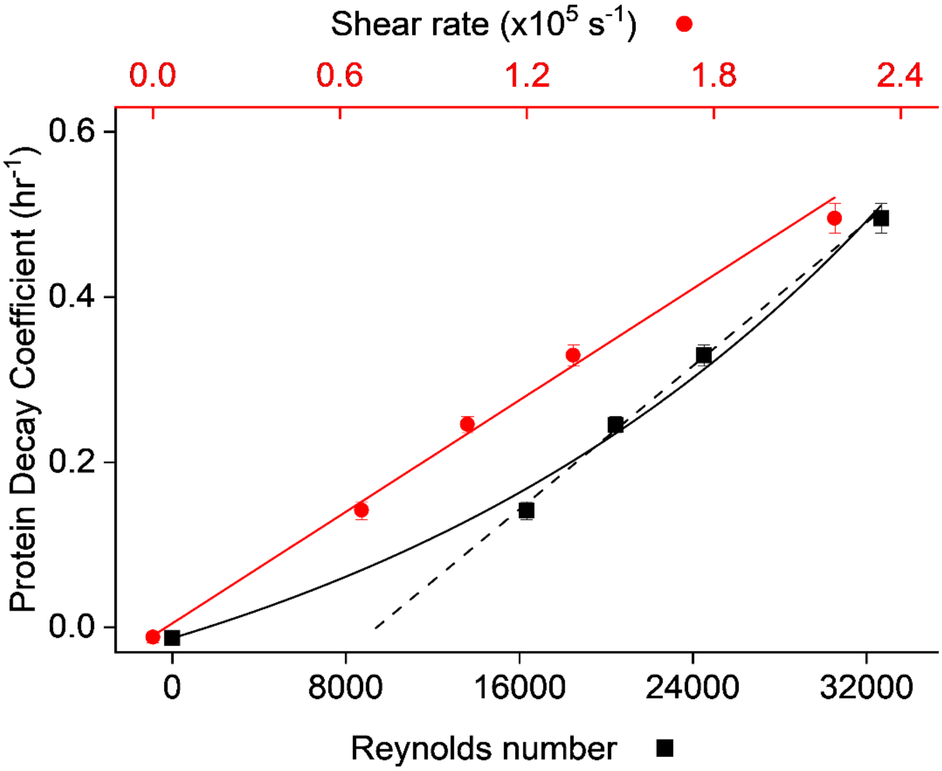

Figure 3-12 -ve BoNT/E protein decay coefficients when processed in the spinning disc device. Device operated at 6000, 7500, 9000 and 12000RPM at 20°C for two hours. -ve BoNT/E formulated at 0.2mg.ml^{-1} 0.1M sodium phosphate 0.1M sodium chloride (pH 7.5). Error bars are representative of the standard deviation (SD=1) of triplcate samples (n=3) processed at 7500RPM.

Whilst a second order-like relationship was suggested between protein decay coefficients and Reynolds number, coefficients calculated within fully turbulent regime (>3700RPM) have a strong linear fit (shown by the dash line with adjusted R^2>0.99) and an x- intercept at Re 9500 (3500RPM). This intercept falls close to the threshold Re value of a fully turbulence regime and as such could indicate a primary role of turbulence in monomer loss by driving the mass transfer of proteins to and from solid-liquid interfaces or increasing protein-protein interactions in the bulk solution.

When increasing disc speed, more monomer was lost due to either shear- or turbulence-induced aggregation. In studies of shear-induced aggregation, monomer loss and particle formation has been found independent of shear and flow rate (Jaspe and Hagen, 2006; Kalonia *et al.*, 2018; Grigolato and Arosio, 2020). In the studies of Jaspe and Hagen (2006), and Grigolato and Arosio (2020), the flow regime within their experimental setup was reported to be laminar.

In the specific works of Grigolato and Arosio (2020), who used interconnected syringes and a microfluidic chamber to expose antibodies to shear and elongation stresses, the proportion of monomer loss to the number of passages remained unchanged when changing flow rate whilst still conducting under purely laminar flow conditions. The cause of monomer loss was thus presumed to be due to mechanical scrapping and hydrodynamic flow. However, that study does not observe similar findings to Deiringer *et al*. and Fanthom *et al*. whom showed that monomer loss and protein particle formation have an inverse relationship to mechanical scrapping-based mechanisms within a peristaltic pump (Deiringer and Friess, 2022a; Fanthom *et al.*, 2023). This was thought due to shorter adsorption times at faster pump speeds that limits the formation of a protein film at the surface which is subsequently disrupted by mechanical scrapping or solid-solid interface contact of inner tubing walls.

While the syringe and peristaltic pump systems cannot be directly compared, it's essential to note that in the syringe system, the rate of monomer loss is constrained by the pace at which the protein layers are disrupted by the moving syringe. When the flow rate is increased, it effectively accelerates the rate of protein layer disruption however remains slower than the rate of protein adsorption. Though it can be hypothesised that when the rate of disruption surpasses the rate of protein adsorption, the significance of turbulence becomes more important as it would facilitate faster mass transfer to the surface and enhances adsorption.

This role of turbulence in improving diffusion of protein to interfaces is supported by other work of Santos *et al*. where the amount of adsorbed protein on to stainless steel surfaces was dependent on Reynolds number (below the apparent unfolding temperature of the protein) (Santos *et al.*, 2006). Moreover, de Guibert *et al*. found that transient and turbulent flow regimes lead to increased collisions of monomers causing increased rate of nucleation of protein aggregates and, vice versa, a far reduced rate of nucleation in low-Re laminar flow conditions (de Guibert *et al.*, 2020). Hence turbulence, could play a primary role in mass transfer of proteins to the solid-liquid interface, behind the synergistic relationship of protein adsorption and disruption, and collision of monomers in protein-protein interactions, behind nucleation events. To expand our understanding of the role of flow-induced aggregation we looked to quantify the formation of protein particles.

3.4.5 Background Formation of Foreign Particles in The Spinning Disc Device

Background particle formation was first investigated in the spinning disc device by performing a negative control which was conducted by processing buffer formulation in the spinning disc device at 12000RPM for two hours. The resulting particles were compared to -ve BoNT/E sample processed under exact conditions. Various particle intrinsic quantities (intensity, SIMI (side-illumination membrane imaging) intensity, convexity, circularity, and aspect ratio) were correlated against particle surface area (Figure 3-13 A-E). Particle area was reported here as the pixel-equivalent surface area (not equivalent circular diameter, ECD) of particle coverage on the membrane, where 1-pixel is equal to 1μm^2 in the BMI system.

In all subgraphs of Figure 3-13 A-E, protein-based particles showed far greater heterogeneity in all intrinsic quantities compared to foreign particles. For protein particles, particle intensity increases with area (Figure 3-13A) whilst descriptive variables, such as circularity, convexity and aspect ratio, all decrease (Figure 3-13 C-E). These all suggested that particles were becoming more elongated with size. These contrasted with particles detected in the negative control which showed no correlation across the particle qualities.

Representative images of particles and the morphologies they take when processing protein buffer in the spinning disc device are shown in Figure 3-14. The structures of particles formed by solid-liquid interfacial and flow-induced aggregation show similar branched and fibrous-like elongated structures to particles formed under other stress mechanisms, such as during piston pumping or peristaltic pumping (Nayak *et al.*, 2011; Dreckmann *et al.*, 2020;

Grigolato and Arosio, 2020; Her and Carpenter, 2020; Wu and Randolph, 2020; Deiringer and Friess, 2022a)

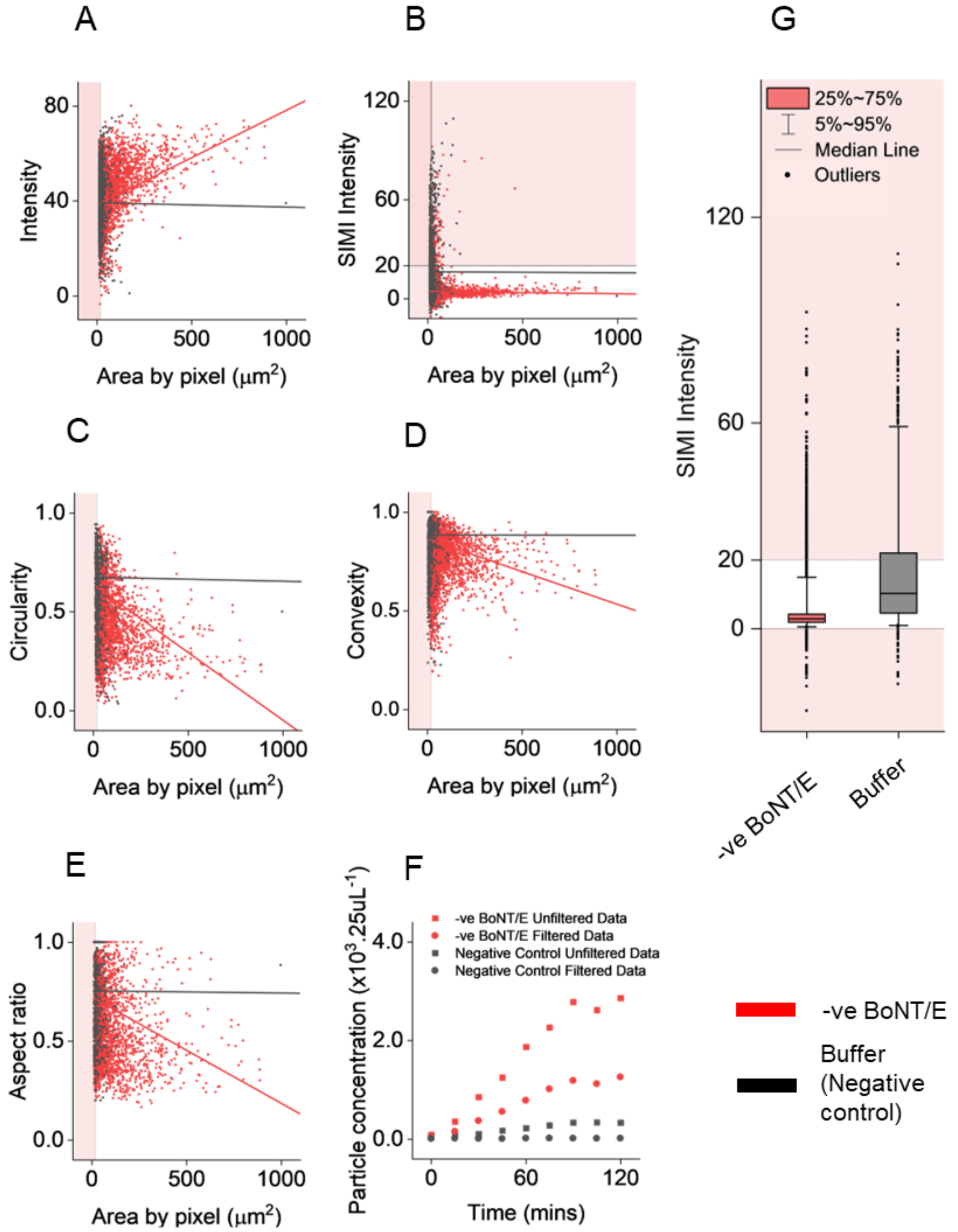

Figure 3-13 Particle data after processing -ve BoNT/E and buffer in the spinning disc device. (A-E) Intrinsic particle qualities correlated against their surface area (μm²). (F) Particle concentration. (G) Distribution of SIMI Intensity of particles. Particle analysis conducted using BMI. -ve BoNT/E was formulated at 0.2mg.ml⁻¹ 0.1M sodium phosphate 0.1M sodium chloride (pH

7.5). Spinning disc device was operated at 12,000RPM and 20^{o}C for two hours. Shaded red regions shows excluded data based on data analysis.

Correlating particle surface areas based on SIMI intensity (Figure 3-13B) showed two distinct groupings, where negative control particles exclusively had a broad SIMI intensity and narrow surface area distributions whilst protein particles had narrow SIMI intensity and broad surface area distribution. This is emphasised in Figure 3-13G where 90% of negative control particles were found within the 1-56 SIMI range and 90% of protein particles were within the 1-15 range. Protein particles were expected to show a low SIMI intensity, specifically reported to be between SIMI 0-20 (Schleinzer *et al.*, 2023), due to their low rigidity thus having a poor ability to scatter side-illuminating light. Large SIMI intensity in the control group suggested the presence of rigid particles that may be introduced via handling or operation of the spinning disc device. It can be noted that the concentration of both negative control particles and protein particles formed during processing trend linearly with time spent under shear (Figure 3-13F).

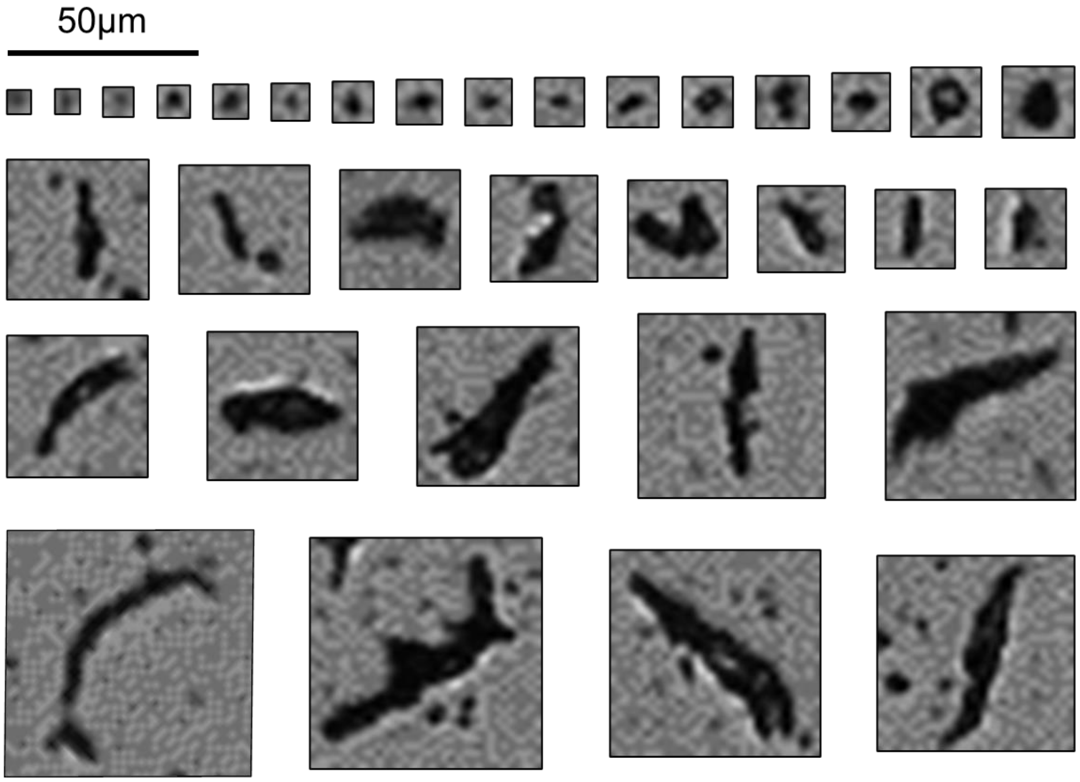

Figure 3-14 Images of particles in -ve BoNT/E samples processed in the spinning disc device from BMI. Device operated at 12,000RPM and 20^{o}C for two hours. -ve BoNT/E was formulated at 0.2mg.ml^{-1} 0.1M sodium phosphate 0.1M sodium chloride (pH 7.5). Scale is 50µm.

3.4.6 Particle Production by Shear-Induced Aggregation

The same samples processed for monomer analysis using SEC were analysed using BMI to quantify aggregate particles and visualise morphologies formed due to shear forces or hydrodynamic flow. Each individual particle surface area was plotted against sample time to understand the size distribution of particles (Figure 3-15). Contour densities were applied to the particle area distribution which show a concentrated production of particles at the statistical mode of 13 µm^2 which was apparent at each sample timepoint, and each disc rotational speed tested (besides 0 RPM). The range of particles sizes extended from 12 µm^2 to above 1,000 µm^2. 12µm^2 was the unanimous minimum particle size detected at all disc speeds tested and is close to the recognised lower limit of detection for the Horizon BMI system (Schleinzer *et al.*, 2023).

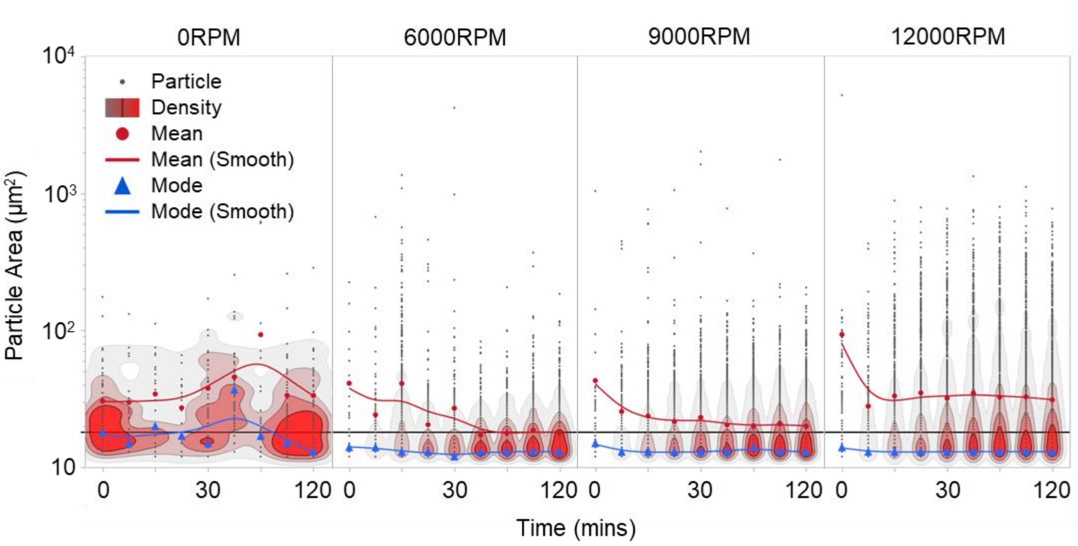

Figure 3-15 Particle area distribution of -ve BoNT/E samples processed in the spinning disc device. Device speeds 0, 6000, 9000 and 12000RPM shown and operated at 20^{o}C for two hours. -veBoNT/E was formulated at 0.2mg.ml^{-1} 0.1M sodium phosphate 0.1M sodium chloride (pH 7.5). Particles detected using BMI analysis. Reference line at 18µm^{2} shows the threshold below which data was excluded. Contour boundaries represent 20%.

The Shapiro-Wilk test was initially used to assess the normality of particle data; however, this was rejected at a level of $p<0.05$. Further, all Weibull, Gamma and Exponential distribution function fits were rejected based on the Kolmogorov-Smirnov test also at a level of $p<0.05$. However, for illustrative purposes, a log-normal distribution function was fitted to particle data to capture the tailing of large particle formations and is shown in Figure 3-16. The proximity of the statistical mode was at the lower limit of detection of the BMI system (12 µm^{2}) which may affect the quality of the data and is considered in later data processing. Additionally, aggregate particle sizes can range from oligomers (dimers, trimers etc.), nano-, sub-micron, sub-visible and visible particles so the presence of particles in the lower detection range of the BMI instrument may indicate an abundance of particles below the sub-micron range.

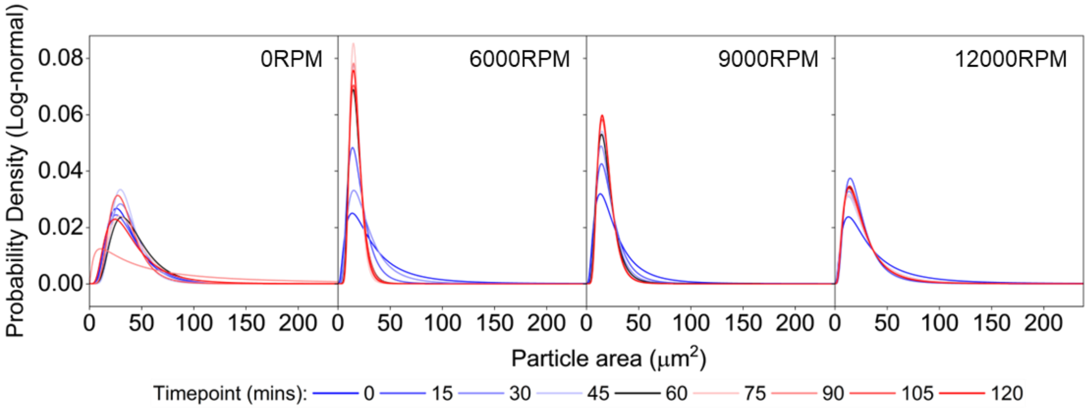

Figure 3-16 Log-normal distributions of particles from -ve BoNT/E samples processed in the spinning disc device. Device speeds 0, 6000, 9000 and 12000RPM shown and operated at 20ºC for two hours. -veBoNT/E was formulated at 0.2mg.ml^{-1} 0.1M sodium phosphate 0.1M sodium chloride (pH 7.5). Particles detected using BMI analysis.

The statistical mode of particle surface area remained unchanged at each disc rotational speed, however the mean particle area increased. The statistical mean areas of particles at each disc rotational speed (RPM) were: 18 µm^2 at 6000 RPM, 20 µm^2 at 9000 RPM, 32 µm^2 at 12000 RPM. At each RPM, the mean area of particles approached a steady state after two hours of processing. The statistical medians also increased with RPM: 15 µm^2 at 6000 RPM, 16 µm^2 at 9000 RPM, 17 µm^2 at 12000 RPM. As did 95th percentiles: 32 µm^2 at 6000 RPM, 39 µm^2 at 9000 RPM, 94 µm^2 at 12000 RPM.

During processing time, all statistical values approached a steady state after two hours in a comparable manner to the previously reported effect of aging time (exposure to shear) on the mean diameter of protein precipitates in agitated vessels (Byrne *et al.*, 2002). Byrne *et al*. also demonstrated that an inverse relationship between shear and precipitate size exists. However, this is in contrast with our results which suggested that increasing RPM increases the mean protein particle size. This may be a result of the detection limit of the BMI system which cannot detect particles in the sub-micron range. These particles may form in greater proportion in the spinning disc device at higher shear creating a bias towards larger particles that remain detectable.

3.4.7 Data Selection to Reduce Foreign Particle Impact on Analysis

To reduce the impact of foreign particles on data analysis, all data was filtered based on SIMI Intensity and particle area. Particles with SIMI intensity less than 0 or greater than 20 were excluded from analysis and, due to the abundant presence of particles in the lower detection limit of the BMI system, particles with a surface area of less than 18 μm^2 (~4.2 μm x 4.2 μm ECD, equivalent circular diameter) were also excluded from analysis. These filtered regions are shown shaded in red in Figure 3-13 A-E. After excluding unwanted particle data, the total particle concentration in each sample timepoint has dropped by 50% (Figure 3-13 F).

Whilst it has not been explored in this work, an improved method of excluding foreign particles from the data would be by utilising machine learning and neural network algorithms. These techniques have been successfully trained on libraries of protein particle images to find particles of unknown compositions, for example whether it is proteinaceous, silicone oil-based etc. There have also been examples in literature where these tools have been used for root-cause analysis of protein particle formation during bioprocessing to address and rectify the stress mechanism that led to the formation of that individual or group of particles (Witeof *et al.*, 2021; Greenblott *et al.*, 2022; Thite *et al.*, 2022)**.** In future, such techniques could also be applied in cases such as in this work to examine each individual particle and more accurately remove unwanted foreign particles for analysis.

3.4.8 Particle Concentration and Sizes by Area

Particle data from the processed samples collected from each timepoint was filtered by parameters, as discussed, and summated together to obtain particle concentration and total particle area then correlated against time (Figure 3-17). Before starting processing, all filtered samples introduced into the shear device had a concentration range between $0.7\text{x}10^4$ - $4.2\text{x}10^4$ particles.ml^{-1}. Upon commencing shear, changes in particle concentration were immediate in the first sample taken at 15 mins and continued to increase on a linear trend to $8.0\text{x}10^6$ particles.ml^{-1} (12000 RPM) for the total two hours of processing and at disc speeds studied (adjusted R^2 values >0.96) (Figure 3-17-left). Slopes of linear regression applied to particle concentration changes under shear and hydrodynamic flow were significantly different from zero ($p < 0.05$).The slope of the quiescent control study conducted at 0RPM for two hours, where the particle concentration remained unchanged at $1.7\text{x}10^4$ particles.ml^{-1}, was not significantly different from zero ($p = 0.15$). In addition to particle concentration, the aggregate surface area of particles was also seen to trend linearly with time (adjusted $R^2 > 0.89$, at speeds 7500 RPM and above) (Figure 3-17-right).

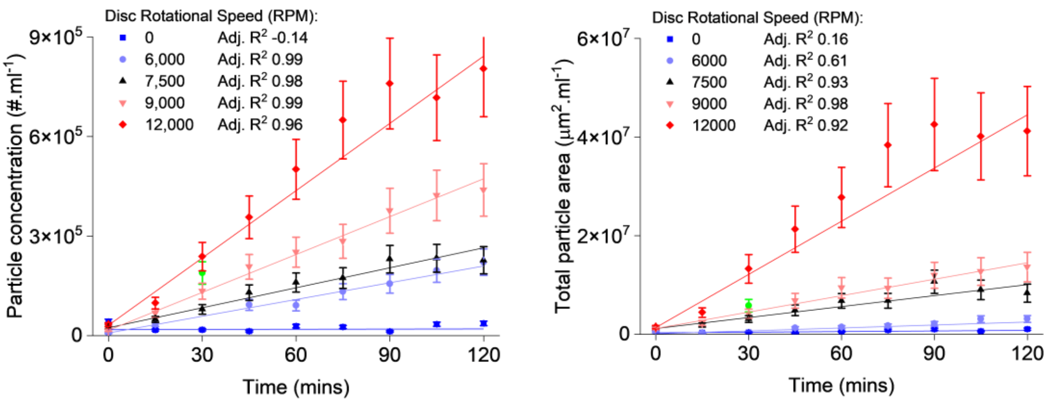

Figure 3-17 Particle concentration and total particle area of -ve BoNT/E samples processed in the spinning disc device. Device operated at 0, 6000, 7500, 9000 and 12000RPM and $20^{o}C$ for two hours. -veBoNT/E was formulated at $0.2mg.ml^{-1}$ 0.1M sodium phosphate 0.1M sodium chloride (pH 7.5). Particles detected using BMI analysis. Error bars are representative of the standard deviation (SD=1) of sample processed at 7500RPM in triplicate (n=3).

To understand the effect of disc rotational speed (and turbulence) and shear on the rate of particle formation and the rate of aggregate surface area, the gradients were extracted from the linear fits and plotted. Reynolds number correlated on an exponential-like relationship with respect to both the rate of particle formation (adjusted R^2 0.98) and the rate of particle area growth (adjusted R^2 0.95) (Figure 3-18). Whilst shear strain rates correlated on a linear-like relationship with the rate of particle area formation (adjusted R^2 0.93) and an exponential-like relationship the rate of particle area formation (adjusted R^2 0.96) (Figure 3-19).

When looking at the correlation of the rate of particle formation and Reynolds number (Figure 3-18), at low-Re numbers (<12000) there was an early stagnation in the formation rate but rapid acceleration as Re approaches the turbulent regime. Interestingly, the x-axis intercept of a linear trend fitted to data excluding 0 RPM, was Re 10000 (with an adjusted R^2 0.83). This was the threshold Reynolds number at which fluid flow was expected to be fully turbulent.

When looking at correlation of the rate of particle area and Reynolds number in Figure 3-18, the stagnation at low-Re number and acceleration is more apparent and suggested that systems with hydrodynamic flow at Reynolds number below 15,000 do not significantly promote flow-induced aggregation of -ve BoNT/E samples. This data confers with the findings of de Guibert *et al*. that discussed nucleation events are limited in systems with hydrodynamic flow that is under laminar flow conditions thus prevents the formation of both numerous and large particles (de Guibert *et al.*, 2020).

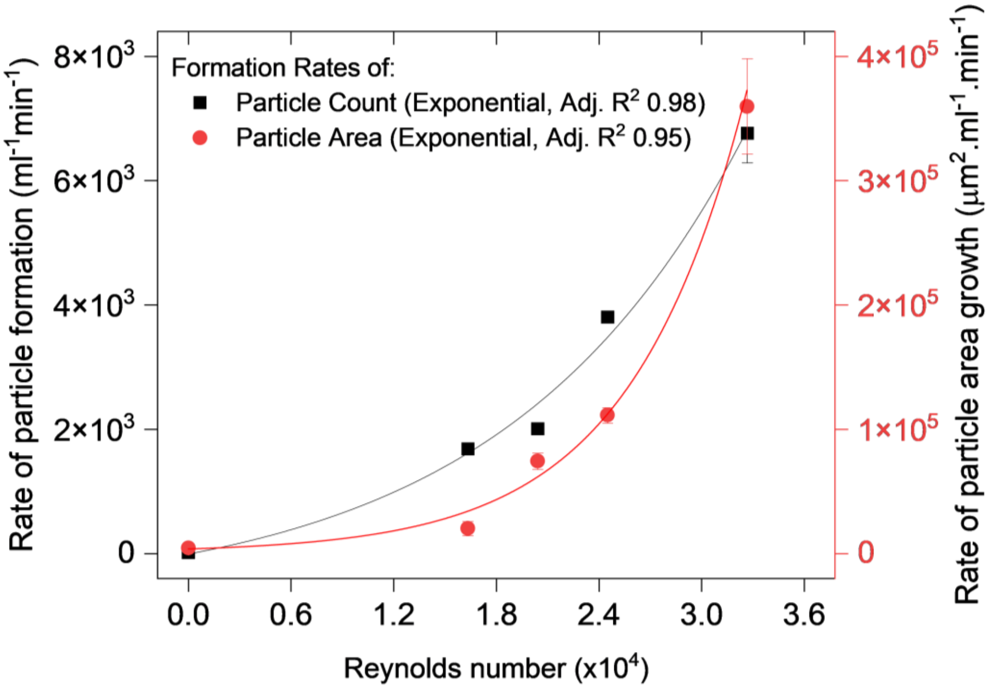

Figure 3-18 Rate of particle formation and particle area growth of -ve BoNT/E samples correlated to Reynolds number. Device operated at 0, 6000, 7500, 9000 and 12000RPM and 20°C for two hours. -veBoNT/E was formulated at 0.2mg.ml^{-1} 0.1M sodium phosphate 0.1M sodium chloride (pH 7.5). Particles

quantified using BMI. Error bars are representative of the standard deviation (SD=1) of sample processed at 7500RPM in triplicate (n=3).

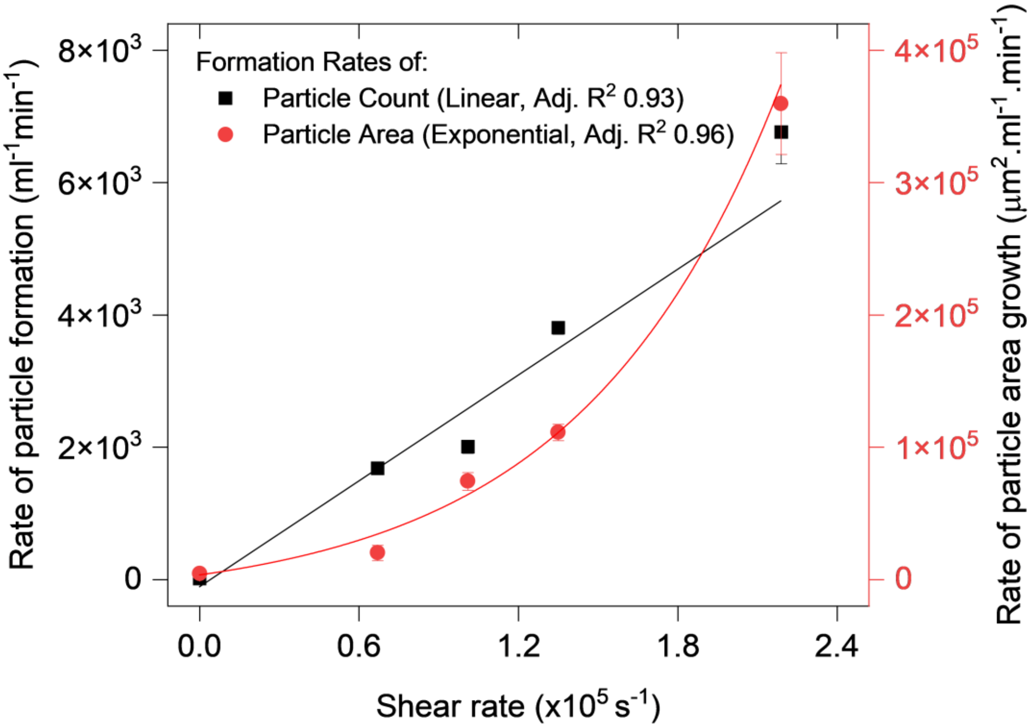

Figure 3-19 Rate of particle formation and particle area growth of -ve BoNT/E samples correlated to shear rates. Device operated at 0, 6000, 7500, 9000 and 12000RPM and 20ºC for two hours. -veBoNT/E was formulated at 0.2mg.ml^{-1} 0.1M sodium phosphate 0.1M sodium chloride (pH 7.5). Particles detected using BMI. Error bars are representative of the standard deviation (SD=1) of sample processed at 7500RPM in triplicate (n=3).

3.4.9 Kolmogorov Microscale Eddies and Protein Aggregates

Eddy motion are swirling fluid structures with strong velocity gradients that are the essence of turbulence and hence control transport and mixing within fluid flow. Eddies may exist at a wide range of lengths, but turbulent eddies at the micro-scale are described by the Kolmogorov length scale, which can be microns in size in laboratory settings (George, 2013), and have been observed to cause damage to biologics during bioprocessing (Cherry and Papoutsakis, 1986; Croughan, Hamel and Wang, 2006). It may be possible that Kolmogorov length scale eddies could penetrate through the laminar sub-layer of flow in contact with the solid-liquid interface and disrupt protein layers to desorb protein aggregates or directly fragment aggregate particles.

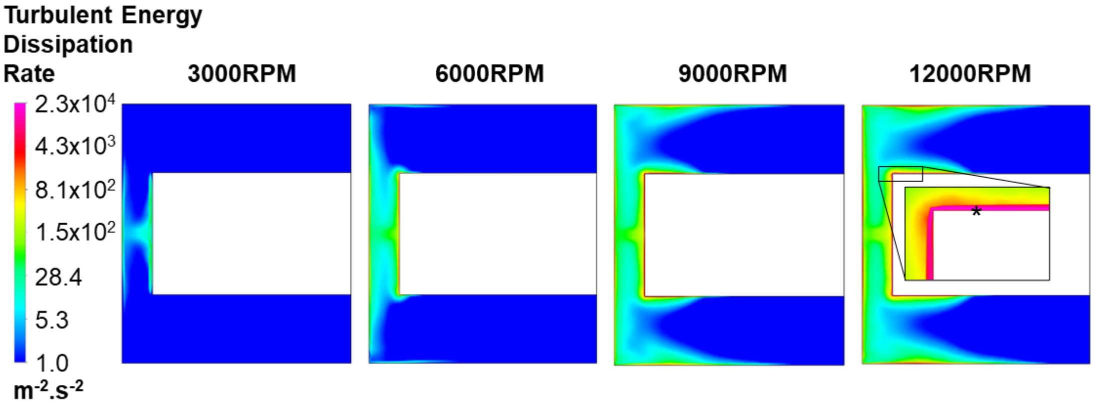

Figure 3-20 CFD analysis of turbulent energy dissipation rates within the spinning disc device sample chamber. Insert at 12000RPM shows the point at which the largest rate occurs. CFD was simulated under 3000, 6000, 9000 and 12000RPM and data representative of a steady state.

Kolmogorov length scale eddies in the spinning disc device were investigated by looking at the maximum turbulent energy dissipation rates (ε_{max}) predicted in CFD models (Figure 3-20). Due to the rotational velocity of the disc creating flow and turbulence, the largest rates were found confined to the regions closest to the outer disc edge within the radial gap and the top (and bottom) disc surfaces close to the tip. Using the maximum rates will yield the minimum possible eddy size within the spinning disc device.

The maximum turbulent energy dissipation rates obtained at each RPM were: $1.4x10^3$ $m^2.s^{-3}$ at 6000 RPM, $3.2x10^3$ $m^2.s^{-3}$ at 75000 RPM, $7.7x10^3$ $m^2.s^{-3}$ at 9000 RPM and $23.0x10^3$ $m^2.s^{-3}$ at 12000 RPM (Table 3-3). For comparison, pilot and industrial scale pump and centrifuges may be within the size of 10^5 $m^2.s^{-3}$ (Boychyn *et al.*, 2004). The maximum rates in the spinning disc device were used to estimate the Kolmogorov length scale eddies by using Equation 3-4 and are predicted to be: 5.1 μm at 6000 RPM, 4.2 μm at 7500RPM, 3.4 μm at 9000 RPM and 2.1 μm at 12000 RPM (Table 3-3).

Table 3-3 Turbulent dissipation rates and Kolmogorov length scale eddies at different disc speeds in the spinning disc device.

Disc rotational speed (RPM)	**Max Turbulent Dissipation Rate (ε_{max}) ($m^2.s^{-3}$)**	**Min Kolmogorov Length Scale (η) (μm)**
3000	77.2	10.7
6000	1.42×10^3	5.1
7500	3.19×10^3	4.2
9000	7.74×10^3	3.4
12000	23.0×10^3	2.7

The calculated eddy sizes were similar or smaller than the statistical modes of particle sizes detected using BMI analysis, as discussed earlier. Based on this and other literature that has observed their damage to biologics – for example, adherent cells on microcarriers (Cherry and Papoutsakis, 1986; Croughan, Hamel and Wang, 2006) - it may be possible that these eddies can interact with all protein aggregates in a manner seen in Figure 3-21, due to the dissipation effect from larger eddy sizes to these smallest lengths. Whilst higher dissipation rates and shear strain rates can cause the formation of smaller protein particles (Byrne *et al.*, 2002), this cannot be observed in this work due to the detection limitations of the BMI system. Laser light diffraction techniques could aid in the detection of particles below the limit of BMI.

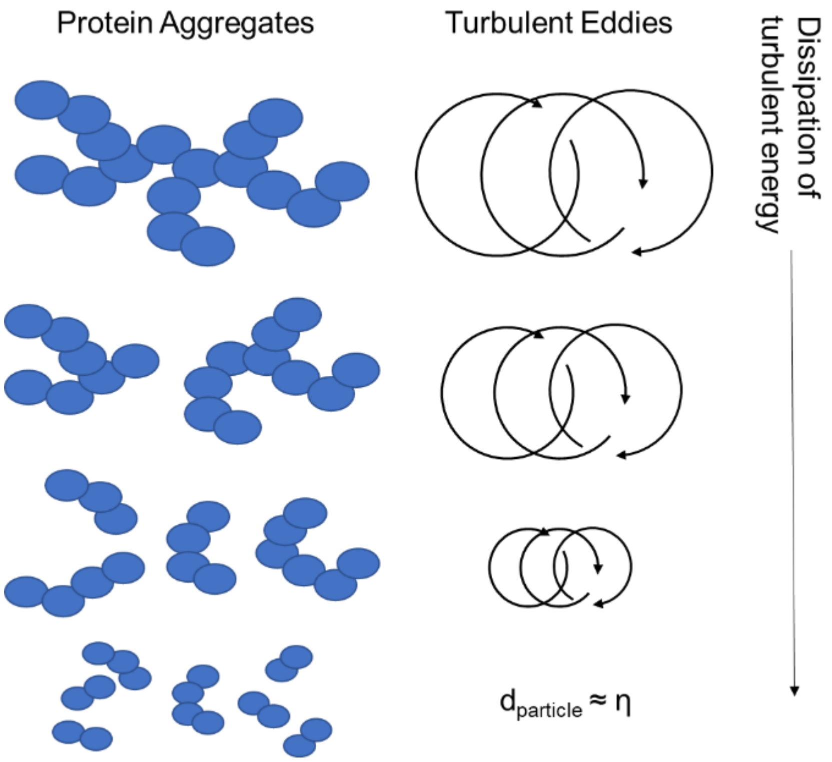

Figure 3-21 Illustration of turbulent eddy interactions with protein aggregates. As turbulent energy dissipates down to Kolmogorov length scale eddies (η) eddies could cause fragmentation of aggregates into smaller particle lengths ($d_{particle}$).

Finally, it should be noted that the size of Kolmogorov length scale eddies complicate the energy balances during CFD analysis and the smallest predicted eddies are limited to approximately half of the size of the cells used in the mesh pre-CFD simulations (George, 2013). For example, in the case of CFD simulations at 12000RPM, the smallest Kolmogorov eddy length at 2.7µm was found at the top (and bottom, due to symmetry) of the rotating disc close to the tip edge (as highlighted in Figure 3-20). The first cell height of the inflation mesh used along this wall was 2.8µm, but turbulent energy dissipation rate was in the 4th inflated cell. Given that a growth rate of 1.1 was used to inflate the mesh, the cell height at this point is 4.1µm. As this is within the half-size limit mentioned earlier, it is possible that the determination of Kolmogorov microscale eddies are limited to the mesh design used and that they may be smaller than what we can determine in our models. Nonetheless, as the smallest measurable Kolmogorov microscale eddy was within the size range of the protein aggregates detected, the cascade and dissipation of larger eddies down to this scale may affect all sub-visible aggregates.

3.5 Conclusion

The hydrodynamics of the spinning disc device have been thoroughly characterised using computational fluid dynamics (CFD). Given the dimensions of this device, Reynolds number (Re) increased at a rate of 2.72RPM^{-1} and a fully turbulent flow regime existed above a disc rotational speed (RPM) of 3700 RPM (Re > 10000). Shear strain rates increased with a second-order like relationship with disc rotational speed achieving up to 220,000s^{-1} at 12000RPM. The impact of turbulence was investigated on the stability of endopeptidase negative botulinum neurotoxin serotype-E (-ve BoNT/E) by processing samples within the device at different RPM and quantifying monomer using size-exclusion chromatography. When observing the effect of turbulence on the protein decay coefficient (based on an exponential decay function), a second-order like relationship was seen. However, without considering the laminar flow regime, the protein decay coefficient had a strong linear relationship with a turbulent flow-regime inside the spinning disc device. At all RPM evaluated, protein decay coefficients correlated linearly with shear strain rates.

Backgrounded membrane imaging (BMI) was used to validate the spinning disc device for background (foreign) protein particle production. Based on background particle production in negative controls, data produced from processing -ve BoNT/E samples was filtered based on SIMI intensity and particle area before further analysis was conducted. In brief, particles with SIMI intensity >20, and particle area sizes <18 μm^2 were excluded from analysis. The protein particles produced inside the spinning disc device displayed increased elongation, more fibrous, when particle area increased, and morphologies of these particles were highly comparable to other particles imaged in literature investigating other protein aggregation mechanisms. After an initial lag-phase, the rate of particle formation and rate of particle area growth increased exponentially with Reynolds number. A strong linear relationship was clear when correlating data within the turbulent flow regime. Turbulence was therefore a strong factor in promoting the formation of protein aggregates and the rate of monomer loss of -ve BoNT/E.

The dimensions of Kolmogorov length scale eddies, based on predicted turbulent energy dissipation rates from CFD analysis, fell within the size range of the protein aggregates produced and are likely to be capable of interfering with the formation or breakage of protein aggregates. However, the eddy sizes may be overestimated due to the mesh used in CFD and the impact of them on particle formation cannot be fully concluded due to the lower limit of the BMI system used.

Laminar hydrodynamic flow causes minimal -ve BoNT/E monomer loss and protein aggregate production. Turbulent flow accelerates the loss of monomer by either 1) improving the mass transfer of proteins from the bulk solution to solid-liquid interfaces adsorption where they adsorb, or 2) by increasing protein-protein interactions in the bulk solution creating nucleation events sparking protein aggregation. Turbulence also accelerated the formation of protein particles which may results due to 1) the increased nucleation events in the bulk solution or 2) flow-induced disruption of the solid-liquid interface. At higher turbulent flow larger particles formed however, it is possible that Kolmogorov length scale eddies interacted with protein particles, causing cases of breakage. Though, improvements to understanding the effect of Kolmogorov eddies and protein particle distribution would be in mesh refinement for the CFD model and the use of particle analysers within suitable size range, such as laser light diffraction.

4 Spinning Disc vs. Peristaltic Pump: Investigating Botulinum Neurotoxin Stability in Novel Processing Devices under Variable Conditions.

4.1 Chapter Summary

The previous chapter demonstrated the sensitivity of Botulinum neurotoxin (BoNT) to protein aggregate formation under turbulent hydrodynamic flow and shear stress. These factors influence protein decay coefficients and particle formation, mediated by electrostatic, van der Waals, and hydrophobic interactions. Changes in buffer conditions, such as pH and ionic strength, modulate these attractions and impact aggregation. Additionally, BoNT's protein structure responds to chemical stimuli, becoming more flexible and hydrophobic at lower pH levels which brings about structural instabilities. During bioprocessing, physiochemical conditions are often exploited to separate biologics base on their charge. Thus, variations in conditions may induce inherent instabilities in BoNTs, leading to monomer loss and protein aggregation.

To understand how -ve BoNT/E stability is affected by changing buffer conditions, the spinning disc device was used to generate shear and hydrodynamic flow at different buffer compositions. A novel device consisting of a closed-loop of tubing was also created in this chapter to test the stability during peristaltic pumping and determine whether the spinning disc device could be used as a mimic for this pump system.

Changes in protein aggregation rates were not consistent across both devices, likely due to material differences in device construction. In the spinning disc device, favourable electrostatic attractions to stainless-steel interfaces promoted aggregation. At 0.1M NaCl, protein decay coefficients were 0.16 hr^{-1} and 0.36 hr^{-1} for buffers at pH 7.5 and 5.5. Increasing NaCl to 1.0M increased the coefficient at pH 7.5 to 0.25 hr^{-1} and decreased the coefficient at pH 5.5 to 0.12 hr^{-1}.

In the closed-loop peristaltic pump device, favourable hydrophobic attractions to the silicone tubing interfaces promoted aggregation. At 0.1M NaCl, protein decay coefficients were 0.50 hr^{-1} and 0.0.67hr^{-1} for buffers at pH 7.5 and 5.5. Increasing NaCl to 1.0M increased the coefficient at pH 7.5 to 0.55 hr^{-1} and increased the coefficient at pH 5.5 to 1.13 hr^{-1}.

Distinct particle morphologies emerged between devices and buffer conditions. The spinning disc device consistently produced particles with elongated and fibrous qualities at all buffer conditions, while the peristaltic pump device primarily generated these at pH 7.5, transitioning to more circular particles at pH 5.5. In the spinning disc device, significantly ($p < 0.05$) larger particles formed at pH 7.5 compared to pH 5.5 at 0.1M NaCl with means 54 μm^2 and 33 μm^2. However, in the closed-loop peristaltic pump device, significantly ($p < 0.05$) larger particles formed at pH 5.5 compared to pH 7.5 at 0.1M NaCl with means 63 μm^2 and 25 μm^2.

A novel method was tested involving altering pH conditions during -ve BoNT/E processing in the spinning disc device, creating a dynamic physiochemical environment. Changes in pH affected monomer decay rates, accelerating when transitioning from pH 7.5 to 5.5 and slowing when doing the reverse. Despite the dynamic changes, monomer loss data remained within the range of static conditions. However, higher particle concentrations were observed, potentially influenced by the high molarity of the buffer (0.7M) buffer used for titrations inside the spinning disc device effecting results.

Aggregation temperature (T_{agg}) values indicated that -ve BoNT/E protein-protein interactions were favoured at low pH and ionic strength, corresponding to lower T_{agg} values. Available literature on molecular dynamics simulations of BoNT/E structure also supported these findings, highlighting reduced salt bridge content and increased structural flexibility at low pH, increasing hydrophobicity and susceptibility to aggregation. These factors likely contributed to increased monomer loss and aggregation of -ve BoNT/E during processing under low pH conditions in both devices.

Size-exclusion chromatography (SEC), and backgrounded membrane imaging (BMI) can be valuable tools for understanding protein stability in different buffers and aggregation mechanisms using low samples volumes. Unique changes in protein decay coefficients and particles morphologies were observed in each device when processing -ve BoNT/E at different buffer conditions, showing that separate mechanisms for monomer loss and protein aggregation exist in each device. However, further investigations are needed to understand the mechanisms within peristaltic pumping, a topic explored in the next chapter.

4.2 Introduction

Therapeutic proteins can be exposed to stresses during their manufacturing which can result in protein monomer loss and protein aggregation. In Chapter Three, the stability of endopeptidase negative (i.e., non-toxic) botulinum neurotoxin serotype-E (-ve BoNT/E) under hydrodynamic flow and shear was assessed using the spinning disc device. Increasing turbulence hastened protein decay coefficients and particle formation thought due to increased protein-protein interactions in bulk phase and mass transfer of proteins to solid-liquid interfaces to cause protein aggregation. The interactions have been observed to be mediated by electrostatic, van der Waals, hydrogen bonds and hydrophobic forces (Boubeta, Soler-Illia and Tagliazucchi, 2018; Wu and Randolph, 2020; Bergfreund, Bertsch and Fischer, 2021; Deiringer *et al.*, 2022) and have been shown to be modulated by changing pH and ionic strength (Biddlecombe *et al.*, 2009; Sahin *et al.*, 2010; Dufrechou *et al.*, 2012; Zheng *et al.*, 2023).

. Manipulating pH and ionic strength is necessary during bioprocessing to separate and purify biologics from product and process related impurities that would otherwise harm patients if left in drug products. In fact, as well as inflicting stresses on to biologics, bioprocessing is a very dynamic physiochemical environment presenting challenges to product stability during manufacture. For example, in the bioprocessing of BoNT/E, tangential flow filtration (TFF) takes place after hydrophobic interaction chromatography (HIC) to desalt and lower the pH of the buffer via dialysis before anion exchange chromatography (AEX) (Gessler, 2005). In Chapter 1.1.2, the mechanism of action of botulinum neurotoxin and how it causes the flaccid paralysis disease botulism was discussed and the role of changing physiochemical conditions in changing the toxin structure during its migration through the gut lining and cellular uptake via endocytosis was highlighted.

TFF is a unit operation that can utilise a peristaltic pump to recirculate biologics up to several hours thus continuously exposing them to stresses. Peristaltic pumping generates shear during operation (Dreckmann *et al.*, 2020) and protein aggregation has been observed to occur. (Her *et al.*, 2020; Deiringer and Friess, 2022a, 2022b; Fanthom *et al.*, 2023). Therefore, it can be anticipated that the physiochemical changes made during this TFF-dialysis step may invoke instabilities that make BoNT susceptible to monomer loss and protein aggregation during manufacturing. However, there are few resources investigating BoNT stability and aggregation tendency during changing physiochemical conditions.

In this chapter, the spinning disc device was used to expose process-intermediate -ve BoNT/E product to turbulent stresses whilst changing the physiochemical conditions of the buffer. This chapter will also begin studies into protein aggregation during peristaltic pumping and observe if the spinning disc device would be able to mimic the protein aggregation mechanisms within the pump. A novel method of observing the effect of dynamic physiochemical conditions is used in tandem with the spinning disc device, within the conditions of the dialysis step, to reflect how this impacts -ve BoNT/E stability. Monomer loss was quantified using size-exclusion chromatography (SEC) and protein aggregation by imaging particles using backgrounded membrane imaging (BMI) to understand the changes in aggregation mechanisms.

4.3 Materials and Methods

4.3.1 Materials

Stock solution of an endopeptidase negative (i.e., non-toxic) botulinum neurotoxin serotype-E, herein referred to as -ve BoNT/E, was provided by IPSEN Biopharm. This stock solution is intermediate material and partially purified following an initial hydrophobic interaction chromatography (HIC) step, hence there are host-cell proteins present but -ve BoNT/E makes up 90% of the total protein. The stock solution was buffer exchanged using Slide-A-Lyzer® G2 2,500 MWCO PES 70mL dialysis cassettes purchased from Thermo Scientific (Rockford, IL, USA). Dialysis was conducted following manufacturer's instructions to exchange the protein stock solution buffer with a buffer using a total dialysate buffer volume that is 200-times the sample volume used. Sodium phosphate buffers consisting of 0.1M sodium phosphate had ionic strength adjusted by adding sodium chloride at concentration 0.1M, 0.55M or 1.0M, and were adjusted to pH 5.5, 6.5 or 7.5. Acetic acid buffers consisting of 0.1M acetic acid had 0.55M sodium chloride added only and were adjusted to pH 4.5 and 5.5. All buffer components were acquired from Sigma-Aldrich Co. (St. Louis, MO, USA) and water obtained from a Milli-Q® Advantage A10 water system (Merck KGaA, Darmstadt, Germany).

The protein concentration was adjusted to 0.2mg.ml^{-1} using the respective buffers described above. Final protein concentration in these buffers were confirmed by 280nm absorbance readings using the Little Lunatic UV-Vis Spectrophotometer (Unchained Labs, Pleasanton, CA) by loading 4µL of sample into each well of the Little Lunatic microfluidic chips (Unchained Labs, Pleasanton, CA). After formulation, solution was filtered through a 0.22μm PVDF filter and stored at 4^{o}C until ready for use. Samples were stored for no longer than a week. Protein solutions were filtered once again using a 13mm 0.22μm PVDF filter to remove any particles before their use in any studies.

4.3.2 Spinning Disc Device Operation

The spinning disc device is prepared with -ve BoNT/E and cooling supplied following the methods described in Chapter 3.3.4.

To process -ve BoNT/E, the spinning disc device was operated at 9000RPM (corresponding to a shear rate of $1.4 \times 10^5 s^{-1}$) for two-hours. Samples of 100μL (1.3% of the total chamber volume at 7.8mL) were taken from the device at 15-minute intervals by displacing the chamber sample with the protein buffer. In between samples, the device was cleaned by operating at 9000RPM for 15 mins each with 40mM phosphoric acid, then MilliQ®, then 40mM sodium hydroxide and a final MilliQ® step.

4.3.3 Closed-loop Peristaltic Pump Device

Two 160mm lengths of Masterflex® L/S® 15 High-Performance CFlex® Precision Pump Tubing were joined together using two 3/16” Y-connectors to form a closed loop. To provide an air-tight seal, and sample infusion and withdrawal during experiments, Luer-lock valves were joined to the ends of the Y-connectors with 1cm lengths of additional tubing (Figure 4-1). The final volume of this closed-loop was 7.8ml. All tubing, Y-connectors and Luer locks were purchased form Cole-Palmer Instrument Company LTD (St. Neots, UK).

Pumping was facilitated using a Masterflex L/S Console Drive 7521-40 (Cole-Parmer Instruments Company LTD) with a Masterflex L/S Easy-Load® II Pump Head with four rollers and a variable occlusion bed (Cole-Parmer Instruments Company LTD).

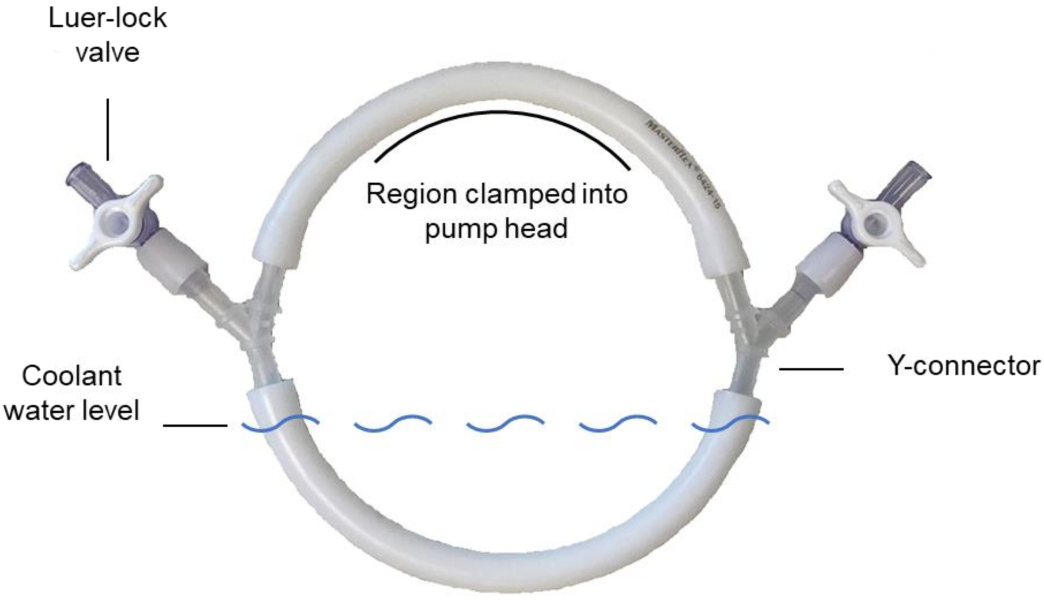

Figure 4-1 Image of the closed-loop peristaltic pump device.

The closed-loop device was prepared prior to pumping by first wearing-in tubing by recirculating buffer solution at 40RPM for 10-minutes, then rinsing with MilliQ water and leaving to dry. The closed-loop device containing protein solution was allowed to incubate for five minutes prior to pumping. Pumping was conducted at 40RPM (4.1L.hr^{-1}) and 103.5% occlusion for two-hours (1200 total circulations). 40RPM was chosen as one of the lowest settings available to choose on the pump device, but also to limit any temperature increase caused by tubing friction and spallation caused by occlusion which might also cause protein aggregation. Nevertheless, internal temperature of 20^{o}C was maintained by submerging the bottom half of the closed loop into coolant water pre-calibrated to a temperature for the pump speed selected. New pieces of tubing were cut for each new experiment.

Figure 4-2 shows the closed-loop peristaltic pump device clamped into a peristaltic pump, but without the water bath used to provide cooling to the device.

Figure 4-2 Picture of the closed-loop peristaltic pump device clamped in place in a peristaltic pump.

4.3.4 Determination of Titration Buffers for Dynamic pH Conditions Using the Spinning Disc Device

To conduct dynamic pH physiochemical changes within the spinning disc device during processing of -ve BoNT/E, titration buffers were formulated. To determine the molarity to titration buffer to add to process protein solution in the spinning disc device, initial titrations were made to 3mL of 0.1M sodium phosphate 0.1M sodium chloride (pH 7.5 or 5.5) 0.1M sodium phosphate, 0.1M sodium chloride and using 4M of hydrochloric acid (HCl) (pH step change from 7.5 to 5.5) or 4M sodium hydroxide (NaOH) (pH step change from 5.5 to 7.5).

Based on these initial titrations, final titration buffers for the spinning disc device consisted of 0.1M sodium phosphate, 0.1M sodium chloride and 0.7M hydrochloric acid or 0.7M sodium hydroxide to conduct the pH step changes during spinning disc device processing. Each 100uL sample withdrawal every 15 mins from the spinning device by displacement using the titration buffer caused a incremental step change in pH during processing for two hours. Due to the concentrated and high molarity of these acidic and basic solutions, personal protective equipment was used, and extra care and precaution was taken by handling solutions in a fume cupboard when not operated in a closed system. Material compatibility with high molarity acidic and caustic solutions was checked prior to use. It was expected that the concentration of sodium phosphate provided in these titration buffers provided no buffering power.

4.3.5 Size-Exclusion Chromatography

Analysis and quantification of -ve BoNT/E monomer was conducted following the methods outlined in Chapter 3.3.6. However, samples recovered from the closed-loop peristaltic pump device were prepared by filtering sample through a 4mm 0.22µm PVDF filter to remove spalled tubing particles and protein aggregates. Otherwise, samples were centrifuged using a Centrifuge 5430 R (Eppendorf, Hamburg, Germany) at 18,000g for 10mins at 4^{o}C.

In addition, a two-component exponential function (Equation 4-1), , was used to model monomer decay curves for the pH step changes during processing in the spinning disc device.

$$C_{\mathrm{t}} = C_0 e^{(-At+Bt^2)}$$

Equation 4-1

4.3.6 Backgrounding Membrane Imaging

Backgrounded membrane imaging (BMI) was performed using the Horizon system (Halo Labs, Burlingame, CA). BMI works by comparing two images taken before and after samples are filtered on to a filter plate. The image of filter plate wells before sample filtration show the backgrounded state of the filter plate to capture any intrinsic properties relating to the plate. These background images are then subtracted from the images of wells after sample application and filtration to produce a final image only containing the particles within samples.

This technique was performed by first capturing the background image of all filter plate wells. Samples were prepared by diluting them in their respective buffer to be within the 7% membrane coverage limit. For the spinning disc device and peristaltic pump samples dilutions were determined to be 1:16 and 1:96, respectively. Diluted samples (25µL) were then applied to the wells of a 0.4µm filter plate and vacuum filtered in a laminar flow hood. When moving between the laminar flow hood and the Horizon system the filter plate was kept in an airtight container to prevent any dust and foreign particles contaminating the filter plate. Images were then acquired of each well with filtered samples and image analysis conducted by subtracting the original backgrounded image. This process was conducted using Horizon Vue (Halo Labs, Burlingame, CA) image analysis software using the recommended software algorithm to analyse every particle in each well image. Particle sizes are reported as the pixel area where one pixel is equivalent to 1µm^2.

4.3.7 Particle Data Analysis and Selection

Particle data obtained from BMI analysis was structured into a tidy-format table with dimensions of 9 columns and ~19,000 rows where each row represents an individual particle detected. Key variables included are disc speed (RPM), timepoint (min), intensity, SIMI intensity, equivalent circular diameter (ECD, µm), aggregate surface area by pixel coverage (px, 1px = 1µm^2), aggregate surface area by ECD (µm^2), perimeter (µm^2), circularity, convexity and aspect ratio. Data selection was conducted by filtering and excluding particles with SIMI intensity less than 0 and greater then 20, and aggregate surface area less than 18µm^2. These values were determined carefully by analysis of foreign particles produced during a negative control study processing buffer and eliminating particles in the lower limits of detection in the Horizon BMI system.

4.3.8 Thermal Stability

UNcle system (Unchained Labs, Pleasanton, CA) was used to determine the thermal stability of -ve BoNT/E formulated solutions by conducting static light scattering during thermal ramping. Samples (9µL) were aspirated into the wells and the system was set to expose samples to a thermal ramp ranging from 20 to 80^{o}C taking 1.2 reads at every 1^{o}C. Apparent melting temperature (T_m), onset aggregation temperature (T_{onset}) and aggregation temperatures (T_{agg}) were quantified from the resulting absorbance curves and determined by the UNcle software. Presets wavelengths of 266nm and 473nm were used for data acquisition as they capture are sensitive to the formation of small and large particles resulting from the thermal unfolding of proteins in solutions determined by their apparent melting temperature (T_m).

4.3.9 Statistics

Linear and non-linear regression analysis on data was performed using OriginPro Version 2023b 64-bit SR1 data analysis software (OriginLab Corporation, Northampton, MA). performing ordinary least squares (OLS) method. T-tests were calculated using the two-sample model and significance level at $p < 0.05$.

4.4 Results and Discussion

4.4.1 Protein Decay Coefficient Changes During Flow-Induced Aggregation and Peristaltic Pumping

The processing took place in the spinning disc device set at 9000RPM (a shear rate of $1.4x10^5 s^{-1}$) and the closed-loop device with a peristaltic pump set at 40RPM with 103.5% occlusion using CFlex tubing. Samples of 100µL were collected at fifteen-minute intervals from both devices. Over time, the samples turned increasingly cloudy indicating the formation of large and insoluble protein aggregates, especially for the peristaltic pumped samples which additionally showed notably large, rigid and white particles which are determined to have been spalled from the peristaltic tubing surface.

Monomer quantification allowed tracking of the fraction of monomer loss of -ve BoNT/E for four different buffers in both the spinning disc and closed-loop peristaltic pump devices. The results are shown in Figure 4-3. Consistent with the previous findings in Chapter 3, monomer decay in the spinning disc device exhibited an exponential decay trend (adjusted R^2 of >0.99) for all buffers tested.

However, monomer decay in the closed-loop peristaltic pump device exhibited a sigmoidal curve (S-shape) trend. This was attributed to a lag-phase occurring from time 0mins to 30mins for buffers 'pH 7.5 [NaCl] 0.1M' and 'pH 7.5 [NaCl] 1.0M', and 0mins to 15mins for the others. Neglecting the lag phase, an exponential decay curve fits the sample time above 30mins for all buffers with an adjusted R^2 of >0.99 (Figure 4-3). The lag phase may be attributed to the construction of the closed-loop device which has a ‘stagnant’ zone of solution within the Y-connectors that join the Luer lock valves to the loop of tubing.

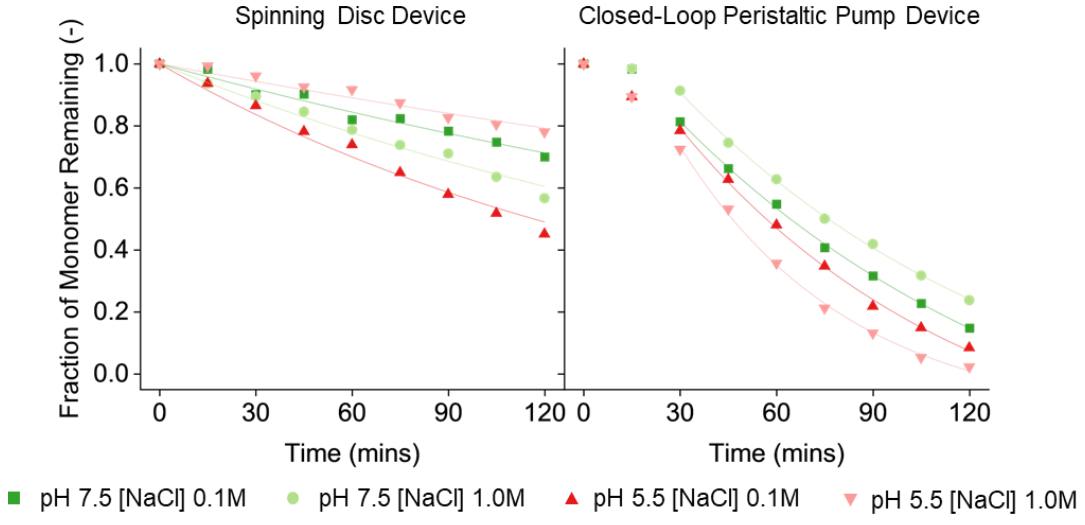

Figure 4-3 Comparison of -ve BoNT/E loss in the spinning disc and peristaltic pump device under different buffers. Spinning disc device was operated at 9000RPM ($1.4x10^5 s^{-1}$) and the closed-loop peristaltic pump device operated at 40RPM and 103% occlusion. Both devices maintained at 20^{o}C for two hours.

-ve BoNT/E formulated at 0.2mg.ml^{-1} in different buffer conditions 0.1M sodium phosphate and 0.1M or 1.0M sodium chloride at pH 5.5 or 7.5. Monomer quantified using SEC analysis. Error bars are representative of the standard deviation (SD=1) of triplcate samples (n=3) processed at 7500RPM.

Control studies were conducted for the spinning disc device in Chapter 3 and closed-loop device in Chapter 5 using buffer ‘pH 7.5 [NaCl] 0.1M’. It was found that adsorption processes of -ve BoNT/E during a two-hour incubation are negligible for the spinning disc device. However, in the closed-loop device a control study showed 5% of monomer loss due to adsorption during a two-hour incubation.

The exponential decay function (Equation 3-6) fitted to monomer loss data provided the protein decay coefficient for each -ve BoNT/E buffer processed in the respective device (Figure 4-4). The coefficient of 0.17hr^{-1} for -ve BoNT/E in buffer 'pH 7.5 [Salt] 100mM' was lower than the expected 0.33hr^{-1} as calculated in Chapter 3. It was observed that even though all material preparation methods were identical, this was a different batch of intermediate -ve BoNT/E.

In the spinning disc device (Figure 4-4), changing the buffer from ‘pH 7.5 [NaCl] 0.1M’ to ‘pH 5.5 at [NaCl] 0.1M’ resulted in a significant increase of more than two-fold in the protein decay coefficients, from 0.17hr^{-1} to 0.36hr^{-1}. At pH 7.5, increasing the salt concentration ten-fold from ‘pH 7.5 [NaCl] 0.1M’ to ‘pH 7.5 [NaCl] 1.0M’ significantly increased the coefficient from 0.17hr^{-1} to 0.25hr^{-1}, while at pH 5.5, the opposite occurred, decreasing the coefficient from 0.36hr^{-1} to 0.12hr^{-1}. All changes here were significantly different at the p-level < 0.001).

In the peristaltic pump (Figure 4-4), changing the buffer from ‘pH 7.5 [NaCl] 0.1M’ to ‘pH 5.5 at [NaCl] 0.1M’ resulted in an increase in the protein decay coefficients from 0.50hr^{-1} to 0.67hr^{-1} however this was not significant ($p = 0.09$). At pH 7.5, increasing the concentration of sodium chloride (NaCl) ten-fold from ‘pH 7.5 [NaCl] 0.1M’ to ‘pH 7.5 [NaCl] 1.0M’ did not significantly affect the coefficient from 0.50 hr^{-1} to 0.55hr^{-1} ($p > 0.50$), but at pH 5.5, the same salt concentration increase substantially increased the coefficient from 0.67hr^{-1} to 1.13hr^{-1} ($p < 0.01$). An opposite response to the observation in the spinning disc device.

The changes in protein decay coefficients can be attributed to the amphoteric nature of proteins, the result of both acidic and basic functional groups in amino acids, and the materials comprising each device. Altering buffer pH can lead to variations in the net charges of proteins and the material surface thereby influencing the electrostatic forces between them and affecting protein adsorption processes at solid-liquid interfaces ((McUmber, Randolph and Schwartz, 2015; Deiringer *et al.*, 2022).

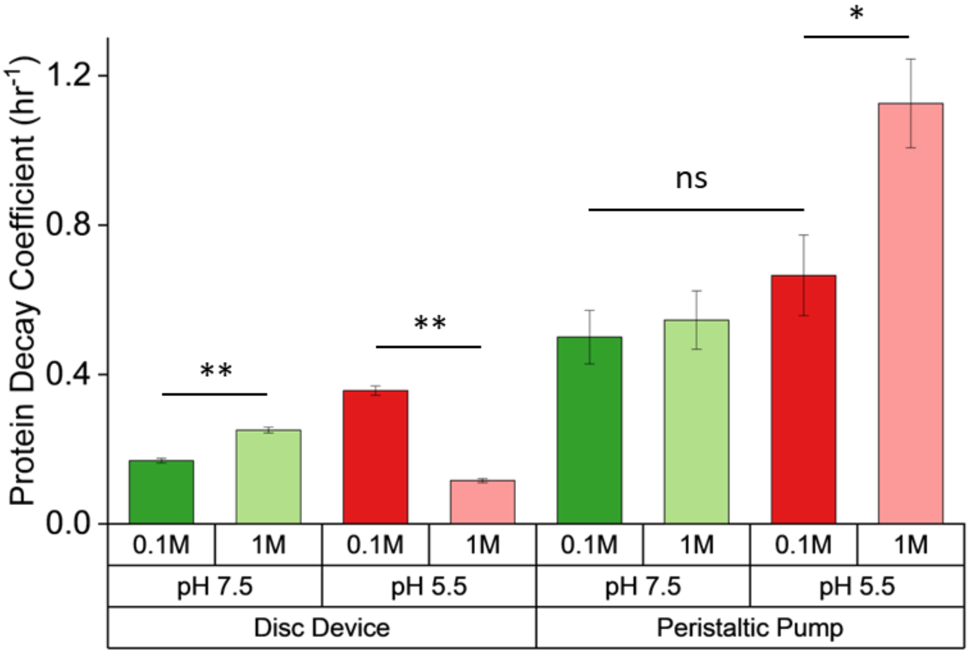

Figure 4-4 Comparision of -ve BoNT/E protein decay coefficients in the spinning disc and peristaltic pump device under different buffers. Spinning disc device was operated at 9000RPM (1.4x10^{5}s^{-1}) and the closed-loop peristaltic pump device operated at 40RPM and 103% occlusion. Both devices maintained at 20^{o}C for two hours. -ve BoNT/E formulated at 0.2mg.ml^{-1} in different buffer conditions 0.1M sodium phosphate and 0.1M or 1.0M sodium chloride at pH 5.5 or 7.5. Error bars are representative of the standard deviation (SD=1) of triplcate samples (n=3) processed at 7500RPM. Error bars represent standard error of the fitted data. Not significant (ns) and p-levels < 0.01(*) and <0.001(**) shown.

Proteins have an isoelectric point (pI) at which they possess a net-neutral surface charge. Above the pI, proteins carry a net positive charge, while below, they have a net negative charge. Studies using PyMOL have shown that the net charge of BoNT/E structure switches from negative to positive at just below pH 6.0 (Lalaurie *et al.*, 2022). On the other hand, stainless-steel (SS) alloys typically have low pI values within the range of 2.4-3.0 (Biddlecombe *et al.*, 2009; Lefèvre *et al.*, 2009) (Figure 4-5).

Ionic strength plays a significant role in modulating electrostatic forces by shielding them and reducing their effective range, which can influence protein-protein interactions and protein-interface interactions (McUmber, Randolph and Schwartz, 2015; Roberts *et al.*, 2015; Pindrus *et al.*, 2018; Deiringer *et al.*, 2022). Additionally, high ionic strength can also increase protein hydrophobicity where salt ions disrupt water molecules surrounding proteins and exposing hydrophobic patches. This effect is more pronounced inside the peristaltic pump device where the higher ionic strength increases protein hydrophobicity and drives adsorption to the hydrophobic silicone tubing (CFlex). Adsorption of proteins on to hydrophobic surfaces is observed to be very quick (Deiringer *et al.*, 2022).

At pH 7.5 and low ionic strength, the negative net charges of -ve BoNT/E and SS create repulsion forces acting between them and limit aggregation. However, adding salt ions shields these forces allowing for more protein-interface interactions and protein-protein interactions to occur (Roberts *et al.*, 2015; Pindrus *et al.*, 2018). On the other hand, at pH 5.5 and low ionic strength, -ve BoNT/E and SS have opposite net charges, leading to favourable electrostatic forces which drive interactions and encouraging more monomer loss compared to pH 7.5. However, adding salt ions at pH 5.5 has an inverse effect compared to pH 7.5 by shielding the favourable forces driving interactions thus reducing monomer loss. A similar response has been observed when processing a monoclonal antibody inside the spinning disc device at different pH values above and below the pI (Biddlecombe *et al.*, 2009). Protein adsorption onto stainless steel solid-liquid interfaces in piston pumps have similarly been observed to be governed by electrostatic attractions (Wu and Randolph, 2020).

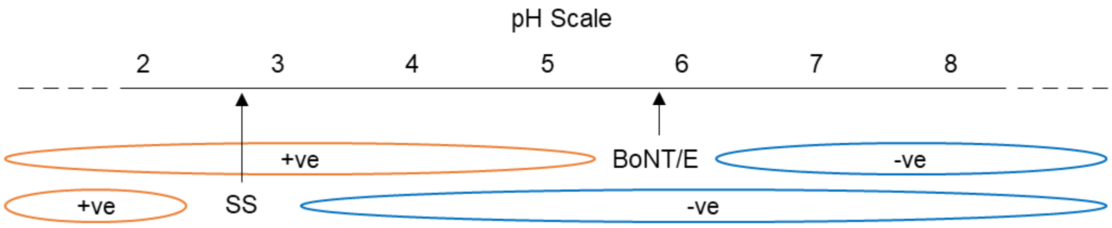

Figure 4-5 Illustration of BoNT/E and stainless steel (SS) isoelectric points (black arrows) and their net surface charge (positive '+ve' or negative '-ve') at different pH.

4.4.2 Particle Formation During Processing of Endopeptidase Botulinum Neurotoxin Serotype-E

Samples taken from both the spinning disc and closed-loop peristaltic pump devices for SEC analysis were also analysed for particles using backgrounded membrane imaging (BMI) (Figure 4-6). Similar data selection methods as described in Chapter 3, were used to exclude particles smaller than 18µm² and with a SIMI intensity greater than 20 (particles >20 are considered non-proteinaceous) (Schleinzer *et al.*, 2023).

After processing the -ve BoNT/E solution in the spinning disc device for two hours, a buffer of pH 5.5 and [NaCl] 0.1M resulted in the highest particle concentration at $4.0x10^5ml^{-1}$ (Figure 4-6). Increasing sodium chloride to 1.0M at pH 5.5 decreased the particle concentration by almost two-fold to $1.9x10^5ml^{-1}$. This response was similar at pH 7.5, where increasing [NaCl] from 0.1M to 1.0M decreased particle concentration from $3.4x10^5ml^{-1}$ to $2.4x10^5ml$.

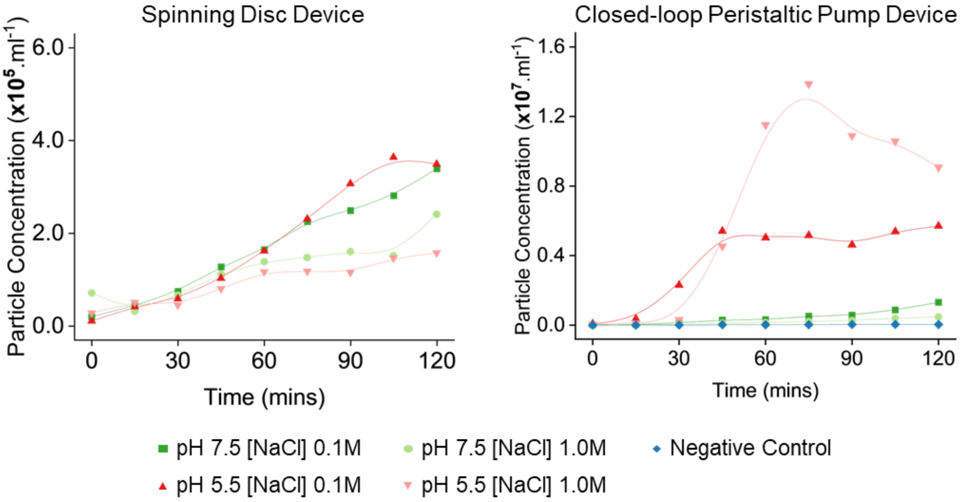

Figure 4-6 Comparison of -ve BoNT/E particle concentrations per mL in the spinning disc and peristaltic pump device. Spinning disc device was operated at 9000RPM (1.4x10^{5}s^{-1}) and the closed-loop peristaltic pump device operated at 40RPM and 103% occlusion. Both devices maintained at 20^{o}C for two hours. -ve BoNT/E formulated at 0.2mg.ml^{-1} in different buffer conditions 0.1M sodium phosphate and 0.1M or 1.0M sodium chloride at pH 5.5 or 7.5. Particles quantified using BMI analysis. Points show data from sample size n=1.

When processing -ve BoNT/E solution in the closed-loop peristaltic pump device, the buffer of ‘pH 5.5 [NaCl] 1.0M’ led to the highest particle concentration of 1.4x10^7.ml^{-1} (Figure 4-6) which occurred at 75 minutes into processing and started to decrease afterward. Lowering the ionic strength to 0.1M sodium chloride at pH 5.5 resulted in a lower particle concentration of 0.5x10^{7}ml^{-1} reaching a maximum at 45 minutes, which then remained constant.

These behaviours were unexpected and there is no immediate reason for this to occur considering that monomer loss continued to deplete during processing (Figure 4-3). In addition, the membrane coverage threshold of the BMI system remained below 7% above which the software algorithm can fail to accurately identify overlapping particles on the membrane. Furthermore, the peristaltic pump operated as normal with unchanged parameters.

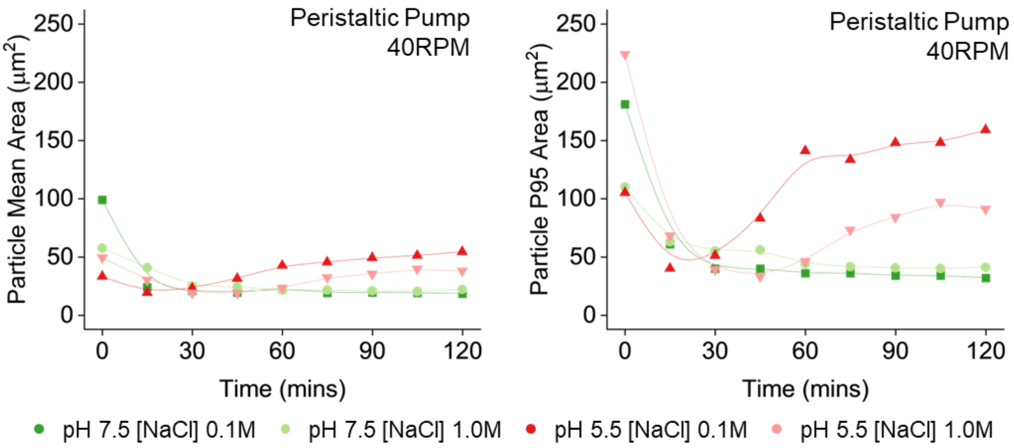

Figure 4-7 Mean and 95th percentile (P95) area of particles in -ve BoNT/E samples processed in the peristaltic pump device. Closed-loop peristaltic pump device operated at 40RPM and 103% occlusion at 20°C for two hours. -ve BoNT/E formulated at 0.2mg.ml^{-1} in different buffer conditions 0.1M sodium phosphate and 0.1M or 1.0M sodium chloride at pH 5.5 or 7.5. Particles quantified using BMI analysis.

Figure 4-7 shows the changes in mean and P95 particle area (µm^2) increasing for buffer conditions at pH 5.5 whilst decreasing for buffer conditions at pH 7.5. This could indicate that protein aggregates were condensing into larger particles corresponding to the decrease in total particle concentration observed in Figure 4-6.

For the remaining buffers at pH 7.5 in the peristaltic pump, particle concentrations were overall lower, measuring 0.7x10^{7}ml^{-1} at [NaCl] 0.1M and 0.2x10^{5}ml^{-1} at [NaCl] 1.0M.

4.4.3 Comparison of Monomer Loss and Protein Aggregation in the Spinning Disc Device and Peristaltic Pump Device

Protein decay coefficients (Figure 4-4) correlated well with the extent of particle formation for each buffer within each respective device. Buffers of pH 7.5 with [NaCl] 0.1M and 1.0M tended to yield the best results in terms of reduced monomer loss and particle concentration, while the buffer of pH 5.5 with 0.1M tended to yield the worst results in both devices. In the peristaltic pump device, the two-fold increase in particle concentration upon increasing sodium chloride aligned with Deringer *et al*.'s findings upon a similar ionic strength increase during the pumping of mAb using silicone tubing, like CFlex (Deiringer et al., 2022).

Between the two devices, particle formation was greater in the peristaltic pump, with the lowest concentration observed when using ‘pH 7.5 [NaCl] 1.0M’ buffer still being 50-fold higher than the maximum concentration observed in the spinning disc device when using buffer ‘pH 5.5 [NaCl] 0.1M’. However, a direct comparison cannot be drawn between the respective devices as whilst the hydrodynamic and shear profiles in the spinning disc device are characterised, they are yet to be determined in the peristaltic pump device. Nonetheless, for an identical protein buffer of ‘pH 5.5 [NaCl] 0.1M’, the peristaltic pump had a final particle concentration 100-fold higher at 0.5×10^{7} ml^{-1} compared to the spinning disc device at 4.0×10^{5} ml^{-1}, whilst having an equivalent monomer loss of 50%.

The lack of alignment between protein decay coefficients and the extent of particle formation across the two devices suggests different aggregation mechanisms exist within the spinning disc device and the peristaltic pump. To better understand the effect of device and buffer on protein particle formation, the morphologies of particles were more closely looked at.

4.4.4 Unique Particle Morphologies Influenced by Device and Physiochemical Conditions

Figure 4-8 presents images of particles taken during backgrounded membrane imaging (BMI) after two-hours of processing of -ve BoNT/E solution in various buffer buffers using both the spinning disc and closed-loop peristaltic pump devices. The spinning disc device produced elongated and fibrous particles greater than approximately 25µm^2 in size.

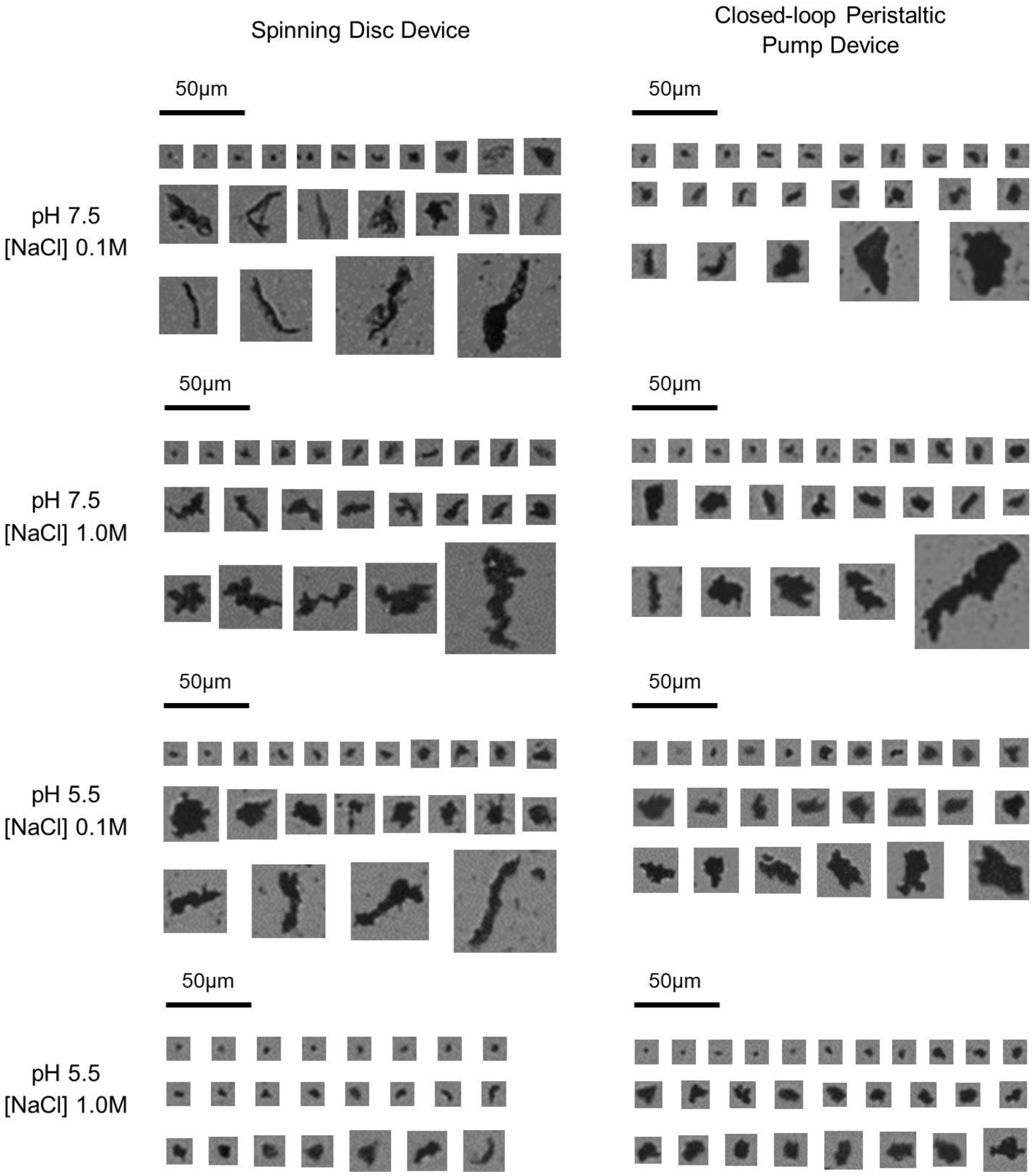

Figure 4-8 Comparison of particles in -ve BoNT/E samples processed in the spinning disc and peristaltic pump device. Spinning disc device was operated at 9000RPM (1.4x10^{5}s^{-1}) and the closed-loop peristaltic pump device operated at 40RPM and 103% occlusion. Both devices maintained at 20^{o}C for two hours. -ve BoNT/E formulated at 0.2mg.ml^{-1} in different buffer conditions 0.1M sodium phosphate and 0.1M or 1.0M sodium chloride at pH 5.5 or 7.5. Particles quantified using BMI analysis. Scale is 50μm.

These held a resemblance to those particles shown in the previous chapter and reported in literature (Nayak *et al.*, 2011; Dreckmann *et al.*, 2020; Grigolato and Arosio, 2020; Her and Carpenter, 2020; Wu and Randolph, 2020; Deiringer and Friess, 2022a). In the case of particles produced in the peristaltic pump device, there were fewer of the elongated particles and in general exhibited more globular structures by inspection the images.

Figure 4-9 displays probability density functions for particle surface area, circularity, and aspect ratio to quantify differences in particle morphologies. These parameters have often been used to gather information about the particles that form (Salami *et al.*, 2023). Mean values for these parameters are calculated off number ‘n’ of particles and compared based on two-sample t-test. At pH 7.5, the spinning disc device generated significantly larger particles, with mean surface areas of 54μm^2 (n = 2361) and 99μm^2 (n = 361) at [NaCl] 0.1M and 1.0M, respectively, with a significant difference between this group ($p < 0.001$). This is compared to the significantly smaller sizes produced by the peristaltic pump, measuring 25μm^2 (n = 1750) and 27μm^2 (n = 452) at the corresponding salt concentrations, with a significant difference between this group ($p < 0.001$).

Conversely, at pH 5.5, the spinning disc device yielded significantly smaller particles, with mean surface areas of 33μm^2 (n = 2535) and 33μm^2 (n = 1337) at [NaCl] 0.1M and 1.0M, respectively, with no significant difference between this group ($p = 0.88$), while the peristaltic pump produced significantly larger particles measuring 63μm^2 (n = 1424) and 44μm^2 (n = 2278) under the same salt conditions, with a significant difference between this group ($p = 0.001$). Based on the probability density curves in Figure 4-9 and two-sample t-tests conducted, all particle size distributions collected at a particular buffer condition within a particular device were significantly different ($p < 0.05$) from each other, including similar buffer conditions across devices used, however this was not true when using buffer at pH 5.5 [NaCl] 0.1M and pH 5.5 [NaCl] 1.0M within the spinning disc device ($p = 0.88$).

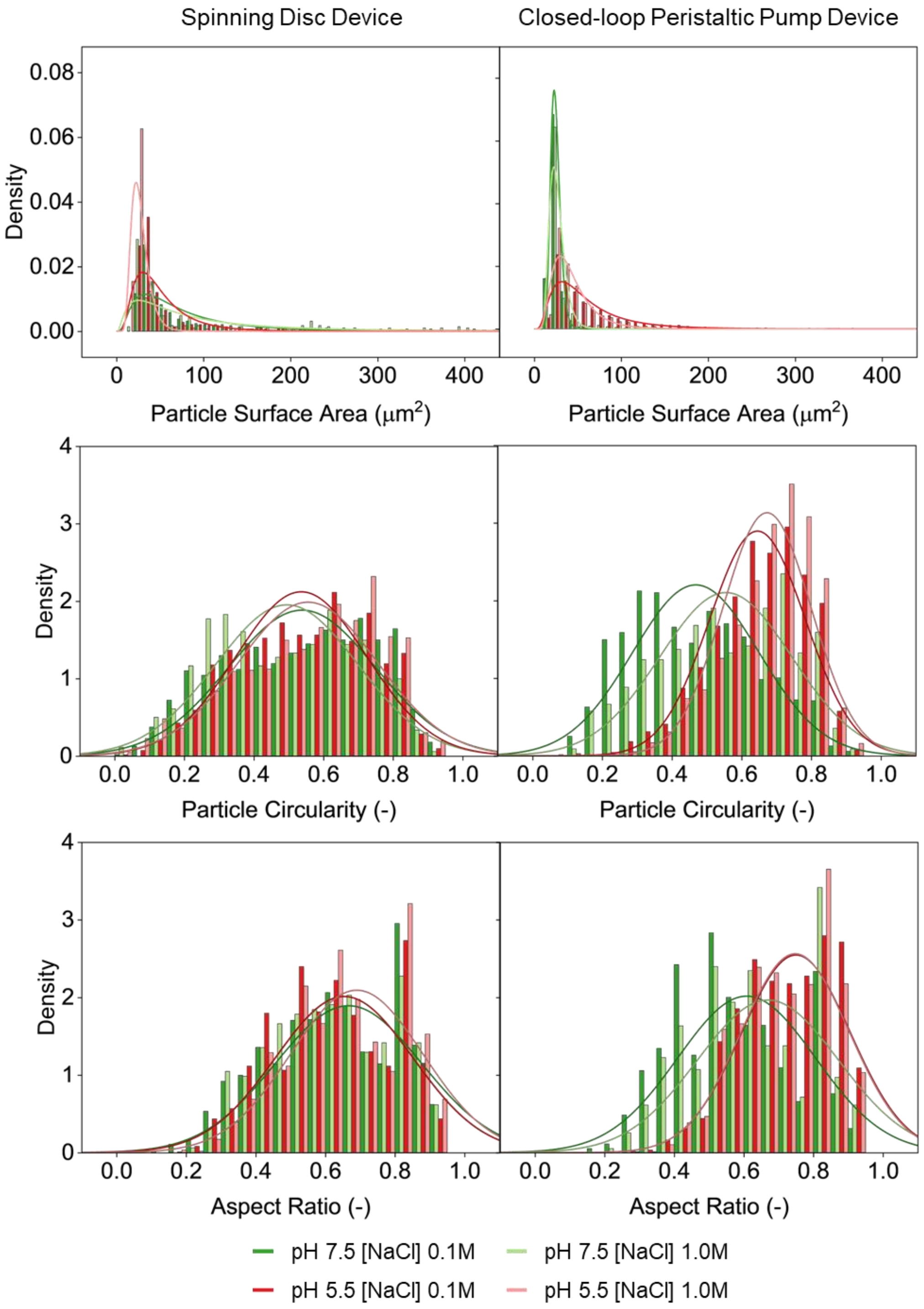

Figure 4-9 Log-normal particle distributions from -ve BoNT/E samples processed in the spinning disc and peristaltic pump device. Spinning disc device was operated at 9000RPM (1.4x10^5 s^{-1}) and the closed-loop peristaltic pump device operated at 40RPM and 103% occlusion. Both devices maintained at 20^{o}C for two hours. -ve BoNT/E formulated at 0.2mg.ml^{-1} in different buffer conditions 0.1M sodium phosphate and 0.1M or 1.0M sodium chloride at pH 5.5 or 7.5. Particles quantified using BMI analysis.

Particle circularity represents the degree to which a particle appears circular, with values of ‘1.0’ indicating perfect roundness, whilst particle aspect ratio measures the ratio of a particle's Feret minimum length to its maximum length, with a value of ‘1.0’ indicating equal height and width.

In the spinning disc device, particle circularity ranged from 0.49 to 0.57 and the mean particle aspect ratios ranged from 0.64 to 0.71 across all buffers. In contrast, particles from the peristaltic pump showed variations depending on the buffer's pH. At pH 7.5, particle circularities ranged from 0.46 to 0.57 for [NaCl] 0.1M and 1.0M, while at pH 5.5 circularity increased to 0.62 and 0.64 at the corresponding concentrations. Similarly, at pH 7.5, particle aspect ratios ranged from 0.60 to 0.64 for [NaCl] 0.1M and 1.0M, but at pH 5.5, the aspect ratio was higher at 0.68 at both [NaCl].

The spinning disc device and closed-loop peristaltic pump generated distinct particle morphologies, influenced by the buffer of -ve BoNT/E. For example, at 1.0M sodium chloride, particles were smaller in both devices compared to 0.1M sodium chloride. Morphological differences extended to the production of more circular particles in the peristaltic pump at pH 5.5 compared to pH 7.5 (at both sodium chloride concentrations) and compared to the spinning disc device at both pH 7.5 and pH 5.5.

Recent literature has deployed the use of deep learning tools to characterise and monitor the formation of particles during bioprocessing to help guide root-cause analysis (Witeof *et al.*, 2021; Greenblott *et al.*, 2022; Thite *et al.*, 2022; Salami *et al.*, 2023). Databases trained on libraries of particle images, which have been generated experimentally under defined methods, are the basis on which mathematical model are used to extract features that give that particle or group of particles to aid classification. These methods have been proven successful in identifying particles produced from a particular stress (freeze-thaw, agitation, peristaltic pumping, pH swing), the protein and the buffer conditions it was in. Such methods can be applied here to better understand the morphologies that form in each buffer and device they formed in.

4.4.5 Dynamic pH Effects on Monomer Loss and Particle Formation During Hydrodynamic Flow-Induced Aggregation

Unit operations are seldom conducted at static physiochemical conditions particularly during tangential flow filtration (TFF) diafiltration where biologic solution can be continuously circulated across a membrane and through pump to concentrate and dialyse biologics into entirely different buffer components. In this study we used the spinning disc to evaluate how dynamically changing the pH of a buffer effects the stability of endopeptidase negative neurotoxin serotype-E during processing at 9000RPM.

Figure 4-10 illustrates the fractions of remaining monomer in -ve BoNT/E samples formulated at pH 7.5 [NaCl] 0.1M and pH 5.5 [NaCl] 0.1M processed in the spinning disc device and analysed using SEC. These are considered 'static' as pH remained constant during processing. The monomer loss follows typical exponential decay curves, reflective of the results presented in Figure 4-3. The protein decay coefficients are similar, with values of 0.19hr^{-1} and 0.39hr^{-1} at pH 7.5 [NaCl] 0.1M and pH 5.5 [NaCl] 1.0M, comparable to 0.17hr^{-1} and 0.36hr^{-1} at the corresponding buffers, as shown in Figure 4-4.

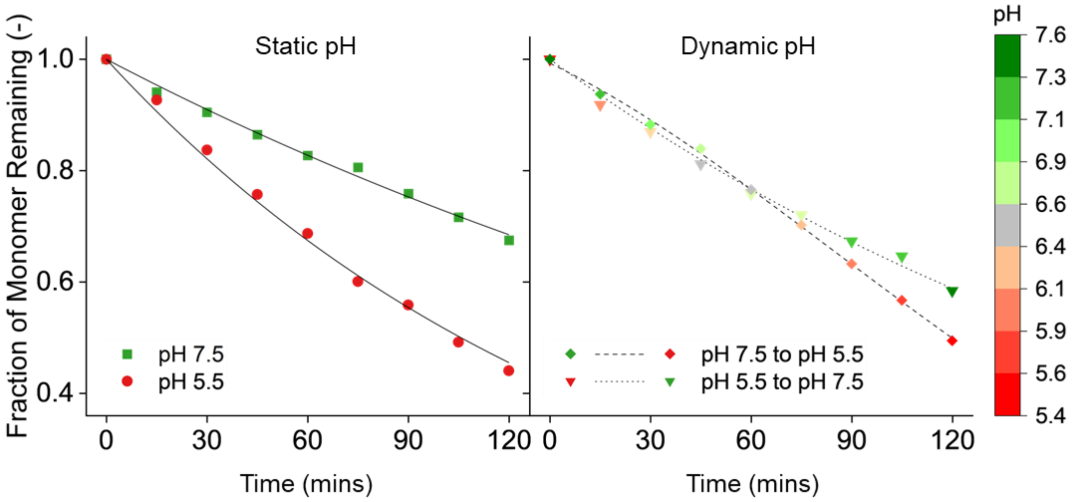

Figure 4-10 -ve BoNT/E loss during processing in the spinning disc device under static and dynamic buffers. Spinning disc device was operated at 9000RPM (1.4x10^5s^{-1}) at 20^{o}C for two hours. -ve BoNT/E formulated at 0.2mg.ml^{-1} in different buffer conditions: static buffers (left) at 0.1M sodium phosphate and 0.1M sodium chloride at pH 5.5 or 7.5 and dynamic buffers (right) at 0.1M sodium phosphate and 0.1M sodium chloride transitioning from pH 5.5 to 7.5 or 7.5 to 5.5. Monomer quantified using SEC analysis.

In contrast, 'dynamic changes' were introduced to the buffers during processing by adjusting the pH from 7.5 to 5.5 and vice versa while maintaining [NaCl] at 0.1M. The monomer loss trends follow different decay curves due to the additional function introduced by changing pH, affecting the net charges of the stainless-steel spinning disc and the protein. Equation 4-1, a two-parameter exponential decay curve, was used to model the dynamic data, with adjusted R^2 values exceeding 0.99.

For the dynamic buffer from pH 5.5 to 7.5 at [NaCl] 0.1M (Figure 4-10, dotted line), the rate of monomer loss initially resembles the rapid loss seen during static pH 5.5 conditions. However, after 45 minutes, the decay curve slowed down, indicating a reduction in the rate of monomer loss, with 58% remaining after two hours. Thus, changing the pH of the buffer from pH 5.5 to pH 7.5

shifts the rate of monomer loss observed at static pH 5.5, which promotes electrostatic attractions, towards the rate at static pH 7.5, which is less favourable for electrostatic attractions.

In the case of dynamic buffer from pH 7.5 to 5.5 at [NaCl] 0.1M (Figure 4-10, dashed line), the rate of monomer loss initially appears like the previous dynamic conditions. However, after transitioning through the -ve BoNT/E pI at 6.0, the decay curve inflects downward, accelerating monomer loss. At the end of two hours, 50% of the monomer remains.

These samples were also analysed for particle changes using BMI (Figure 4-11). During processing under static pH 7.5 and pH 5.5 conditions (at constant [NaCl] 0.1M), particle concentrations overlapped over time resulting in $3.4\text{x}10^5.\text{ml}^{-1}$ and $4.4\text{x}10^5.\text{ml}^{-1}$ particles after two hours. These particle concentrations are comparable to those reported earlier in Figure 4-6 for the corresponding buffers, despite 2.0-fold higher protein decay coefficients at pH 5.5.

In contrast, particle formation under dynamic pH 5.5 to 7.5 conditions diverged significantly from both static pH conditions, resulting in 4.6-fold higher particle concentrations after two hours. For dynamic pH conditions 7.5 to 5.5, this was 2.6-fold. However, the total amount of monomer loss was not greater than that observed under static pH changes thus the higher particle concentration is surprising.

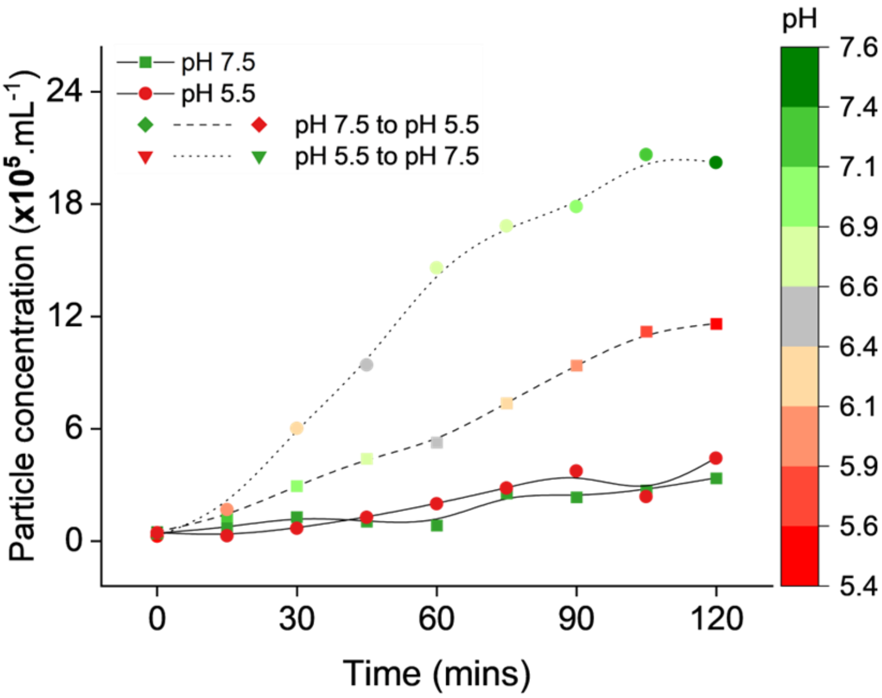

Figure 4-11 Particle concentration -ve BoNT/E samples processed in the spinning disc device under static and dynamic buffer conditions. Spinning disc device was operated at 9000RPM (1.4x10^{5}s^{-1}) and 20^{o}C for two hours. -ve BoNT/E formulated at 0.2mg.ml^{-1} in different buffer conditions: static buffers at 0.1M sodium phosphate and 0.1M sodium chloride at pH 5.5 or 7.5 and dynamic buffers at 0.1M sodium phosphate and 0.1M sodium chloride transitioning from pH 5.5 to 7.5 or 7.5 to 5.5. Particles quantified using BMI analysis.

The initial rapid rate of particle formation during dynamic pH 5.5 to 7.5 conditions (15 to 30 mins) may be attributed to processing near the pI of -ve BoNT/E at pH 6.0. Shear-induced monomer loss has been known to cause higher protein decay coefficients at the pI of proteins (Biddlecombe *et al.*, 2009) and may also cause higher particle formation. Between 30 mins and 90 mins the rate of particle formation remains at a consistent maximum until the rate of particle formation reduces corresponding to a total +1.0-point pH shift to pH 7.1. However, despite this high particle formation, rate of monomer loss is not greater than during static conditions.

Another possible cause of excessive particle formation may be due to the contact of liquid-liquid interfaces between the formulated -ve BoNT/E solution within the spinning disc device and the concentrated titration buffer (acidic or basic) infused into the device to dynamically change pH. This is illustrated in Figure 4-12. Protons or hydroxyl groups diffusing across the interface can cause the local pH to swing significantly, as mixing may be reduced, causing protein unfolding and hydrolysis, exposing hydrophobic regions in the protein structure. This exposure allows self-association between similarly hydrophobic proteins, leading to aggregate formation, as reported in various proteins exposed to extreme pH (Kristinsson and Hultin, 2004; Zhao *et al.*, 2020; Li *et al.*, 2022).

To mitigate the potential effects of extreme pH buffer, this technique should be implemented with the ultra-scale down (USD) device developed to mimic tangential flow filtration (TFF) processes (Fernandez-Cerezo *et al.*, 2019, 2020). This device, generates high turbulence, mixing and shear forces, above a membrane against which constant transmembrane pressure and flux can be monitored. Thus, dynamic physiochemical changes can be conducted via diafiltration during the operation of a spinning disc using correctly formulated buffer, which would be chemically ‘gentler’.

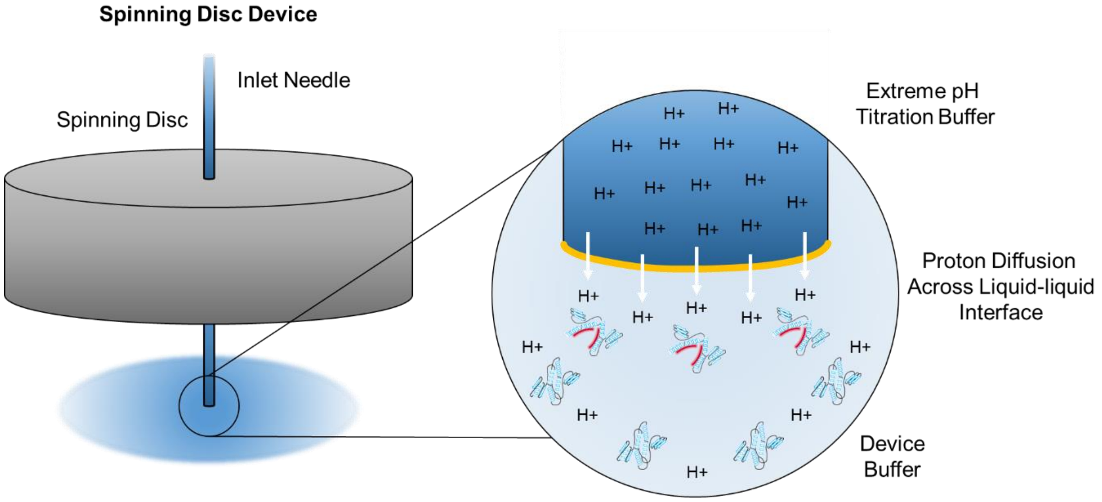

Figure 4-12 llustration of high molarity acid or base buffer impact on protein aggregation in the spinning disc device. Protons (H+, in the case of extreme acidic buffer) diffuse across a liquid-liquid interface between two different buffers and produce a localised high pH gradient exposing proteins to extreme pH, potentially causing protein unfolding, hydrolysis and aggregation.

4.4.6 Thermal stability

The thermal stability of intermediate -ve BoNT/E samples at different physiochemical conditions was tested. Buffers composed of 0.1M sodium phosphate at varying pH (7.5, 6.5 and 5.5) and sodium chloride concentrations (0.1M, 0.55M and 1.0M), and 0.1M sodium acetate at varying pH (5.5 and 4.5) at 550mM sodium chloride were monitored using static light scattering while the temperature was increased from 20°C to 80°C. Buffers 100mM sodium phosphate with 0.1M and 1,0M sodium chloride (pH 5.5 and pH 7.5) are the same as those used in the previous comparison study between peristaltic pump and spinning disc device. However, an additional mid-point buffer composing of 100mM sodium phosphate with 0.55M sodium chloride at pH 5.5, 6.5 and 7.5, and 0.1M and 1.0M sodium chloride at pH 6.5. 100mM sodium acetate 1ith 0.55M sodium chloride only is introduced when testing the thermal stability of -ve BoNT/E at lower pH ranges of 4.5 and 5.5 to allow for appropriate buffering. The resulting apparent melting temperature (T_m), onset temperature (T_{onset}), and aggregation temperature (T_{agg}) are presented in Figure 4-13.

No clear insights on the T_m of -ve BoNT/E could be determined when changing buffer, particularly at pH 7.5 where the error bars of four data points were wide. Generally, increasing the pH of the buffer raised the T_m, while changing ionic strength did not show a clear trend. The lowest T_m at 42.8^oC was observed for sodium acetate buffer at 550mM sodium chloride at pH 4.5. Sodium phosphate buffer at 100mM and 550mM sodium chloride at pH 5.5 had the highest T_m at 51.6^oC and 52.4^oC

T_{agg} the temperature at which irreversible aggregation occurs is linked to the self-association of exposed hydrophobic regions in the protein structure driving protein-protein interactions. T_{agg} data (266nm and 473nm) showed clearer trends and the effect of changing pH and ionic strength on stability. Increasing pH at any ionic strength significantly increases the T_{agg} of the -ve BoNT/E samples. For example, sodium acetate at 550mM sodium chloride at pH 4.5 and 5.5 had respective T_{agg} (273nm) values of 36.6^oC and 42.6^oC. For sodium phosphate buffer at 550mM sodium chloride at increasing pH 5.5, 6.6 and 7.5 the respective T_{agg} were 41.6^oC, 44.6^oC and 45.2^oC.

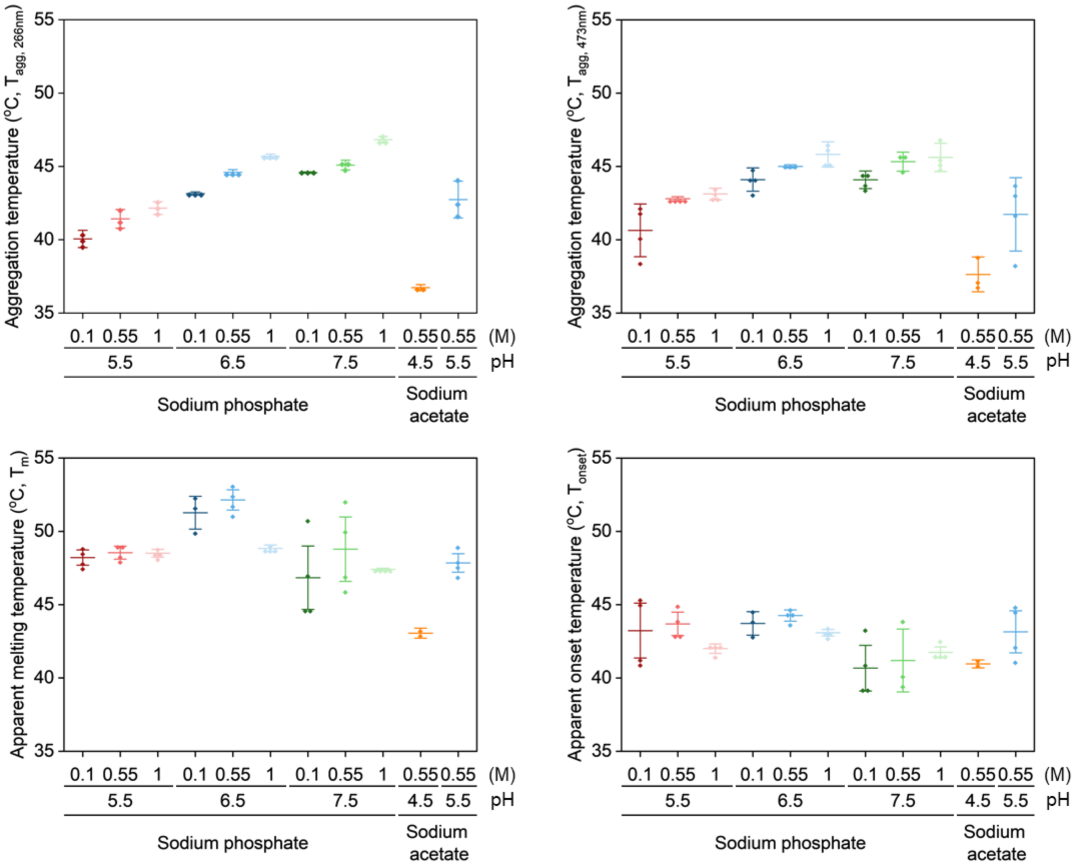

Figure 4-13 Thermal stability of -ve BoNT/E sample under different buffers. -veBoNT/E formulated at 0.2mg.ml^{-1} in different buffer conditions: 0.1M sodium phosphate (consisting of 0.1M, 0.55M or 1.0M sodium chloride and pH 5.5, 6.5 or 7.5) and 0.1M sodium acetate (consisting of 0.55M sodium chloride and pH 5.5 or 4.5). Samples were conducted in quadruplicate (n=4) and error bars represent a standard deviation SD=1. Analysis conducted using static light scattering during increasing temperature between 20-80^{o}C.

Ionic strength also had an increasing effect on the T_{agg}, stabilising -ve BoNT/E samples. Sodium phosphate at pH 5.5 and sodium chloride concentrations of 100mM, 550mM, and 1000mM led to T_{agg} values of 40.0°C, 41.6°C, and 42.2°C, respectively. Similarly, at pH 7.5, sodium phosphate with sodium chloride concentrations of 100mM, 550mM, and 1000mM led to T_{agg} values of 44.6°C, 45.4°C, and 46.8°C, respectively.

The results of T_{agg} data aligned closely with the molecular dynamic and structural simulations of BoNT/E from Lalaurie et al (Lalaurie *et al.*, 2022). Their findings indicated a decrease in the number of salt bridges within the -ve BoNT/E structure when pH reduces from 7.0 to below 5.5, with the most rapid decrease occurring below pH 5.5. This reduction in salt bridges leads to a weakening of electrostatic interactions between amino acid residues, destabilising the conformation of the structure.

Specific key domains in the structure also experience changes in net charge. Above pH 6.0, the translocation domain and light chain are negatively charged, but below pH 6.0, they transition to a positive charge, creating electrostatic repulsion with the binding domain (Lalaurie *et al.*, 2022). These changes resulted in the destabilisation of the typical compact globular state of the protein above pH 6, leading to an increase in the solvent-accessible surface area (SASA) and flexibility of the structure, as determined by root mean squared deviation (RMSD), which measures the deviation of a structure with respect to a reference structure.

Increasing SASA and conformational flexibility is concomitant to proteins susceptible to aggregation (Codina *et al.*, 2019). At low pH, conformational instabilities caused by reduced salt bridges lead to the exposure of more hydrophobic regions on the -ve BoNT/E structure. This exposure results in more protein-protein interactions, which contribute to the lower T_{agg} values observed and are responsible for the increased hydrophobic protein-interface interactions governing monomer loss and particle formation during processing in the closed-loop peristaltic pump device.

4.5 Conclusion

Testing protein buffers in the spinning disc device to understand kinetics of monomer loss by quantification using size-exclusion chromatography (SEC), and protein particle formation, by quantification using backgrounded membrane imaging (BMI), can be a powerful tool to use to understand how different buffers effect the stability of proteins. However, when comparing the buffers with a novel closed-loop device, the resulting protein decay coefficients and rates of particle formation did not align with those seen in the spinning disc device.

This highlights unique protein aggregation mechanisms at play in each device possibly due to the construction materials used in each respective device (stainless-steel in the spinning disc device and silicone in the closed-loop peristaltic pump device) that effect protein-interface behaviours. In the spinning disc device, electrostatic forces primarily drove protein adsorption mechanisms inside the spinning disc device at pH below the pI of endopeptidase negative botulinum neurotoxin serotype-E (-ve BoNT/E). However, inside the peristaltic pump device, hydrophobic attractions primarily drove protein adsorption mechanisms inside the closed-loop peristaltic pump device at low pH and high ionic strength buffers.

Thermal stability studies alluded to the sensitivity of -ve BoNT/E at low ionic strength and low pH conditions. The melting temperature of -ve BoNT/E was on average 48^{o}C and was not affected by pH changes above 5.5 pH, whilst ionic strength had no effect. Aggregation temperatures were strongly influenced also, decreasing with pH and increasing with ionic strength.

Coupled with literature discussing molecular dynamics simulations of the BoNT/E structure, at low pH salt bridge content reduces, the structure is more flexible making it more susceptible to aggregation due to greater hydrophobicity. This explained the increased monomer loss and aggregation behaviour of -ve BoNT/E during processing in the two devices at low pH conditions.

Operating the spinning disc device under single buffers could lead to the development of an effective process mimic of peristaltic pumping if characterised only by protein decay coefficients (varying spinning disc rotational speed to match peristaltic pump speed). However, given the materialistic differences, studies would need to be replicated at each buffer wished to be tested to apply equivalent shear/turbulence to encourage monomer loss. However, the aggregate particles that form in these respective devices, have unique morphologies that vary in size, circularity and aspect ratio. In short, particles from the spinning disc device were more elongated and fibrous than the circular particles from the peristaltic pump device. The morphologies changed depending on the buffer used.

Whilst the monomer loss and protein aggregation mechanisms occurring inside spinning disc device have been extensively established, those mechanisms inside peristaltic pump apparatus are still wholly unknown. At one of the lowest selectable pump speeds (40RPM, 4.1L.hr^{-1}), monomer loss and protein aggregation mechanisms of -ve BoNT/E were violent compared to the spinning disc device and led to 80% of monomer loss and formation of 1.4x10^{7}particles.mL^{-1} after two hours of processing (1200 solution circulations). In the next results chapter, the mechanism responsible for such losses are to be investigated using novel device and methods.

5 Solid-Solid Interfacial Contact of Tubing Walls Drives Therapeutic Protein Aggregation During Peristaltic Pumping

Contents of this chapter have been published in the following peer-reviewed article:

Fanthom, T. B. *et al*. (2023) “Solid-Solid Interfacial Contact of Tubing Walls Drives Therapeutic Protein Aggregation During Peristaltic Pumping”. *Journal of Pharmaceutical Sciences.* 16th August 2023.
https://doi.org/10.1016/j.xphs.2023.08.012

5.1 Chapter Summary

Turbulent hydrodynamic flow and shear forces can induce monomer loss and protein aggregation in endopeptidase-negative botulinum neurotoxin serotype-E (-ve BoNT/E). A comparative analysis of the mechanisms at play in this device was conducted in relation to those within a closed-loop peristaltic pump device under varying buffer conditions. That showed that fundamental differences in the materials constituting each device resulted in distinct driving forces governing protein-protein and protein-interface interactions. Consequently, the spinning disc device proved unsuitable as a mimic for peristaltic pumping.

Peristaltic pumping in bioprocessing applications can result in the loss and aggregation of therapeutic proteins. Given the intricate nature of this apparatus, identifying the root causes of protein loss has been a persistent challenge. In this study, we have introduced novel methodologies aimed at isolating distinct peristaltic pump mechanisms to assess their impact on monomer loss. Our approach involves employing closed-loop configurations of peristaltic tubing to investigate how various peristaltic pump parameters influence temperature and monomer loss. Additionally, we utilise two mechanism isolation techniques to separately analyse solid-solid interface contact and expansion-relaxation of peristaltic tubing.

Heat generated during peristaltic pumping in the closed-loop device can cause heat-induced monomer loss and the extent of heat gain is dependent on pump speed and tubing type. Pump speed exhibits an inverse relationship with monomer loss rates, where reducing speed by four-fold increases monomer loss by 1.8- to 2.4-fold. This is due to slower pump speeds providing more time for processes like protein adsorption, film renewal, and protein-protein interactions on tubing walls. Occlusion, indicating the degree of tubing compression, triggers an immediate 20-30% monomer loss as tubing walls make contact at 100% occlusion, suggesting changes in underlying mechanisms or abrasion at tubing interfaces.

Strain on peristaltic pumping was isolated via a device expanding and relaxing tubing but was found to cause minor monomer losses. However, tubing material can influence the extent of loss. In addition to strain, compression of tubing can drive the contact of peristaltic tubing inner walls. By, isolating solid-solid interface contact in another isolation device, monomer loss was observed to be a function of the contact area. Comparing rates of monomer loss to pumping showed higher losses in the pump which may be attributed to the rotating rollers causing friction, abrasion or grinding of interfaces during contact enhancing monomer loss during solid-solid interface contact.

Our study revealed that different types of peristaltic tubing can significantly affect monomer loss and foreign particle generation. Some tubing types caused up to five-fold more monomer loss and four-fold more foreign particles via spallation compared to the best-performing tubing. This highlights the importance of considering tubing choice in process development as well as correct setup of peristaltic pump operations. Considering that protein film adsorption and disruption are synergistic processes, surfactants could be employed to prevent the establishment of a protein film on tubing interfaces can limit the disruption caused by solid-solid interface contact.

In conclusion, our findings suggest that the solid-solid contact mechanism is the primary driver of protein aggregation during peristaltic pumping. This mechanism disrupts protein films, releasing protein aggregates and allowing for the reconstitution of these films, creating a cycle that poses a significant challenge in peristaltic pump applications.

5.2 Introduction

Tangential flow filtration (TFF) stands as a fundamental unit operation in the manufacture of therapeutic proteins, playing a crucial role in both upstream and downstream applications. It is employed in various processes, including perfusion culture (Wang *et al.*, 2017; Nie *et al.*, 2022) and ultrafiltration and diafiltration (UF/DF) operations (Rosenberg *et al.*, 2009; Daniel J. Callahan, Stanley and Li, 2014; Arunkumar *et al.*, 2016), where solution is often recirculated for multiple hours using a pump to facilitate fluid transport. Peristaltic pumping is a commonly employed liquid-handling solution in such settings, prized for its low-shear characteristics, which are particularly important when handling sensitive biologics. However, it is noted that during peristaltic pumping, protein aggregation can occur (Rosenberg *et al.*, 2009; Daniel J Callahan, Stanley and Li, 2014; Arunkumar *et al.*, 2016; Her and Carpenter, 2020; Her *et al.*, 2020; Deiringer and Friess, 2022a) This irreversible aggregation process leads to reduced manufacturing yields and complications in downstream processing, including membrane and resin fouling (Steinhauer *et al.*, 2015; Jasulaityte, Johansson and Bracewell, 2020).

Controlling the extent of therapeutic protein aggregation during bioprocessing is important to maintain the critical quality attributes of drug products. This is due to the known propensity of aggregated proteins to induce immunogenic responses and potentially neutralise therapeutic efficacy (Wang *et al.*, 2012; Moussa *et al.*, 2016; Heljo *et al.*, 2023b). Hence, a comprehensive understanding of protein aggregation mechanisms during bioprocessing is vital to develop effective mitigation strategies in the process development phase.

Protein aggregation can be initiated through several mechanisms that lead to the exposure of hydrophobic sites for non-specific protein interactions (Simpson, Good and Leach, 2020). Often, proteins adsorb onto interfaces at the boundaries of different phases, such as solid-liquid or air-liquid interfaces, which are prevalent in the manufacturing process. The rates of aggregation are sensitive to materials in contact, local shear stresses, and liquid-phase conditions. Recent research suggests that shear stress is not a reliable indicator to predict a pump's tendency to cause protein aggregation. Instead, it is attributed to the fundamental mechanics of the pump (Dreckmann *et al.*, 2020).

In the context of peristaltic pumping, the mechanics involve rollers compressing flexible tubing to create a seal between the tubing walls, forming pockets of liquid pushed through tubing by the rotational motion of the pump head. The degree of tubing compression is commonly referred to as occlusion, as defined in Equation 5-1. At 100% occlusion, the inner tubing walls come into contact as the rollers compress the tubing. Peristaltic pumps can be equipped with fixed or variable occlusion beds, offering flexibility in adjusting this parameter to meet specific process requirements. However, such values are seldom reported in the literature or by manufacturers.

Peristaltic pumping is a complex process with numerous potential aggregation mechanisms. These include heat generation resulting from friction, adsorption to interfaces, fluidic shear stresses, and the shedding of foreign particles from tubing, acting as nucleation sites.(Deiringer and Friess, 2022a) The impact of heat generated during peristaltic pumping has been examined through thermal imaging (Deiringer and Friess, 2022a), yet its relationship with pump parameters remains untested. Tubing material has been demonstrated to affect tubing particle production and protein aggregate formation during peristaltic pumping (Her and Carpenter, 2020; Her *et al.*, 2020). Notably, particles shed from tubing do not seem to influence the aggregation rate of monoclonal antibodies (mAbs).(Saller *et al.*, 2018) As mentioned, proteins can adsorb to interfaces where they can form protein films. This rapid process (less than one second) has been observed on silicone peristaltic tubing solid-liquid interfaces (Deiringer *et al.*, 2022). Once formed, expansion and relaxation of the solid-liquid interface during peristaltic pumping can cause protein film shedding and lead to the formation of protein particles (Deiringer and Friess, 2022a). This expansion mechanism is reminiscent of isothermal interfacial compression-dilation cycles (IICDs) observed in air-liquid interfaces (Bee *et al.*, 2012; Koepf *et al.*, 2018). In certain pumping systems, cavitation can generate air-liquid interfaces through bubble formation, although this phenomenon does not appear to occur in peristaltic pumping (Deiringer and Friess, 2022a).

One commonly suggested strategy for mitigating protein loss is the addition of surfactants to protein formulations, inhibiting protein adsorption and thus preventing aggregate formation (Sediq *et al.*, 2016; Her and Carpenter, 2020; Her *et al.*, 2020; Deiringer and Friess, 2022a; Deiringer *et al.*, 2022; Žuntar *et al.*, 2022).

Contact- and friction-based mechanisms for disrupting protein films have been documented in previous literature. For instance, friction at interfaces is a known cause of protein aggregation, as observed when a stirrer bar interacts with a container surface during mixing (Sediq *et al.*, 2016). Grinding of moving parts, as demonstrated in a piston pump and a small-scale system modelling contact, has also been linked to protein aggregation (Gikanga *et al.*, 2017). In another context, the milling of freeze-dried protein has shown that grinding can lead to covalent aggregate particle formation (Jing *et al.*, 2022). Given these findings, it's reasonable to hypothesise that the contact of inner tubing walls during occlusion could drive aggregation during peristaltic pumping. However, a systematic investigation of such interface-contact-based mechanical disruption mechanisms has yet to be conducted.

In this study, we employ a specifically developed methodology to investigate the impact of peristaltic pump parameters, specifically pump speed and occlusion, on heat generation during pumping, as well as monomer loss and sample turbidity. Additionally, we endeavour to isolate potential underlying protein aggregation mechanisms and their effects on monomer loss through two key approaches.

Firstly, we employ a methodology to quantify the impact of the expansion-relaxation of solid-liquid interfaces, like the one used by Deiringer *et al*. (Deiringer and Friess, 2022b). This mechanism relates to the elasticity-driven expansion and relaxation of elastomer tubing, which can deform solid-liquid interfaces and potentially induce protein aggregation, akin to isothermal interfacial compression-dilation cycles (IICDs) observed in air-liquid interfaces (Bee *et al.*, 2012; Koepf *et al.*, 2018). Notably, the extent of protein particle formation varies depending on the type of peristaltic tubing used (Deiringer and Friess, 2022a, 2022b).

Secondly, we introduce a novel methodology to quantify the impact of solid-solid interface contact in peristaltic tubing. This mechanism stems from peristaltic pumps operating by occluding tubing, potentially leading to the contact of inner tubing walls. We term this phenomenon "solid-solid interface contact," which could potentially induce protein aggregation, like the abrasion or grinding mechanisms previously described (Sediq *et al.*, 2016; Gikanga *et al.*, 2017; Jing *et al.*, 2022).

In our pumping studies, we investigate two model therapeutic proteins: tocilizumab and endopeptidase-negative botulinum neurotoxin serotype-E (-ve

BoNT/E). These proteins share a molecular weight of approximately 150 kDa and exhibit distinct apparent melting temperatures (T_m), with -ve BoNT/E at 45°C and tocilizumab at 67°C. We employ a neutralised variant of serotype-E, featuring a single mutation in its primary structure that disrupts its cleaving function, following a method described for botulinum neurotoxin serotype-A (Zhou *et al.*, 1995). The utilisation of these two model proteins in tandem enhances our ability to elucidate the root-cause aggregation mechanisms during peristaltic pumping.

5.3 Materials and Methods

5.3.1 Materials

We obtained stock solution of an endopeptidase negative (i.e., non-toxic) recombinant botulinum neurotoxin serotype-E, herein referred to as -ve BoNT/E, from Ipsen Biopharm. This stock solution is intermediate material having been purified partially following an initial chromatography step, hence there are host-cell proteins also present. We obtained a stock solution of tocilizumab from the Department of Biochemical Engineering (University College London, UK).

Both protein stock-solutions were reformulated using Slide-A-Lyzer® G2 2,500 MWCO PES 70mL dialysis cassettes purchased from Thermo Scientific (Rockford, IL, USA). Dialysis was conducted following manufacturer's instructions to exchange the protein stock solution buffer with 0.1M sodium phosphate 0.1M sodium chloride (pH 7.5) using a total dialysate buffer volume that is 200-times the sample volume used. This formulation is used throughout all experiments. All buffer components were acquired from Sigma-Aldrich Co. (St. Louis, MO, USA) and water obtained from a Milli-Q® Advantage A10 water system (Merck KGaA, Darmstadt, Germany).

The protein concentration was adjusted to 0.4mg.mL^{-1} using Vivaspin® 20 3,000 MWCO PES centrifugal filters (Sartorius Stedim Lab Ltd, Stonehouse, UK), following manufacturer's instructions, to 0.4mg.ml^{-1} determined by a Nanodrop™ OneC Microvolume UV-Vis Spectrophotometer (Thermo Scientific) acquisition at 280nm. After formulation and concentration, solutions were filtered through a 0.22µm PVDF and kept at 4°C prior to use. Protein solutions are filtered once again using a 13mm 0.22µm PVDF filter before their use in any studies. All formulations within this chapter are conducted at 0.4mg.ml^{-1} 0.1M sodium phosphate 0.1M sodium chloride (pH 7.5).

5.3.2 Closed-loop Peristaltic Pump Device: Heat Gain During Pumping at Different Pump Speed, Occlusion and Tubing

Construction and operation of the closed-loop peristaltic pump device follows the method described in Chapter 4.3.3.

Temperatures inside the described closed-loop were monitored using two thermocouples positioned in two-separate locations shown in Figure 5-1. To read the buffer temperature, one thermocouple was positioned inside the tubing and upstream of the pump head. To read the tube surface temperature, a second thermocouple was positioned inside and centred within the occlusion zone. The positions of these thermocouples are herein referred to as ‘P1’ (buffer zone) and ‘P2’ (occlusion zone) respectively. To seal Luer valve ends, a custom-shaped male-Luer end was used to fit around the thermocouple cables. The thermocouples used were K-Type, PFA insulated, flat-twin cables of diameter 0.3mm with welded ends. Pumping and temperature monitoring was conducted over two hours at varying occlusion (%) settings and pump speed (RPM) using two different tubing types: CFlex and PharMed BPT.

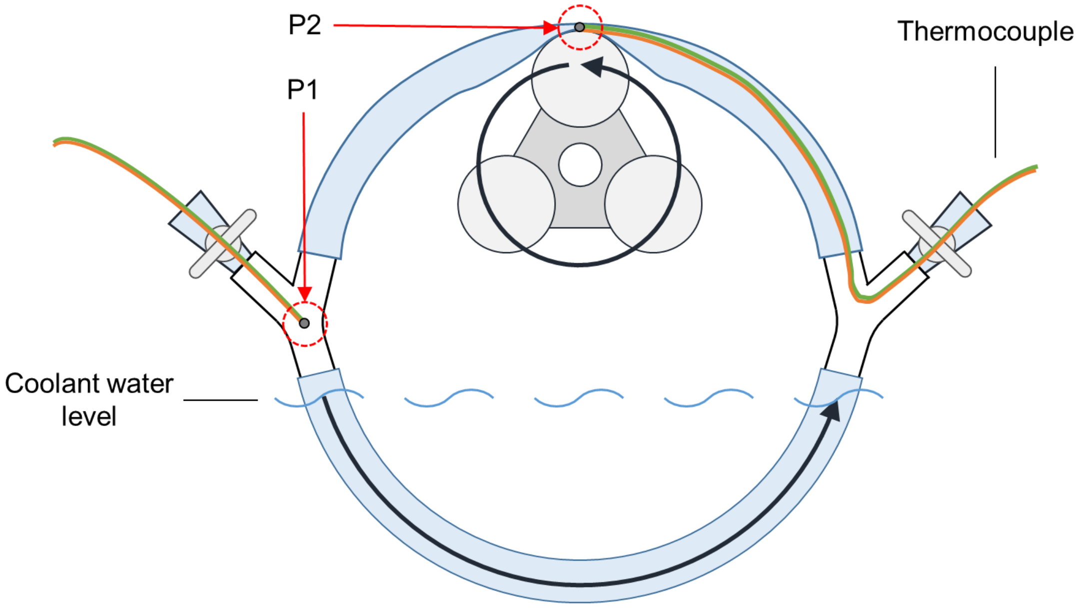

Figure 5-1 Illustration of thermocouple placement inside the closed-loop peristaltic pump device.

5.3.3 Closed-loop Peristaltic Pump Device: Heat-Induced Monomer Loss of -ve BoNT/E

The described closed-loop device was used with -ve BoNT/E solution, infused and formulated as described. -ve BoNT/E solution was recirculated in the closed loop device under the flowing conditions: 80RPM with no heat exchange, 80RPM with heat exchange to 20^{o}C, 160RPM with no heat exchange and 160RPM with heat exchange to 20^{o}C. Cooling was achieved by submerging half of the closed-loop device in cooled water provided by a Lauda Ecoline RE106 (LAUDA Technology Ltd, Stamford, UK) recirculating chiller set to a pre-calibrated temperature to maintain buffer temperatures of 20^{o}C.

Samples of protein solution were analysed using size-exclusion chromatography before and after experiments, which were conducted in duplicate.

5.3.4 Closed-loop Peristaltic Pump Device: Effect of Pump Speed and Occlusion on Monomer Loss and Aggregation

The closed-loop peristaltic pump device was used to recirculate tocilizumab and -ve BoNT/E under different rotational speed (RPM) and occlusion (%) settings to determine their effect on monomer loss and aggregation. During pump speed studies, rotational speeds (RPM) from 0RPM to 200RPM were used at increasing 40RPM intervals and maintaining constant 100% occlusion. During occlusion studies, occlusion settings of 93%, 96.5%, 100%, 103% and 107% were used at constant 80RPM speed. Temperature of the solution was maintained at 20°C during pumping as previously described.

Occlusion is calculated using Equation 5-1 where total tubing wall thickness is 't_{wall}' and distance between peristaltic rollers and occlusion bed is 'g'. All accelerated aggregation studies using the closed-loop device composed of Masterflex L/S 15 High-Performance Precision CFlex tubing. Samples of 100µl were withdrawn from the closed-loop every 15 minutes over two hours for size-exclusion chromatography analysis. These were retrieved by displacement through the infusion of an equivalent volume of buffer solution using a PhD Ultra programmable syringe pump from Harvard Instruments (Cambridge, MA). Experiments were run in duplicate.

$$Occlusion\ (\%) = (1 + \frac{2t_{wall} - g}{2t_{wall}}) * 100\% \qquad \text{Equation 5-1}$$

5.3.5 Closed-loop Peristaltic Pump Device: Screening Peristaltic Tubing Performance

Masterflex L/S 15 High-Performance Precision CFlex, PharMed® BPT, Platinum-cured Silicone, BioPharm® Platinum-cured Silicone, Puri-Flex® and Tygon® E-Lab were purchased from Cole-Parmer Instrument Company LTD (St. Neots, UK) and used to construct the closed-loop peristaltic pump device (Figure 4-1) during tubing screening studies. Coolant temperatures were calibrated against the different tubing used by pumping buffer solution and varying the temperature of coolant water provided by a recirculating chiller until a steady state 20^{o}C was achieved. These calibrated coolant temperatures are shown in Table 5-1.

5.3.6 Expansion-Relaxation of Peristaltic Tubing Solid-Liquid Interfaces

A new device was developed to repeatedly strain tubing and determine what effect expansion and relaxation forces on peristaltic tubing solid-liquid interfaces has on protein aggregation. This device is shown in Figure 5-2. 50mm lengths of two Masterflex L/S 15 High-Performance Precision Pump peristaltic tubing variants, CFlex and PharMed BPT, were cut to be strained by using a PhD Ultra programmable syringe pump. Straining tubing was carried out by using syringe plungers, obtained from dismantled 5ml syringe (Thermo Scientific), with tubing over-locked on plunger-ends to stretch tubing by a syringe pump.

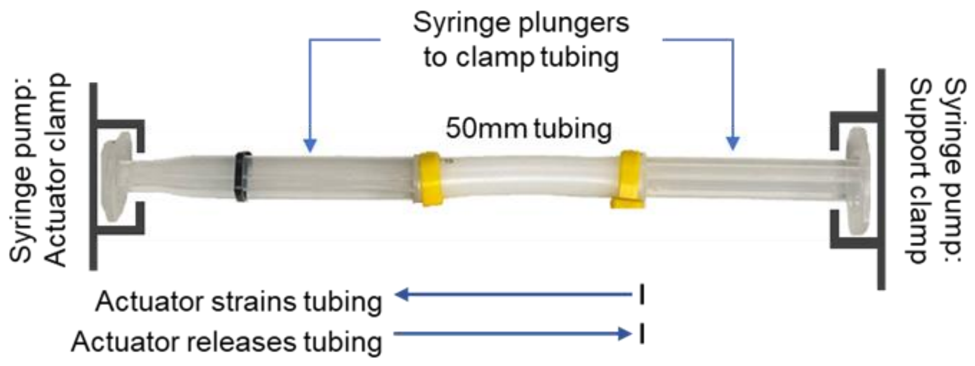

Figure 5-2 Image of the expansion-relaxtion of peristaltic tubing device.

To fill tubes, one tubing-end was initially fastened to a syringe plunger leaving the other end open allowing protein solution containing -ve BoNT/E to be added into the tube. Protein solution was degassed via vacuum prior to this to prevent air bubble formation during straining. The second plunger was pushed into the remaining open end of the tubing coming from a 45º angle to ensure no air was caught inside and removing any air-liquid interfaces. Joins between plungers and tubing were sealed tight using cable ties. Care was made to exclude all air. The syringe pump was programmed to repeatedly stretch them to 60mm (+20% strain) and relax, either 2,000- or 20,000-times, at a constant rate of 180cm.min^{-1}. Strain is defined by Equation 5-2, where l_0 is the initial length and l is the strained length. Foil lined the actuating block and the top of the pump to reflective any radiating heat emanating from the syringe pump. Experiments were run in duplicate.

$$Strain, \% = \frac{l - l_0}{l_0} \qquad \text{Equation 5-2}$$

5.3.7 Solid-Solid Interfacial Contact of Peristaltic Tubing

An adaption of the closed-loop device was developed to create the solid-solid interface contact device shown in Figure 5-3. Once assembled, the total hold-up volume was the same to that of the closed-loop peristaltic pump device. Tubing occlusion was conducted on a shorter 5.5cm piece of tubing using a defined block made of ultra-high-molecular-weight polyethylene (UHMW-PE). This was actuated upon using a programmable PhD Ultra syringe pump. Two blocks of sizes 1.0x1.0cm and 1.0x2.0cm were fabricated to vary the contact area between 0.48cm^2 and 0.96cm^2 during studies. The contact area created by each block was determined using Equation 5-3, where l is the length over which occlusion occurs and d_{id} is the tubing inner diameter. Masterflex L/S 15 tubing has an inner diameter of 0.48cm.

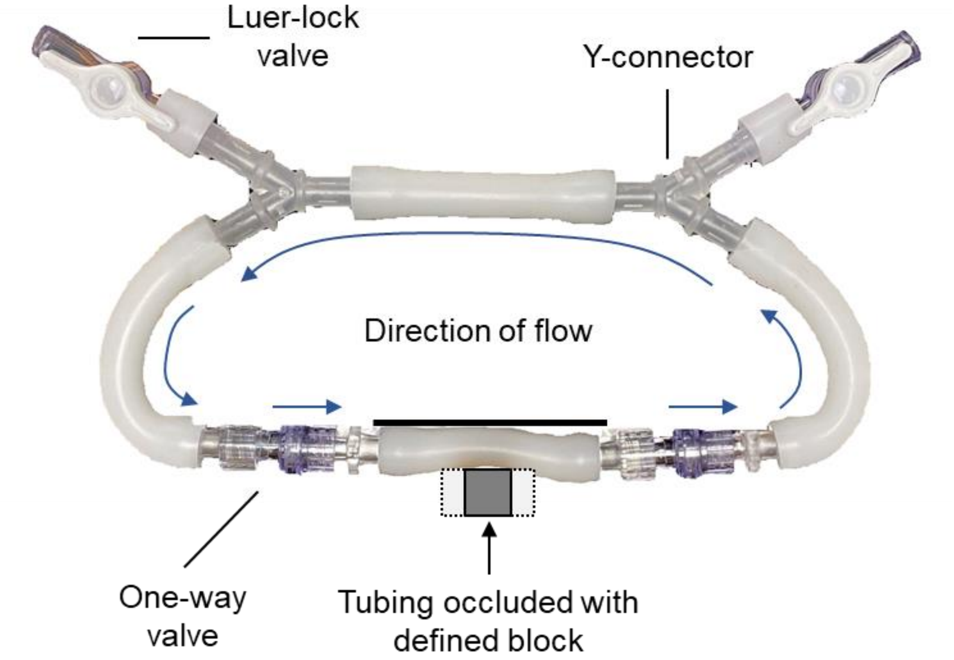

Figure 5-3 Image of the peristaltic tubing solid-solid interface contact device.

When preparing the device, -ve BoNT/E solution was infused carefully to remove all air and thus air-liquid interfaces. Tubing was occluded 20,000 times within the ranges 0-35%, 50-85%, 60-95%, 65-100% and 70-105%. These ranges were selected to maintain a constant time during each study and the amount of strain applied to tubing. Samples were withdrawn every 2,000 occlusions by 100µL buffer displacement. Foil lined the actuating block and the top of the pump to reflective any radiating heat emanating from the syringe pump. Experiments were run in duplicate.

$$Contact\ area = l * d_{id} \qquad \textit{Equation 5-3}$$

5.3.8 Size-exclusion Chromatography

Analysis and quantification of -ve BoNT/E and tocilizumab monomer was conducted following the methods outlined in Chapter 3.3.6. However, samples recovered from the closed-loop peristaltic pump device were prepared by filtering sample through a 4mm 0.22µm PVDF filter to remove spalled tubing particles and protein aggregates. Otherwise, samples were centrifuged at 18,000g for 10mins at 4^{o}C.

5.3.9 Turbidity Measurements

Turbidity of processed protein samples was analysed using a CLARIOstar® Plus plate reader from BMG LABTECH Ltd (Buckinghamshire, UK). 10µL of sample was loaded into a clear flat-bottom 384 well-plate, which briefly spun down in a centrifuge prior to analysis. Absorbance readings were taken at a wavelength of 350nm and blank data was taken from a time point of 0 minutes.

5.3.10 Nanoparticle Tracking Analysis for Tubing Spallation

To analyse spallation during pumping using the closed-loop peristaltic device (during occlusion and tubing screening studies), buffer was formulated at 0.1M sodium phosphate 0.1M sodium chloride (pH7.5) and pumped for two hours at 80RPM at different occlusion settings. Microfluidic device was equilibrated with 200µL of undiluted sample prior to analysis. Sample flow rate was set to 100, thirty second recordings were captured in triplicate and data averaged giving error bars representative of the standard deviation (SD=1). Temperature was set to 20^{o}C, camera level was set to 7 and detection threshold set to 4. Settings were kept constants for all samples within each study.

5.4 Results & Discussion

5.4.1 Peristaltic Pump Parameters Can Affect Heat Generation During Pumping

To ensure that heat generation within the closed-loop device remained within acceptable limits during processing at different pump speeds, temperature was continuously monitored over time. The impact of pump speed on heat generation during peristaltic pumping was assessed under conditions of 100% occlusion, where occlusion refers to the percentage of the total tubing wall thickness compressed between the peristaltic roller and the pump head wall (Equation 5-1).

After two-hours of pumping using CFlex tubing, temperatures at ‘P1’ were as follows: 1.5±0.2^{o}C at 60RPM, 4.6±0.3^{o}C at 120RPM and 8.0±0.3^{o}C at 240RPM (Figure 5-4A). Changing the tubing to PharMed BPT led to higher temperature increases during pumping at the same speeds: 3.7±0.2^{o}C at 60RPM, 9.3±0.2^{o}C at 120RPM and 12.7±0.4^{o}C at 240PRM after two-hours of pumping (Figure 5-4A). This indicates that using PharMed BPT tubing led to an average two-fold increase in heat generation compared to CFlex tubing.

We next investigated occlusion at a constant pump speed of 120RPM using CFlex tubing (Figure 5-4B). After two-hours of pumping using, temperatures at ‘P1’ were as follows for each occlusion setting: 4.5±0.3^{o}C at 93%, +4.8±0.2^{o}C at 100%, +5.1±0.3^{o}C at 103.5% and +5.9±0.4^{o}C at 107%.

Below 100% occlusion the inner tubing walls do not touch, whilst above 100% they increasingly do. It would be reasonable to expect that above 100% occlusion setting, increased friction and compression between the inner tubing walls would cause a notable increase in heat generation. However, it was surprising that the effect in captured data was not as pronounced as expected. To ensure the accuracy of occlusion settings in terms of inner tubing wall contact, these settings were calibrated against flow rates, confirming that fluid flow was established and remained steady from 100% occlusion. Additionally, greater production of foreign tubing particles at >100% occlusion hinted at interfaces contacting each other and causing spallation from the tubing wall (Figure 5-9).

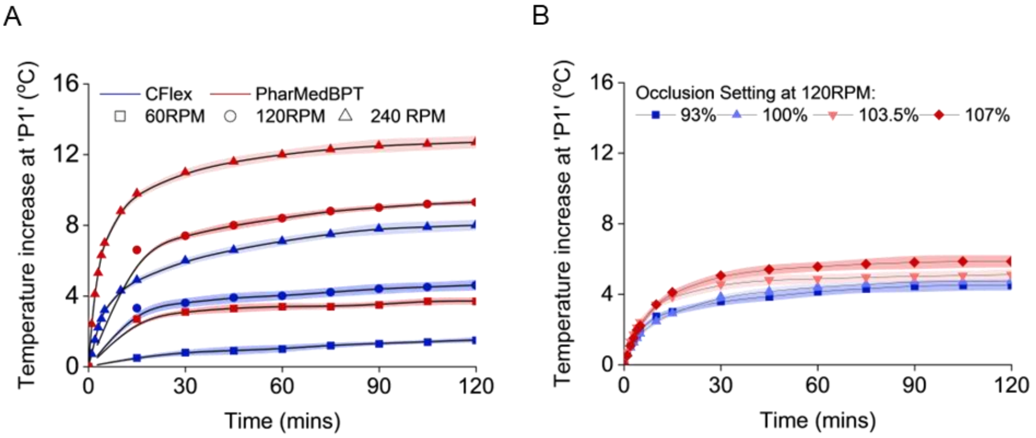

Figure 5-4 Temperature change in the closed-loop peristlatic pump device under different pump speed, occlusion and tubing. (A) Impact of pump speed (60, 120 and 180RPM at 100% occlusion) and tubing (CFlex and PharMed BPT) on temperature at 'P1'. (B) Impact of occlusion (93, 100, 103.5 and 107% at 120RPM) using CFlex tubing on temperature at 'P1. Buffer (0.1M sodium phosphate 0.1M sodium chloride (pH7.5)) was recirculated for two hours. Error bars represent the lower- and upper-limit of temperatures on the thermocouple and points represent the mean.

When comparing temperature changes at 'P1' and 'P2' under 100% occlusion and using CFlex tubing, the temperatures recorded at 'P2' were higher than at 'P1' at both pump speeds tested (Figure 5-5A). Pumping at 80RPM the temperatures at 'P1' and 'P2' increased to 24.8^{o}C and 28.8^{o}C, respectively, whilst at 160RPM these were 27.3^{o}C and 31.6^{o}C. By these readings, temperatures recorded at position 'P2', corresponding to the surface temperature of the CFlex tubing compressed by peristaltic rollers, were 4.3^{o}C higher than at 'P1'.

The effect of peristaltic pumping parameter, such as pump speed and occlusion, as well as two different tubing types, had not previously been investigated. Deiringer *et al.* investigated heat generation during peristaltic pumping operation using external thermal imaging to extrapolate and create a heat temperature profile inside the pump head. (Deiringer and Friess, 2022a)

The new data in this chapter however shows a deeper understanding of the effect of different peristaltic pump parameters on heat gain. Pump speed was proportional to heat gain and, whilst occlusion did not have as great effect as expected, changing tubing type was a strong factor indicated by switching from one tubing type to another lead to a doubling in heat gain.

5.4.2 Heat Generation During Peristaltic Pumping is not a Dominant Protein Aggregation Mechanism

To assess if protein aggregation by could be caused by thermal degradation in the closed-loop device, eat generated during pumping was actively removed using a heat exchange system involving a chilled water bath. The cooling process involved partially submerging the device in a cooled water bath, as illustrated in Figure 4-1, which was adjusted to maintain a temperature of 20°C. The choice of -ve BoNT/E as the model protein was appropriate because it is known to be susceptible to aggregation at lower temperatures, as indicated by earlier static light scattering data in Chapter 4 showing a low apparent melting temperature (T_m) of approximately 45°C (Figure 4-13B and Figure 5-5B).

After two hours of pumping at 80 RPM, there was no significant difference in the recovered monomer when heat exchange was employed compared to when it was not (Figure 5-5C). However, upon increasing the pump speed to 160 RPM, providing heat exchange to cool the closed-loop apparatus resulted in an improved monomer recovery of 7%. While it is evident that protein aggregation during peristaltic pumping can occur via thermal pathways, the fact that 89% of the monomer is still lost suggests that other, more dominant mechanisms are at play, although these remain to be determined.

A

Pump Speed (RPM)	**80**		**160**	
Thermocouple location (-)	P1	P2	P1	P2
Temperature after two-hours pumping (°C)	24.8	28.8	27.3	31.6

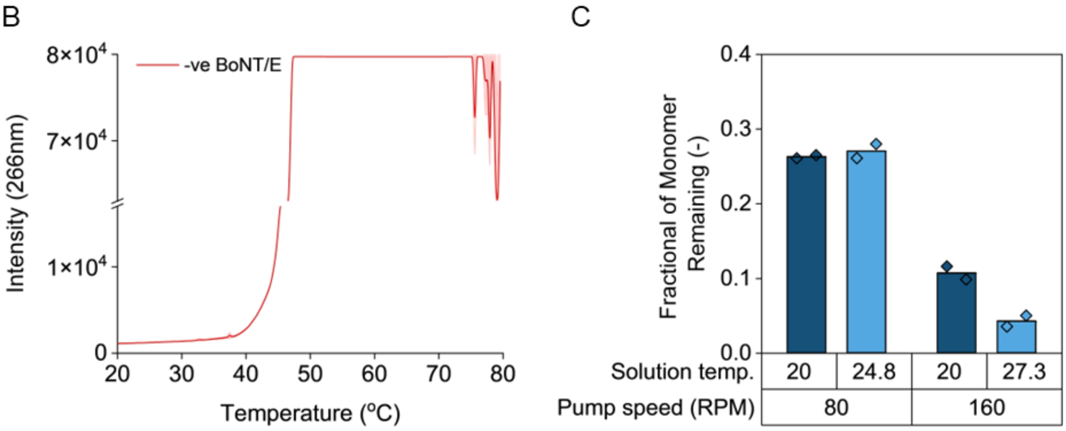

Figure 5-5 Effect of heat generation in the closed-loop peristaltic pump device on -ve BoNT/E loss. (A) Temperature differences between thermocouples ‘P1’ and ‘P2’ after pumping for two hours at 80RPM and 160RPM. (B) Static light scattering intensity (266nm) of –ve BoNT/E sample during thermal ramping. (C) Comparison of –ve BoNT/E monomer loss after pumping at 80RPM and 160RPM and cooling the device to 20°C or not. -ve BoNT/E formulated at 0.4mg.ml^{-1} 0.1M sodium phosphate and 0.1M sodium chloride (pH 7.5). CFlex tubing was used.

Temperature strongly influences protein adsorption and aggregation (Kiesel *et al.*, 2014; Jackman *et al.*, 2017). Thus, it's unsurprising that cooling the device improved monomer recovery post-pumping, especially for a protein like -ve BoNT/E with a low T_m (45°C). Assessing the extent of loss due to thermal degradation within the closed-loop device was essential during its development and in the investigation of aggregation mechanisms during peristaltic pumping. This understanding allows for more controlled studies on pumping parameters by designing experiments with using pre-calibrated coolant temperatures. In large-scale operations such as tangential flow filtration, the impact of heat may not be a concern as the circulated fluid could possess sufficient heat capacity to limit temperature change.

5.4.3 Rate of Monomer Loss per Peristaltic Roller Impact has an Inverse Relationship to Pump Speed

The closed-loop device's sensitivity to heat, particularly at higher peristaltic pump speeds, underscores the necessity for heat exchange to maintain a 20°C temperature, effectively mitigating heat-related effects during investigations into protein aggregation mechanisms. Calibrating pump speed against the required coolant temperature for sustaining 20°C yielded the following values: 17.5°C at 40RPM, 16.4°C at 80RPM, 15.1°C at 120RPM, and 13.8°C at 160RPM.

Figure 5-6A illustrates the decay of tocilizumab and -ve BoNT/E monomer during pumping in SEC chromatograms. Notably, no soluble low-molecular-weight or high-molecular-weight aggregate species were observed in the chromatograms, which is a common occurrence reported in the literature. Based off the SEC analysis, the following monomer data is presented as a duplicate average.

Control studies, conducted by incubating proteins within the closed-loop device for two hours without pumping, showed that 96.3% of tocilizumab and 94.7% of -ve BoNT/E monomer remained (Figure 5-6 B-C). The losses observed here can be attributed to adsorption in the device and during the handling of samples. As the control study does not ‘impact’ the tubing the data points lay on the y-axis at (x=0 impacts).

After pumping tocilizumab for two hours, the percentage of monomer remaining was 76.4% at 40RPM, 64.6% at 80RPM, 56.5% at 120RPM, 49.5% at 160RPM, and 43.4% at 200RPM (Figure 5-6B). For -ve BoNT/E, after two hours of pumping, the percentage of monomer remaining was 49.4% at 40 RPM, 26.5% at 80RPM, 19.8% at 120RPM, and 10.7% at 160RPM (Figure 5-6C). Testing at 200RPM was not conducted for -ve BoNT/E due to an observed significant spalled tubing particle production that risked damage to UPLC equipment.

An interesting relationship emerged from the data. To induce a 20% loss in tocilizumab monomer at 40 RPM, approximately 18,000 pump head impacts were required. However, as the pump speed increased to 80 RPM, 120 RPM, 160 RPM, and 200 RPM, progressively more impacts were needed—approximately 25,000, 32,000, 38,000, and 41,000 impacts, respectively (Figure 5-6B). This trend is more pronounced in the case of -ve BoNT/E (Figure 5-6C).

To better understand this relationship, the maximum rates of monomer loss per roller impact were extracted from linear regressions of the monomer fractions correlated against impacts (Figure 5-6 B-C). A lag phase observed within the first three samples of all monomer time-points led to the assumption of linearity beyond the fourth sample time-point, yielding adjusted R^2 values averaging >0.99 across both model proteins.

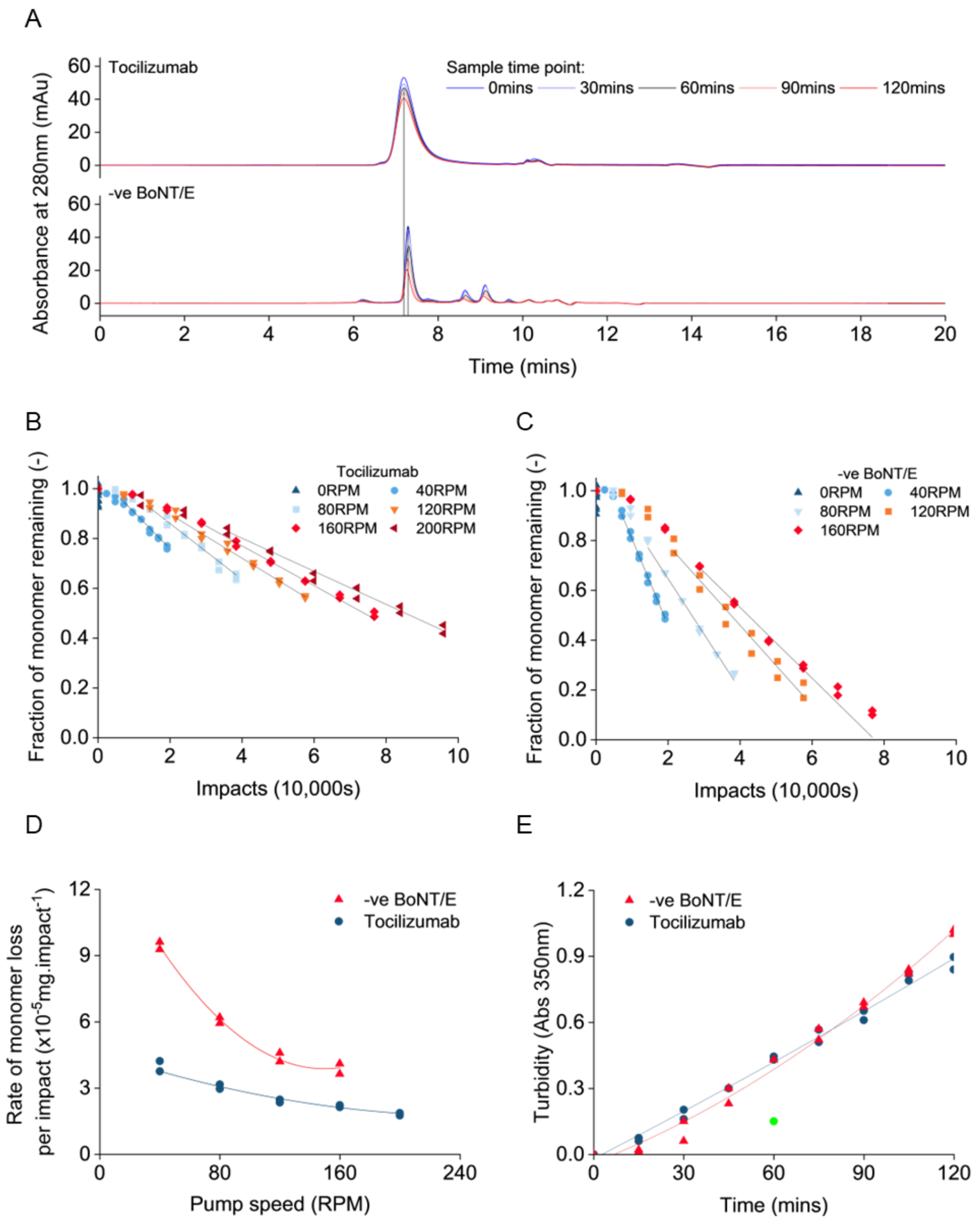

Figure 5-6 -ve BoNT/E and tocilizumab aggregation in the closed-loop peristaltic pump device under different pump speeds. (A) Size-exclusion chromatography analysis of samples (0, 30, 60,90 and 120mins shown). (B) Tocilizumab monomer loss. (C) -ve BoNT/E monomer loss. (D) Maximum rates of tocilizumab and –ve BoNT/E loss per impact. (E) Turbidity of samples during pumping at 40RPM. Pump operated at 0, 40, 80, 120, 160 and 200RPM (not for -ve BoNT/E) and 100% occlusion at 20°C for two hours using CFlex tubing. Tocilizumab and -ve BoNT/E formulated at 0.4mg.ml^{-1} 0.1M sodium phosphate and 0.1M sodium chloride (pH 7.5). Duplicate data shown.

An inverse relationship is evident between monomer loss per impact and pump speed, which follows an apparent second-order relationship (Figure 5-6D). A fitted parabolic curve to the data exhibits an R^2 of >0.99. For tocilizumab, the maximum rates of monomer loss per occlusion at 40 RPM and 160 RPM were $4.0x10^{-5}$mg.impact^{-1} and $2.2x10^{-5}$mg.impact^{-1}. For -ve BoNT/E, these rates at 40RPM and 160RPM were $9.5x10^{-5}$mg.impact^{-1} and $3.9x10^{-5}$mg.impact^{-1}. Consequently, reducing pump speed by a factor of 4.0 resulted in a 1.8-fold increase in the rate of monomer loss for tocilizumab and a 2.4-fold increase for -ve BoNT/E.

Visual inspection of the samples revealed a progressive cloudiness, suggesting potential formation of insoluble aggregates. To assess turbidity changes at 40RPM, absorbance at 350 nm was measured (Figure 5-6E) indicating an increase in absorbance over time for both tocilizumab and -ve BoNT/E. This increase in absorbance is indicative of the presence of insoluble protein aggregates.

The higher rates of -ve BoNT/E monomer loss compared to tocilizumab, as shown in Figure 5-6D, might be attributed to the intrinsic properties of botulinum neurotoxins. These toxins are known to possess electric dipoles across their protein structure, which facilitates their rapid and high-affinity interaction with presynaptic membranes (Fogolari *et al.*, 2009). Considering that the peristaltic tubing is composed of silicone rubber, a negatively charged material, this could potentially explain the faster rates observed for -ve BoNT/E compared to tocilizumab.

Processes of protein adsorption and protein layer disruption can act synergistically to perpetuate protein aggregation (Bee, Stevenson, *et al.*, 2009). Each process is governed by a rate and is a function of total aggregation that can occur. Extending the time for protein adsorption allows the protein layer to fully establish itself, rendering each disruption caused by peristaltic pump roller impacts more damaging. We observed this phenomenon by manipulating pump speed, reducing it from 160RPM to 40RPM, which increased the time for adsorption between each roller impact by 4.0-fold, from 0.09s to 0.37s, resulting in a two-fold increase in monomer loss rates. These findings contradict the thought that higher pump speeds lead to increased hydrodynamic flow, resulting in turbulence and shear effects that would cause monomer loss and aggregation. It is worth noting that, at each examined pump speed, the Reynolds number falls within the turbulent flow regime.

Previous reports indicate that the time required for protein film formation by adsorption is typically shorter than 1.0s at solid-liquid interfaces, and even less, sometimes below 0.01s, at air-liquid interfaces (Deiringer *et al.*, 2022; Žuntar *et al.*, 2022). In the case of solid-liquid interface adsorption, our pump adsorption times fall within these reported ranges, potentially rendering monomer loss rates more susceptible to changes with alterations in pump speed. This phenomenon aligns with the findings of Deiringer *et al*. and Wu *et al*., who demonstrated similar effects in the context of protein particle formation during peristaltic pump and piston pump operation.(Wu and Randolph, 2020; Deiringer and Friess, 2022a).

5.4.4 Varying Occlusion Shows Key Protein Aggregation-mechanism Changes as Inner Tubing Walls Begin to Contact

In the pump apparatus used for these studies, the degree of occlusion can be adjusted within a range of 93% to 107%. During a two-hour pumping session at 80RPM (equivalent to 40,000 roller impacts) using the closed-loop device, occlusion levels were systematically increased in 3.5% increments starting from 93%. These increments followed pre-set notches in the pump apparatus, eventually reaching the critical point of 100% occlusion, where the inner tubing walls meet each other. The following data reflects the average of duplicate measurements.

For tocilizumab (Figure 5-7), the fraction of monomer remaining was quantified at the following occlusion settings: 0.69 at 93%, 0.66 at 96.5%, 0.65% at 100%, 0.46 at 103.5% and 0.24 at 107%. Below 100% occlusion, minimal changes in monomer loss occurred. However, when occlusion settings were increased beyond 100% to 103.5% and 107%, there was a sudden and substantial decrease in the fraction of monomer remaining.

A similar trend and transition were observed for -ve BoNT/E (Figure 5-7). The fraction of monomer remaining was quantified for the following occlusion settings: 0.69 at 93%, 0.58 at 96.5%, 0.26 at 100%, 0.18 at 103.5% and 0.12 at 107% occlusion. Similarly, at 100% occlusion, a greater than two-fold increase in the fraction of monomer remaining occurred in response to a 3.5% increase in occlusion from 96.5% to 100% as inner tubing walls meet.

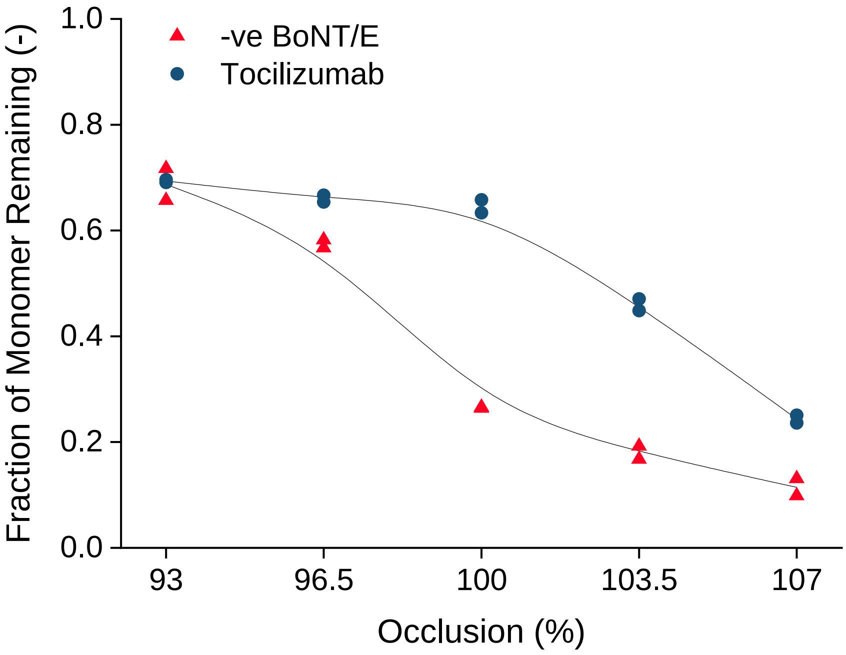

Figure 5-7 -ve BoNT/E and tocilizumab loss in the closed-loop peristaltic pump device under different occlusion settings. Pump operated at 93, 96.5, 100, 103.5 and 107% occlusion and 80RPM at 20^{o}C for two hours using CFlex tubing. Tocilizumab and -ve BoNT/E formulated at 0.4mg.ml^{-1} 0.1M sodium phosphate and 0.1M sodium chloride (pH 7.5). Monomer quanitified using SEC analysis. Duplicate data shown.

Figure 5-8 shows changes in apparent turbidity for the same samples. An increase in absorbance for both proteins was observed, meaning that an increasing formation of insoluble protein aggregates occurs with higher levels of pump occlusion. It's important to note that increasing occlusion can also trigger increased spallation from the tubing. An increasing presence of nanoparticles with occlusion when pumping buffer only was observed using nanoparticle tracking analysis (Figure 5-9). However, these nanoparticles did not influence turbidity data as shown when pumping using CFlex tubing at 100% during later tubing screening studies (Figure 5-12) and is assumed negligible for all other occlusion parameters.

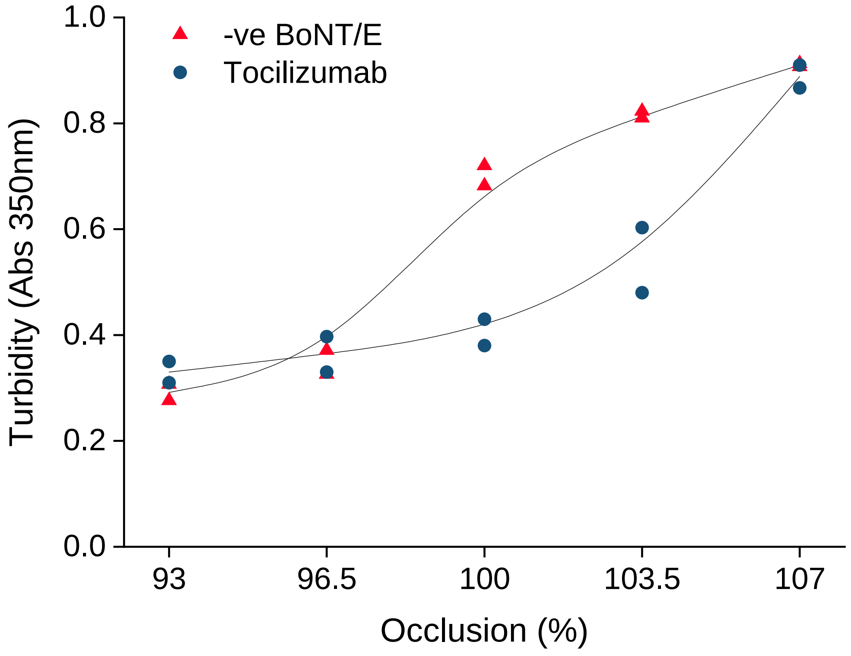

Figure 5-8 -ve BoNT/E and tocilizumab sample turbidity in the closed-loop peristaltic pump device under different occlusion settings. Pump operated at 93, 96.5, 100, 103.5 and 107% occlusion and 80RPM at 20^{o}C for two hours using CFlex tubing. Tocilizumab and -ve BoNT/E formulated at 0.4mg.ml^{-1} 0.1M sodium phosphate and 0.1M sodium chloride (pH 7.5). Turbidity quanitified using absorbance at 350nm. Duplicate data shown.

Efficient peristaltic pump operation requires the inner tubing walls to remain in contact during roller compression. This contact prevents internal backflow of liquid, known as pump-slip, which is particularly critical in high back-pressure environments like ultrafiltration/diafiltration (UF/DF) or when handling viscous fluids. Occlusion, quantified as the percentage of the total tubing wall thickness compressed by the peristaltic roller against the pump head wall, plays a vital role in this process.

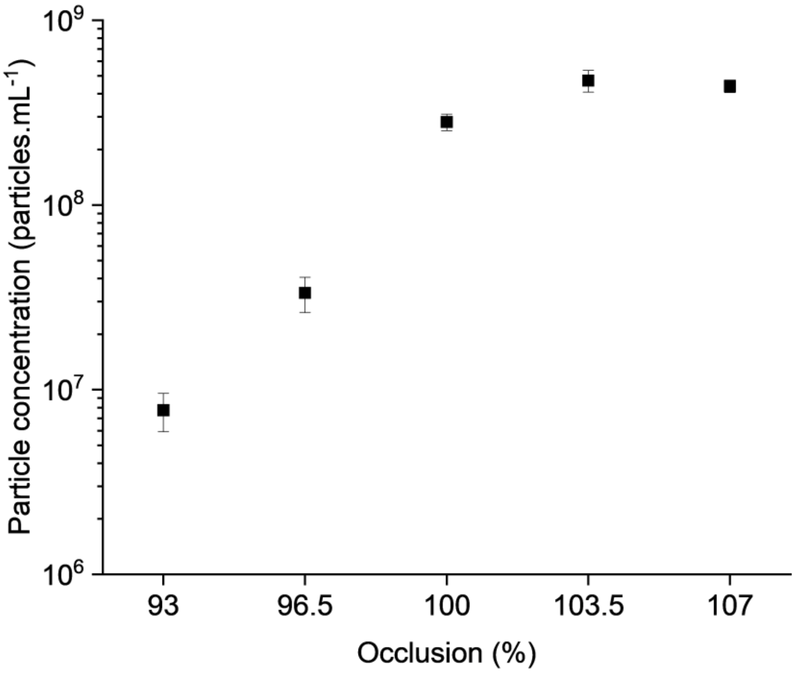

Figure 5-9 Spallation of nanometer and submicron foreign particles in the closed-loop peristaltic device when recirculating buffer solution only. Pump operated at 93, 96.5, 100, 103.5 and 107% occlusion and 80RPM at 20ºC for two hours using CFlex tubing. Buffer formulated at 0.1M sodium phosphate and 0.1M sodium chloride (pH 7.5). Particles (10nm-800nm) quantified using NTA analysis. Mean data of technical triplcates (n=3) shown and error bars represent (SD=1).

During our pumping experiments, we noticed that as the tubing walls came into contact at 100% occlusion, there was a sudden increase of 20-35% in monomer loss and turbidity (Figure 5-7). This observation indicated an additional mechanism at play when compared to under-occlusion (<100%) pumping. We attributed this effect to the disruption of protein films as the inner tubing walls began to contact each other during each roller compression. While this is significant for process yields, it's crucial to recognise that adjusting tubing compression may have secondary effects that impact aggregation, as discussed below.

The compression and flexing of tubing can lead to the deterioration of inner tubing walls, resulting in the development of cracks, corresponding to increased surface roughness (Saunier and Yagoubi, 2021). Greenblott *et al*. demonstrated that the aging of tubing contributes to increased protein and foreign particle formation during pumping operations (Greenblott *et al.*, 2022). This phenomenon is likely due to the escalating surface roughness resulting from the deterioration of tubing walls, as observed by Saunier and Yagoubi.

Beyond the realm of peristaltic pumping, altering the surface roughness of disc inside the spinning disc device was shown to affect monomer loss (Biddlecombe *et al.*, 2009). Additionally, tubing flexing can lead to the spallation of foreign particles from the tubing, a well-recognised issue in haemodialysis equipment (Bommer *et al.*, 1985; Barron *et al.*, 1986; Briceño and Runge, 1992). The frequency, extent and compression of tubing walls could exacerbate crack formation and increase spallation. However, other research has indicated that the presence of foreign particles does not cause protein aggregation (Saller *et al.*, 2018; Wu and Randolph, 2020). Therefore, the increased monomer loss we observed during pumping primarily results from the contact of solid-solid interfaces that disrupt protein layers formed after protein adsorption.

5.4.5 Screening Commercially Available Peristaltic Tubing Evaluating Monomer Loss and Aggregation Performance

The closed-loop peristaltic pump device was constructed out of six different commercially available peristaltic tubing types (Masterflex® L/S® 15) to evaluate their performance on monomer loss and aggregation during peristaltic pumping. To minimise any temperature variations from the different tubing materials used, a coolant temperature was pre-calibrated to maintain an internal fluid temperature of 20^{o}C when pumping buffer at 40RPM and 100% occlusion. Table 5-1 shows the resultant coolant temperatures which were used to pump -ve BoNT/E and tocilizumab.

Table 5-1 Coolant temperatures for tubing to maintain 20^{o}C in the closed-loop peristaltic pump device. Pump operated at 40RPM and 100% occlusion.

Tubing	Legend	Coolant Temperature (^{o}C)
CFlex	CFlex	17.5
PharMed BPT	PMed	16.3
Puri-Flex	PFlex	16
Platinum-cured Silicone	Si-Pt	17.8
BioPharm Platinum-cured Silicone	Si-Pt Bio	17.8
Tygon E-Lab	Tygon	15.6

Among the tested tubing materials, Tygon E-Lab (polyvinylchloride-based) exhibited the lowest coolant temperature requirement, maintaining a temperature of 20°C with a coolant temperature of 15.6°C. Puri-Flex (styrene-ethylene-butylene-based) and PharMed BPT (polypropylene-based) closely followed, requiring slightly higher coolant temperatures. Conversely, the siloxane-based tubing types, platinum-cured silicone and BioPharm platinum-cured silicone, demonstrated superior thermal performance, requiring reduced coolant temperatures of 17.8°C to maintain the target temperature of 20°C. This observation aligns with the earlier findings when changing tubing types has an impact on temperature variations in the closed-loop device.

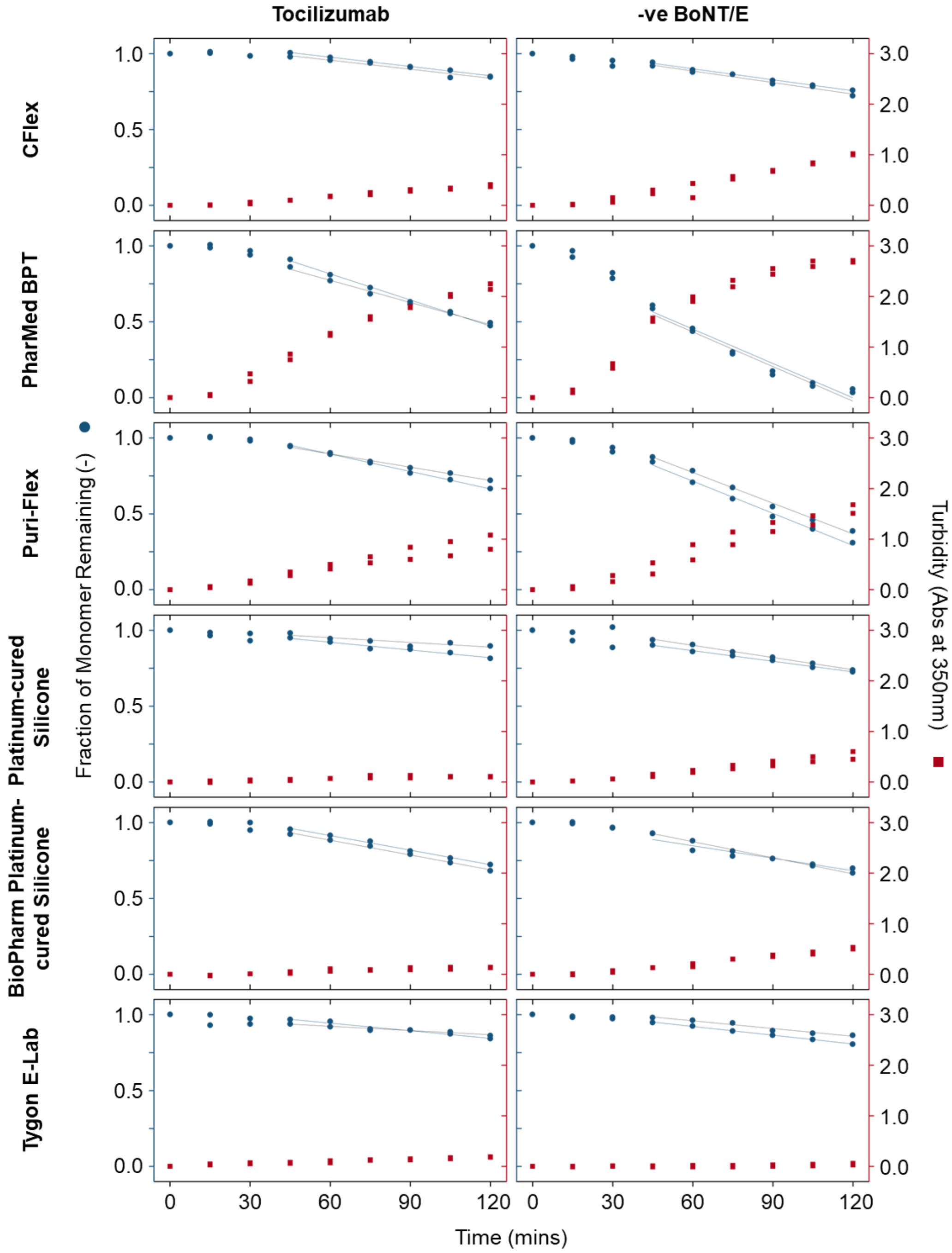

Figure 5-10 Comparison of six peristaltic tubing types on tocilizumab and -ve BoNT/E aggregation in the closed-loop peristaltic pump device. Pump operated at 40RPM and 100% occlusion at 20^{o}C for two hours using tubing: PharMed BPT (PMed), CFlex, Platinum-cured silicone, (Si-Pt), BioPharm Platinum-cured silicone (Bio Si-Pt), Puri-Flex (PFlex) and Tygon E-Lab (Tygon). Tocilizumab and -ve BoNT/E formulated at 0.4mg.ml^{-1} 0.1M sodium phosphate and 0.1M sodium chloride (pH 7.5). Monomer quanitified using SEC analysis. Turbidity quanitified using absorbance at 350nm. Linear regressions fitted from fourth data point. Duplicate data shown.

Figure 5-10 presents the monomer loss and turbidity results associated with different tubing types used in the closed-loop peristaltic pump device. Each monomer decay curve exhibits the characteristic sigmoidal (S-shaped) trend typically observed with this device. This trend is also reflected in the apparent turbidity data, indicating an increase in insoluble protein aggregates during pumping. Higher final turbidity values corresponded to cloudier samples visually, with some larger particles believed to originate from the tubing itself, suggesting spallation during the pumping process.

Figure 5-11 shows the rate of monomer loss as a function of the total number of peristaltic pump roller impacts made during pumping. These were obtained from linear regressions fitted to data points past the fourth sample (45mins), avoiding the ‘lag phase’ in the sigmoidal curve. The effect of tubing appeared significant for some types based on the rates of monomer loss of the two model proteins studied. For -ve BoNT/E and tocilizumab, the top 3 tubing types in order from worst to best based on rate of monomer loss were: PharMed BPT, Puri-Flex and Platinum-cured silicone.

For -ve BoNT/E (Figure 5-11), the tubing types ranked from worst to best in terms of monomer loss rates were PharMed BPT, Puri-Flex, and Platinum-cured silicone. The difference in performance between the worst two tubing types, PharMed BPT and Puri-Flex, with rates of 1.9×10^5mg.impact^{-1} and 1.7×10^5mg.impact^{-1}, compared to Platinum-cured silicone, at 0.8×10^5mg.impact^{-1}, exceeded two-fold. The disparity in performance between Platinum-cured silicone and the remaining tubing types, BioPharm platinum-cured silicone and CFlex, both at 0.6×10^5mg.impact^{-1} was less significant. The best performer was Tygon, with a rate of 0.4×10^5mg.impact^{-1}, resulting in an almost 5.0-fold difference in monomer loss rate between Tygon and PharMed BPT.

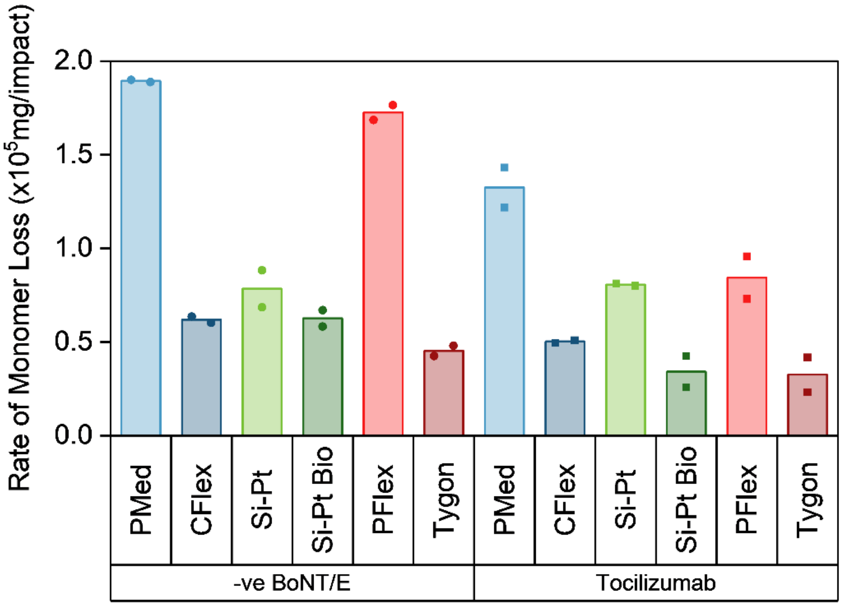

Figure 5-11 Rates of -ve BoNT/E and tocilizumab loss in the closed-loop peristaltic pump device using different tubing. Pump operated at 40RPM and 100% occlusion at 20°C for two hours using tubing: PharMed BPT (PMed), CFlex, Platinum-cured silicone, (Si-Pt), BioPharm Platinum-cured silicone (Si-Pt Bio), Puri-Flex (PFlex) and Tygon E-Lab (Tygon). Tocilizumab and -ve BoNT/E formulated at 0.4mg.ml^{-1} 0.1M sodium phosphate and 0.1M sodium chloride (pH 7.5). Monomer quanitified using SEC analysis. Duplicate data shown.

For tocilizumab (Figure 5-11), the worst-performing tubing was PharMed BPT, with a rate of 1.3x10^{5}mg.impact^{-1}, followed by Puri-Flex and Platinum-cured silicone at 0.8x10^{5}mg.impact^{-1}, representing a 1.6-fold difference. CFlex had a rate of 0.5x10^{5}mg.impact^{-1}, while the two best-performing tubing types were BioPharm platinum-cured silicone and Tygon, both at 0.3x10^{5}mg.impact^{-1}. The contrast in monomer loss rates between BioPharm platinum-cured silicone/Tygon and PharMed BPT was 4.0-fold, illustrating the significant impact of tubing choice on monomer loss.

It is noted that the rates of monomer loss during screening studies do not correlate with those coolant temperatures. This might suggest that aggregation mechanisms induced by heat may be effectively mitigated.

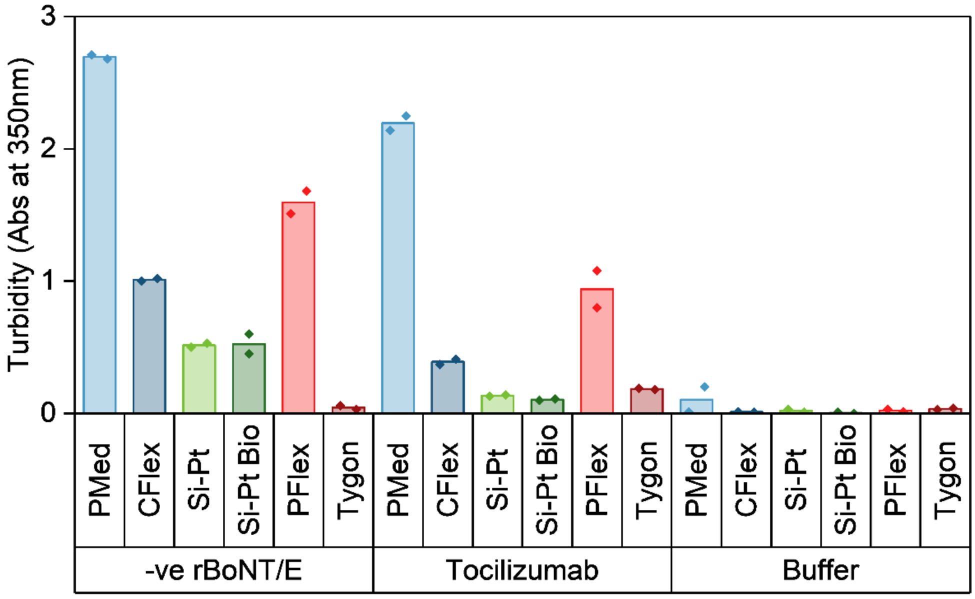

Figure 5-12 -veBoNT/E, tocilizumab and buffer turbidity in the closed-loop peristaltic pump device using different tubing. Pump operated at 40RPM and 100% occlusion at 20°C for two hours using tubing: PharMed BPT (PMed), CFlex, Platinum-cured silicone, (Si-Pt), BioPharm Platinum-cured silicone (Si-Pt Bio), Puri-Flex (PFlex) and Tygon E-Lab (Tygon). Tocilizumab and -ve BoNT/E formulated at 0.4mg.ml^{-1} 0.1M sodium phosphate and 0.1M sodium chloride (pH 7.5). Buffer matched the protein formulations. Turbidity quanitified using absorbance at 350nm. Duplicate data shown.

Figure 5-12 illustrates the apparent turbidity of samples following two hours of processing within the closed-loop device, employing various tubing types. While the extent of turbidity values varies depending on the model proteins studied, their relative performance somewhat aligns. PharMed BPT exhibited the highest observed turbidity for both model proteins, followed by Puri-Flex and CFlex. Platinum-cured silicone and BioPharm platinum-cured silicone tubing performed similarly, with Tygon being the best performer in minimising aggregation. This correlation between monomer loss rates and turbidity is evident, with Tygon and PharMed BPT being the best and worst tubing types for both aspects, respectively.

Spallation is a known phenomenon during peristaltic pumping and causes large particle to ‘spall’ off the tubing surfaces. (Barron *et al.*, 1986; Briceño and Runge, 1992) The extent of spallation is dependent on tubing type, pump speed and acceleration. (Her and Carpenter, 2020; Her *et al.*, 2020) Negative controls were conducted to assess any background effects, including spallation, on absorbance at 350nm, but the data indicated negligible effects (Figure 5-12). However, when these samples were subjected to nanoparticle tracking analysis, significant particle generation was observed with PharMed BPT, producing significant particles at concentrations of $20x10^6$particles.ml^{-1} (Figure 5-13). This value is 4.0-fold higher than that of the next tubing type Tygon at $4x10^6$particles.ml^{-1}.

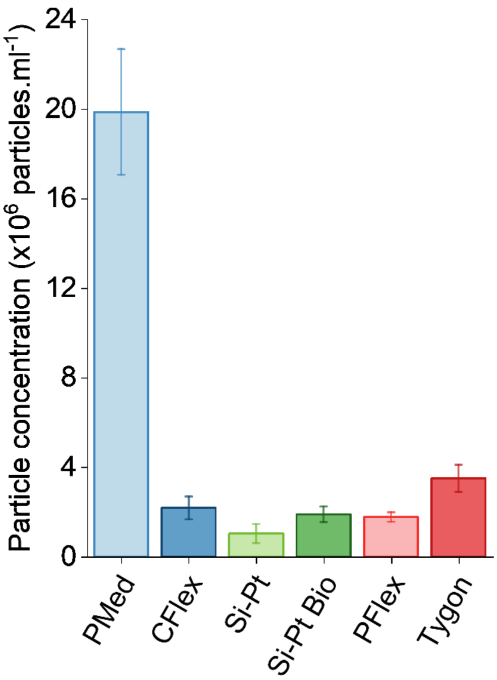

Figure 5-13 Spallation of nanometer and submicron foreign particles from different peristaltic tubing in the closed-loop peristaltic pump device when recirculating buffer solution only. Pump operated at 40RPM and 100% occlusion at 20^{o}C for two hours using tubing: PharMed BPT (PMed), CFlex, Platinum-cured silicone, (Si-Pt), BioPharm Platinum-cured silicone (Si-Pt Bio), Puri-Flex (PFlex) and Tygon E-Lab (Tygon). Mean data of technical triplcates (n=3) shown and error bars represent standard deviation (SD=1).

Presence of foreign nanoparticles can be a concern during processing. If not removed effectively they may clog equipment such as membrane pores and chromatography resin, and if not removed before fill and finish steps could inadvertently be administered to patients. PharMed BPT produced a significate number of foreign particles during processing which has been previously observed before. (Her and Carpenter, 2020) The screening study here shows the importance of making an informed decision on which tubing material to use during peristaltic pumping in bioprocessing. Avoidable consequences include product loses, aggregate formation and foreign particle introduction, the last two of which can impact critical quality attributes of drug products and risk the safety of patients.

5.4.6 Expansion-Relaxation of Peristaltic Tubing Solid-Liquid Interfaces Play a Minor Role in Therapeutic Protein Monomer Loss

The fundamental interactions that peristaltic rollers have on tubing are complex but can be distilled down to two primary mechanisms The first is expansion-relaxation of tubing solid-liquid interfaces, that may shed protein films in a similar manner to those relaxation-dilation of air-liquid interfaces. (Bee *et al.*, 2012; Koepf *et al.*, 2018) The second is solid-solid interface contact of the inner walls of peristaltic tubing, to disrupt protein films in a similar manner like friction, abrasion or grinding mechanisms (Sediq *et al.*, 2016; Gikanga *et al.*, 2017; Jing *et al.*, 2022) However, it is difficult to deconvolute the influence of these two mechanisms without the correct methodologies.

In Figure 5-2, a device was developed to repeatedly strain peristaltic pump tubing to simulate the expansion and relaxation of peristaltic tubing outside of the pumping apparatus – this is like that reported by Deiringer et al. (Deiringer and Friess, 2022a). This was done to determine if straining of the tubing plays a significant role in protein aggregation. In this study, only one model protein, -ve BoNT/E, was used, as it was previously shown to be prone to aggregation.

After subjecting CFlex tubing to 2,000 expansion-relaxation cycles with straining up to +20% of the tubing length, there was no significant difference in the monomer recovery of -ve BoNT/E between the strained and non-strained tubing (Figure 5-14). Monomer remaining was quantified at 96.7% for the strained tubing and 96.9% for the non-strained tubing. When PharMed BPT tubing was used and subjected to 2,000 expansion-relaxation cycles, there was also no notable difference in monomer recovery between the strained and non-strained tubing. Monomer remaining was quantified at 96.6% for the strained PharMed BPT tubing and 97.1% for the non-strained tubing.

However, when the total number of expansion-relaxation cycles was increased to 20,000, there was still no significant difference in monomer quantification between strained and non-strained CFlex tubing. Monomer remaining was 94.4% and 94.0% for non-strained and strained CFlex tubing, respectively. In the case of PharMed BPT tubing subjected to 20,000 expansion-relaxation cycles, there was a slight difference in monomer loss between the strained and non-strained tubing. The strained tubing had 2.3% more monomer loss, with 93.9% monomer remaining compared to 96.2% for the non-strained tubing.

These results suggest that, for CFlex tubing, repeated expansion and relaxation do not significantly impact protein aggregation, even at high cycle numbers. However, for PharMedBPT tubing, extended cycling may have a minor influence on monomer loss. The effect of tubing is also corroborated by the work of others where significant differences in subvisible protein particle concentrations were seen after straining different tubing types by +8.3% up to 2,000 times. We did not study which tubing materialistic properties caused this change, although it has been shown that a combination of tubing material composition and hardness influence protein particle formation (Deiringer and Friess, 2022b).

The extent of tubing strain induced by peristaltic pumping remains poorly understood. Manopoulos *et al*. highlight the current limitations in conducting computational fluid dynamics (CFD) simulations of peristaltic pumping, as there is currently no CFD code capable of accurately modelling fluid flow when tubing occlusion reaches or exceeds 100% (Manopoulos *et al.*, 2020; Manopoulos, Tsoukalis and Mathioulakis, 2022). As such as, the amount of tubing strain caused by roller compression and hydraulic power by fluid flow cannot be computed.

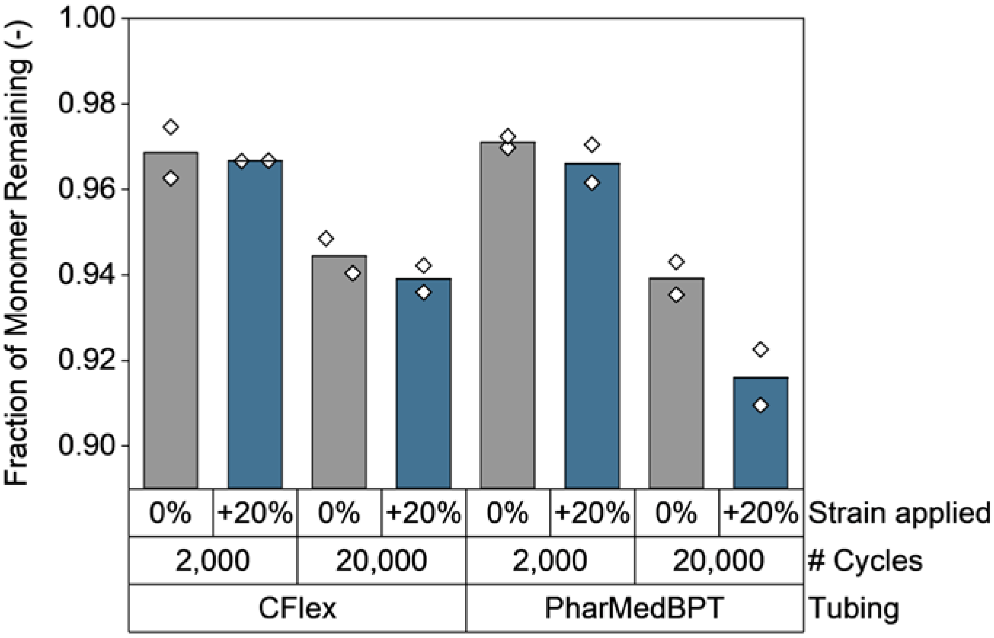

Figure 5-14 -ve BoNT/E loss during expansion-relaxation of peristlatic tubing solid-liquid interfaces. Strain at 20% applied to tubing (CFlex and PharMed BPT) either 2000 or 20000 times using a programmable syringe pump at room temperature. -ve BoNT/E formulated at 0.4mg.ml^{-1} 0.1M sodium phosphate and 0.1M sodium chloride (pH 7.5). Monomer quantified using SEC analysis. Duplicate data shown.

It worth noting that peristaltic rollers can freely rotate about their own axis during tubing compression which effectively reduces frictional forces (Manopoulos, Tsoukalis and Mathioulakis, 2022). This in turn mitigates the strain imposed on the peristaltic tubing and minimises expansion-relaxation of the tubing's solid-liquid interface.

5.4.7 Peristaltic Tubing Solid-Solid Interfacial Contact Can Cause Therapeutic Protein Monomer Loss

Figure 5-3 presents a novel device designed to isolate the impact of solid-solid interfacial contact on monomer loss, distinct from the effects seen within a peristaltic pump. This device enables controlled compressions on tubing to simulate occlusion while allowing for adjustments in the contact area. This approach incorporates elements from the closed-loop device (Figure 4-1) to focus on the impact of the solid-solid interface contact.

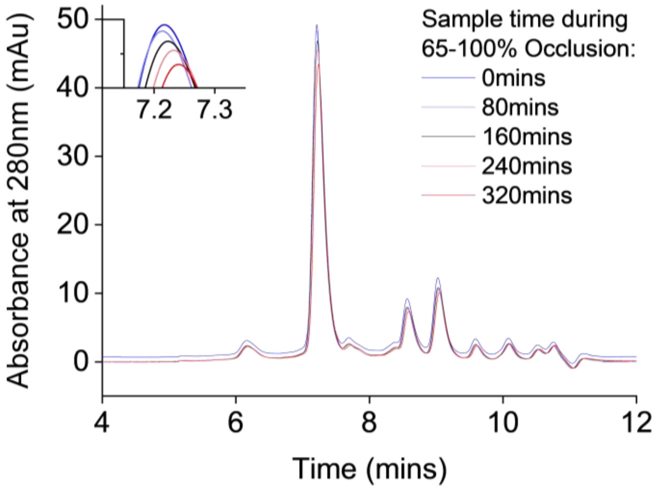

Figure 5-15 Size-exclusion chromatography analysis of -ve BoNT/E samples in solid-solid interface contact device. Samples taken at 0 (0), 80 (4000), 160 (8000), 240 (12000) and 320mins (16000 impacts) during 65-100% occlusion in the solid-solid interface contact device using 0.48cm^2 block. -ve BoNT/E formulated at 0.4mg.ml^{-1} 0.1M sodium phosphate and 0.1M sodium chloride (pH 7.5). CFlex tubing used. Duplicate data shown.

In Figure 5-15 SEC chromatograms of samples analysed after tubing occlusion within the range of 65-100% reveal a decrease in -ve BoNT/E monomer peaks, eluting at 7.4mins, at each time-point. Like previous chromatograms, no soluble low-molecular-weight or high-molecular-weight aggregates were detected.

Plotting the fraction of remaining monomer against the sampling time initially displays a lag-phase in monomer loss between 0 and 6000 impacts (Figure 5-16A). This initial variability may be attributed to low flow rates, which can result in inadequate internal mixing of the infused buffer within the device. However, after 6,000 impacts, the monomer loss data for higher occlusion ranges begins to diverge from the lower ranges, yielding clearer trends (Figure 5-16A). After finishing tubing occlusion, the fraction of remaining monomer consistently decreased, with values of 0.95, 0.94, 0.90, 0.90, and 0.89 observed at occlusion levels of 35%, 85%, 95%, 100%, and 105%, respectively. In a control study without occlusion, 0.96 of -ve BoNT/E monomer remained.

Linear regressions were conducted on the monomer fractions correlated against the number of impacts to determine the rates of monomer loss per impact of the occlusion block as shown in Figure 5-16B. While the data exhibited some noise, it was assumed to be linear from the fourth sample time-point, with an average adjusted R^2 value of 0.81. The rate of monomer loss per impact was obtained from the linear gradients and plotted against the upper limit of the respective occlusion ranges in Figure 5-16B.

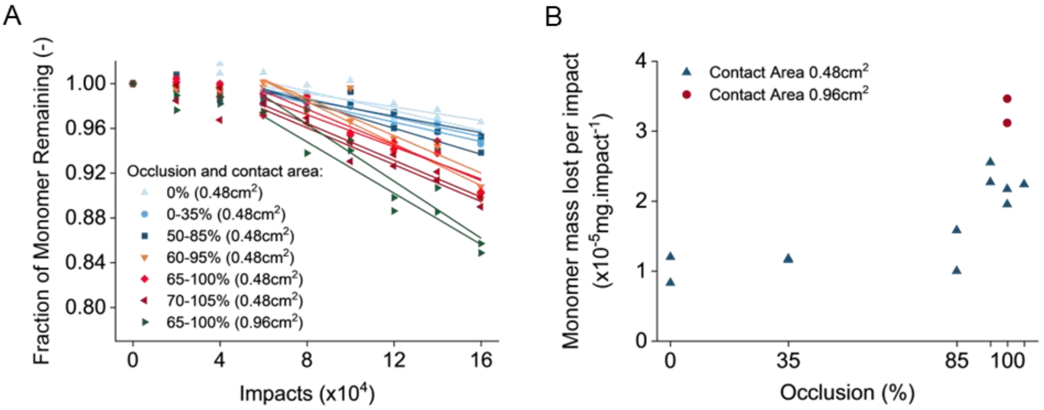

Figure 5-16 -ve BoNT/E loss in the solid-solid interface contact device. (A) -ve BoNT/E loss with linear regressions from fourth data point. (B) Rates of -ve BoNT/E loss per impact. Device operated using 0.48cm^2 block at 0, 0-35, 50-85, 60-95, 65-100, 70-105% occlusion and 0.96cm^2 block at 65-100% occlusion for a total of 16000 impacts using a programmable syringe pump. -ve BoNT/E formulated at 0.4mg.ml^{-1} 0.1M sodium phosphate and 0.1M sodium chloride (pH 7.5). CFlex tubing used. Monomer quantified using SEC analysis. Duplicate data shown.

In the control study with no occlusion (0% occlusion) (Figure 5-16B), where -ve BoNT/E was incubated in the apparatus, the observed monomer loss rate was 1.0x10^{-5}mg.impact^{-1}. When the tubing was occluded between 0-35% and 50-85%, it led to an increase in the rate of losses, resulting in rates of 1.2x10^{-5}mg.impact^{-1} and 1.3x10^{-5}mg.impact^{-1}, respectively. However, these rate of loss were not significantly greater than the control study indicating again that the expansion-relaxation of tubing solid-liquid interfaces does not contribute significantly to the overall aggregation mechanisms any more than adsorption-based losses.

Notably, a significant rise in the loss rates occurred when occluding the tubing between 60-95%, 65-100%, and 70-105%, with corresponding rates of 2.4x10^{-5}mg.impact^{-1}, 2.1x10^{-5}mg.impact^{-1}, and 2.2x10^{-5}mg.impact^{-1}. This notable increase in loss rates around the 100% occlusion mark could be attributed to solid-solid interface contact mechanisms. This inflection in rates of monomer loss at 100% occlusion mirrors the trends seen when changing occlusion using the closed-loop device in the peristaltic pump. This occurred when solid-solid interfaces of tubing walls began to contact thus causing the mechanical disruption of protein films on tubing walls.

5.4.8 Solid-solid Interfacial Contact is a Function of Area and Rates of Monomer Loss in an Isolated Mechanism Method are Comparable to Peristaltic Pumping

In the solid-solid interface contact study, where occlusion ranged from 65% to 100%, using an occlusion block double the length of the previous one resulted in a decrease in remaining monomer fractions from an average of 0.90% to 0.85% (Figure 5-16A). Consequently, the corresponding monomer loss rate increased from $2.1x10^{-5}$mg.impact^{-1} to $3.3x10^{-5}$mg.impact^{-1} (Figure 5-16B). Doubling the occlusion block size, and thereby doubling the contact area from 0.48cm^2 to 0.96cm^2, led to a 1.6-fold rate change.

The contact area that can be applied experimentally is limited here due to the solid-solid interface contact device design. In a peristaltic pump the contact length may be many times the length of the larger block we use due to the rotation of the pump head and rollers along the tubing. To compare the amount of monomer loss over different contact areas, rates were normalised to allow for a direct comparison. The normalised values of the 0.48cm^2 to 0.96cm^2 occluding tubing to 65% to 100% are $4.3x10^{-5}$mg.cm^{-2} and $3.4x10^{-5}$mg.cm^{-2}, respectively (Figure 5-17C).

We compared these rates to those obtained in our earlier accelerated protein aggregation studies using the peristaltic pump and closed-loop device. In a peristaltic pump, the contact area can be represented as a rectangle with a length equal to the roller's contact length on the tubing and a width equal to the tubing's inner diameter at 4.8mm. We estimated the roller length to be approximately 30mm based on wear from roller contact on the tubing itself. Assuming full contact along this length, we calculated a contact area of 1.44cm^2 per impact (Figure 5-17B).

At 40RPM, the rate of monomer loss per impact was previously determined to be 9.51x10^{-5}mg.impact^{-1}, accounting for four roller impacts per revolution. Thus, the corresponding rate of monomer loss normalised to area is 6.61x10^{-5}mg.cm^{-2} (Figure 5-17C). We selected 40RPM for comparison to minimise heat effects and potential spallation. A lower speed wasn't feasible as the pump couldn't maintain regular compressions at slower speeds. When comparing the normalised rates based on contact area between isolated occlusion and pumping studies, the difference in monomer loss per area in these two systems falls within a 1.5- to 1.9-fold range, with the peristaltic pump showing the faster rates (Figure 5-17C).

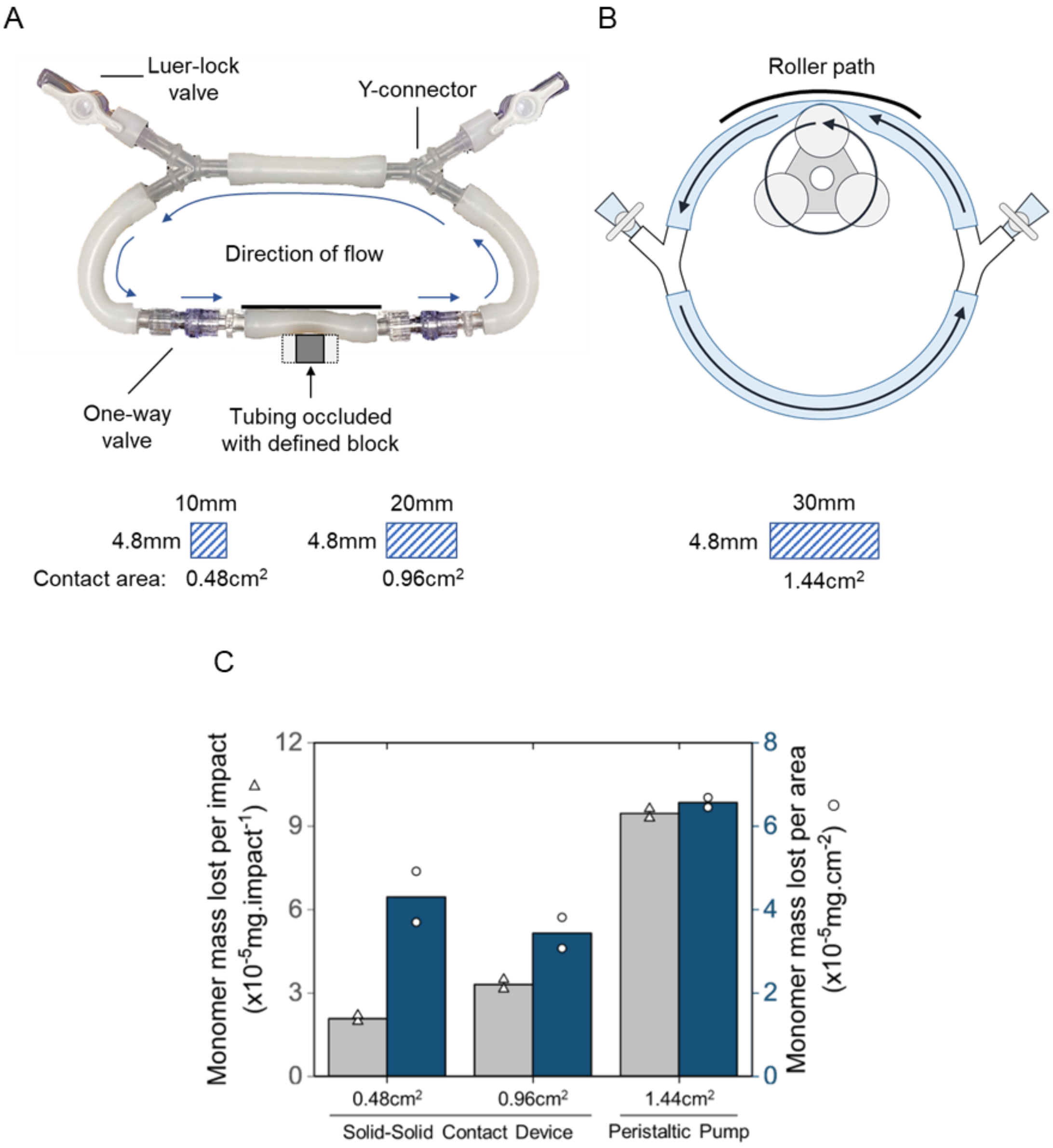

Figure 5-17 Comparison of rates of -ve BoNT/E loss per impact in solid-solid interface contact and closed-loop peristaltic pump devices. (A) Images of solid-solid interface contact device and block sizes (0.48cm^2 and 0.96cm^2) used. (B) Image of closed-loop peristaltic pump device and contact area (1.44cm^2) of the roller. (B) Comparison of rates per impact and normalised rates per contact area of -ve BoNT/E loss in the devices. -ve BoNT/E was formulated at 0.4mg.ml^{-1} 0.1M sodium phosphate and 0.1M sodium chloride (pH 7.5). Solid-solid interface contact device operated at 65-100% occlusion for 16000 impacts at room temprature. Peristaltic pump data conducted at 40RPM and 100% occlusion at 20^{o}C for two hours. CFlex tubing used. Monomer quantified using SEC analysis. Duplicate data shown.

Whilst these two methods subject tubing to occlusion, peristaltic pump rollers occlude tubing rotationally whilst our solid-solid contact method enacts conducts linear occlusion perpendicular to the tubing. Rotational impact during occlusion in the pump could provide additional friction, grinding or abrasion forces, like those reported in literature (Sediq *et al.*, 2016; Gikanga *et al.*, 2017; Jing *et al.*, 2022), to the tubing surface during contact that enhance protein layer disruption upon contact.

5.5 Conclusion

In this chapter, various mechanisms contributing to protein aggregation during peristaltic pumping have been explored. While heat generation plays a role, its impact is relatively minor compared to other mechanisms. Heat is primarily generated by frictional forces between rollers and tubing, and variations in process parameters can influence the heat produced.

Pump speed exhibits an inverse relationship with monomer loss rates. Reducing speed by four-fold increases monomer loss rates by 1.8- to 2.4-fold. Slower pump speeds provide more time for processes like protein adsorption, film renewal, and protein-protein interactions at tubing wall contact points. Occlusion, indicating the degree of tubing compression, triggers an immediate 20-30% monomer loss as tubing walls make contact at 100% occlusion, suggesting changes in underlying mechanisms or abrasion at tubing interfaces.

Our study revealed that different types of peristaltic tubing can significantly affect monomer loss and foreign particle generation. Some tubing types caused up to five-fold more monomer loss and four-fold more foreign particles via spallation compared to the best-performing tubing. This highlights the importance of considering tubing choice in process development to impact bioprocessing yields and product quality.

Strain on peristaltic pumping was isolated via a device expanding and relaxing tubing but was found to cause minor monomer losses. However, tubing material can influence the extent of these losses. In addition to strain, compression of tubing can drive the contact of peristaltic tubing inner walls. By, isolating solid-solid interface contact in another isolation device, monomer loss was observed to be a function of the contact area. Comparing rates of monomer loss to pumping showed higher losses in the pump which may be attributed to the rotating rollers causing friction, abrasion or grinding of interfaces during contact enhancing monomer loss during solid-solid interface contact.

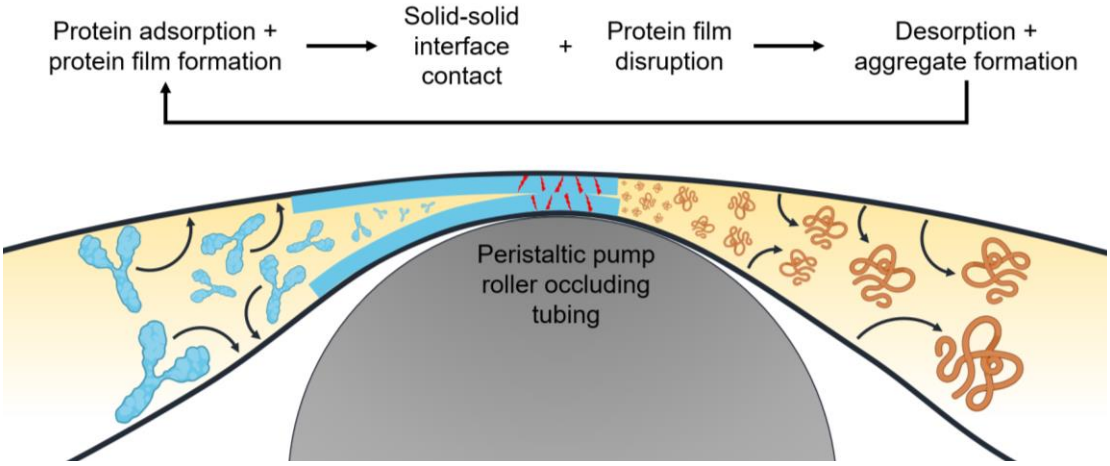

Figure 5-18 Illustration of solid-solid interface contact of peristlatic tubing causing aggregation during peristaltic pumping. Proteins adsorb to solid-liquid interfaces prior to occlusion which then causes inner wall interface to contact (solid-solid interface contact), disrupting protein layers and causing aggregate formation.

Considering that protein film adsorption and disruption are synergistic processes, surfactants could be employed to reduce monomer loss and aggregation. Whilst their effect is not discussed in this study, previous research indicates that surfactants can decrease monomer loss and protein particle formation. (Biddlecombe *et al.*, 2009; Daniel J. Callahan, Stanley and Li, 2014; Sediq *et al.*, 2016; Her *et al.*, 2020; Wu and Randolph, 2020; Deiringer and Friess, 2022a) Thus, preventing the establishment of a protein film on tubing interfaces can limit the disruption caused by solid-solid interface contact. However, Rafferty *et al*. (2017) noted that the addition of surfactants can pose challenges in controlling tangential flow filtration (TFF) diafiltration operations. These challenges arise from the inconsistent filtration of surfactant sizes, which can exist in monomer, micelle, or larger non-spherical micelle forms, as well as interactions between proteins and surfactants that can hinder separation via TFF (Rafferty *et al.*, 2017).

In conclusion, our findings suggest that the solid-solid contact mechanism is the primary driver of protein aggregation during peristaltic pumping. An illustration of this process can be seen in Figure 5-18. This mechanism disrupts protein films, releasing protein aggregates and allowing for the reconstitution of these films, creating a cycle that poses a significant challenge in peristaltic pump applications.

6 Thesis Conclusion

The thesis aimed to uncover the fundamental mechanism responsible for protein aggregation during peristaltic pumping. Initially, we sought to establish a baseline understanding of the stability of endopeptidase-negative botulinum neurotoxin serotype-E (-ve BoNT/E) when exposed to hydrodynamic flow and shear forces. Subsequently, we conducted a comparative study to assess the device's capacity to replicate protein aggregation under varying physiochemical conditions within a novel scale-down peristaltic pumping device. Lastly, our investigation delved into the exploration of pumping parameters and the development of innovative devices, ultimately leading us to the conclusion that the primary driver of protein aggregation lies in the solid-solid contact between the inner tubing walls during tubing occlusion by the peristaltic pump. This continuous contact disrupts the adsorbed protein layer, perpetuating a cycle of reabsorption processes during pump operation.

In Chapter 3, we conducted in-depth computational fluid dynamics (CFD) simulations to enhance our understanding of hydrodynamic flow and shear rates within the spinning disc ultra-scale-down device during its operation. By subjecting -ve BoNT/E to various shear rates, we established a foundational comprehension of its stability under shear conditions. Notably, our findings challenged previous assumptions regarding the correlation between protein decay coefficients and shear, revealing a shift from second-order behaviour, as previously documented (Biddlecombe *et al.*, 2007) to a first-order linear relationship.

Furthermore, when we correlated decay coefficients with turbulence, we observed an exponential-like relationship that rapidly accelerated during turbulent-flow regimes. This underscores the susceptibility of -ve BoNT/E stability to hydrodynamic flow and shear conditions, especially within turbulent environments characterised by heightened mass transfer rates, facilitating protein-protein and protein-interface interactions, as well as the presence of Kolmogorov-scale eddies. Although the influence of eddies on subvisible particle formation remains inconclusive, the possibility of interactions between these eddies, owing to their comparable sizes, warrants further investigation.

In Chapter 4, we conducted a comparative study between the spinning disc device and a novel scaled-down device, the closed-loop peristaltic pump device, using -ve BoNT/E under various physiochemical conditions. Our objective was to ascertain whether the spinning disc device could effectively serve as an ultra-scale-down tool to replicate protein aggregation mechanisms encountered during peristaltic pumping. As we explored changes in buffer conditions, we arrived at the conclusion that fundamental disparities in the material composition of both devices dictated the underlying forces governing protein adsorption to interfaces and subsequent aggregation. Specifically, electrostatic attraction predominated in the stainless-steel spinning disc device, while hydrophobic attraction was the driving force in the peristaltic pump device. These alterations in protein stability and aggregation patterns align with prior literature reports (Biddlecombe *et al.*, 2009; Deiringer and Friess, 2022a).

At a macroscopic level, these distinctions extended to the morphologies of subvisible particles, known to adopt various shapes depending on the initial stress conditions experienced by the native protein (Witeof *et al.*, 2021; Greenblott *et al.*, 2022; Thite *et al.*, 2022). Thus, our investigation prompted further exploration into understanding how peristaltic pump parameters influence protein aggregation.

Furthermore, in Chapter 4, we conducted thermal stability analysis of -ve BoNT/E under varying buffer conditions and compared the results with existing conformational stability data. Interestingly, we observed insignificant changes in the apparent melting temperatures of -ve BoNT/E in different buffers. However, the aggregation temperature exhibited notable variations. Specifically, the aggregation temperature decreased notably under lower pH and ionic strength conditions, aligning with available molecular dynamics data that reported a reduction in salt bridges and an increase in solvent-accessible surface area (SASA) under similar circumstances (Lalaurie *et al.*, 2022).

These structural alterations can potentially expose hydrophobic regions within a protein's structure, which is concomitant with protein aggregation (Codina *et al.*, 2019), This observation is in concurrence with the trends observed in protein decay coefficients and particle formation during the processing of -ve BoNT/E in both the spinning disc and peristaltic pump devices. Consequently, our findings underscore the profound impact of buffer conditions, commonly encountered during the bioprocessing of -ve BoNT/E, when exposed to hydrodynamic flow and shear forces, on its stability.

Lastly, in Chapter 5, the closed-loop peristaltic pump device was further used to evaluate how peristaltic parameters affected protein aggregation. investigating the impact of peristaltic parameters on protein aggregation.

Notably, we observed an inverse relationship between pump speed and the rate of monomer loss per roller occlusion, suggesting a synergistic effect arising from the interplay between protein adsorption and disruption of protein layers. This phenomenon extended to the formation of protein particles, as similarly concluded (Deiringer and Friess, 2022a).

Our examination of occlusion uncovered a critical threshold, where increased occlusion resulted in the sudden increase in rates of monomer loss due to the contact between the inner tubing walls. Additionally, the screening of different tubing materials emphasised the role of interfaces in driving protein aggregation and the generation of extrinsic foreign particles. Consequently, these findings underscore the need to consider interfaces during the stages of process development.

To further pinpoint the primary mechanism responsible for monomer loss, we designed novel devices specifically aimed at isolating peristaltic expansion-relaxation of solid-liquid interfaces and solid-solid interface contact. Our investigations unequivocally pointed towards the contact of inner tubing walls as the predominant mechanism, contingent on the surface area over which this contact occurs.

In conclusion, this thesis has provided insights into mechanisms of protein aggregation during peristaltic pumping. Through comparative studies between different devices and thermal stability analyses, we have unravelled the critical factors driving protein aggregation of -ve BoNT/E. Our findings shed light on the pivotal role of buffer conditions, surface interfaces, and peristaltic parameters in influencing protein stability. Understanding these mechanisms is paramount for improving bioprocessing and ensuring the production of safe and effective biologics. This research paves the way for more precise process development and underscores the significance of considering these factors in industrial and academic settings alike.

7 Future Work

Process development is an important method to help improve the manufacturing efficiency and yields but to also continue to innovate in manufacturing technology. This process is costly, expensive and resource intensive. Scaled-down tools at the bench scale are often developed to mimic large-scale processes to reduce those burdens in process development. This chapter considers validation of protein aggregation mechanisms in other botulinum neurotoxin serotypes, designing an analytical platform for high-throughput particle quantification with machine learning analysis and modifications to the spinning disc device and solid-solid interface contact device.

7.1 Validate monomer loss data against an the toxic BoNT/E variant and other serotypes (/A) for similar mechanisms.

Botulinum neurotoxin serotype-E (BoNT/E) is just one of several naturally occurring botulinum neurotoxins (BoNTs). The most commercially significant BoNT is serotype-A, which serves as the primary active pharmaceutical ingredient in three of the largest BoNT-based drugs on the market—abobotulinumtoxinA, incobotulinumtoxinA, and onabotulinumtoxinA. These drugs are collectively approved to treat 20 different medical indications. However, BoNT/E is not currently used clinically.

Comparing the stability of BoNT/A against BoNT/E through the spinning disc device or peristaltic pump could aid in the process development botulinum neurotoxins and potentially reveal stability similarities among different serotypes. This knowledge would be instrumental in predicting the stability of forthcoming commercialised serotypes. However, it's essential to acknowledge that handling toxin materials requires close collaboration under industrial and academic partners possessing the expertise to train investigators and ensure the safe conduct of experiments.

7.2 Spinning Disc Device: Modifications to Improve its Suitability as a Peristaltic Pump Mimic

The spinning disc device is an example of a scaled-down model utilised for investigating monomer loss and protein aggregation under conditions of high hydrodynamic flow and shear stress. Its design serves to reduce the quantities of biologic materials required for process development and allows for the timely retrieval of samples suitable for various low-volume analytical techniques. However, the differences in materials between the spinning disc and the closed-loop peristaltic pump device result in varying protein decay coefficients and particle concentrations observed under different buffer conditions.

It is well-established that materials can impact rates of protein aggregation. For instance, different disc coatings in the spinning device have been shown to affect protein decay coefficients (Biddlecombe, 2009) and various types of peristaltic tubing can influence protein decay coefficients and protein aggregation, as demonstrated in Chapter 4, and as reported in the literature (Her *et al.*, 2020; Deiringer and Friess, 2022b; Fanthom *et al.*, 2023). In one notable observation, tubing material affected the performance of tangential flow filtration by reducing flux and fouling the membrane (Deiringer, Leitner and Friess, 2023).

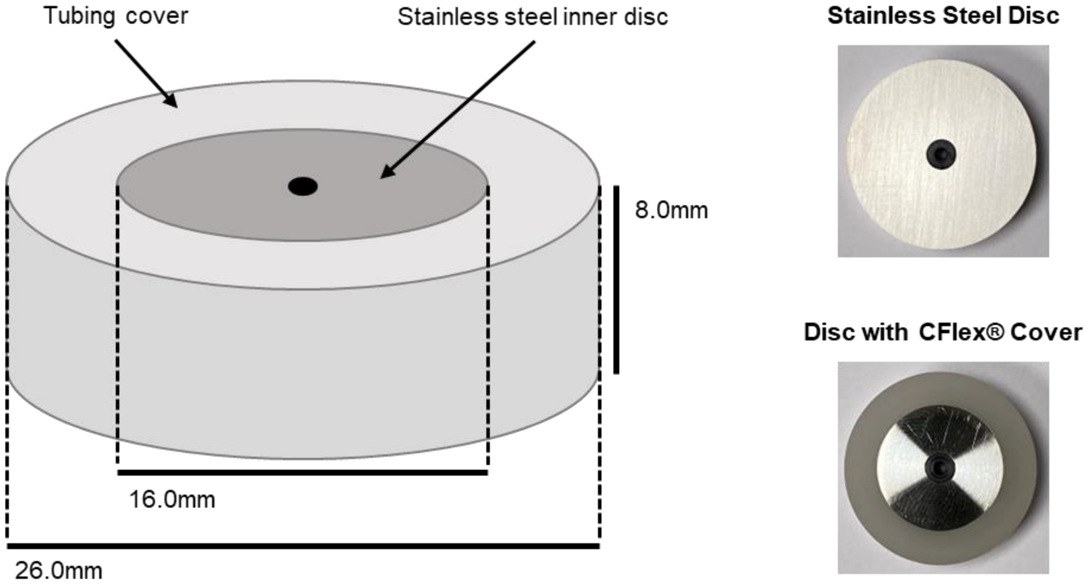

Figure 7-1 Design and images of a prototype disc covered with peristlatic tubing for use with the spinning disc device. Tubing coverage is 80% of the total disc surface area. Comparison images of the stainless steel disc (top right) with no tubing cover and a modified disc (bottom right) with a CFlex tubing cover.

To address these material considerations, a prototype disc was created, which could be covered with tubing (specifically, Masterflex L/S 89 tubing). Figure 7-1 illustrates the final design of this prototype, which consist of a combination of stainless steel and peristaltic tubing. The internal cylinder of the disc is constructed from stainless steel to securely house the magnets needed to drive the disc's rotation. The remaining 80% of the outer surface area is composed of tubing material. Importantly, the placement of the tubing material is concentrated in areas of the disc predicted to experience the highest shear and turbulence, as determined by computational fluid dynamics (CFD) simulations presented in Chapter 3. Additionally, the identical dimensions of this new disc avoid the need for new CFD simulations to predict the shear rates generated during its rotation.

7.3 Improved Solid-Solid Interface Contact Device

The first solid-solid interfacial contact device showed that the solid-solid interface contact of inner tubing walls leads to monomer loss as a function of the contact area – when the contact area doubled, rate of monomer loss increased 1.6-fold. It is thought that this occurs due to a continuous cycle of mechanical disruption and absorption of monomer to re-establish disrupted protein layers. Whilst this device was adept at controlling the compressions to make contacts, at its fastest contact rate, it was 2.6-fold slower at approximately 1 contact per second compared to the slowest steady pump speed at 40RPM. This had an impact on experiment times as well which could last as long as five hours per sample making investigation time consuming.

To add further, data point reflecting the remaining monomer during processing could be erratic making interpretation of trends difficult. These issues were primarily a results of the limitations of the syringe pump programmed to actuate the occlusion of tubing which is not its intended purpose.

A characteristic curve of monomer loss observed during processing in the closed-loop peristaltic pumping device was a polynomial relationship, where increasing pump speeds reduced the rate of monomer loss until a point where it appeared to plateau. At the plateau, the rate of pump speed may inhibit protein layer establishment on the tubing wall. To replicate this plateau and create a mimic of peristaltic pumping, a new actuator that can occlude tubing and control solid-solid interface contacts within rates comparable to peristaltic pumping should be used.

7.4 Particle analysis platform: Deployment of Deep Learning Techniques and High-throughput Particle Analysis

Analysis of particles during research can be challenging due to the range of sizes they can be. Development of a rapid particle analysis platform that can perform high-throughput analysis of low-volume samples in a 96-well plate formats would improve process workflow. Consideration of this would also benefit investigations into hydrodynamic flow, shear and Kolmogorov eddies on protein aggregation that produce submicron particles undetectable by size-exclusion chromatography and backgrounded membrane imaging.

Further, the deployment of deep learning algorithms to analyse particle observed forming during bioprocessing is becoming more common. (Witeof *et al.*, 2021; Greenblott *et al.*, 2022; Thite *et al.*, 2022; Salami *et al.*, 2023) These tools have the capability to extract features from a library of particles formed under various known process stresses, such as pH fluctuations, peristaltic pumping, freeze-thaw cycles, and more. This extraction results in unique identifiers or 'fingerprints.' Once these fingerprints are established, unidentified particles can be compared to identify the most likely stressor that caused their formation.

In the research described in this thesis, particularly in Chapters 3 and 4, we created a library of images using backgrounded membrane imaging. These images captured particles formed during processing in both the spinning disc and closed-loop peristaltic pump devices under different buffer conditions. Deep learning tools can be employed here to gain deeper insights into the morphologies of these particles produced by each respective device.

Furthermore, deep learning can be applied alongside the spinning disc device, closed-loop peristaltic pump device, solid-liquid interface expansion-relaxation device, and solid-solid interface contact device to compare the particles they generate. This comparison can lead to conclusions regarding the primary mechanism of peristaltic pumping based on the unique particle 'fingerprints' detected. Backgrounded membrane imaging (BMI) has proven to be a valuable tool for imaging particles, especially when used in conjunction with the mentioned devices, allowing for the analysis of small sample volumes during processing to track the evolution of particles over time.

8 Validation

8.1 Regulatory Guidance on Scale-down Models and Bioprocess Validation

Process development is essential for establishing consistent and robust manufacturing processes, facilitating continuous improvement, and ensure the production safe and efficacious therapeutic biologics. However, large-scale process development efforts are often resource, time, and cost-intensive. As a result, scale-down tools are frequently developed to streamline these endeavours allowing for practical investigative studies in process development, characterisation, and validation. These tools support innovation and expedite the knowledge acquisition process for scientists engaged in process development mitigating inherent risks associated with bioprocess development and expedite the time-to-market for novel therapeutics.

Regulatory authorities recognise the significance of scale-down models as techniques that can significantly enhance the process development. The International Council for Harmonisation of Technical Requirements for Registration of Pharmaceuticals for Human Use (ICH) document Q11 (European Medicines Agency (EMA), 2013) serves as the primary international regulatory guidance for scale-down models. Under this guidance, validation packages are expected to provide data from studies justifying the scalability of the model and its representativeness of the commercial process. These studies should validate the scale-down model's capability to deliver performance equivalent to the commercial-scale in removing process- and product-related impurities and viral safety evaluation, as mandated by ICH

Q6B and ICH Q5A, respectively (European Medicines Agency (EMA), 2000, 2022).

While process validation is a prerequisite before submitting an obtaining marketing authorisation, continuous process validation is indispensable throughout the product's lifecycle. This ensures that the product consistently meets all critical quality attributes (CQAs) and verifies the validation of any revised or modernised manufacturing techniques, assays, or material changes that replace outdated technologies while continuing to maintain product CQAs.

8.2 Case Study: Implementing New Process Understanding from the Closed-loop Peristaltic Pump Device into Manufacturing

This thesis explores the utilisation of a scaled-down model, specifically the closed-loop peristaltic pump device. The study reveals that various pump parameters, including pump speed, occlusion, and tubing selection, can significantly impact process yields, as well as the presence of product-related impurities such as protein aggregation and process-related impurities such as tubing particles (due to spallation) during pump operation. However, these effects have not been validated in a full-scale tangential flow filtration (TFF) process.

One notable outcome of using is scale-down model was the examination of different tubing (elastomer materials) and how changing tubing can influence CQAs, such as protein aggregates and foreign particles. Typically, the choice of tubing material can depend on the suitable processing application and specific material qualification requirements. For instance, elastomer materials employed in the bioprocessing of therapeutic biologics must undergo biocompatibility testing to ensure patient safety in case any toxic compounds leach out of the material during use.

The United States Pharmacopeia and National Formulary (USP-NF) provides distinct classifications of elastomer materials, ranging from Class I to VI. Class VI signifies the most stringent level of material qualification for biological compatibility, involving in vivo biological reactivity tests in accordance with USP <88> (United States Pharmacopeia, 2023). Typically, material manufacturers are responsible for conducting these tests, but biopharmaceutical manufacturers should select compendial materials that have already received acceptance for pharmaceutical manufacturing purposes, particularly those falling under Class VI.

The biopharmaceutical company bears the responsibility of validating the process, according to ICH Q11 and following ICH Q6B and Q5A, and any changes made post-authorisation. It is crucial to recognise that altering tubing material can significantly impact critical process parameters (CPP) during tangential flow filtration (TFF), specifically parameters like flux (Deiringer, Leitner and Friess, 2023), Moreover, the significance of flux as a CPP with a high potential to affect CQAs has been emphasised in a Quality by Design (QbD) study (Wee *et al.*, 2020). Consequently, tubing material should be regarded as a CPP in TFF processes that use peristaltic pumps during early process development.

Post-authorisation process variations follow the guidelines in ICH Q12 (European Medicines Agency (EMA), 2020). These variations are classified by the EMA, for example, based on their potential impact on product safety and efficacy. Type IA variations, having no significant impact, employ a "do and tell" approach, allowing the pharmaceutical manufacturer to implement changes and subsequently inform regulatory authorities. Conversely, Type IB and Type II variations require a "tell and do" approach, necessitating regulatory approval before changes can be implemented due to their potential impact on product safety. However, it's unlikely that changing compendial tubing during TFF would fall under the latter variations.

9 Appendix

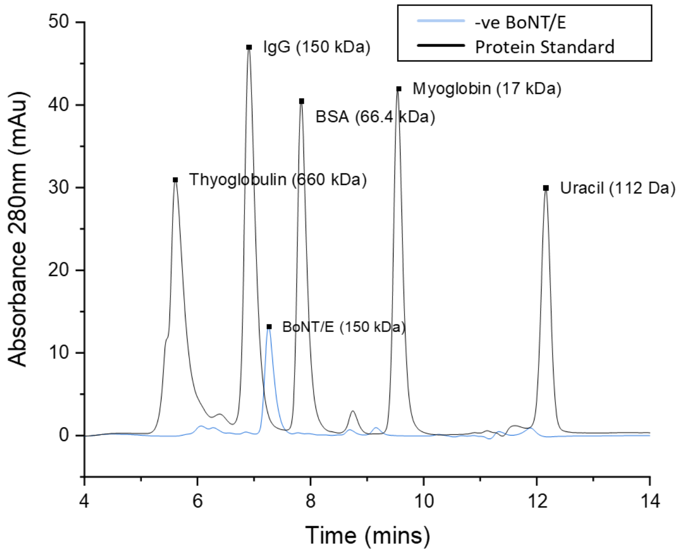

Figure 9-1 Size-exclusion chromatography analysis of a protein standard and endopeptidase negative botulinum neurotoxin serotype-E sample.10μL of sample was injected into the Acquity UPLC BEH SEC with BEH SEC guard column and analysis performed at 0.2ml.min^{-1} of 100mM L-arginine hydrochlordie 50mM sodium phostphate and 100mM sodium chloride (pH7.0)

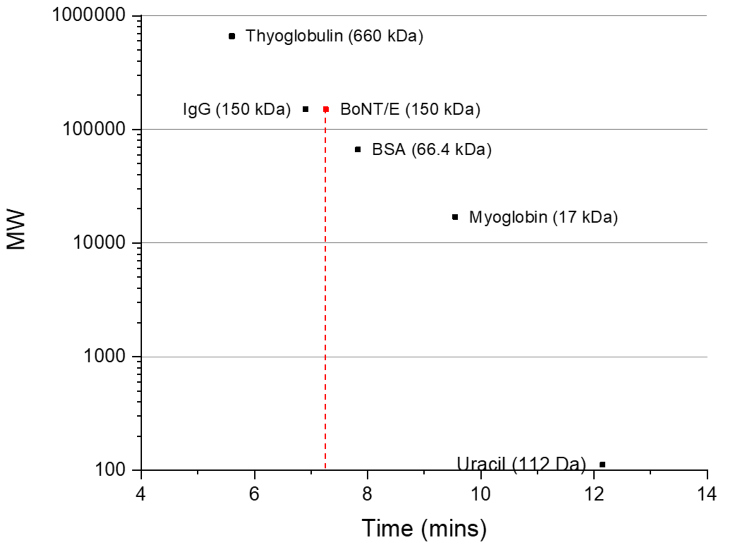

Figure 9-2 Size-exclusion chromatography calibration showing the correlation between entity molecular weight (MW) against elution time (mins).

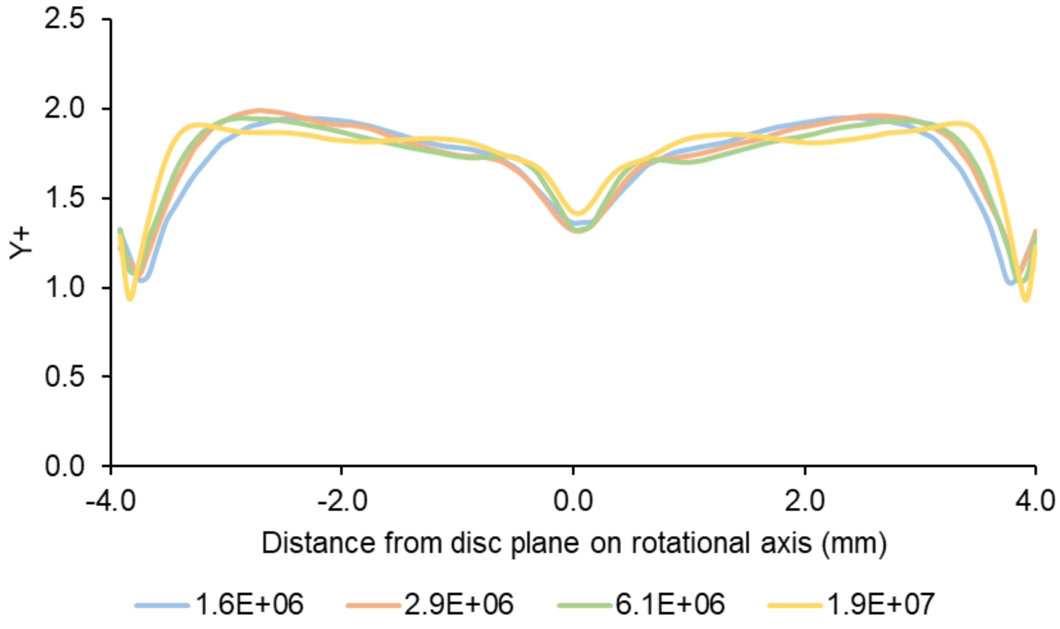

Figure 9-3 Changes in Y+ values across the disc outer edge obtained after computational fluid dynamic simulations of the spinning disc device at different mesh element counts.

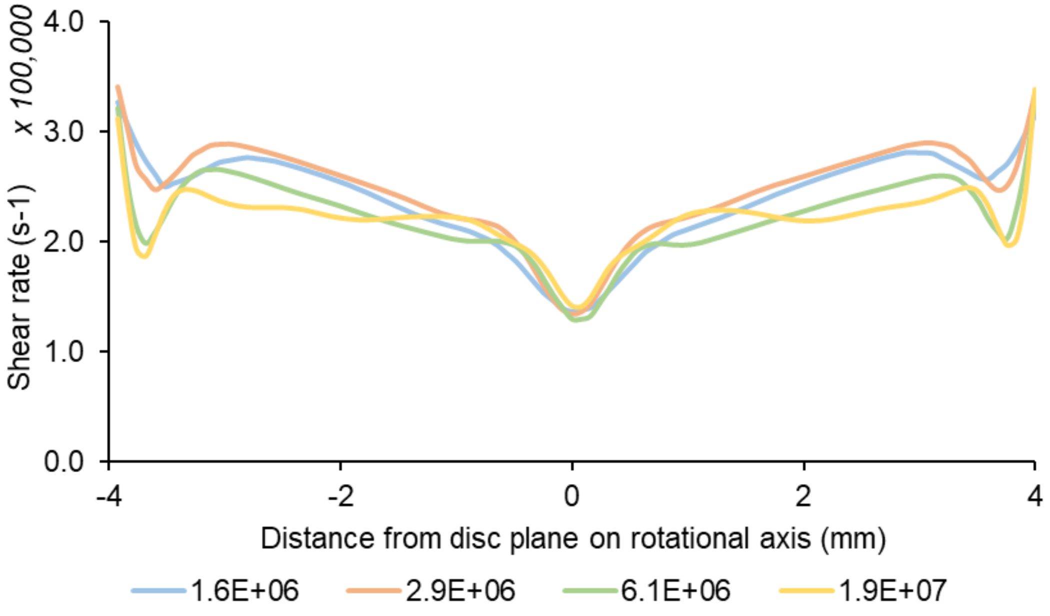

Figure 9-4 Changes in shear rate (s^{-1}) across the disc outer edge at first cell height obtained after computational fluid dynamic simulations of the spinning disc device at different mesh element counts.

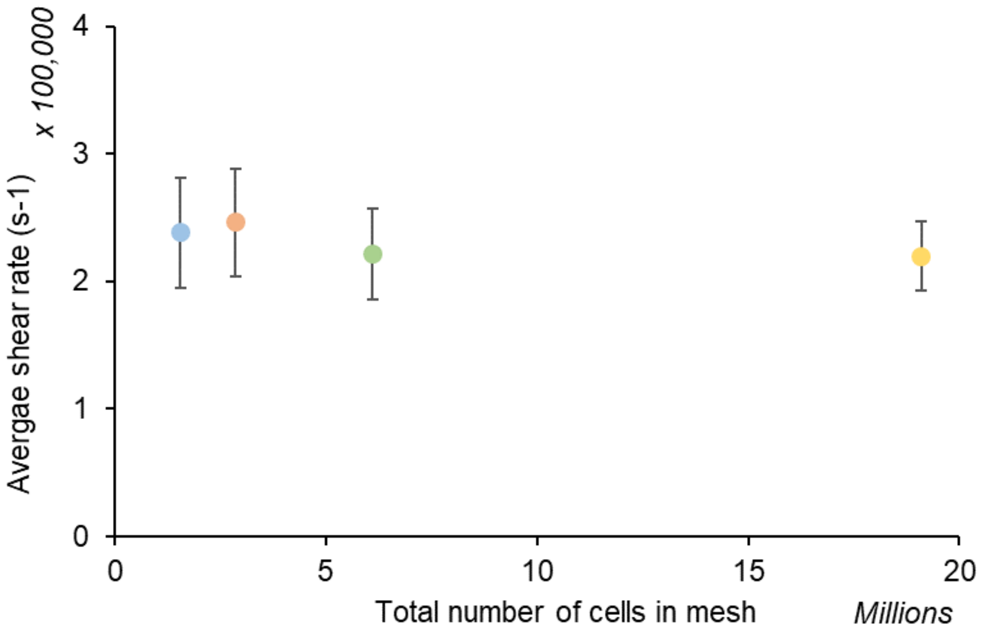

Figure 9-5 Correlation of mean shear rates (s^{-1}) across the disc outer edge at first cell height obtained after computational fluid dynamic simulations of the spinning disc device at different mesh element counts.

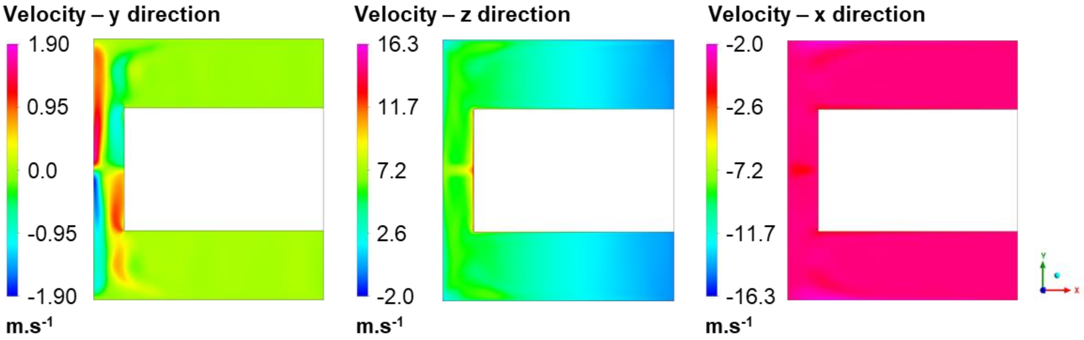

Figure 9-6 Directional (y, z and x) velocity ($m.s^{-1}$) of fluid inside the spinning disc device simulated at a disc rotational speed of 12000 RPM. Mesh size used was 6 million elements and analysis iterated 200 times and converging within a residual error of $1x10^{-4}$ s^{-1} and conservation error of 0.01

10 Bibliography

Al-Ghobashy, M.A. *et al.* (2017) ‘Correlation between Dynamic Light Scattering and Size Exclusion High Performance Liquid Chromatography for Monitoring the Effect of pH on Stability of Biopharmaceuticals’, *Journal of Chromatography B*, 1060, pp. 1–9. Available at: https://doi.org/https://doi.org/10.1016/j.jchromb.2017.05.029.

Amin, S. *et al.* (2014) ‘Protein aggregation, particle formation, characterization & rheology’, *Current Opinion in Colloid and Interface Science*, 19(5), pp. 438–449. Available at: https://doi.org/10.1016/j.cocis.2014.10.002.

Andrews, J.M. and Roberts, C.J. (2007) ‘A Lumry-Eyring nucleated polymerization model of protein aggregation kinetics: 1. Aggregation with pre-equilibrated unfolding’, *Journal of Physical Chemistry B*, 111(27), pp. 7897–7913. Available at: https://doi.org/10.1021/jp070212j.

Arunkumar, A. *et al.* (2016) ‘Effect of channel-induced shear on biologics during ultrafiltration/diafiltration (UF/DF)’, *Journal of Membrane Science*, 514, pp. 671–683. Available at: https://doi.org/10.1016/j.memsci.2016.05.031.

Avila-Sierra, A., Zhang, Z.J. and Fryer, P.J. (2019) ‘Effect of surface characteristics on cleaning performance for CIP system in food processing’, *Energy Procedia*, 161, pp. 115–122. Available at: https://doi.org/10.1016/j.egypro.2019.02.067.

Ávila-Sierra, A., Zhang, Z.J. and Fryer, P.J. (2021) ‘Effect of surface roughness and temperature on stainless steel - Whey protein interfacial interactions under pasteurisation conditions', *Journal of Food Engineering*, 301, p. 110542. Available at: https://doi.org/10.1016/j.jfoodeng.2021.110542.

Bahal, S.M. and Romansky, J.M. (2002) 'Spalling and Sorption of Tubing for Peristaltic Pumps', *Pharmaceutical Development and Technology*, 7(3), pp. 317–323. Available at: https://doi.org/10.1081/PDT-120005728.

Bai, S. *et al.* (2011) 'Aggregation of recombinant human botulinum protein antigen serotype c in varying solution conditions: Implications of conformational stability for aggregation kinetics', *Journal of Pharmaceutical Sciences*, 100(3), pp. 836–848. Available at: https://doi.org/10.1002/jps.22345.

Bam, N.B. (1998) 'Tween protects recombinant human growth hormone against agitation-induced damage via hydrophobie interactions', *Journal of Pharmaceutical Sciences*, 87(12), pp. 1554–1559. Available at: https://doi.org/10.1021/js980175v.

Banks, D.D. *et al.* (2012) 'Native-state solubility and transfer free energy as predictive tools for selecting excipients to include in protein formulation development studies', *Journal of Pharmaceutical Sciences*, 101(8), pp. 2720–2732. Available at: https://doi.org/10.1002/jps.23219.

Barron, D. *et al.* (1986) 'Particle Spallation Induced by Blood Pumps in Hemodialysis Tubing Sets', *Artificial Organs*, 10(3), pp. 226–235. Available at: https://doi.org/10.1111/j.1525-1594.1986.tb02551.x.

Bee, J.S., Chiu, D., *et al.* (2009) 'Monoclonal antibody interactions with micro- and nanoparticles: Adsorption, aggregation, and accelerated stress studies', *Journal of Pharmaceutical Sciences*, 98(9), pp. 3218–3238. Available at: https://doi.org/10.1002/jps.21768.

Bee, J.S., Stevenson, J.L., *et al.* (2009) 'Response of a concentrated monoclonal antibody formulation to high shear', *Biotechnology and Bioengineering*, 103(5), pp. 936–943. Available at: https://doi.org/10.1002/bit.22336.

Bee, J.S. *et al.* (2010) 'Aggregation of a monoclonal antibody induced by adsorption to stainless steel', *Biotechnology and Bioengineering*, 105(1), pp. 121–129. Available at: https://doi.org/10.1002/bit.22525.

Bee, J.S. *et al.* (2012) 'Production of particles of therapeutic proteins at the air-water interface during compression/dilation cycles', *Soft Matter*, 8(40), pp. 10329–10335. Available at: https://doi.org/10.1039/c2sm26184g.

Bekard, I.B. *et al.* (2011) 'The effects of shear flow on protein structure and function', *Biopolymers*, pp. 733–745. Available at: https://doi.org/10.1002/bip.21646.

Bergfreund, J., Bertsch, P. and Fischer, P. (2021) 'Adsorption of proteins to fluid interfaces: Role of the hydrophobic subphase', *Journal of Colloid and Interface Science*, 584, pp. 411–417. Available at: https://doi.org/10.1016/j.jcis.2020.09.118.

Berrill, A., Biddlecombe, J. and Bracewell, D. (2011) 'Product Quality During Manufacture and Supply', *Peptide and Protein Delivery*, pp. 313–339. Available at: https://doi.org/10.1016/B978-0-12-384935-9.10013-6.

Biddlecombe, J. (2009) *Antibody stability in bioprocessing focusing on shear effects at solid-liquid interfaces*, *University College London*. University College London. Available at: http://eprints.ucl.ac.uk/18499/.

Biddlecombe, J.G. *et al.* (2007) ‘Determining antibody stability: Creation of solid - Liquid interfacial effects within a high shear environment’, *Biotechnology Progress*, 23(5), pp. 1218–1222. Available at: https://doi.org/10.1021/bp0701261.

Biddlecombe, J.G. *et al.* (2009) ‘Factors influencing antibody stability at solid-liquid interfaces in a high shear environment’, *Biotechnology Progress*, 25(5), pp. 1499–1507. Available at: https://doi.org/10.1002/btpr.211.

Bommer, J. *et al.* (1985) ‘Reduction of silicone particle release during haemodialysis’, *Proceedings of the European Dialysis and Transplant Association - European Renal Association. European Dialysis and Transplant Association - European Renal Association. Congress*, 21, pp. 287–290. Available at: https://pubmed.ncbi.nlm.nih.gov/3991512.

Boubeta, F.M., Soler-Illia, G.J.A.A. and Tagliazucchi, M. (2018) ‘Electrostatically Driven Protein Adsorption: Charge Patches versus Charge Regulation’, *Langmuir*, 34(51), pp. 15727–15738. Available at: https://doi.org/10.1021/acs.langmuir.8b03411.

Boychyn, M. *et al.* (2004) ‘Performance prediction of industrial centrifuges using scale-down models.’, *Bioprocess and biosystems engineering*, 26(6), pp. 385–391. Available at: https://doi.org/10.1007/s00449-003-0328-y.

Bremer, M.G.E.G. *et al.* (2004) ‘Electrostatic interactions between immunoglobulin (IgG) molecules and a charged sorbent’, *Colloids and*

Surfaces A: Physicochemical and Engineering Aspects, 250(1-3 SPEC. ISS.), pp. 29–42. Available at: https://doi.org/10.1016/j.colsurfa.2004.05.026.

Briceño, J.C. and Runge, T.M. (1992) ‘Tubing spallation in extracorporeal circuits. An in vitro study using an electronic particle counter’, *The International journal of artificial organs*, 15(4), pp. 222–228. Available at: https://pubmed.ncbi.nlm.nih.gov/1587644.

Byrne, E.P. *et al.* (2002) *Innuence of shear on particle size and fractal dimension of whey protein precipitates: implications for scale-up and centrifugal clariÿcation eeciency*, *Chemical Engineering Science*. Available at: www.elsevier.com/locate/ces.

Cai, S. *et al.* (2006) ‘Botulinum Neurotoxin Light Chain Refolds at Endosomal pH for its Translocation’, *The Protein Journal*, 25(December), pp. 455–462. Available at: https://doi.org/10.1007/s10930-006-9028-1.

Calero-Rubio, C. *et al.* (2018) ‘Predicting Protein-Protein Interactions of Concentrated Antibody Solutions Using Dilute Solution Data and Coarse-Grained Molecular Models’, *Journal of Pharmaceutical Sciences*, 107(5), pp. 1269–1281. Available at: https://doi.org/https://doi.org/10.1016/j.xphs.2017.12.015.

Callahan, Daniel J., Stanley, B. and Li, Y. (2014) ‘Control of protein particle formation during ultrafiltration/diafiltration through interfacial protection’, *Journal of Pharmaceutical Sciences*, 103(3), pp. 862–869. Available at: https://doi.org/10.1002/jps.23861.

Callahan, Daniel J, Stanley, B. and Li, Y. (2014) ‘Control of Protein Particle Formation During Ultrafiltration/Diafiltration Through Interfacial Protection’, *Journal of Pharmaceutical Sciences*, 103(3), pp. 862–869. Available at: https://doi.org/10.1002/jps.23861.

Chakroun, N. *et al.* (2016) ‘Mapping the Aggregation Kinetics of a Therapeutic Antibody Fragment’, *Molecular Pharmaceutics*, 13(2), pp. 307–319. Available at: https://doi.org/10.1021/acs.molpharmaceut.5b00387.

Chellappan, G. *et al.* (2015) ‘Structural and functional analysis of botulinum neurotoxin subunits for pH-dependent membrane channel formation and translocation’, *Biochimica et Biophysica Acta (BBA) - Proteins and Proteomics*, 1854(10), pp. 1510–1516. Available at: https://doi.org/10.1016/j.bbapap.2015.05.013.

Chen, R. *et al.* (2010) ‘Improved soluble expression and characterization of the Hc domain of Clostridium botulinum neurotoxin serotype A in Escherichia coli by using a PCR-synthesized gene and a Trx co-expression strain’, *Protein Expression and Purification*, 71(1), pp. 79–84. Available at: https://doi.org/10.1016/j.pep.2009.11.007.

Cherry, R.S. and Papoutsakis, E.T. (1986) *Hydrodynamic effects on cells in agitated tissue culture reactors*, *Bioprocess Engineering*.

Chi, E.Y. *et al.* (2005) ‘Heterogeneous nucleation-controlled particulate formation of recombinant human platelet-activating factor acetylhydrolase in pharmaceutical formulation’, *Journal of Pharmaceutical Sciences*, 94(2), pp. 256–274. Available at: https://doi.org/10.1002/jps.20237.

Codina, N. *et al.* (2019) ‘An Expanded Conformation of an Antibody Fab Region by X-Ray Scattering, Molecular Dynamics, and smFRET Identifies an

Aggregation Mechanism’, *Journal of Molecular Biology*, 431(7), pp. 1409–1425. Available at: https://doi.org/10.1016/j.jmb.2019.02.009.

Croughan, M.S., Hamel, J.F. and Wang, D.I.C. (2006) ‘Hydrodynamic effects on animal cells grown in microcarrier cultures’, *Biotechnology and Bioengineering*, 95(2), pp. 295–305. Available at: https://doi.org/10.1002/bit.21158.

Deiringer, N. *et al.* (2022) ‘Catching Speedy Gonzales: Driving forces for Protein Film Formation on Silicone Rubber Tubing During Pumping’, *Journal of Pharmaceutical Sciences*, 111(6), pp. 1577–1586. Available at: https://doi.org/10.1016/j.xphs.2022.02.013.

Deiringer, N. and Friess, W. (2022a) ‘Proteins on the Rack: Mechanistic Studies on Protein Particle Formation During Peristaltic Pumping’, *Journal of Pharmaceutical Sciences*, 111(5), pp. 1370–1378. Available at: https://doi.org/10.1016/j.xphs.2022.01.035.

Deiringer, N. and Friess, W. (2022b) ‘Reaching the breaking point: Effect of tubing characteristics on protein particle formation during peristaltic pumping’, *International Journal of Pharmaceutics*, 627. Available at: https://doi.org/10.1016/j.ijpharm.2022.122216.

Deiringer, N., Leitner, I. and Friess, W. (2023) ‘Effect of the Tubing Material Used in Peristaltic Pumping in Tangential Flow Filtration Processes of Biopharmaceutics on Particle Formation and Flux’, *Journal of Pharmaceutical Sciences*, 112(3), pp. 665–672. Available at: https://doi.org/10.1016/j.xphs.2022.10.005.

Dobson, J. *et al.* (2017) ‘Inducing protein aggregation by extensional flow’, *Source*, 114(18), pp. 4673–4678. Available at: https://doi.org/10.2307/26481856.

Dreckmann, T. *et al.* (2020) ‘Low volume aseptic filling: Impact of pump systems on shear stress’, *European Journal of Pharmaceutics and Biopharmaceutics*, 147(December 2019), pp. 10–18. Available at: https://doi.org/10.1016/j.ejpb.2019.12.006.

Duerkop, M. *et al.* (2018) ‘Influence of cavitation and high shear stress on HSA aggregation behavior’, *Engineering in Life Sciences*, 18(3), pp. 169–178. Available at: https://doi.org/10.1002/elsc.201700079.

Dufrechou, M. *et al.* (2012) ‘Stability of white wine proteins: Combined effect of pH, ionic strength, and temperature on their aggregation’, *Journal of Agricultural and Food Chemistry*, 60(5), pp. 1308–1319. Available at: https://doi.org/10.1021/jf204048j.

European Medicines Agency (EMA) (2000) *ICH Q6B Specifications: test procedures and acceptance criteria for biotechnological/biological products - Scientific guideline*. Available at: https://www.ema.europa.eu/en/ich-q6b-specifications-test-procedures-acceptance-criteria-biotechnological-biological-products (Accessed: 20 September 2023).

European Medicines Agency (EMA) (2013) *ICH Q11 Development and manufacture of drug substances (chemical entities and biotechnological/biological entities) - Scientific guideline*. Available at: https://www.ema.europa.eu/en/ich-q11-development-manufacture-drug-substances-chemical-entities-biotechnological-biological (Accessed: 19 September 2023).

European Medicines Agency (EMA) (2020) *ICH Q12 Technical and regulatory considerations for pharmaceutical product lifecycle management - Scientific guideline*. Available at: https://www.ema.europa.eu/en/ich-q12-technical-regulatory-considerations-pharmaceutical-product-lifecycle-management-scientific (Accessed: 19 September 2023).

European Medicines Agency (EMA) (2022) *ICH Guideline Q5A(R2) on viral safety evaluation of biotechnology products derived from cell lines of human or animal origin - Scientific guideline*. Available at: https://www.ema.europa.eu/en/ich-guideline-q5ar2-viral-safety-evaluation-biotechnology-products-derived-cell-lines-human-animal (Accessed: 20 September 2023).

Fanthom, T.B. *et al.* (2023) 'Solid-Solid Interfacial Contact of Tubing Walls Drives Therapeutic Protein Aggregation During Peristaltic Pumping', *Journal of Pharmaceutical Sciences* [Preprint]. Available at: https://doi.org/10.1016/j.xphs.2023.08.012.

Fernández, C. and Minton, A.P. (2009) 'Static light scattering from concentrated protein solutions II: Experimental test of theory for protein mixtures and weakly self-associating proteins', *Biophysical Journal*, 96(5), pp. 1992–1998. Available at: https://doi.org/10.1016/j.bpj.2008.11.054.

Fernandez-Cerezo, L. *et al.* (2019) 'An ultra scale-down method to investigate monoclonal antibody processing during tangential flow filtration using ultrafiltration membranes', *Biotechnology and Bioengineering*, 116(3), pp. 581–590. Available at: https://doi.org/10.1002/bit.26859.

Fernandez-Cerezo, L. *et al.* (2020) 'The prediction of the operating conditions on the permeate flux and on protein aggregation during membrane processing of monoclonal antibodies', *Journal of Membrane Science*, 596(June 2019), p. 117606. Available at: https://doi.org/10.1016/j.memsci.2019.117606.

Fischer, A. and Montal, M. (2007) 'Single molecule detection of intermediates during botulinum neurotoxin translocation across membranes', *Proceedings of the National Academy of Sciences of the United States of America*, 104(25), pp. 10447–10452. Available at: https://doi.org/10.1073/pnas.0700046104.

Fogolari, F. *et al.* (2009) 'Electric dipole reorientation in the interaction of botulinum neurotoxins with neuronal membranes', *FEBS Letters*, 583(14), pp. 2321–2325. Available at: https://doi.org/10.1016/j.febslet.2009.06.046.

Frachon, T. *et al.* (2016) 'Insulin Aggregation at a Dynamic Solid-Liquid-Air Triple Interface', *Langmuir*, 32(49), pp. 13009–13019. Available at: https://doi.org/10.1021/acs.langmuir.6b03314.

Frevert, J. (2010) 'Content of botulinum neurotoxin in botox®vistabel ®, dysport®azzalure®, and xeomin®bocouture', *Drugs in R and D*, 10(2), pp. 67–73. Available at: https://doi.org/10.2165/11584780-000000000-00000.

Gao, Y.L. *et al.* (2010) 'Expression of Hc fragment from Clostridium botulinum neurotoxin serotype B in Escherichia coli and its use as a good immunogen', *Human Vaccines*, 6(6), pp. 462–466. Available at: https://doi.org/10.4161/hv.6.6.11709.

García-Salas, S. *et al.* (2021) ‘Shear rate as scale-up criterion of the protein production with enhanced proteolytic activity by phosphate addition in the Jacaratia mexicana cell culture’, *Biotechnology and Biotechnological Equipment*, 35(1), pp. 1031–1042. Available at: https://doi.org/10.1080/13102818.2021.1944317.

Garidel, P., Blume, A. and Wagner, M. (2015) ‘Prediction of colloidal stability of high concentration protein formulations’, *Pharmaceutical Development and Technology*, 20(3), pp. 367–374. Available at: https://doi.org/10.3109/10837450.2013.871032.

George, W.K. (2013) *Lectures in Turbulence for the 21st Century*. Available at: www.turbulence-online.com.

Gessler, F. (2005) ‘A new scaleable method for the purification of botulinum neurotoxin type E’, *Journal of Biotechnology*, 119(2), pp. 204–211. Available at: https://doi.org/10.1016/j.jbiotec.2005.03.013.

Gikanga, B. *et al.* (2017) ‘Processing Impact on Monoclonal Antibody Drug Products: Protein Subvisible Particulate Formation Induced by Grinding Stress’, *PDA journal of pharmaceutical science and technology*, 71(3), pp. 172–188. Available at: https://doi.org/10.5731/pdajpst.2016.006726.

Goldberg, D.S. *et al.* (2011) ‘Formulation Development of Therapeutic Monoclonal Antibodies Using High-Throughput Fluorescence and Static Light Scattering Techniques: Role of Conformational and Colloidal Stability’, *Journal of Pharmaceutical Sciences*, 100(4), pp. 1306–1315. Available at: https://doi.org/10.1002/jps.22371.

Gomme, P.T. *et al.* (2006) ‘Effect of lobe pumping on human albumin: investigating the underlying mechanisms of aggregate formation1’, *Biotechnology and Applied Biochemistry*, 43(2), p. 103. Available at: https://doi.org/10.1042/ba20050147.

Grabarek, A.D. *et al.* (2019) ‘What Makes Polysorbate Functional? Impact of Polysorbate 80 Grade and Quality on IgG Stability During Mechanical Stress’, *Journal of Pharmaceutical Sciences*, pp. 1–10. Available at: https://doi.org/10.1016/j.xphs.2019.10.015.

Greenblott, D.N. *et al.* (2022) ‘Machine learning approaches to root cause analysis, characterization, and monitoring of subvisible particles in monoclonal antibody formulations’, *Biotechnology and Bioengineering* [Preprint]. Available at: https://doi.org/10.1002/bit.28239.

Grigolato, F. and Arosio, P. (2020) ‘Synergistic effects of flow and interfaces on antibody aggregation’, *Biotechnology and Bioengineering*, 117(2), pp. 417–428. Available at: https://doi.org/10.1002/bit.27212.

Gu, S. *et al.* (2012) ‘Botulinum Neurotoxin Is Shielded by NTNHA in an Interlocked Complex’, *Science*, 335(6071), pp. 977–981. Available at: https://doi.org/10.1126/science.1214270.

de Guibert, D. *et al.* (2020) ‘Flow process and heating conditions modulate the characteristics of whey protein aggregates.’, *Journal of Food Engineering*, 264. Available at: https://doi.org/10.1016/j.jfoodeng.2019.07.022.

Hara, S. *et al.* (2015) ‘Effects of a radial gap on vortical flow structures around a rotating disk in a cylindrical casing’, *Journal of Visualization*, 18(3), pp. 501–510. Available at: https://doi.org/10.1007/s12650-015-0292-z.

Heljo, P. *et al.* (2023a) ‘Impact of Stress on the Immunogenic Potential of Adalimumab’, *Journal of Pharmaceutical Sciences*, 112(4), pp. 1000–1010. Available at: https://doi.org/10.1016/j.xphs.2022.12.027.

Heljo, P. *et al.* (2023b) ‘Impact of Stress on the Immunogenic Potential of Adalimumab’, *Journal of Pharmaceutical Sciences*, 112, pp. 1000–1010. Available at: https://doi.org/10.1016/j.xphs.2022.12.027.

Her, C. *et al.* (2020) ‘Effects of Tubing Type, Operating Parameters, and Surfactants on Particle Formation During Peristaltic Filling Pump Processing of a mAb Formulation’, *Journal of Pharmaceutical Sciences*, 109(4), pp. 1439–1448. Available at: https://doi.org/10.1016/j.xphs.2020.01.009.

Her, C. and Carpenter, J.F. (2019) ‘Effects of Tubing Type, Formulation, and Postpumping Agitation on Nanoparticle and Microparticle Formation in Intravenous Immunoglobulin Solutions Processed With a Peristaltic Filling Pump’, *Journal of Pharmaceutical Sciences*, pp. 1–11. Available at: https://doi.org/10.1016/j.xphs.2019.05.013.

Her, C. and Carpenter, J.F. (2020) ‘Effects of Tubing Type, Formulation, and Postpumping Agitation on Nanoparticle and Microparticle Formation in Intravenous Immunoglobulin Solutions Processed With a Peristaltic Filling Pump’, *Journal of Pharmaceutical Sciences*, 109(1), pp. 739–749. Available at: https://doi.org/10.1016/j.xphs.2019.05.013.

Hop, C.J.W. *et al.* (2023) ‘Hydrodynamics of a rotor-stator spinning disk reactor: Investigations by large-eddy simulation’, *Physics of Fluids*, 35(3). Available at: https://doi.org/10.1063/5.0137405.

Hutchinson, N. *et al.* (2006) ‘Shear stress analysis of mammalian cell suspensions for prediction of industrial centrifugation and its verification’, *Biotechnology and Bioengineering*, 95(3), pp. 483–491. Available at: https://doi.org/10.1002/bit.21029.

Jackman, J.A. *et al.* (2017) ‘Indirect Nanoplasmonic Sensing Platform for Monitoring Temperature-Dependent Protein Adsorption’. Available at: https://doi.org/10.1021/acs.analchem.7b03921.

Jaspe, J. and Hagen, S.J. (2006) ‘Do protein molecules unfold in a simple shear flow?’, *Biophysical Journal*, 91(9), pp. 3415–3424. Available at: https://doi.org/10.1529/biophysj.106.089367.

Jasulaityte, G., Johansson, H.J. and Bracewell, D.G. (2020) ‘Chromatography process development aided by a dye-based assay’, *Journal of Chemical Technology and Biotechnology*, 95(1), pp. 132–141. Available at: https://doi.org/10.1002/jctb.6214.

Jing, Z.Y. *et al.* (2022) ‘Characterization of Grinding-Induced Subvisible Particles and Free Radicals in a Freeze-Dried Monoclonal Antibody Formulation’, *Pharmaceutical Research*, 39(2), pp. 399–410. Available at: https://doi.org/10.1007/s11095-022-03170-9.

Jiskoot, W. *et al.* (2012) ‘Protein instability and immunogenicity: Roadblocks to clinical application of injectable protein delivery systems for sustained release’, *Journal of Pharmaceutical Sciences*, 101(3), pp. 946–954. Available at: https://doi.org/10.1002/jps.23018.

Johnson, E.A. (2018) ‘Manufacture of Commercial Botulinum Neurotoxins for Human Treatment’, *Treatment of Dystonia*, pp. 120–127. Available at: https://doi.org/10.1017/9781316459324.027.

Kalonia, C.K. *et al.* (2018) ‘Protein Adsorption and Layer Formation at the Stainless Steel-Solution Interface Mediates Shear-Induced Particle Formation for an IgG1 Monoclonal Antibody’, *Molecular Pharmaceutics*, 15(3), pp. 1319–1331. Available at: https://doi.org/10.1021/acs.molpharmaceut.7b01127.

Kamaraju, H., Wetzel, K. and Kelly, W.J. (2010) ‘Modeling shear-induced CHO cell damage in a rotary positive displacement pump’, *Biotechnology Progress*, 26(6), pp. 1606–1615. Available at: https://doi.org/10.1002/btpr.479.

Khan, T.A., Mahler, H.C. and Kishore, R.S.K. (2015) ‘Key interactions of surfactants in therapeutic protein formulations: A review’, *European Journal of Pharmaceutics and Biopharmaceutics*, 97, pp. 60–67. Available at: https://doi.org/10.1016/j.ejpb.2015.09.016.

Kiesel, I. *et al.* (2014) ‘Temperature-Driven Adsorption and Desorption of Proteins at Solid–Liquid Interfaces’, *Langmuir*, 30(8), pp. 2077–2083. Available at: https://doi.org/10.1021/la404884a.

Koepf, E. *et al.* (2017) ‘The film tells the story: Physical-chemical characteristics of IgG at the liquid-air interface’, *European Journal of Pharmaceutics and Biopharmaceutics*, 119, pp. 396–407. Available at: https://doi.org/10.1016/j.ejpb.2017.07.006.

Koepf, E. *et al.* (2018) ‘Notorious but not understood: How liquid-air interfacial stress triggers protein aggregation’, *International Journal of Pharmaceutics*, 537(1–2), pp. 202–212. Available at: https://doi.org/10.1016/j.ijpharm.2017.12.043.

Kristinsson, H.G. and Hultin, H.O. (2004) ‘Changes in trout hemoglobin conformations and solubility after exposure to acid and alkali pH’, *Journal of Agricultural and Food Chemistry*, 52(11), pp. 3633–3643. Available at: https://doi.org/10.1021/jf034563g.

Lalaurie, C.J. *et al.* (2022) ‘Elucidation of critical pH-dependent structural changes in Botulinum Neurotoxin E’, *Journal of Structural Biology*, 214(3), p. 107876. Available at: https://doi.org/10.1016/j.jsb.2022.107876.

Lefèvre, G. *et al.* (2009) ‘Determination of isoelectric points of metals and metallic alloys by adhesion of latex particles’, *Journal of Colloid and Interface Science*, 337(2), pp. 449–455. Available at: https://doi.org/10.1016/j.jcis.2009.05.005.

Li, R. *et al.* (2022) ‘Formation of whey protein aggregates by partial hydrolysis and reduced thermal treatment’, *Food Hydrocolloids*, 124. Available at: https://doi.org/10.1016/j.foodhyd.2021.107206.

Li, Y. and Roberts, C.J. (2009) ‘Lumry-eyring nucleated-polymerization model of protein aggregation kinetics. 2. Competing growth via condensation and chain polymerization’, *Journal of Physical Chemistry B*, 113(19), pp. 7020–7032. Available at: https://doi.org/10.1021/jp8083088.

Lin, G.L. *et al.* (2016) ‘Interfacial dilatational deformation accelerates particle formation in monoclonal antibody solutions’, *Soft Matter*, 12(14), pp. 3293–3302. Available at: https://doi.org/10.1039/c5sm02830b.

Lippok, S. *et al.* (2016) ‘Shear-Induced Unfolding and Enzymatic Cleavage of Full-Length VWF Multimers’, *Biophysical Journal*, 110(3), pp. 545–554. Available at: https://doi.org/10.1016/j.bpj.2015.12.023.

Mahler, H.C. and Jiskoot, W. (2012) *Analysis of Aggregates and Particles in Protein Pharmaceuticals*, *Analysis of Aggregates and Particles in Protein Pharmaceuticals*. Available at: https://doi.org/10.1002/9781118150573.

Majhi, P. *et al.* (2006) ‘Electrostatically driven protein aggregation: beta-lactoglobulin at low ionic strength’, *Langmuir*, 22(22), pp. 9150–9159.

Manopoulos, C. *et al.* (2020) ‘Optimal design in roller pump system applications for linear infusion’, *Computation*, 8(2). Available at: https://doi.org/10.3390/COMPUTATION8020035.

Manopoulos, C., Tsoukalis, A. and Mathioulakis, D. (2022) ‘Suppression of flow pulsations and energy consumption of a drug delivery roller pump based on a novel tube design’, *Proceedings of the Institution of Mechanical Engineers, Part C: Journal of Mechanical Engineering Science*, 236(14), pp. 7759–7770. Available at: https://doi.org/10.1177/09544062221084188.

Martos, A. *et al.* (2017) ‘Trends on Analytical Characterization of Polysorbates and Their Degradation Products in Biopharmaceutical Formulations’, *Journal of Pharmaceutical Sciences*, 106(7), pp. 1722–1735. Available at: https://doi.org/10.1016/j.xphs.2017.03.001.

McUmber, A.C., Randolph, T.W. and Schwartz, D.K. (2015) ‘Electrostatic Interactions Influence Protein Adsorption (but Not Desorption) at the Silica-Aqueous Interface’, *Journal of Physical Chemistry Letters*, 6(13), pp. 2583–2587. Available at: https://doi.org/10.1021/acs.jpclett.5b00933.

Menter, F. (1993) ‘Zonal Two Equation k-w Turbulence Models For Aerodynamic Flows’, in *23rd Fluid Dynamics, Plasmadynamics, and Lasers Conference*. American Institute of Aeronautics and Astronautics (Fluid Dynamics and Co-located Conferences). Available at: https://doi.org/doi:10.2514/6.1993-2906.

Minton, A.P. (2007) ‘Static light scattering from concentrated protein solutions, I: General theory for protein mixtures and application to self-associating proteins’, *Biophysical Journal*, 93(4), pp. 1321–1328. Available at: https://doi.org/10.1529/biophysj.107.103895.

Montal, M. (2010) ‘Botulinum Neurotoxin: A Marvel of Protein Design’, *Annual Review of Biochemistry*, 79(1), pp. 591–617. Available at: https://doi.org/10.1146/annurev.biochem.051908.125345.

Moussa, E.M. *et al.* (2016) ‘Immunogenicity of Therapeutic Protein Aggregates’, *Journal of Pharmaceutical Sciences*, 105(2), pp. 417–430. Available at: https://doi.org/10.1016/j.xphs.2015.11.002.

Mulligan, S. *et al.* (2018) ‘Understanding turbulent free-surface vortex flows using a Taylor-Couette flow analogy’, *Scientific Reports*, 8(1), pp. 1–14. Available at: https://doi.org/10.1038/s41598-017-16950-w.

Nayak, A. *et al.* (2011) ‘Characterization of Subvisible Particle Formation During the Filling Pump Operation of a Monoclonal Antibody Solution’, *Journal of Pharmaceutical Sciences*, 100(10), pp. 4198–4204. Available at: https://doi.org/10.1002/jps.22676.

Nicoud, L. *et al.* (2014) ‘Kinetic Analysis of the Multistep Aggregation Mechanism of Monoclonal Antibodies’, *The Journal of Physical Chemistry B*, 118(36), pp. 10595–10606. Available at: https://doi.org/10.1021/jp505295j.

Nie, J. *et al.* (2022) ‘The efficient development of a novel recombinant adenovirus zoster vaccine perfusion production process’, *Vaccine*, 40(13), pp. 2036–2043. Available at: https://doi.org/10.1016/j.vaccine.2022.02.024.

Oliva, A., Fariña, J.B. and Llabrés, M. (2016) ‘Pre-study and in-study validation of a size-exclusion chromatography method with different detection modes for the analysis of monoclonal antibody aggregates’, *Journal of Chromatography B: Analytical Technologies in the Biomedical and Life Sciences*, 1022, pp. 206–212. Available at: https://doi.org/10.1016/j.jchromb.2016.04.022.

Paul, E.L., Atiemo-Obeng, V.A. and Kresta, S.M. (2003) ‘7.3 Overview of Pipeline Device Options by Flow Regime’, in *Handbook of Industrial Mixing - Science and Practice*. John Wiley & Sons, pp. 394–395. Available at: https://app.knovel.com/hotlink/pdf/id:kt007ENVV3/handbook-industrial-mixing/overview-pipeline-device.

Perry, C. *et al.* (2023) ‘Insights into product and process related challenges of lentiviral vector bioprocessing’, *Biotechnology and Bioengineering* [Preprint]. Available at: https://doi.org/10.1002/bit.28498.

Pharmacopeia, U.S. (2006) ‘USP/NF General Chapter< 788> Particulate Matter in Injections’, *National Formulary, USP29-NF-24 (suppl 2). Rockville, MD: USP* [Preprint].

Pharmacopeia, U.S. (2018) ‘USP/NF General Chapter<787> Subvisible Particulate Matter in Therapeutic Protein Injections’, *National Formulary, USP41. Rockville, MD: USP* [Preprint].

Pindrus, M.A. *et al.* (2018) ‘The Effect of Low Ionic Strength on Diffusion and Viscosity of Monoclonal Antibodies’, *Molecular Pharmaceutics*, 15(8), pp. 3133–3142. Available at: https://doi.org/10.1021/acs.molpharmaceut.8b00210.

Rafferty, K. *et al.* (2017) ‘Polysorbate 80 Disposition Following Tangential Flow Filtration’, in *AIChE Annual Meeting*.

Randolph, T.W. *et al.* (2015) ‘Do not drop: Mechanical shock in vials causes cavitation, protein aggregation, and particle formation’, *Journal of Pharmaceutical Sciences*, 104(2), pp. 602–611. Available at: https://doi.org/10.1002/jps.24259.

Rayat, A.C. *et al.* (2016) ‘Ultra scale-down approaches to enhance the creation of bioprocesses at scale: impacts of process shear stress and early recovery stages’, *Current Opinion in Chemical Engineering*. Elsevier Ltd, pp. 150–157. Available at: https://doi.org/10.1016/j.coche.2016.09.012.

Reinke, P., Schmidt, M. and Beckmann, T. (2018) ‘The cavitating Taylor-Couette flow’, *Physics of Fluids*, 30(10). Available at: https://doi.org/10.1063/1.5049743.

Riek, R. (2017) ‘The three-dimensional structures of amyloids’, *Cold Spring Harbor Perspectives in Biology*, 9(2). Available at: https://doi.org/10.1101/cshperspect.a023572.

Riesz, P. and Kondo, T. (1992) ‘Free radical formation induced by ultrasound and its biological implications’, *Free Radical Biology and Medicine*, 13(3), pp. 247–270. Available at: https://doi.org/10.1016/0891-5849(92)90021-8.

Roberts, C.J. (2014) ‘Therapeutic protein aggregation: Mechanisms, design, and control’, *Trends in Biotechnology*, 32(7), pp. 372–380. Available at: https://doi.org/10.1016/j.tibtech.2014.05.005.

Roberts, D. *et al.* (2015) ‘Specific ion and buffer effects on protein-protein interactions of a monoclonal antibody’, *Molecular Pharmaceutics*, 12(1), pp. 179–193. Available at: https://doi.org/10.1021/mp500533c.

Rosenberg, A.S., Verthelyi, D. and Cherney, B.W. (2012) ‘Managing uncertainty: A perspective on risk pertaining to product quality attributes as they bear on immunogenicity of therapeutic proteins’, *Journal of Pharmaceutical Sciences*, 101(10), pp. 3560–3567. Available at: https://doi.org/https://doi.org/10.1002/jps.23244.

Rosenberg, E. *et al.* (2009) ‘Ultrafiltration concentration of monoclonal antibody solutions: Development of an optimized method minimizing aggregation’, *Journal of Membrane Science*, 342(1–2), pp. 50–59. Available at: https://doi.org/10.1016/j.memsci.2009.06.028.

Rossetto, O. and Montecucco, C. (2018) ‘Molecular Mechanisms of Botulinum Toxin’, in *Treatment of Dystonia*. Cambridge University Press, pp. 102–105. Available at: https://doi.org/10.1017/9781316459324.023.

Rossetto, O., Pirazzini, M. and Montecucco, C. (2014) ‘Botulinum neurotoxins: Genetic, structural and mechanistic insights’, *Nature Reviews Microbiology*, 12(8), pp. 535–549. Available at: https://doi.org/10.1038/nrmicro3295.

Sahin, E. *et al.* (2010) ‘Comparative effects of pH and ionic strength on protein-protein interactions, unfolding, and aggregation for IgG1 antibodies’, *Journal of Pharmaceutical Sciences*, 99(12), pp. 4830–4848. Available at: https://doi.org/10.1002/jps.22198.

Salami, H. *et al.* (2023) ‘Deep learning image analysis models pretrained on daily objects are useful for the preliminary characterization of particulate pharmaceutical samples’, *Biotechnology and Bioengineering* [Preprint]. Available at: https://doi.org/10.1002/bit.28488.

Saller, V. *et al.* (2015) ‘Particle Shedding from Peristaltic Pump Tubing in Biopharmaceutical Drug Product Manufacturing’, *Journal of Pharmaceutical Sciences*, 104(4), pp. 1440–1450. Available at: https://doi.org/10.1002/jps.24357.

Saller, V. *et al.* (2018) ‘Influence of particle shedding from silicone tubing on antibody stability’, *Journal of Pharmacy and Pharmacology*, 70(5), pp. 675–685. Available at: https://doi.org/10.1111/jphp.12603.

Santos, O. *et al.* (2006) ‘Whey protein adsorption onto steel surfaces-effect of temperature, flow rate, residence time and aggregation’, *Journal of Food Engineering*, 74(4), pp. 468–483. Available at: https://doi.org/10.1016/j.jfoodeng.2005.03.037.

Schleinzer, F. *et al.* (2023) ‘Backgrounded Membrane Imaging—A Valuable Alternative for Particle Detection of Biotherapeutics?’, *Journal of Pharmaceutical Innovation* [Preprint]. Available at: https://doi.org/10.1007/s12247-023-09734-5.

Sediq, A.S. *et al.* (2016) ‘No Touching! Abrasion of Adsorbed Protein Is the Root Cause of Subvisible Particle Formation during Stirring’, *Journal of Pharmaceutical Sciences*, 105(2), pp. 519–529. Available at: https://doi.org/10.1016/j.xphs.2015.10.003.

Simpson, D.M. *et al.* (2016) ‘Practice guideline update summary: Botulinum neurotoxin for the treatment of blepharospasm, cervical dystonia, adult spasticity, and headache: Report of the Guideline Development Subcommittee of the American Academy of Neurology.’, *Neurology*, 86(19), pp. 1818–26. Available at: https://doi.org/10.1212/WNL.0000000000002560.

Simpson, L.W., Good, T.A. and Leach, J.B. (2020) ‘Protein folding and assembly in confined environments: Implications for protein aggregation in hydrogels and tissues’, *Biotechnology Advances*, 42(June). Available at: https://doi.org/10.1016/j.biotechadv.2020.107573.

Sparkes, J. and Holland, C. (2017) ‘Analysis of the pressure requirements for silk spinning reveals a pultrusion dominated process’, *Nature Communications*, 8(1). Available at: https://doi.org/10.1038/s41467-017-00409-7.

Steinhauer, T. *et al.* (2015) ‘Membrane fouling during ultra- and microfiltration of whey and whey proteins at different environmental conditions: The role of aggregated whey proteins as fouling initiators’, *Journal of Membrane Science*, 489, pp. 20–27. Available at: https://doi.org/10.1016/j.memsci.2015.04.002.

Stetefeld, J., McKenna, S.A. and Patel, T.R. (2016) ‘Dynamic light scattering: a practical guide and applications in biomedical sciences’, *Biophysical*

Reviews, 8(4), pp. 409–427. Available at: https://doi.org/10.1007/s12551-016-0218-6.

Stroev, P. V., Hoskins, P.R. and Easson, W.J. (2007) ‘Distribution of wall shear rate throughout the arterial tree: A case study’, *Atherosclerosis*, 191(2), pp. 276–280. Available at: https://doi.org/10.1016/j.atherosclerosis.2006.05.029.

Suslick, K.S. (1990) ‘Sonochemistry’, *Science*, 247(4949), pp. 1439–1445. Available at: https://doi.org/10.1126/science.247.4949.1439.

Tavakoli-Keshe, R. *et al.* (2014) ‘Understanding the relationship between biotherapeutic protein stability and solid-liquid interfacial shear in constant region mutants of IgG1 and IgG4’, *Journal of Pharmaceutical Sciences*, 103(2), pp. 437–444. Available at: https://doi.org/10.1002/jps.23822.

Taylor, G.I. (1923) ‘VIII. Stability of a viscous liquid contained between two rotating cylinders’, *Philosophical Transactions of the Royal Society of London. Series A, Containing Papers of a Mathematical or Physical Character*, 223(605–615), pp. 289–343. Available at: https://doi.org/10.1098/rsta.1923.0008.

Thite, N.G. *et al.* (2022) ‘Machine Learning Analysis Provides Insight into Mechanisms of Protein Particle Formation Inside Containers During Mechanical Agitation’, *Journal of Pharmaceutical Sciences*, 111(10), pp. 2730–2744. Available at: https://doi.org/10.1016/j.xphs.2022.06.017.

Tian, X. *et al.* (2016) ‘A Comprehensive Evaluation of Nanoparticle Tracking Analysis (NanoSight) for Characterization of Proteinaceous Submicron Particles’, *Journal of Pharmaceutical Sciences*, 105(11), pp. 3366–3375. Available at: https://doi.org/10.1016/j.xphs.2016.08.009.

Toth, S.I., Smith, L.A. and Ahmed, S.A. (2009) ‘Extreme sensitivity of botulinum neurotoxin domains towards mild agitation’, *Journal of Pharmaceutical Sciences*, 98(9), pp. 3302–3311. Available at: https://doi.org/10.1002/jps.21676.

Tyagi, A.K. *et al.* (2009) ‘IgG particle formation during filling pump operation: A case study of heterogeneous nucleation on stainless steel nanoparticles’, *Journal of Pharmaceutical Sciences*, 98(1), pp. 94–104. Available at: https://doi.org/10.1002/jps.21419.

United States Pharmacopeia (2023) ‘General Chapter, ⟨88⟩ Biological Reactivity Tests, In Vivo’, in *USP-NF*. Rockville, MD: United States Pharmacopeia.

Valotta Rodrigues, R. *et al.* (2019) ‘Parameters Influencing Cavitation Within Vials Subjected to Drop Shock’, *Scientific Reports*, 9(1), pp. 1–14. Available at: https://doi.org/10.1038/s41598-019-55668-9.

Vasudev, R., Mathew, S. and Afonina, N. (2015) ‘Characterization of submicron (0.1-1 μm) particles in therapeutic proteins by nanoparticle tracking analysis’, *Journal of Pharmaceutical Sciences*, 104(5), pp. 1622–1631. Available at: https://doi.org/10.1002/jps.24411.

Visscher, F. *et al.* (2013) ‘Residence time distribution in a single-phase rotor-stator spinning disk reactor’, *AIChE Journal*, 59(7), pp. 2686–2693. Available at: https://doi.org/10.1002/aic.14036.

Wallace, E.W.J. *et al.* (2015) ‘Reversible, Specific, Active Aggregates of Endogenous Proteins Assemble upon Heat Stress’, *Cell*, 162(6), pp. 1286–1298. Available at: https://doi.org/10.1016/j.cell.2015.08.041.

Wang, S. *et al.* (2017) ‘Shear contributions to cell culture performance and product recovery in ATF and TFF perfusion systems’, *Journal of Biotechnology*, 246, pp. 52–60. Available at: https://doi.org/10.1016/j.jbiotec.2017.01.020.

Wang, T. *et al.* (2013) ‘Effect of ionic strength and pH on the physical and chemical stability of a monoclonal antibody antigen-binding fragment.’, *Journal of pharmaceutical sciences*, 102(8), pp. 2520–2537. Available at: https://doi.org/10.1002/jps.23645.

Wang, W. *et al.* (2012) ‘Immunogenicity of protein aggregates - Concerns and realities’, *International Journal of Pharmaceutics*, 431(1–2), pp. 1–11. Available at: https://doi.org/10.1016/j.ijpharm.2012.04.040.

Wang, W. and Ohtake, S. (2019) ‘Science and art of protein formulation development’, *International Journal of Pharmaceutics*, 568, p. 118505. Available at: https://doi.org/https://doi.org/10.1016/j.ijpharm.2019.118505.

Wang, W. and Roberts, C.J. (2013) ‘Non-Arrhenius Protein Aggregation’, *The AAPS Journal*, 15(3), pp. 840–851. Available at: https://doi.org/10.1208/s12248-013-9485-3.

Watanabe, T. and Furukawa, H. (2010) ‘Flows around rotating disks with and without rim-shroud gap’, in *Experiments in Fluids*, pp. 631–636. Available at: https://doi.org/10.1007/s00348-009-0785-4.

Wee, H. *et al.* (2020) ‘Quality by Design approaches to assessing the robustness of tangential flow filtration for MAb’, *Biologicals*, 63, pp. 53–61. Available at: https://doi.org/10.1016/j.biologicals.2019.12.001.

Whitcup, S.M. (2021) ‘The History of Botulinum Toxins in Medicine: A Thousand Year Journey BT - Botulinum Toxin Therapy’, in S.M. Whitcup and M. Hallett (eds). Cham: Springer International Publishing, pp. 3–10. Available at: https://doi.org/10.1007/164_2019_271.

Willis, L.F. *et al.* (2018) ‘Using extensional flow to reveal diverse aggregation landscapes for three IgG1 molecules’, *Biotechnology and Bioengineering*, 115(5), pp. 1216–1225. Available at: https://doi.org/10.1002/bit.26543.

Witeof, A.E. *et al.* (2021) ‘Machine Learning and Accelerated Stress Approaches to Differentiate Potential Causes of Aggregation in Polyclonal Antibody Formulations During Shipping’, *Journal of Pharmaceutical Sciences*, 110(7), pp. 2743–2752. Available at: https://doi.org/10.1016/j.xphs.2021.02.029.

Woldeyes, M.A. *et al.* (2019) ‘How Well Do Low- and High-Concentration Protein Interactions Predict Solution Viscosities of Monoclonal Antibodies?’, *Journal of Pharmaceutical Sciences*, 108(1), pp. 142–154. Available at: https://doi.org/10.1016/j.xphs.2018.07.007.

Wood, C. V. *et al.* (2020) ‘Kinetics and Competing Mechanisms of Antibody Aggregation via Bulk- and Surface-Mediated Pathways’, *Journal of Pharmaceutical Sciences*, 109(4), pp. 1449–1459. Available at: https://doi.org/10.1016/j.xphs.2020.01.005.

Wu, H. and Randolph, T.W. (2020) ‘Aggregation and Particle Formation During Pumping of an Antibody Formulation Are Controlled by Electrostatic Interactions Between Pump Surfaces and Protein Molecules’, *Journal of*

Pharmaceutical Sciences, 109(4), pp. 1473–1482. Available at: https://doi.org/10.1016/j.xphs.2020.01.023.

Wu, S.J. *et al.* (2010) ‘Structure-based engineering of a monoclonal antibody for improved solubility’, *Protein Engineering, Design and Selection*, 23(8), pp. 643–651. Available at: https://doi.org/10.1093/protein/gzq037.

Zhang, H. *et al.* (2007) ‘Prediction of shear damage of plasmid DNA in pump and centrifuge operations using an ultra scale-down device’, *Biotechnology Progress*, 23(4), pp. 858–865. Available at: https://doi.org/10.1021/bp070066z.

Zhao, X. *et al.* (2020) ‘Influence of extreme alkaline pH induced unfolding and aggregation on PSE-like chicken protein edible film formation’, *Food Chemistry*, 319. Available at: https://doi.org/10.1016/j.foodchem.2020.126574.

Zheng, X. *et al.* (2023) ‘Soy protein particles with enhanced anti-aggregation behaviors under various heating temperatures, pH, and ionic strengths’, *Food Research International*, 170. Available at: https://doi.org/10.1016/j.foodres.2023.112924.

Zhou, L. *et al.* (1995) ‘Expression and Purification of the Light Chain of Botulinum Neurotoxin A: A Single Mutation Abolishes Its Cleavage of SNAP-25 and Neurotoxicity after Reconstitution with the Heavy Chain’, *Biochemistry*, 34(46), pp. 15175–15181. Available at: https://doi.org/10.1021/bi00046a025.

Žuntar, T. *et al.* (2022) ‘Real-time imaging of monoclonal antibody film reconstitution after mechanical stress at the air-liquid interface by Brewster angle microscopy’, *Colloids and Surfaces B: Biointerfaces*, 218(August), pp. 1–7. Available at: https://doi.org/10.1016/j.colsurfb.2022.112757.